



A new approach towards understanding the ion transfer dynamics in nanostructured carbon-based thin films for energy storage applications

Freddy David Escobar Teran

► To cite this version:

Freddy David Escobar Teran. A new approach towards understanding the ion transfer dynamics in nanostructured carbon-based thin films for energy storage applications. Chemical Physics [physics.chem-ph]. Université Pierre et Marie Curie - Paris VI, 2016. English. NNT : 2016PA066363 . tel-01480252

HAL Id: tel-01480252

<https://theses.hal.science/tel-01480252>

Submitted on 1 Mar 2017

HAL is a multi-disciplinary open access archive for the deposit and dissemination of scientific research documents, whether they are published or not. The documents may come from teaching and research institutions in France or abroad, or from public or private research centers.

L'archive ouverte pluridisciplinaire **HAL**, est destinée au dépôt et à la diffusion de documents scientifiques de niveau recherche, publiés ou non, émanant des établissements d'enseignement et de recherche français ou étrangers, des laboratoires publics ou privés.

Université Pierre et Marie Curie

École doctorale 388 – Chimie physique et chimie analytique de Paris Centre

Laboratoire Interfaces et Systèmes Electrochimiques – UMR 8235

A New Approach towards Understanding the Ion Transfer Dynamics in Nanostructured Carbon-Based Thin Films for Energy Storage Applications

Par Freddy ESCOBAR TERAN

Thèse de doctorat

Dirigée par Hubert PERROT

Présentée et soutenue publiquement le 30 septembre 2016

Devant un jury composé de :

M. Michael HOLZINGER	Directeur de Recherche CNRS	Rapporteur
M. Francisco VICENTE	Professeur Université Valencia	Rapporteur
Mme Stéphanie BETELU	Directeur de Recherche BRGM	Examineur
Mme Christel LABERTY	Professeure UPMC	Examineur
M. Hubert PERROT	Directeur de Recherche CNRS	Directeur de thèse
Mme Ozlem SEL	Chargée de Recherche CNRS	Co-encadrante de thèse

Dedicate to my parents....

Acknowledgements

I would like to thank the research director of LISE, Professor François Huet, for providing the laboratories, and SENESCYT for funding this research work.

Special thanks to my manuscript reviewers, Dr. Francisco Vicente and Dr. Michael Holzinger as well as Dr. Christel Laberty, and Dr. Stéphanie Betelu as jury members for my oral defence.

Many thanks go to my main Ph.D. supervisor, Dr. Hubert Perrot, for these years of cultivating me as a researcher. Thank you for giving me this opportunity to work under your guidance and to learn from your research expertise. Thank you for your support and available for discussions despite your busy schedules.

To co-supervisor, Dr. Ozlem Sel, I would like to express my gratitude for your scientific guidance and encouragement throughout these 4 years. Thank you for the constructive discussions and being supportive at work, with positive and pleasant disposition all the time.

I would like to express my appreciation to the colleagues behind the logistic, administrative and technical assistance, Françoise Pillier, Cyril Bazin, Florence Billon, Daniel Rose, Axel Desnoyers, Veronique Martin, Martine Chaduc, Isabelle Lefebvre and all colleagues at LISE. Merci pour vos délicatesses!

I would also like to express a special thanks to my wife for her collaboration in the manuscript of the thesis.

Table of Contents

Introduction.....	5
CHAPTER I. Bibliography.....	8
I-1. Energy Storage: Batteries and Supercapacitors.....	8
I-1.1. Batteries.....	8
I-1.1.1. History	9
I-1.1.2. Types of Batteries.....	10
I-1.1.3. Principle of Operation	11
I-1.1.4. Battery Performance	13
I-1.1.5. Battery Applications.....	16
I-1.2. Supercapacitors.....	16
I-1.2.1. History	17
I-1.2.2. Principle of Operation for EDLC	18
I-1.2.3. Components of the Supercapacitors	19
I-1.2.4. Proposed Strategies Towards Higher Performance in Supercapacitors.....	30
I-1.2.5. Supercapacitor Applications.....	34
I-2. Diagnostic Tools for Electrodes in Energy Storage.....	35
I-2.1. Electrochemical Methods	35
I-2.1.1. Cyclic Voltammetry (CV)	35
I-2.1.2. Galvanostatic Charge-Discharge method (GCD)	37
I-2.1.3. Electrochemical Impedance Spectroscopy (EIS)	38
I-2.2. Structural and Morphological Analysis: XRD, SEM, TEM, EDX and BET.....	40
I-2.2.1. X-Ray Diffraction (XRD).....	40
I-2.2.2. Scanning Electron Microscopy (SEM) and FEG-SEM.....	41
I-2.2.3. Transmission Electron Microscopy (TEM or HRTEM).....	42
I-2.2.4. Energy-Dispersive X-ray Spectroscopy (EDX)	43
I-2.2.5. Brunauer Emmett and Teller (BET)	44
I-2.3. Classical Electrogravimetric Investigations: Quartz Crystal Microbalance Based Methods.....	45
I-3. The Scope and Objectives of the Ph.D. Thesis.....	49
CHAPTER II. Experimental Part.....	51
II-1. Preparation Procedure of Carbon Based Thin Film Electrodes.....	51
II-1.1. Preparation of Carbon Nanotube (CNT) Based Thin Film Electrodes.....	52
(Single Wall CNT, Double Wall CNT, Multi Wall CNT)	52
II-1.2. Elaboration of Nanocomposite Structures.....	52
II-1.2.1. SWCNT/Prussian Blue Thin Film Electrodes.....	53
II-1.2.2. SWCNT/Polypyrrole Thin Film Electrodes	53

Table of Contents

II-1.3. Elaboration of Electrochemically Reduced Graphene Oxide (ERGO) Thin Film Electrodes	53
II-2. Structural and Morphological Investigation Methods.....	53
II-2.1. Scanning Electron Microscopy (SEM).....	54
II-2.2. Transmission Electron Microscopy (TEM).....	55
II-2.3. Energy Dispersive X-rays (EDX).....	56
II-2.4. X-ray Diffraction.....	57
II-2.5. Nitrogen Physisorption and BET Surface Area Determination.....	58
II-3. Electrochemical and (Electro)gravimetric Techniques.....	60
II-3.1. Quartz Crystal Microbalance (QCM).....	60
II-3.1.1. Piezoelectricity	60
II-3.1.2. Working Principle of QCM.....	63
II-3.1.3. Experimental Set-Up.....	65
II-3.2. Cyclic Electrogravimetry(EQCM).....	66
II-3.2.1. Principle	66
II-3.2.2. Experimental Set-Up.....	67
II-3.2.3. Calculation of the $F(dm/dq)$ Function.....	68
II-3.3. Electrochemical Impedance Spectroscopy (EIS)	69
II-3.3.1. Principle	69
II-3.3.2. Experimental Set-Up.....	72
II-3.4. <i>Ac</i> -Electrogravimetry - A Fast Electrogravimetric Method	73
II-3.4.1. Principle	73
II-3.4.2. Experimental Method: $\Delta V/\Delta V$	75
II-3.4.3. Calibration and Corrections of the <i>Ac</i> -Electrogravimetry System.....	76
II-3.5. Data Treatment of <i>Ac</i> -Electrogravimetry	80
II-3.5.1. Experimental data.....	80
II-3.5.2. Fitting from Mathcad Simulation Data	81
CHAPTER III. Ion dynamics in SWCNT Based Thin Film Electrodes.....	85
III-1. Structure and Morphology of the SWCNT Powders and Prepared Thin Film Electrodes.....	85
III-2. Classical Electrogravimetric Study of SWCNT Thin Film Electrodes in Aqueous NaCl Electrolyte..	88
III-2.1. EQCM measurements on SWCNT Thin Film Electrodes	88
III-2.2. Fdm/dq Function Calculations	89
III-2.3. Specific Capacitance Calculations	90
III-3. <i>Ac</i> -Electrogravimetric Studies of SWCNT Thin Film Electrodes in Aqueous NaCl Electrolyte.....	91
III-3.1. EQCM <i>versus</i> <i>Ac</i> -Electrogravimetry	91
III-4. <i>Ac</i> -Electrogravimetric Study of SWCNT Thin Films in Organic Electrolytes.....	101
III-5. Conclusions.....	105

Table of Contents

CHAPTER IV. Influence of the CNT Type, Structure and Electrolyte Properties on Ion Dynamics..	106
IV-1. Structure and Morphology of the DWCNT and MWCNT Powder and Thin Film Electrodes.....	106
IV-2. Influence of the CNT Types.....	111
IV-2.1. EQCM Study of SWCNT, DWCNT and MWCNT in Aqueous NaCl Electrolyte	111
IV-2.2. <i>Ac</i> -electrogravimetric Study of various CNT Thin Film Electrodes in Aqueous NaCl Electrolyte	113
IV-3. Influence of the Electrolyte Properties.....	122
IV-3.1. EQCM Study of SWCNTs in Aqueous NaCl Electrolyte at different pH	122
IV-3.2. <i>Ac</i> -electrogravimetric Study of SWCNT Thin Film Electrode in Aqueous NaCl Electrolyte at different pH values.	124
IV-3.3. EQCM Study of SWCNT in Different Aqueous Electrolyte: effect of the cation size.....	131
IV-3.4. <i>Ac</i> -electrogravimetric Study of various SWCNT Thin Film Electrodes in Different Aqueous Electrolytes: effect of the cation size.....	133
IV-4. Conclusions.....	141
 CHAPTER V. Composite Thin Film Electrodes and Beyond Carbon Nanotubes.....	143
V-1. Composite Thin Film Electrodes.....	143
V-1.1. SWCNT/Prussian Blue Thin Film Electrodes.....	143
V-1.1.1. Structure and Morphology of the SWCNT/PB Composites	143
V-1.1.2. EQCM Study of the SWCNT/PB Composites.....	145
V-1.1.3. <i>Ac</i> -electrogravimetry Study of the SWCNT/PB Composites	147
V-1.2. SWCNT/Polypyrrole Thin Film Electrodes	153
V-1.2.1. Structure and Morphology of the SWCNT/PPy Composites.....	153
V-1.2.2. EQCM Study of the SWCNT/PPy Composites	153
V-1.2.3. <i>Ac</i> -electrogravimetry Study of the SWCNT/PPy Composites.....	155
V-2. Beyond Carbon Nanotube Based Electrodes.....	160
V-2.1. Electrochemically Reduced Graphene Oxide (ERGO) Thin Film Electrodes	160
V-2.1.1. Structure and Morphology of the ERGO Thin Film Electrodes	161
V-2.1.2. EQCM Study of the ERGO Thin Film Electrodes.....	166
V-2.1.3. <i>Ac</i> -electrogravimetry Study of ERGO Thin Film Electrodes	170
V-3. Conclusions.....	178
 General Conclusions.....	180
Future work.....	182
References.....	183
<i>Résumé de la Thèse en Français.....</i>	194

Introduction

Introduction

Challenges in advanced energy storage devices such as batteries and supercapacitors have led to many recent studies on nanostructured electrode materials associated to various applications. The physical properties such as large specific surface area and a suitable pore size of these nanostructured materials must be optimized in order to improve the performance of these energy storage devices. Nevertheless, these goals even if they are achieved are not sufficient to obtain perfect devices with high performance. Therefore, it is highly significant to meticulously study and understand the electrochemical mechanism related to the ionic transfer between the electrode and the electrolyte which constitutes an important part of the operating principle.

Electrochemical double layer capacitors (EDLC) store charge at the electrode/electrolyte interface based on a reversible adsorption of ions. The EDLCs have been launched using porous carbon electrodes. A marked improvement in performance has been obtained thanks to recent progress in the understanding of the charge storage mechanisms and the development of nanostructured materials with high specific surface area and sophisticated structures.

Nevertheless, even when sophisticated methods of investigations are used, a fair exploration of the different mechanisms of transfer related to the charge storage in a certain material is not as easy as envisaged. For example, when certain coupled methods are used, basically current and gravimetric measurements under cycling potentials, the determination of the species involved in the electrochemical process can be challenging or even questionable. In this case, unreasonable assumptions must be done such as a large contribution of the solvent or the cancellation of the anion contribution.^{1,2} Another legitimate question can be raised on the efficiency of these nanostructured films and the utility of a large surface specific area associated to well-constructed pores and their accessibility to ions.

To answer these key questions, a non-conventional coupled electrochemical and gravimetric method, specifically the electrochemical impedance spectroscopy (EIS) coupled to a fast quartz crystal microbalance (QCM) also called *ac*-electrogravimetry, will be used to study the capacitive

Introduction

charge storage behavior of nanostructured carbon electrodes. Indeed, ion transfer phenomena will condition largely the performances of these materials for energy storage applications. *Ac*-electrogravimetry methodology was largely used for characterizing redox materials such as Prussian Blue or conducting polymers such as polypyrrole or polyaniline.³⁻⁶ It was demonstrated that highly relevant information can be obtained: (i) kinetics and identification of species transferred between the electrode and the electrolyte, (ii) separation of the different contributions related to the charged and non-charged species involved in the electrochemical processes, and (iii) variation of the relative concentrations of the species inside the examined material. Therefore, the *ac*-electrogravimetry methodology appears to be an attractive tool to study the nature of the ionic fluxes located at the electrode/electrolyte interface.

This Ph.D. thesis aims to clarify the relationship between morphology/structure of the prepared carbon films with the motion of ions and free solvent, simply to obtain a better understanding of the mechanisms of ion/solvent transfer and thus, to validate the positive impact of employment of nanostructured electrodes in energy storage devices.

This manuscript is divided into five chapters; experimental results are presented in the last three:

- Chapter I begins with a comprehensive literature review of different energy storage devices, *i.e.* batteries and supercapacitors, including history, principle of operation and different applications. More details are given on the components of these systems in terms of materials and electrolytes, and their impact on the supercapacitor performances is discussed. Thereafter, a literature review of different techniques used for characterizing and evaluating the performances of carbon based electrodes in energy storage is provided. Finally, the scope and objectives, starting from the state of art of the present Ph.D. thesis, are introduced.

- Chapter II begins with a detailed description of sample preparation. Mainly three kinds of samples were prepared: Carbon nanotubes (CNTs), Carbon Nanocomposites (CNT/PB or PPY) and Electrochemically Reduced Graphene Oxide (ERGO). Thereafter follows a description of the methods used for the structural and morphological characterization of samples, particularly, the principle of operation of the methods, the type of instruments used and under which conditions the experiments were performed. Finally, the electrochemical characterization techniques applied in this Ph.D. thesis will be presented/described.

- Chapter III aims to clarify the mechanism of the ion transfer of carbon-based electrodes in order to have a better understanding of the charge storage mechanisms and to validate the positive

Introduction

impact of the use of nanostructured electrodes in energy storage devices. Here, a pertinent example is presented and detailed to demonstrate the power of our approach for single wall CNT (SWCNT) films tested in aqueous NaCl electrolyte. At the end, a key question, which is on the possibility of deconvolution of the classical EQCM responses, was raised by using *ac*-electrogravimetry methodology.

- Chapter IV is dedicated to the study of the influence of the CNT structure (single wall, double walls and multi walls) and electrolyte properties on ion electroadsorption dynamics at the electrode/electrolyte interfaces. The influence of electrolyte pH on the capacitive charge storage behavior is also studied in detail. For these kinds of studies, morphological and structural characterization methods (FEG-SEM, HR-TEM, XRD, N₂ sorption, Raman spectroscopy), and electrochemical methods such as EQCM and *ac*-electrogravimetry were employed.

- Chapter V is dedicated to the interpretation of the results obtained from the study of SWCNT/Prussian Blue and SWCNT/Polypyrrole composite electrodes and ERGO thin film electrodes. This approach was examined in order to increase the performances of the pure CNT films either by elaboration of composite electrodes comprised of CNT and redox films or by employing alternative graphene like materials such as ERGO structures. Firstly, the morphological and structural analyses results from the FEG-SEM, HRTEM, EDX and XRD are presented and discussed. Thereafter follows the discussion of the results from the EQCM and the *ac*-electrogravimetry studies in order to reach a profound examination of the electrochemical behavior of such layers.

Chapter I. Bibliography

CHAPTER I

Bibliography

Chapter 1 begins with a comprehensive literature review of different energy storage devices like batteries and supercapacitors including history, principle of operation and different applications. More details are given about the components of these systems in terms of materials and electrolytes, and their impact on (supercapacitor) performance is discussed. Thereafter, a literature review of different techniques used for characterization and evaluation of performance of carbon based electrodes in energy storage is provided. Finally, the scope and objectives, starting from the state of art of the present Ph.D. thesis, are introduced.

I-1. Energy Storage: Batteries and Supercapacitors

Electrical energy storage can be divided in two different devices – **batteries** and **supercapacitors**. In batteries, the electrochemical processes give rise to redox reactions, which will be discussed in Section I-1.1. Capacitors where *in priori* no redox reactions take place (electrical double layer capacitors (EDLCs) and the systems involving both capacitive and redox processes (pseudo-capacitors) will be discussed in Section I-1.2.

I-1.1. Batteries

A battery is an electrochemical device that transforms stored electrochemical energy into electric energy through a redox reaction (oxidation/reduction).^{7,8} There are two general classes of batteries: primary batteries (the chemical energy stored in the cell can be used only once) and secondary or rechargeable batteries (which can be recharged; *i.e.* the redox reaction can be reversed by supplying electric energy to the cell, approximately restoring the original composition of the battery/cell).^{9,10} Both primary and secondary batteries are composed of two electrodes (one is called the anode and the other is called the cathode), electrolytes, separators and current collectors.⁷

I-1.1.1. History

It can be considered that the history of the modern battery started with the scientific studies of electricity in the 17th and 18th centuries by scientists such as C. Du Fay, B. Franklin and L. Galvani.

In 1799, the Italian physicist A. Volta invented the first electrochemical cell, the Voltaic Pile. It consisted of zinc and copper or silver discs, alternately stacked and separated by brine-soaked felt spacers or cardboard. Although there had been other devices that could produce electricity, the Voltaic Pile was the first to generate a stable and continuous current.^{11,12}

In 1866, G. Leclanché, developed and patented a battery with electrodes based on zinc, carbon and manganese dioxide and with a solution of ammonium chloride as the electrolyte. The original Leclanché cell (a wet cell) was gradually developed into the carbon-zinc cell (a dry cell), which was the most commonly used small battery during the 20th century until the introduction of the alkaline cells in the late 1950s.^{13,14}

The first rechargeable battery was invented by G. Planté in 1859. This lead-acid battery could be recharged by reversing the chemical reaction. Developed forms of Planté's lead-acid battery are still in use, especially in automobiles and in industry. However, lead-acid batteries are heavy and their performance is relatively low in comparison to more modern systems.^{15,16}

Another rechargeable battery, the nickel-cadmium battery, was invented by W. Jungner in 1899. This battery uses nickel oxide hydroxide (NiO(OH)) and cadmium (Cd) as electrodes and aqueous alkaline potassium hydroxide as an electrolyte (KOH). The nickel-cadmium battery can be over-discharged or stay discharged a long time without losing its performance. However, cadmium is highly toxic and, therefore, the nickel-cadmium battery is gradually replaced by nickel-metal hydride (Ni-MH) and lithium-ion batteries.^{8,17,18}

In the 1970s, the nickel-hydrogen battery was developed for the space industry. Instead of a cadmium electrode, the nickel-hydrogen battery uses a hydrogen gas electrode. The nickel-hydrogen battery has a remarkably long lifetime and it has a higher energy density than the nickel-cadmium battery, *i.e.* more Wh/kg. The nickel-hydrogen battery has been widely used in satellite power systems.^{9,17}

In 1991, Sony and A. Kasei launched the first rechargeable lithium-ion battery (Li-ion battery or LIB) for commercial consumption. The first generation of Li-ion batteries uses a graphite anode and a lithium cobalt oxide cathode. The electrolyte is a lithium salt (LiPF₆) dissolved in an organic solvent, for example ethylene carbonate (EC) and dimethylene carbonate (DMC).

I-1.1.2. Types of Batteries

Primary batteries and secondary (rechargeable) batteries include a variety of electrochemical systems for storing chemical energy. However, only a few of these are efficient enough, taking into account cost as well as storage/size, to be used commercially⁷ (Table I-1).

Table I-1: Types of Batteries.¹⁹

Battery type	Features	Environmental Impact
Ni-MH	Low voltage, moderate energy density, high power density Applications: portable, large-scale	Nickel not green (difficult extraction/unsustainable), toxic. Not rare but limited Ni
Lead-acid	Poor energy density, moderate power rate, low cost Applications: large-scale, start-up power	Lead is toxic but recycling efficient to 95%
Lithium ion	High energy density, power rate, cycle life, costly Applications: portable, possibly large-scale	Depletable elements (cobalt) in most applications, replacements manganese and iron green (abundant and sustainable) Lithium chemistry relatively green (abundant but the chemistry needs to be improved)
Zinc-air	Medium energy density, high power density Applications: large-scale	Mostly primary or mechanically rechargeable Zinc smelting not green, especially if primary Easily recyclable
Lithium-organic	High capacity and energy density but limited power rate. Technology amenable a low cost Applications: medium- and large-scale, with the exception of power tools	Rechargeable Excellent carbon footprint Renewable electrodes Easy recycling
Lithium-air	High energy density but poor energy efficiency and rate capability Technology amenable a low cost Applications: large-scale, preferably stationary	Rechargeability to be proven Excellent carbon footprint Renewable electrodes Easy recycling
Magnesium-Sulfur (future)	Predicted: high energy density, power density unknown, cycle life unknown	Magnesium and sulfur green Recyclable Small carbon footprint

I-1.1.3. Principle of Operation

Batteries convert chemical energy into electric energy through a redox reaction. The energy released during this reaction is derived from the redox potential (E) of the materials involved. This is expressed in the following equation:

$$\Delta G = -nF\Delta E \quad \text{I-1}$$

where ΔG stands for the change in free energy, n for moles of electrons, F for Faraday's constant and ΔE for the redox potential difference.²⁰

A redox couple consists of two species of the same chemical element. These species are referred to as oxidized species and reduced species, since they have different oxidation states. In the following examples, the oxidized species are written to the left in each redox couple: Cu^{2+}/Cu ; Cl_2/Cl^- ; $\text{Fe}^{3+}/\text{Fe}^{2+}$; Mg^{2+}/Mg ; Zn^{2+}/Zn ; Ag^+/Ag . A redox reaction is often described as two half-reactions: a reduction half-reaction, which takes place at the cathode when discharging and an oxidation half-reaction, which takes place at the anode.^{21,22}



The standard potential of a redox couple is obtained by coupling the electrode in question to a reference electrode (*i.e.* a standard hydrogen electrode, SHE) under standard conditions (concentration of 1 M, a pressure of 1 bar and a temperature of 298°K). Thus, different redox potentials may be compared *via* the reference electrode. The redox potential can be considered as a way to describe how readily an element forms ions in comparison to other elements through an electrochemical process.

Normally, if there is a direct contact between the two species involved in a spontaneous redox reaction, the energy released dissipates in the form of heat and is of little use. Therefore, the two electrodes of an electrochemical battery/cell are separated and the electrons are exchanged *via* an electric circuit. To obtain this, a separator allowing only ionic conduction between the electrodes is necessary. To ensure conductivity, the separator, usually a membrane of cellulose or polycarbonate, is soaked in the electrolyte. Since the membrane/separator does not allow the electrons to pass, the electrons are forced to pass *via* the electric circuit instead.²³ In doing so, the electrons produce a current (See Figure 1). The other function of the separator, to ensure that there is no direct contact between the electrodes, prevents short circuits as the electrodes must be electrically conductive.

Chapter I. Bibliography

The electrodes consist of a solid part in contact with the electrolyte. The contact zone between the solid part and the electrolyte, called the electrode/electrolyte interface, is crucial for the performance of the electrode/battery.²³

The electrolyte contains free ions and, therefore, it is conductive. The most commonly used electrolytes consist of a compound that ionizes when molten or dissolved in an adequate medium, although there are also electrolytes in form of gases or solid (*e.g.* dry polymer or glass).⁸

The current collectors are usually metal foils or grids that are inert under the operational chemical and electrochemical conditions. Frequently, they have also the important role of imparting mechanical stability to the electrodes.²⁴

A typical structure of a commercial LIB consists of a graphite anode, a cathode formed by lithium metal oxide such as LiCoO_2 , and a separator embedded in an organic electrolyte containing a lithium salt (*e.g.* LiPF_6 , LiAsF_6). The electrolyte promotes the ionic transport, which is separated from the electronic transport that happens in the external circuit *via* electron flow to supply power.

The scheme in Figure I-1 illustrates the working principle of LIBs involving the electrochemical reactions at both electrodes in Eqn (I-2) and (I-3):

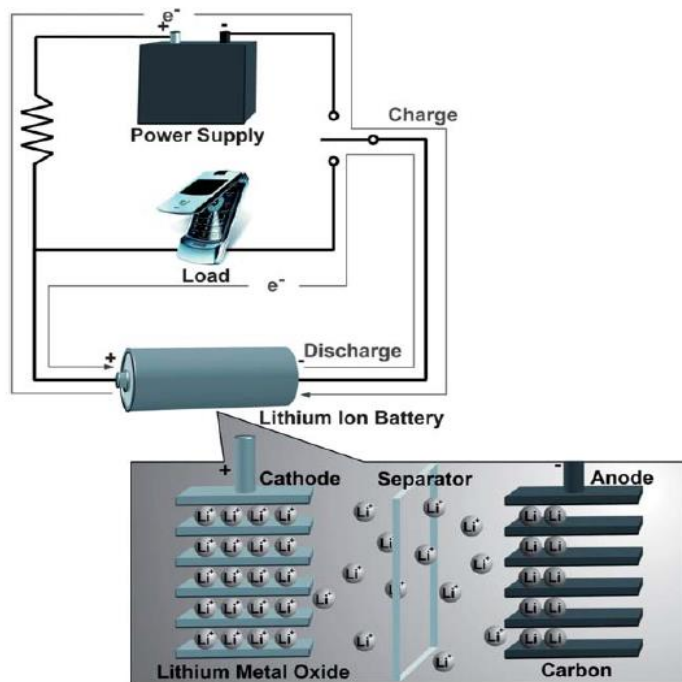
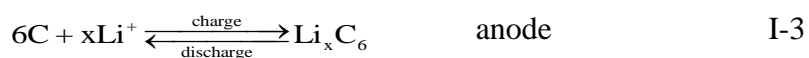
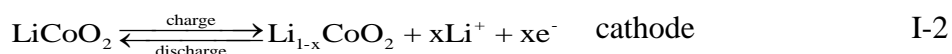


Figure I-1: Schematic operating principle of a typical rechargeable LIB.²⁵

Table I-2. Standard electrode potentials in an aqueous electrolyte at 298 K.

Reduction Half-Reaction	E° (V)
$\text{F}_2(\text{g}) + 2\text{e}^- \rightarrow 2\text{F}^-(\text{aq})$	+2.866
$\text{MnO}_2(\text{s}) + 4\text{H}^+(\text{aq}) + 2\text{e}^- \rightarrow \text{Mn}^{2+}(\text{aq}) + 2\text{H}_2\text{O}(\text{l})$	+1.23
$\text{O}_2(\text{g}) + 4\text{H}^+(\text{aq}) + 4\text{e}^- \rightarrow 2\text{H}_2\text{O}(\text{l})$	+1.229
$2\text{IO}_3^-(\text{aq}) + 12\text{H}^+(\text{aq}) + 10\text{e}^- \rightarrow \text{I}_2(\text{s}) + 6\text{H}_2\text{O}(\text{l})$	+1.20
$\text{Br}_2(\text{l}) + 2\text{e}^- \rightarrow 2\text{Br}^-(\text{aq})$	+1.065
$\text{NO}_3^-(\text{aq}) + 4\text{H}^+(\text{aq}) + 3\text{e}^- \rightarrow \text{NO}(\text{g}) + 2\text{H}_2\text{O}(\text{l})$	+0.956
$\text{Ag}^+(\text{aq}) + \text{e}^- \rightarrow \text{Ag}(\text{s})$	+0.800
$\text{Fe}^{3+}(\text{aq}) + \text{e}^- \rightarrow \text{Fe}^{2+}(\text{aq})$	+0.771
$\text{O}_2(\text{g}) + 2\text{H}^+(\text{aq}) + 2\text{e}^- \rightarrow \text{H}_2\text{O}_2(\text{aq})$	+0.695
$\text{I}_2(\text{s}) + 2\text{e}^- \rightarrow 2\text{I}^-(\text{aq})$	+0.535
$\text{Cu}^{2+}(\text{aq}) + 2\text{e}^- \rightarrow \text{Cu}(\text{s})$	+0.340
$\text{S}(\text{s}) + 2\text{H}^+(\text{aq}) + 2\text{e}^- \rightarrow \text{H}_2\text{S}(\text{g})$	+0.14
$2\text{H}^+(\text{aq}) + 2\text{e}^- \rightarrow \text{H}_2(\text{g})$	0
$\text{Na}^+(\text{aq}) + \text{e}^- \rightarrow \text{Na}(\text{s})$	-2.713
$\text{Li}^+(\text{aq}) + \text{e}^- \rightarrow \text{Li}(\text{s})$	-3.040

Throughout the charging process, lithium migrates from the cathode (LiCoO_2 in this case) through the electrolyte and is intercalated into the graphite anode (Li_xC_6). During discharge, the movement of lithium is in a reverse process: Li ions are extracted from the anode and intercalated into the cathode.^{26,27}

I-1.1.4. Battery Performance

When discussing the performance of batteries, there are various aspects that need to be considered. In this section, the most important ones will be discussed, *i.e.* cell potential, capacitance, specific energy density, specific power density and the C-rate.

Cell Potential (Voltage)

The theoretical standard cell potential (E°_{cell}) can be defined as the difference between the theoretical standard potentials of the two half cells in an electrochemical cell:

$$E^\circ(\text{cell}) = E^\circ(\text{cathode}) - E^\circ(\text{anode}) \quad \text{I-4}$$

However, in practice, the cell potential will be lower due to various factors, ranging from polarization during the charge process to the age of the cell. The cell potential is measured in volts (V) and, therefore, it is often referred to as the voltage of the cell. The standard electrode potential, E° , for an electrode reaction is the potential generated by that reaction under the condition that the

reactants and the products are in their standard state in relation to a reference electrode. In aqueous systems, the standard hydrogen potential is taken as the universal reference electrode²² previously mentioned in Section I-1.1.3. A list containing selected standard electrode potentials is given in Table I-2.

Capacitance

Capacitance is the term used for referring to the quantity of electricity involved in the redox reactions. The theoretical capacitance, Q , can be calculated using the following equation:

$$Q_{\text{charge}} = xnF \quad \text{I-5}$$

where x denotes the number of moles of the electrochemical reaction, n the number of electrons transferred per mole of this reaction and F Faraday's constant.

However, capacitance is usually expressed in Ampere-hours per kilogram (Ah/Kg), *i.e.* in mass rather than in number of moles, and, then, it is often referred to as specific capacitance (C_{specific}). Some values of specific capacitance are shown in Table I-3.

In practice, the theoretical capacitance cannot be obtained, partly because of mass contribution from nonreactive components and partly because various factors impede the completion of the electrochemical reactions.^{20,28}

Specific Energy Density

If the specific capacitance is multiplied by the average operating cell voltage, the specific energy density is obtained, *i.e.* the energy stored per unit mass (of the cell or of the active electrode material). The specific energy density is expressed in Watt-hours per kilogram (Wh/kg) (Gravimetric energy density).

Specific Power Density

The specific power density states the quantity of power stored per unit mass, which is expressed in Watt per kilogram (W/kg). The relationship between the specific power density and the specific energy can be visualized in the so-called Ragone plot (Figure I-2). As the Ragone plot shows, the specific energy density has a tendency to drop fairly quickly at higher drains.²⁹

C-rate

The charge and discharge current of a battery is measured in C-rate.^{22,30} In fact, a C-rate is a measure of the rate at which a battery is discharged relative to its maximum capacitance. A 1C rate

Table I-3. Characteristics of different battery technologies.⁸

Battery Type	Anode	Cathode	Reaction	Theoretical Capacitance (Ah/Kg)	Theoretical Specific Energy (Wh/Kg)
Lead	Pb	PbO ₂	$\text{Pb} + \text{PbO}_2 + 2\text{H}_2\text{SO}_4 \rightarrow 2\text{PbSO}_4 + 2\text{H}_2\text{O}$	120	252
Ni-Cd	Cd	Nickel oxide	$\text{Cd} + 2\text{NiOOH} + 2\text{H}_2\text{O} \rightarrow 2\text{Ni(OH)}_2 + \text{Cd(OH)}_2$	181	244
Ni-MH	Metal hydride	Nickel oxide	$\text{MH} + \text{NiOOH} \rightarrow \text{M} + \text{Ni(OH)}_2$	178	240
Li-ion	Li _x C ₆	Li _x C ₆	$\text{Li}_x\text{C}_6 + \text{Li}_{1-x}\text{CoO}_2 \rightarrow \text{LiCoO}_2 + \text{C}_6$	100	410
Li-S	Li	Li	$\text{Li}_x + \text{S} \rightarrow \text{SLi}_x + \text{Li}_{1-x}$		500-600
Li-air	Li	Li	$2\text{Li} + \text{O}_2 \rightarrow \text{Li}_2\text{O}_2$	3840	11400

means that the discharge current will discharge the entire battery in 1 hour. For example, a battery with a capacitance of 100 Amp-hrs equates to a discharge current of 100 Amps.³¹

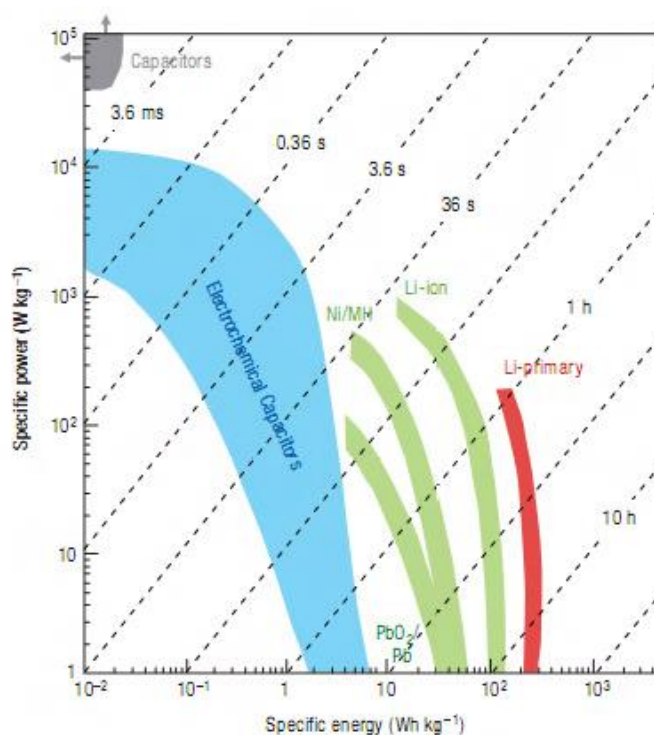


Figure I-2: Ragone plot for electrochemical energy storage devices.²⁹

I-1.1.5. Battery Applications

Secondary batteries are mainly applied in portable electronics, transport and stationary storage. If measured by the number of units produced, portable electronics constitute the largest of these three groups. Presently, the lithium-ion technology has the highest market share, although Ni/MH batteries are also frequently used in portable electronic devices. In addition, the use of primary alkaline batteries is still significant in these devices. In the transport sector, the demand for batteries is expected to increase rapidly over the next decade due to environmental reasons (Figure I-3).

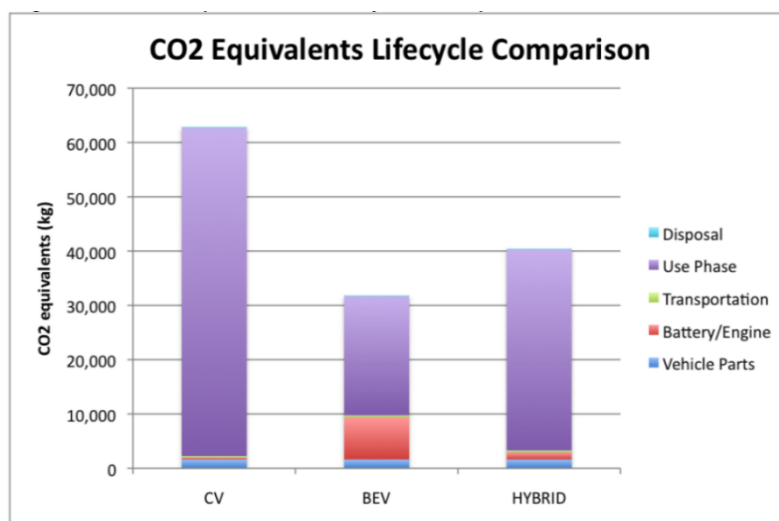


Figure I-3. CO₂ Equivalents Lifecycle Comparison: conventional gasoline vehicle (CV), battery electric vehicle (BEV) and hybrid vehicle.

Because of the international commitments to significantly reduce carbon dioxide emissions from the transport section, government incentives (*e.g.* subsidies, tax reductions and access to bus lanes) for electric vehicles (EV) and hybrid electric vehicles (HEV) have been implemented in many countries. The most common batteries in EVs and HEVs are Ni/MH, lithium-ion and ZEBRA (sodium-nickel chloride) batteries.³²

I-1.2. Supercapacitors

Supercapacitors, also known as electrochemical capacitors (EC) or ultracapacitors,³³ are a relatively new energy storage system that has contributed significantly to the scientific and industrial developments in recent years.³⁴ The principle of storage is purely electric and the global charge transfer kinetics is faster than that in the batteries. Compared to the latter, supercapacitors store less energy, but they are able to deliver it in a short time, thus, providing high power, as shown in the Ragone plot given in Figure I-2.³⁵

I-1.2.1. History

The first patented supercapacitor was developed by H. Becker of GEC (General Electric Company) in 1957.³⁶⁻⁴⁰ Becker used electrodes composed of porous carbon and an aqueous electrolyte based on sulfuric acid, which formed an electric double-layer at the electrode/electrolyte interface.³⁶⁻³⁹ A few years later, SOHIO (Standard Oil of Ohio) patented a device using graphite.³⁶⁻³⁸ SOHIO experimented with organic electrolytes, which provided a higher operating voltage than those obtained in aqueous electrolytes.^{10,36,37,39,40} In 1971, the SOHIO patent was licensed by NEC (Nippon Electric Company). Under the name of “supercapacitors”, NEC successfully introduced these new devices on the market as back-up memories for electronics.^{36,38-40} Following the success of NEC, several companies started the production and development of supercapacitors.^{36,38} For example, in 1982, Pinnacle Research Institute designed the first high-power supercapacitor, mainly for military applications.^{10,38}

Today, there are several types of supercapacitors applying different charge storing mechanisms to be able to meet different kinds of energy demands.³⁹ The two main types are the **Electric double-layer capacitors (EDLC)** and the so-called **Pseudo-capacitors**. These are non-faradaic processes (electrostatic interaction) and faradaic processes, respectively (Figure I-4).

In supercapacitors, if both electrodes have the same design and the same mass loading, the supercapacitor is called symmetric. In contrast, if the electrodes are different, the supercapacitor is called asymmetric.

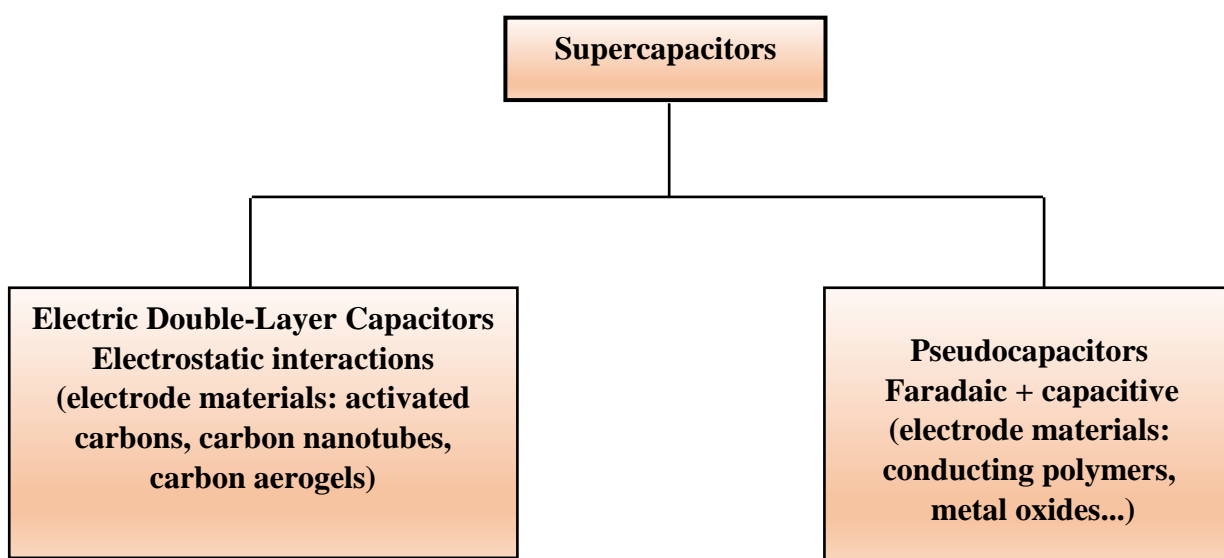


Figure I-4. Categorization of supercapacitors.

I-1.2.2. Principle of Operation for EDLC

An EDLC is composed of two electrodes immersed in an electrolyte and separated by a dielectric separator^{36,40-42} (Figure I-5). The two electrodes can be of identical or different materials, usually nanostructured and porous carbons with high specific surface areas.³⁶ The electrode materials play a key role, since they largely affect the capacitance values^{40,41} and the charge stored in the EDLC. As is the case with capacitors, no redox reactions are involved in EDLCs.⁴⁰ The operating principle is based on an electrochemical double layer, which is formed through electrostatic attraction at the electrode/electrolyte interface.^{10,36,41} When applying a potential difference across the current collectors, electrostatic charge is stored at the two electrode/electrolyte interfaces, which function as two capacitors in series.^{36,41,43} During discharge, the charge accumulated causes a parallel movement of the electrons in the external circuit, thus, generating electric energy, as indicated in Figure I-5.^{10,36} Due to the high specific surface area of the electrode materials, the amount of energy that may be stored is much larger than in traditional capacitors⁴² and the stored charge can be restored with greater efficiency than in batteries.⁴⁴ Furthermore, in theory, the cycle life of an EDLC is infinite, while batteries have a cycle life of approximately 500-2000 cycles.⁴³ As mentioned above, the two electrode/electrolyte interfaces in an EDLC function as two capacitors in series (C_1 and C_2). Thus, the total specific capacitance of the cell (C) depends on the capacitance of each electrode as given by the following equation:⁴³

$$\frac{1}{C} = \frac{1}{C_1} + \frac{1}{C_2} \quad (\text{I-6})$$

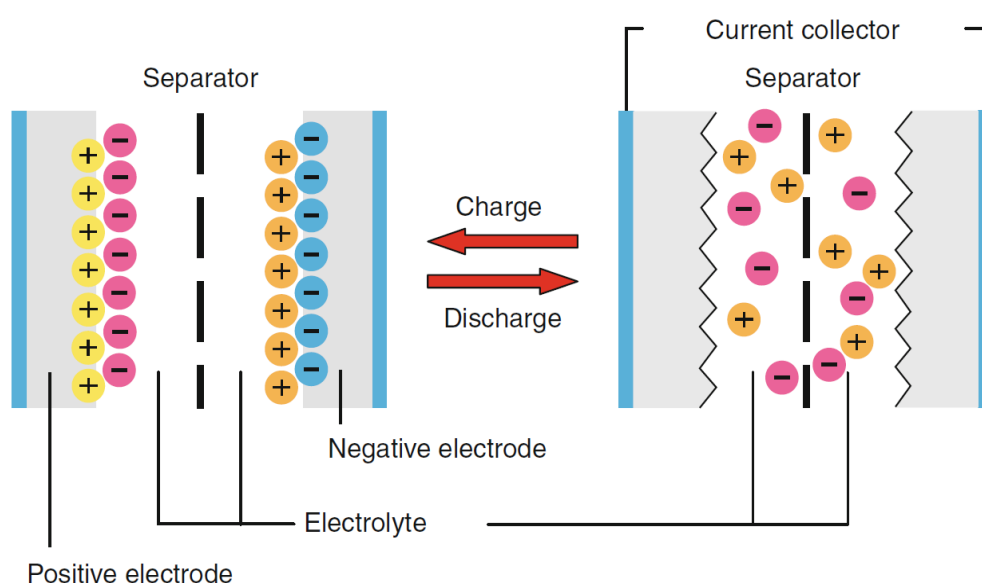


Figure I-5. Discharged (*right*) and charged (*left*) states of an electrochemical capacitor.⁴⁵

Chapter I. Bibliography

The relationship between the capacitance C (in Farad), the quantity of stored electrical charge Q (in Coulomb) and the rated voltage V (in Volt) is as follows:³³

$$C = \frac{Q}{V} \quad (\text{I-7})$$

where the charge Q equals the current I (in Ampere) multiplied with time t (in seconds):³⁶

$$Q = I \cdot t \quad (\text{I-8})$$

Usually, the charge Q is expressed in Ah/g (1 Ah=3600 C) and the specific capacitance C is given as the specific capacitance in F/ cm² or F/g.³⁶

I-1.2.3. Components of the Supercapacitors: Active Electrode Materials, Electrolytes, Separator and Current Collectors

Supercapacitors are composed of (i) active electrode materials, (ii) electrolytes, (iii) separator and (iv) current collectors.

(i) Active Electrode Materials:

The electrodes, which are composed of active materials and additives, store/deliver charges.^{36,46} The electrode material plays a key role in determining the capacitance, the energy density and the power density of the supercapacitor.⁴⁷ Furthermore, it affects the series resistance and self-discharge characteristics.^{40,46} Therefore, the selection of the electrode materials is crucial and a great number of parameters need to be considered: specific surface area, porosity, structure⁴⁸ “tunability” of the morphology (*i.e.* how readily the material allows manipulation of pore size, pore distribution, surface functional groups *etc.*),^{38,49,48} surface wettability, electrical conductivity³⁸, electrochemical stability,⁴⁰ thermodynamic stability for a wide operational potential range, cycle stability,³⁸ mechanical resilience⁵⁰ and cost.^{38-40,48} Since pore size is an important factor, the IUPAC (International Union of Pure and Applied Chemistry) has suggested the following classification:

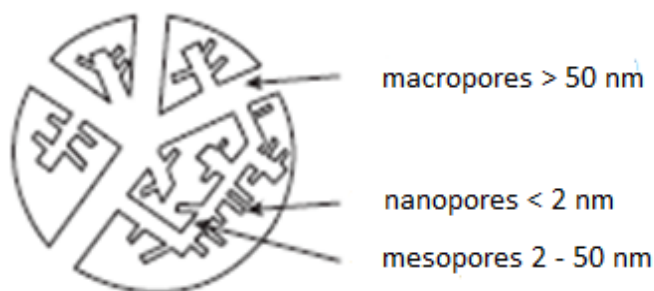


Figure I-6. The IUPAC classification of pore sizes.³⁷

Chapter I. Bibliography

macropores, mesopores and nanopores, with diameters of > 50 nm, 2-50 nm and < 2 nm, respectively (Figure I-6).³⁷

Currently, the three main categories of active electrode materials are based on the carbon materials³⁶, transition metal oxides,^{36,46} and conducting polymers.³⁶ Of these three classes of materials, carbon is the most frequently employed in EDLCs.^{39,48} Carbons may have very diverse structures, which affect their properties. The most commonly used structures in EDLCs are: (1) onion-like carbons (OLCs), (2) carbon nanotubes (CNTs), (3) graphene, (4) carbide-derived carbons (CDCs), (5) activated carbons (ACs), and (6) templated carbons (Table I-4).^{39,41,51}


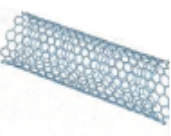
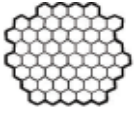

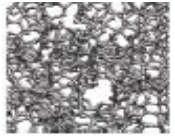

(1) Onion-Like Carbons (OLCs)

OLCs are zero-dimensional (0D) materials^{39,52,53} consisting of concentric graphitic shells with a specific surface area that ranges from 200 to 980 m²/g depending on the synthesis conditions.³⁹ OLCs are generally prepared by annealing nanodiamond powders in vacuum or under argon.^{39,52} They offer high electrical conductivity,⁵² high power^{39,52} and high energy densities³⁹, but a limited capacitance (around 30 F/g).^{39,52}

(2) Carbon nanotubes (CNTs)

CNTs are regarded as one-dimensional, since the graphitic walls of which they consist are assembled in tubes that are almost one-dimensional³⁸ and as the transport of charges only occurs along the tube axis. The diameters of these tubes are approximately 1-50 nm.³⁹ Depending on the number of graphitic layers (walls), CNTs are divided into two subgroups: single-walled nanotubes (SWNT) and multi-walled nanotubes (MWNT).^{39,42,50} Both SWNTs and MWNTs are appreciated for their high electrical conductivity,^{42,50} unique pore structure,⁵⁴

Table I-4. Different carbon structures and some of their characteristics.⁴¹

Material	Carbon onions	Carbon nanotubes	Graphene	Activated carbon	Carbide derived carbon	Templated Carbon
Dimensionality	0-D	1-D	2-D	3-D	3-D	3-D
Conductivity	High	High	High	Low	Moderate	Low
Volumetric Capacitance	Low	Low	Moderate	High	High	Low
Cost	High	High	Moderate	Low	Moderate	High
Structure						

Chapter I. Bibliography

excellent mechanical properties^{38,54}, chemical reactivity⁵⁴ and thermal stability⁵⁰ and relatively low equivalent series resistance (ESR) (lower than activated carbon).⁵¹ Although their surface area is relatively moderate compared to activated carbon, it may be used more efficiently due to the fact that the mesopores are interconnected, thus, providing access to nearly all the surface area and enabling a continuous distribution of charges.^{50,51,54} Altogether, these properties make CNTs suitable for high power devices.^{42,50,51} The specific capacitance of CNT electrode material ranges between 15 and 200 Fg⁻¹, depending on the morphology and purity obtained at the production procedure and any subsequent treatment.^{38,50} CNTs in sizeable quantities can be produced by three major methods: arc discharge, laser ablation and chemical vapor deposition (CVD).⁵⁵⁻⁵⁷ Each of these methods presents advantages and disadvantages resulting in different growth results (Table I-5).

Table I-5. Summary and comparison of synthesis methods of CNTs.

Method	Arc-discharge	Laser-ablation	CVD
Pioneer	Iijima ⁵⁸	Guo <i>et al.</i> ⁵⁹	Yacaman <i>et al.</i> ⁶⁰
How	CNT growth on graphite electrodes during direct current arc-discharge evaporation of carbon in presence of an inert gas	Vaporization of a mixture of carbon (graphite) and transition metals located on a target to form CNTs	Fixed bed method: acetylene decomposition over graphite-supported iron particles at 700°C
Yields	< 75%	< 75%	>75%
SWCNT or MWCNT	Both	Only SWCNTs	Both
Advantage	Simple, inexpensive	Relatively high purity CNTs, room-temperature synthesis option with continuous laser	Simple, inexpensive, low temperature, high purity and high yields, aligned growth is possible, fluidized bed technique for large-scale
Disadvantage	Purification of crude product is required, method cannot be scaled up, must have high temperature	Cannot produce MWCNTs, method only adapted to lab-scale, crude product purification required	CNTs are usually MWNTs, parameters must closely be watched to obtain SWNTs

Thus, the choice of the method is dependent on the requested properties of the CNTs. Prasek, J. *et al.*⁶¹ reported that the choice of catalyst is one of the most important parameters when using the CVD method, since it affects the CNT growth. In addition, the production of CNTs (the CNT growth) depends on the processing conditions such as pressure and temperature. Temperatures $> 900^{\circ}\text{C}$ result in SWCNTs, whereas MWCNTs are produced at temperatures in the range of $700\text{--}800^{\circ}\text{C}$.⁶²

(3) Graphene

Another active material that is commonly used in energy-storage mechanisms is the graphene. The usage of graphene can range from hosting ions (such as Li^+ or Na^+ in metal-ion batteries) to storing electrostatic charges on the electrode double-layer (as in EDLC applications)⁶³ (Figure I-7).

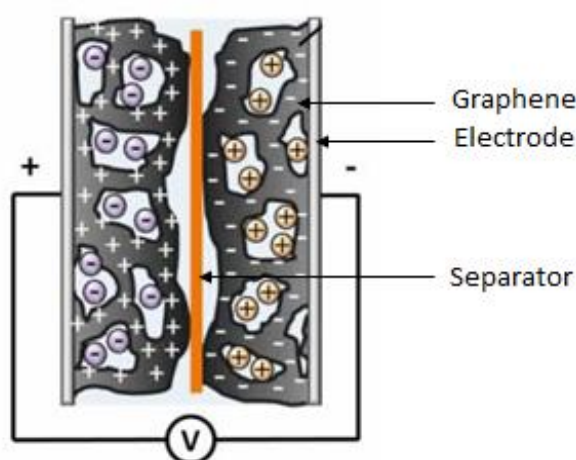


Figure 1-7. Double Layer Energy Storage in Graphene when a potential is applied.

Graphene is composed of pure carbon organized in hexagonal structure in the form of a one atom thick transparent sheet. Graphene can be produced with a mechanical exfoliation of graphite (which is composed of intercalated graphene sheets) with a method called the Scotch tape method. This approach consists of peeling off a chunk of graphite until only one layer remains. However, this technique does not allow a large scale production of graphene and, since the vast majority of chemical and electrochemical energy storage systems require bulk quantities of graphene, many other methods to synthesize graphene-like materials have been proposed. For example, the reduction of graphene oxide (GO) can be used to elaborate graphene-like materials. GO is commonly synthesized with the Hummers method,⁶⁴ which is a reaction involving graphite, sulphuric acid and potassium permanganate. Once the GO is synthesized, its reduction can be performed in different manners: chemically, thermally or electrochemically. The reduction process has a decisive influence, because it determines the quality of the reduced graphene-like material.⁶⁵ Many approaches can be performed for chemical reduction with the aim to bring GO structures as

Chapter I. Bibliography

close as possible to that of the graphene obtained by the Scotch Tape method. The most common method involves hydrazine. This compound is particularly interesting because, unlike other reducing species such as lithium aluminum hydride (LiAlH_4),⁶⁵ it does not react with water, thus, avoiding a number of side reactions. However, a large scale production involving hydrazine would be difficult, since this toxic compound cannot be used in the context of sustainable development. Another method to produce graphene-like material is thermal reduction, which can be performed by thermal treatment of graphene oxide at 1050°C . This thermal process causes the release of CO_2 , which leads to an increase of the pressure within the material. However, thermal treatment of graphene oxide in this way may cause damage to the material, causing surface defects affecting electronic properties.⁶⁵ Electrochemical reduction, which will be discussed in Chapter II, seems to be a good alternative to produce large scale graphene-like samples.

This eco-friendly method avoids using dangerous species like hydrazine and allows high-quality graphene-like material to be produced.⁶⁵

Some examples of reduced graphene oxide used as electrode material are shown in Table I-6.

Table I-6. Summary of graphene based EDLCs using aqueous electrolytes.

Year	Electrode material	Electrolyte	Specific Capacitance F g^{-1}	Specific Current A g^{-1}	Ref.
2008	Thermally exfoliated graphite oxide	1M H_2SO_4	117	0.12	⁶⁶
2008	Chemically modified graphene	5.5M KOH	135	1.3	⁶⁷
2009	Low temperature exfoliated graphene	5.5M KOH	264	0.1	⁶⁸
2009	Reduced graphene oxide sheets	30% KOH	205	0.1	⁶⁹
2010	Graphene nanosheets	30% KOH	150	0.1	⁷⁰
2011	Graphene hydrogel	5M KOH	222	1	⁷¹
2011	Graphene paper	1M H_2SO_4	120	0.12	⁷²
2011	Multilayered graphene film	1M H_2SO_4	215	0.1	⁷³
2011	Reduced graphene oxide	1M H_2SO_4	348	0.2	⁷⁴
2014	Reduced graphene oxide by flame-induced reduction of oxide graphite oxide	6M KOH	221	0.1	⁷⁵

(4) Carbide-Derived Carbons (CDCs)

CDCs are produced by high temperature extraction of metals from carbide precursors.^{39,52} Porosity is formed by leaching out metal atoms from the crystal structure of the carbide precursor⁵² and the pore structure strongly depends on the carbide precursor and the synthesis temperature.⁷⁶ Carbon growth can be controlled on the atomic level, leading to a highly controllable pore size with better than angstrom accuracy. The specific surface area ranges from 1000 to 3000 m²/g.

(5) Activated Carbons (ACs)

ACs are generally produced by carbonization of carbonaceous organic precursors (*e.g.* nut shells, wood, peat or coal)^{39,52,53,77} and subsequent activation processes.^{52,53,77} The activation processes, which can be physical and/or chemical,^{39,77} aim to create a three-dimensional porous network in the bulk of the carbon material.^{39,52} In physical activation, the carbon precursor is thermally treated at high temperature in the presence of an oxidizing gas,^{39,53,77} *e.g.* air,^{53,77} water vapor, CO₂,^{52,53,77} or KOH.⁵² Chemical activation is performed using an activating agent *e.g.* phosphoric acid, potassium hydroxide, sodium hydroxide or zinc chloride (H₃PO₄, KOH, NaOH, ZnCl₂).^{52,53,77} During the activation processes, micropores and mesopores are created and the specific surface area can exceed 2000 m²/g.⁵² However, the control over porosity is limited, resulting in a wide pore size distribution, which means that not all pores are accessible to ions.³⁹ By selecting carbon precursor, activation method and control of synthesis conditions, AC materials with different functional groups on the carbon surface may be obtained, resulting in a variety of physicochemical properties.^{53,77} The most common functional groups contain oxygen and/or nitrogen.⁵³

In the last few years, the capacitive performance of ACs has improved significantly and ACs have a higher density than CNTs and graphene (AC volumetric capacitance reaches 50-80 F/cm³).⁵² Scalable manufacturing and reasonable cost also contribute to ACs being widely used in commercial EDLCs.^{52,77}

(6) Templated carbons

Templated carbons are produced by carbonization of a carbon precursor in nanochannels of a template inorganic material and the subsequent removal of the template.^{52-54,76,77} By the selection of carbon precursor and template, and by the control of carbonization parameters, porous carbons with different physical and chemical properties may be obtained.⁵³ The template method enables the preparation of 1D, 2D and 3D carbons, *e.g.* carbon nanotubes, graphene and nanoporous carbons,⁵² and can form both microporous and mesoporous carbons.⁷⁶ Furthermore, it allows the precise

control of pore structure; pore volume⁷⁶ and pore size⁵² can be controlled through tuning the pore size of the template.⁵⁴ Depending on the templates used, the template method can be subdivided into hard-template and soft-template methods. The former refers to a replication synthesis with pre-synthesized hard templates (inorganic materials such as silica nanoparticles, zeolites, mesoporous silica and MgO) and includes infiltration, carbonization and removal of templates,⁵⁴ while the latter uses triblock copolymers as the template^{52,54} and includes cocondensation and carbonization. The hard-template method is expensive and time-consuming, making it unsuitable for large-scale production. In addition, the removal of the template requires toxic acids. The soft-template method is less expensive, faster and more environmentally friendly.⁵⁴ Because of their precise controllability, templated carbons are suitable to study the effects of pore size, pore shape, channel structures and other parameters concerning ion diffusion and charge storage in nano-confined systems.⁵³

In addition to carbon structures, the porous texture plays an important role in understanding the correlation between the specific surface area and the capacitance, and the properties of the latter. Ion sizes and pore sizes, and the connection between the pores may have a strong impact on capacitance values, particularly under the high operating current densities that are present in supercapacitors. Four important porous characteristics for carbon materials will be presented: (a) ion sieving, (b) ion desolvation (c) pore saturation and (d) distortion.

a. Ion Sieving

Ion sieving was defined by Aurbach *et al.* and denotes the possibility of selective electrosorption of ions based on size.⁷⁸⁻⁸⁰ The findings of Aurbach *et al.* can be summarized as follows (Figure I-8):

❖ There is a typical capacitive rectangular-shape of the cyclic voltammogram (CV) with MgSO_4 electrolyte, when the average pore size (0.58 nm) of the carbon material is significantly larger than the size of ions.

❖ When the average pore size (0.51 nm) of the carbon material is smaller than the size of ions, the current is negligible in all the potential range.

❖ When the average pore size (0.51 nm) of the carbon materials is larger than one of the electrolyte ions and smaller than the other, as is the case with Li_2SO_4 and MgCl_2 aqueous electrolytes, a triangular shape and narrowing of the two CV curves appear, which confirm the adsorption of the smaller ion into the pores and the absence of adsorption of the larger ion on the other side of the point of zero charge.

There is no direct relationship between the electrosorption and insertion of a certain ion in pores of different sizes and the capacitance. The latter will be controlled by the correlation between

the average pore size and the effective size of ions, which can be studied by CV. By slowing down the applied scan rate, it is possible to force the insertion of ions into the pores if the ions are slightly larger than the average pore size.

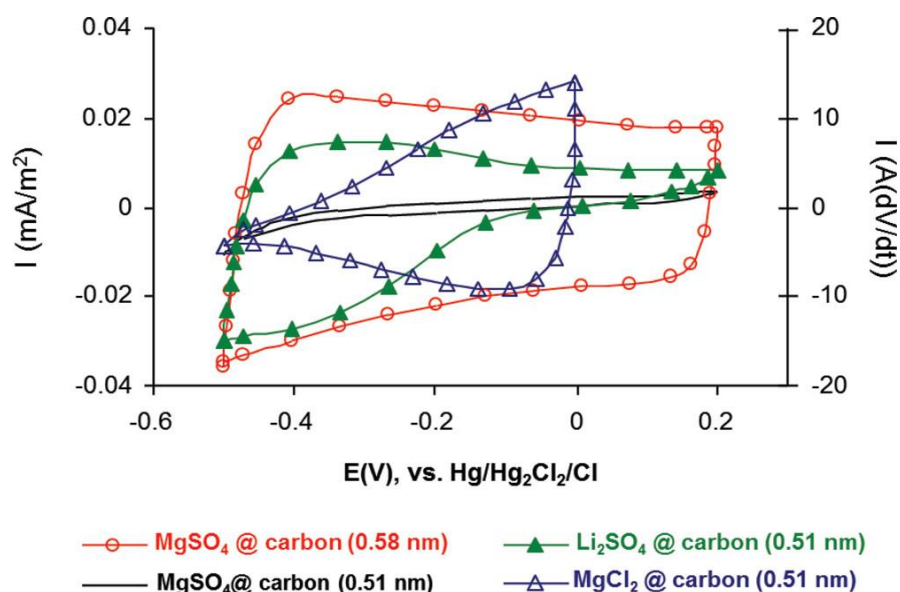


Figure I-8. Voltammograms of activated carbon electrodes with average pore size of 0.58 nm and 0.51 nm obtained in 0.1 M MgSO_4 solution. For comparison, curves are also given for pores of 0.51 nm in 0.1 M Li_2SO_4 and MgCl_2 solutions. The current is normalized per unit of BET SSA.⁴⁸

In this case, ion sieving also results in increased, yet reversible swelling of the pore network. Another parameter that affects electrosorption is the geometry of the ions from aqueous solutions, as shown by Noked *et al.* They found that planar solvated ions, *e.g.* NO_3^- , are adsorbed in slit-shaped pores, while spherical solvated ions, *e.g.* Cl^- , are excluded. In a similar study, the preference of hydrated monovalent ions (Na^+) to hydrated bivalent ions (Ca^{2+} and Mg^{2+}) in micropores was shown.

Furthermore, the sieving effect was demonstrated in a study of the capacitance of an active carbon (AC) in a series of ILs of increasing cation size. Since ILs are solvent-free, the capacitance properties can be interpreted by comparing the size of pores and ions calculated by molecular modeling. This study showed an extensive mismatch between the pore size and the effective size of the cations.⁴⁸

b. Ion Desolvation

The effective ion size in aqueous and organic electrolytes is larger than the actual ion size itself due to the solvation shell. Solvation shells are formed around the ions in aqueous and organic electrolytes. Therefore, the effective ion size is larger than the actual ion size itself. Although it is

clear that pore size and effective ion size need to be matched, it is difficult to identify the optimum pore size, *i.e.* the pore size leading to the best EDLC performance. For template carbons, Vix-Guterl

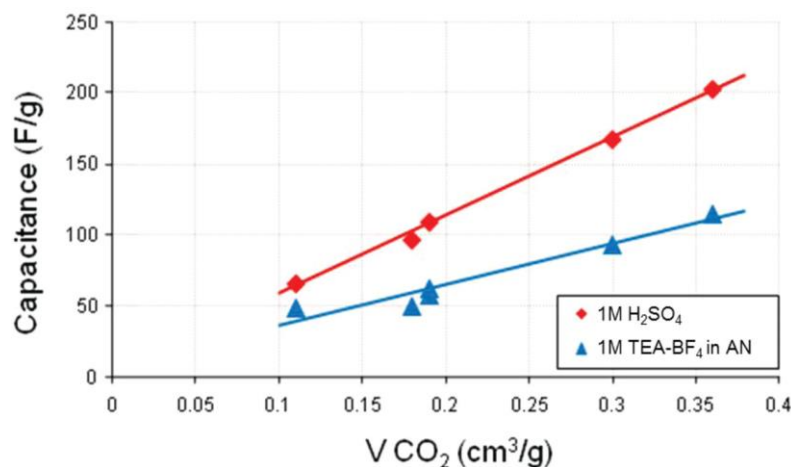


Figure I-9. Capacitance in two electrolytic media versus the volume of micropores smaller than 0.7-0.8 nm for various template carbons.⁴⁸

*et al.*⁸¹ showed that the capacitance is proportional to the ultra-micropore volume (pores smaller than 0.7-0.8 nm) measured by CO₂ gas sorption, in both aqueous and organic media (Figure I-9). Furthermore, it was shown that the ions needed to be at least partially desolvated to access into the pores (for a two-electrode set-up). The importance of the sieving effect, associated to the desolvation process, is highest at the anode (negative electrode), which means that the cell capacitance is essentially controlled by the anode according to Equation I-9.

c. Pore Saturation

Mysyk *et al.* has shown that the porosity of carbons with subnanometer sized pores (APC carbon) can be saturated with electrolyte ions for high voltage values in 1.5 M TEA-BF₄/AN electrolyte. It was found that the capacitive current decreased significantly at voltage higher than 1.5 V, despite that the pore size most probably matched the ion size (Figure I-10). The charge was approximately equal to the theoretical maximum charge storable in the pores larger than the desolvated cations. Therefore, the authors proposed that the observed capacitive current decrease was due to the saturation of the pore volume accessible to ions.

d. Distortion

Ania *et al.*⁸² observed an unexpectedly high capacitance (92 F/g) for a microporous carbon in TEA-BF₄/AN electrolyte, where 63 % of the pores were smaller than the desolvated ion size. The authors proposed that distorted cations penetrate the pores under the effect of the electric field, showing slightly smaller dimensions than their computed rigid size. For some TEA⁺ conformations, a size smaller than the average pore size of the carbon has been computed.

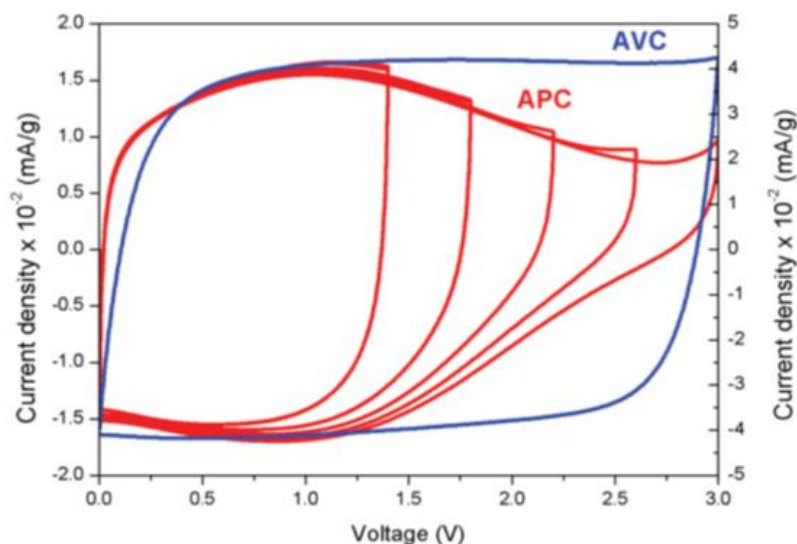


Figure I-10. (a) Cyclic voltammograms for EDLCs based on APC carbon (left-hand side y-axis for current) and AVC carbon (right-hand side y-axis for current).⁴⁸

(ii) Electrolytes:

The role of the electrolyte is to supply and allow the movement of ions to form the electrical double-layer at the electrode/electrolyte interface.^{36,48,83} Consequently, electrolytes need to be good ionic conductors. Along with ionic conductivity, which largely affects the specific power density, the electrolyte stability voltage window is the main criterion for the selection of an electrolyte.^{36,48} The stability voltage window sets the limits for the voltage that may be applied to the electrodes without causing decomposition of the electrolyte. This explains the importance of this property, since the specific energy density (E) is proportional to the voltage squared as shown in the following equation:²⁹

$$E = -\frac{1}{2}CV^2 \quad (\text{I-9})$$

Another important parameter to consider when choosing the electrolyte is ion size,⁵⁰ which is discussed in the literature. There are three types of electrolytes used in supercapacitors: aqueous, organic and ionic liquids (ILs) (Table I-7).

The most common aqueous electrolytes are H_2SO_4 , KOH and KCl . They have high ionic conductivity, but narrow voltage windows (approximately 1.2 V).³⁸ Some of their advantages are low cost, easy handling in an open environment and the availability of diverse pH values.^{38,48,84} The most commonly used organic electrolytes are solvents based either on propylene carbonate (PC) or acetonitrile (ACN). These electrolytes have wider voltage windows (approximately up to 2.2 – 3 V)³⁸, but much lower ionic conductivity than aqueous electrolytes, especially PC, which has an ionic conductivity more than four times lower than acetonitrile.

Table I-7. Voltage windows and ionic conductivity for different kinds of electrolytes.

Electrolyte	Voltage Window (V)	Ionic Conductivity (mS.cm ⁻¹)
Aqueous	$\leq 1,2$ ^{37,38}	>400 ^{37,40}
Organic (NEt ₄ BF ₄ /PC)	$3,0$ ³⁷	13 ³⁷
Organic (NEt ₄ BF ₄ /ACN)	$2,7$ ³⁷	56 ³⁷
Ionic Liquids	$3-5$ ^{38,40}	<15 ^{37,40}

On the other hand, acetonitrile is both toxic and flammable, making PC attractive for safety and environmental reasons.^{37,38,48,50} ILs are salts that are liquid (molten) at room-temperature.^{38,48} Since they do not contain any solvent, their stability voltage windows only depend on the electrochemical stability of the ions. These electrolytes have wider voltage windows than both aqueous and organic electrolytes (approximately up to 3-5 V).³⁸ However, the ionic conductivity is low at room temperature, so they are preferably used at higher temperatures. With their many advantages, *i.e.* having higher energy density and power density than other electrolytes, having a well-defined ion size (no solvation shell to consider),⁴¹ being nontoxic, nonflammable and chemically stable, the ILs are expected to significantly contribute to the improved performance of supercapacitors in the future, at least for high temperature operation.^{29,38,48}

(iii) Current collectors:

The role of the current collectors is to transport the electric current between the electrodes and the external loads.^{36,38} Consequently, current collectors need to present good electrical conductivities, which also contributes to increase the specific power and to reduce the total resistance of the supercapacitor.³⁶ Furthermore, they are required to be chemically and electrochemically stable to resist corrosion.^{36,38,40} Considering these factors, stainless steel is generally used in aqueous electrolytes, while aluminum alloys are preferred in organic electrolytes^{36,38,40} due to its low density and good thermal conductivity.³⁸

Another important factor to consider is the contact between current collectors and the active layers of the electrodes.^{29,36,38} It should be the lowest possible as the interface resistance makes a significant contribution to the total resistance.³⁶ To obtain this, polymeric binding agents (*i.e.* Nafion® and polytetrafluoroethylene) are used.³⁸

(iv) Separators:

The two main roles of the separator are to electrically isolate the two electrodes to prevent short-circuits and to ensure ionic conductivity.^{36,40} In general, the separator consists of a porous membrane.³⁶ In designing or selecting these membranes, there are several properties that need to be considered. The membrane must be electrically nonconducting, while electrolyte ion permeable with a minimum of ionic resistance. Furthermore, it needs to be chemically resistant (*i.e.* resistant to electrolytes and electrode materials)³⁸, thermally resistant⁴⁰, flexible (*i.e.* endure pressure and volume changes) and easily soaked in electrolytes.³⁸ The most commonly used materials are cellulose⁴⁰ and polymers.³⁸ Polymer separators can be categorized according to structures: fibrous structures and monolithic networks with defined pores³⁸ (Figure I-11).

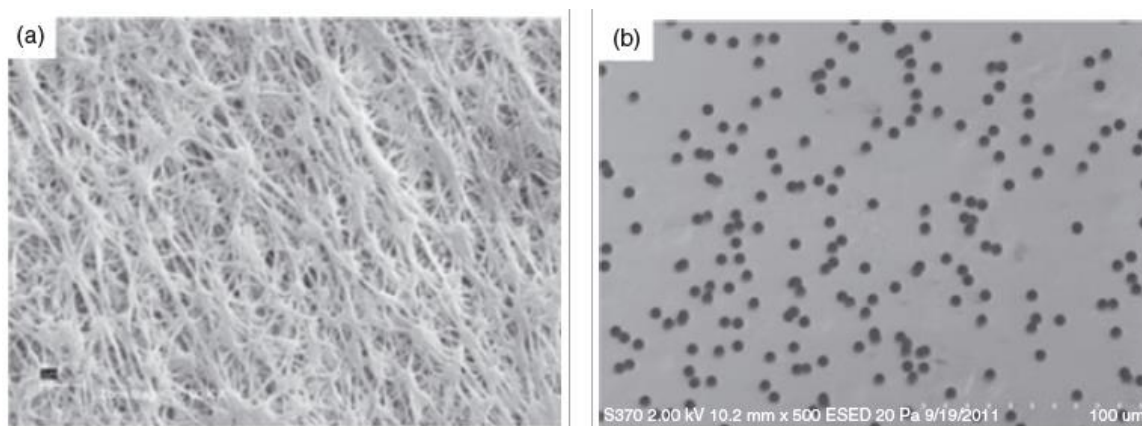


Figure I-11: Scanning electron microscopy (SEM) images of (a) Millipore JVWP separator with fibrous structure and (b) GE Osmotics K50CP01300 separator with monolithic/defined pores.³⁸

I-1.2.4. Proposed Strategies Towards Higher Performance in Supercapacitors: (Nano)structuring, Electrolyte Composition, Pseudo-Capacitance, and Hybrid and Composite Electrodes

With the objective of improving the performance of supercapacitors, investigations concerning (i) nanostructuration, (ii) electrolyte composition, (iii) pseudo-capacitance behavior and (iv) hybrid and composite electrodes have been proposed.

(i) Nanostructuration

The study of different carbon structures and pore textures to increase supercapacitor performance has been briefly discussed in Section I-1.2.3. Also, in the literature,⁸⁵ it has been discussed that physical and chemical properties of pure CNTs, including size, purity, defect, shape, functionalization and annealing, affect the performance of supercapacitors. Furthermore, it has been discussed that the composites, including CNT/oxide and CNTs/polymer, enhance the capacitance

and keep the stability of the supercapacitor by optimally engineering the composition, particle size, and coverage.⁸⁵ For example, pyrrole treated-functionalized SWCNTs have reported high values of specific capacitance (350 F/g), power density (4.8 kW/kg) and energy density (3.3 kJ/kg).⁸⁶ Also high values of specific capacitance (485 F/g), specific power (228 Wh/kg) and specific energy (2250 W/kg) were observed for 73 wt% PANI deposited onto SWCNTs.⁸⁷

(ii) Electrolyte Composition

The criteria for an ideal EDLC electrolyte such as a wide electrochemical window (>4), specific conductance of $> 75 \text{ mS.cm}^{-1}$ at room temperature, thermal stability up to 300°C , low toxicity have been discussed in Section I-1.2.3. However, numerous research efforts regarding the Equation I.9 in different electrolytes have been directed at the design of highly conductive, stable electrolytes with a wider voltage window²⁹ (Figure I-12).

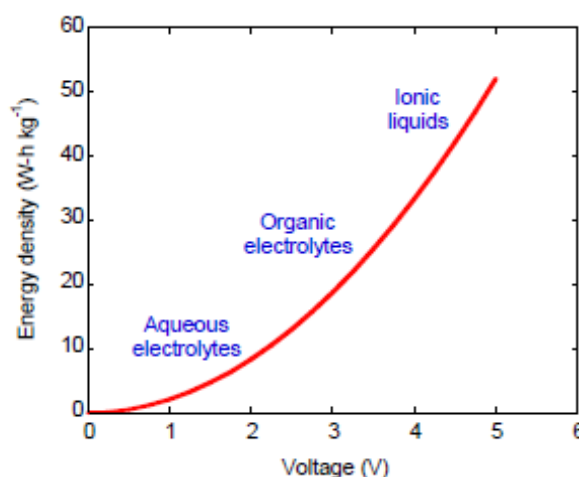


Figure I-12. Graph depicting the increase of energy density with ILs compared to other electrolytes³⁹

According to Figure I-12, ILs seem to be the most important electrolyte in terms of energy density and wider voltage window. However, as mentioned previously, the ionic conductivity is low at room temperature. Another example found in the literature⁴⁸ considering the wide voltage window is shown in Figure I-13.

Lin, R³⁹ has mentioned that the composition and associated properties of ILs depend on the cation and anion combinations. There are literally millions of different structures that may form an IL; the number of cation-anion combinations can be as high as 10^{18} combinations.⁸⁸ However, there are three basic main classes that are specific to different types of applications: Aprotic, Protic and Zwitterionic as shown in Figure I-14.^{39,89} Aprotic ILs seem to be the most used for EDLC applications, because there are a huge interest in increasing the cell voltage above 3V.³⁹ Therefore,

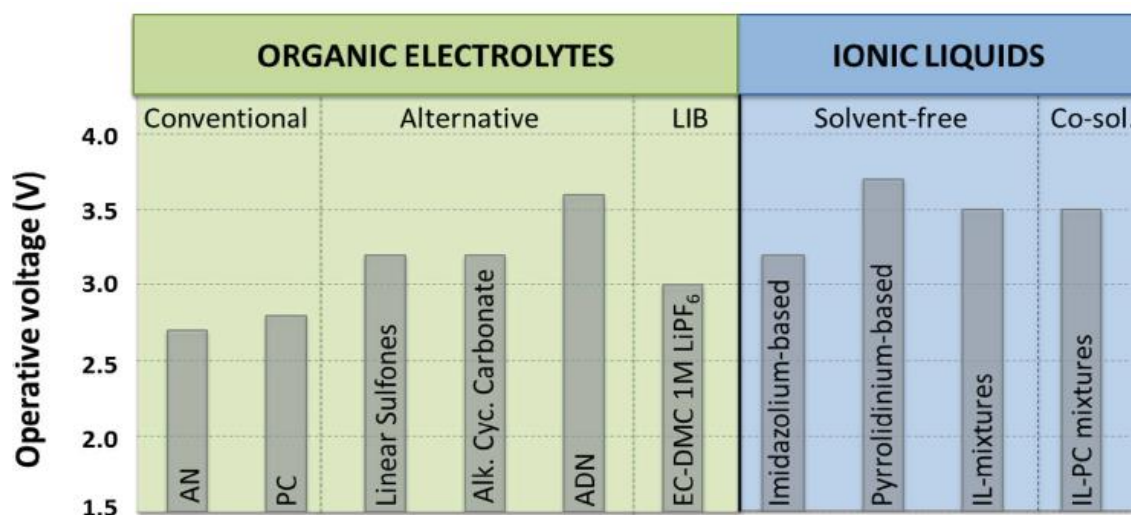


Figure 1-13. Comparison of the EDLC operating voltage achievable with organic electrolyte and ionic liquids based electrolytes. AN (acetonitrile), PC (propylene carbonate), AND (adiponitrile), AlKylat. Cyc. Carb. (alkylated cyclic carbonate), EC (ethylene carbonate), DMC (dimethyl carbonate), LiPF₆ (lithium hexafluorophosphate), IL (ionic liquids).⁴⁸

ILs, being reputed for high electrochemical stability and thermal stability, are largely studied for energy storage applications.⁹⁰

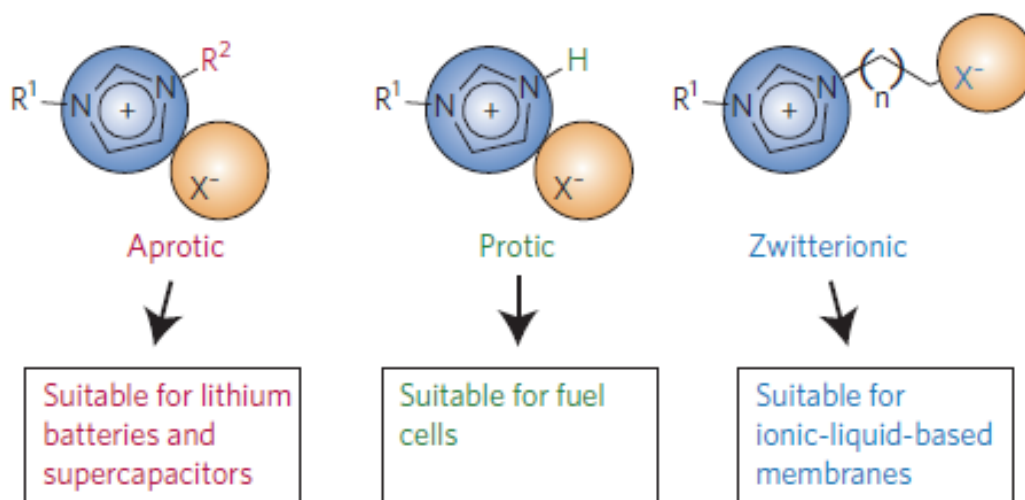


Figure I-14. Design of ILs for specific applications.⁸⁹

(iii) Pseudo-Capacitance

The pseudo-capacitors are another type of technology that store charge by means of a fast and reversible faradic redox reaction at the electrode surface (Figure I-15a), which has the effect of increasing the specific capacitance and the energy density.^{40,84,91}

In these devices, only part of the charge storage is assured by the double layer at the electrode/electrolyte interface, while another amount of transfer and storage is due to faradic mechanisms (redox reactions and intercalation).^{33,51}

The principal electrode materials used for charge storage in pseudo-capacitors are metal oxides, such as RuO_2 ⁹² and MnO_2 ,⁹³ and conducting polymers.⁹⁴⁻⁹⁶ However, as in batteries, the redox reactions affect cycle stability due to aging. Therefore, pseudo-capacitors are mainly used when the energy density is a larger issue than cycle stability.²⁹

(iv) Hybrid Electrodes

The hybrid technology aims to obtain an ideal storage device that has the high power density of a supercapacitor as well as the high energy density of a battery. In the literature, some examples of asymmetrically structured hybrid supercapacitors can be found. These combine a carbon electrode (of supercapacitor type) with a faradaic electrode (of battery type) (Figure I-15 d and e).

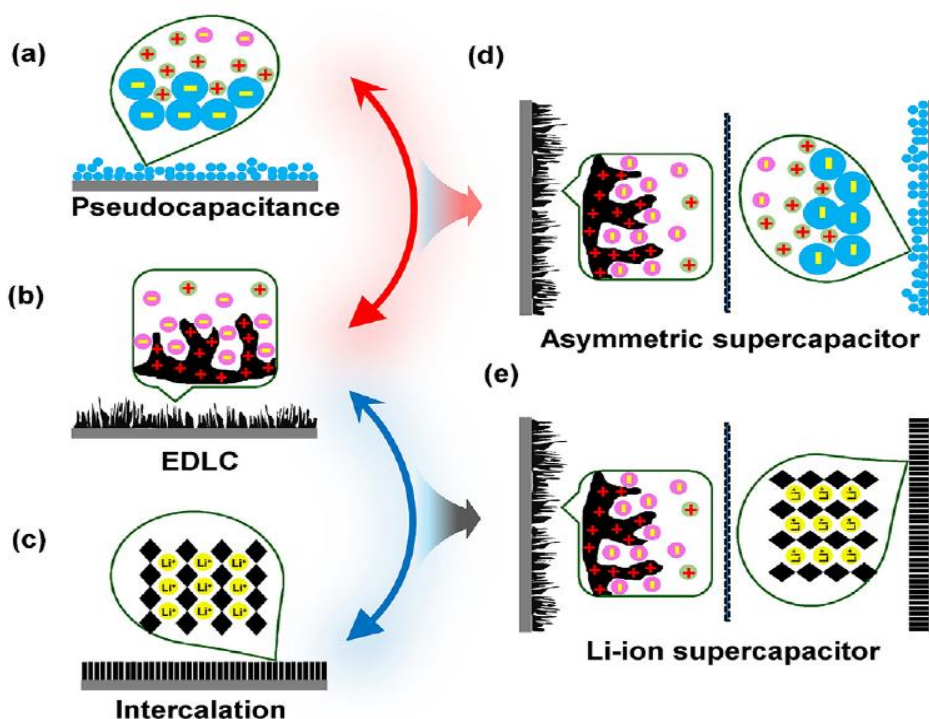


Figure I-15. Schematic illustrations of different storage mechanisms. Faradic reactions are involved in a) pseudocapacitance and c) intercalation; non-Faraday process is represented in EDLCs in b). Combining either a/b or c/d forms an asymmetric supercapacitor d) or a Li-ion supercapacitor e).⁹¹

However, in practice, these hybrid systems have intermediate characteristics: a charge/discharge speed slower than the classic supercapacitor (due to the speed of the redox reactions at the faradic electrode) and a shorter lifetime (due to the consumption of the active material caused by the chemical reactions). The evaluation of the actual performance of the hybrid

Chapter I. Bibliography

supercapacitors, in terms of power density and energy density and/or cyclability and lifetime, has been the objective of numerous studies.^{33,51,97} Recently, JSR Micro and JM Energy Corporation proposed two Li-ion hybrid supercapacitors called the 2300F and 3300F prototypes. Their energy density is about 10 Wh/kg.⁹⁸

In order to improve the performance of supercapacitors, another type of electrode materials named nanocomposite electrodes has been reported in the literature,²⁶ which is summarized in Table I-8.

Table I-8. Electrochemical performance of various carbon-metal oxide nanocomposites.²⁶

Metal oxides-carbon Nanocomposites	Amount of metal oxides loading (%)	Specific capacitance based on composite electrodes (F g^{-1})	Specific capacitance based on metal oxides alone (F g^{-1})	Electrolyte
$\text{RuO}_2/\text{carbon black}^{31}$	27	221	854	1 M H_2SO_4
$\text{RuO}_2/\text{carbon black}^{31}$	40	407	863	1 M H_2SO_4
$\text{RuO}_2/\text{CNT}^{99}$	17	—	1192	0.5 M H_2SO_4
$\text{RuO}_2/\text{graphene}^{100}$	38.3	—	570	1 M H_2SO_4
$\text{MnO}_2/\text{CNT}/\text{PEDOT-PSS}^{101}$	60	—	129	1M Na_2SO_4
$\text{MnO}_2/\text{carbon}^{102}$	70	218	—	1M Na_2SO_4
$\text{MnO}_2/\text{graphene oxide}^{103}$	90.7	197.2	211.2	1M Na_2SO_4
$\text{Co}_3\text{O}_4/\text{graphene}^{104}$	24.4	—	243.2	6 M KOH
$\text{NiO}/\text{CNT}^{105}$	50	523.37	1037.74	6 M KOH
$\text{NiO}/\text{CNT}^{105}$	80	326.2	405.5	6 M KOH
$\text{V}_2\text{O}_5/\text{CNT}^{106}$	80	288	—	1 M LiClO_4

I-1.2.5. Supercapacitor Applications

Initially, supercapacitors were mainly used for applications requiring low voltage and low capacitance, such as back-up memories, security and alarm systems, toys and watches *etc.*³³ Still, these kinds of consumer electronics are the main domain for supercapacitors. However, the development of low cost supercapacitors with higher capacitance that also can be used at high voltage has opened up new markets, for example, industrial applications (uninterruptible power

supply (UPS), elevators, cranes *etc.*), electric utility applications (electricity grids) and transportation applications (starting engines, electric and hybrid vehicles, hybrid buses, trolley buses, trams *etc.*).³³ These markets are expected to grow rapidly in the coming years,³³ although supercapacitor technology still needs to overcome or circumvent the problem of low energy density to improve their performance.^{33,107}

I-2. Diagnostic Tools for Electrodes in Energy Storage

In order to improve the performances of these various storage systems, it is necessary to use pertinent tools to examine the electrochemical behavior of the different materials suggested. Electrochemical methods, surface structural analysis procedures and electrogravimetric methods will be discussed in this section. The electrode/electrolyte interfaces of the supercapacitors can be investigated and the energy storage properties can be related to the structural characteristics.

I-2.1. Electrochemical Methods

In this section, three electrochemical methods will be detailed. These are specifically (i) cyclic voltammetry, (ii) galvanostatic charge-discharge and (iii) electrochemical impedance spectroscopy.

I-2.1.1. Cyclic Voltammetry (CV)

The CV is a potentiodynamic electrochemical measurement technique that measures current versus potential. The principle is to impose two successive potential scans (cyclic) between the working electrode and the reference electrode while the current is measured across the working electrode and the counter electrode.^{108,109} These data are plotted as current (i) vs applied potential (E/V) to give the cyclic voltammogram trace. The potential range is in general limited by the electrolyte stability window.

In the literature, it has been reported that cyclic voltammetry provides quantitative and qualitative information on the capacitive behavior between the electrolyte ions and the active materials. Also, the presence of parasitic faradic reactions has been identified.^{39,40} A typical cyclic voltammogram curve, for capacitance diagnosis, is shown in Figure I-16.

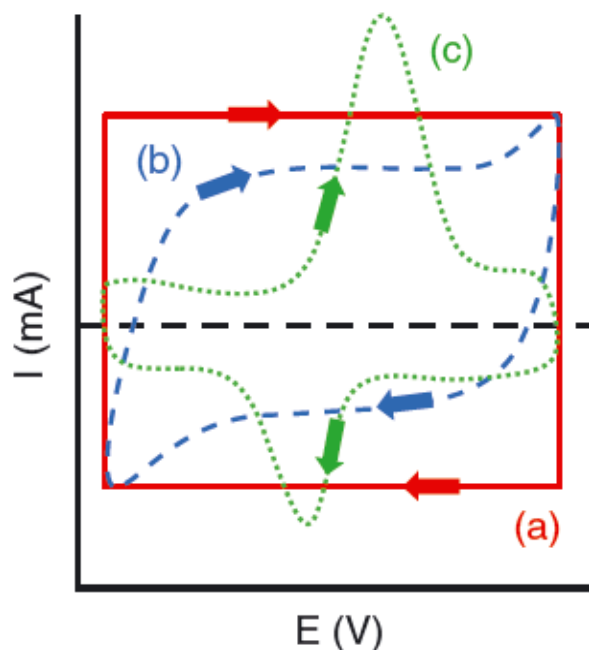


Figure I-16. Cyclic voltammogram curves of (a) ideal electrochemical capacitor, (b) EDLC, and (c) pseudocapacitive materials.³⁸

In Figure I-16a, the rectangular CV represents an ideal supercapacitor response. However, in practice, a more or less deformed rectangular shape is obtained due to contact resistance and electrolyte resistance in the pores (Figure I-16b). Two redox peaks are observed in Figure I-16c. These are caused by faradic reactions, which are characteristic for pseudo-capacitive behavior.

Using CV, the capacitive and pseudo-capacitive behavior of activated carbon materials and metal oxide (MnO_2), respectively, have been reported in the literature (See Figure I-17 and I-18).²⁹

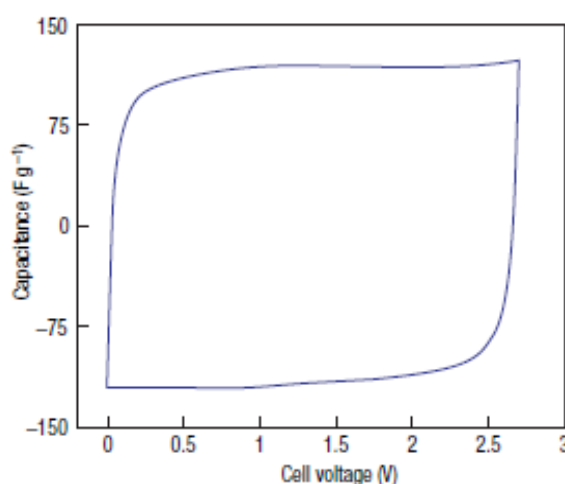


Figure I.17. Cyclic voltammetry of a two-electrode EDCL cell in 1.5 M Net_4^+ , BF_4^- in acetonitrile-base electrolyte, containing activated carbon powders coated on aluminum current collectors. Scan rate of 20 mVs^{-1} .²⁹

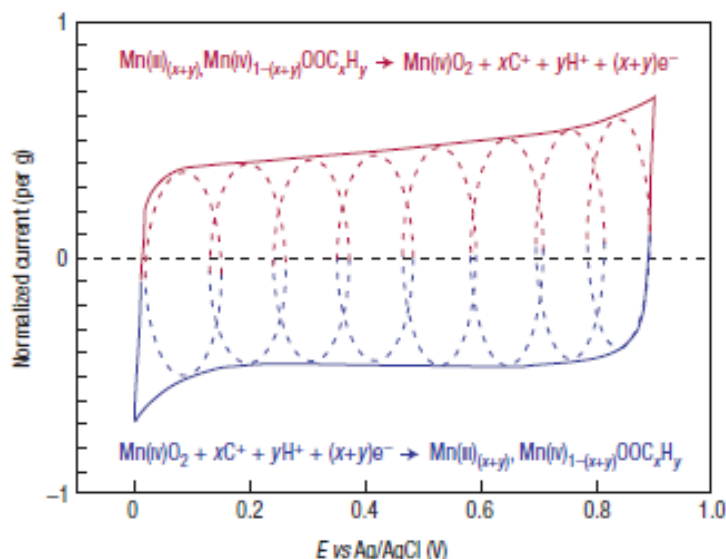


Figure I-18. Cyclic voltammetry a MnO₂- electrode cell in K₂SO₄(0.1 M) shows the successive multiple surface redox reactions leading to the pseudo-capacitive charge storage mechanism. The red (upper) part is related to the oxidation from Mn(III) to Mn(IV) and the blue (lower) part refers to the reduction from Mn(IV) to Mn(III).²⁹

I-2.1.2. Galvanostatic Charge-Discharge method (GCD)

GCD is an alternative method to measure the capacitance, resistance and cyclability of the electrode materials.³⁹ This technique consists in performing charge/discharge cycles. A constant current density is applied and the potential response is measured over time¹¹⁰ (Figure I-19). From the slope of the discharge curve shown in Figure I-19, the cell capacitance (C) can be calculated using the following equation:¹¹³

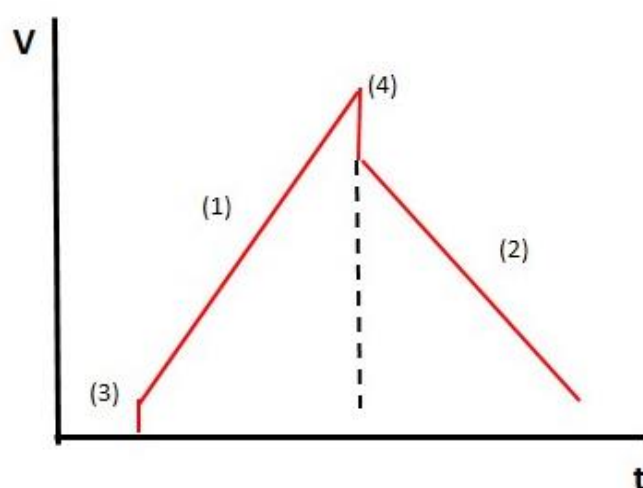


Figure I-19. The typical curve of a galvanostatic charge-discharge process. 1. The cell behavior during charging; 2. The cell behavior during discharging; 3. The initial process; 4. This section is responsible for the negative resistive ohmic lost associated with the resistance of the cell.^{111,112}

$$C = \frac{I}{\frac{dV}{dt}} \quad \text{I-10}$$

where I is the discharge current and dV/dt the slope of the discharge curve. The specific capacitance C_s is related to the capacitance of the cell C by:

$$C_s = \frac{2C}{m} \quad \text{I-11}$$

where m is the mass per electrode of the active material.

I-2.1.3 Electrochemical Impedance Spectroscopy (EIS)

The EIS measurements, which are based on frequency modulation, provide qualitative information on the studied system (capacitive, resistive, diffusive behavior *etc.*) and allow the calculation of the capacitance of the electrodes.¹¹⁰ In contrast to cyclic voltammetry, electrochemical impedance is based on the collection of an alternating current (AC) resulting from applying a sinusoidal potential perturbation with a small amplitude (typically 10 mV rms).^{109,114} The Nyquist diagram ($-ImZ$, ReZ Cartesian coordinates) and the Bode diagram (polar coordinates) are the plots normally used for EIS measurements, which will be further detailed in Chapter II.

In the literature, there are a number of works employing EIS to study carbon electrodes in supercapacitors.^{52,115} An example reported by Portet *et al.*¹¹⁵ is presented in Figure I-20 which shows the EIS Nyquist plot of a 4 cm² cell supercapacitor constituted with activated carbon between 10mHz and 50kHz at OCV. The authors observed that at higher frequencies, the supercapacitor behaves like a pure resistance. When the frequency is decreased, the ion migration inside the porous active material can be seen. At low frequencies, the imaginary part of the impedance increases, showing the capacitive behavior of the supercapacitor.¹¹⁵

Simon, P *et al.*¹¹⁶ have reported another example of an electrochemical impedance spectroscopy study of ion transport into sub-nanometer carbon pores in EDLC electrodes. Figure I-21 shows the Nyquist plots of the various CDC samples (pore size of 0.68; 0.76; 1.00 nm) in 1.5M Net_4BF_4 in AN at 0.5V/Ref.

For these experimental records, the authors observed that the Nyquist plots of the three CDC samples show a similar shape in disregard of the pore size, characteristics of the capacitive behavior of a porous electrode. At high frequency (> 1 KHz), where the plots intercept the real axis, the supercapacitor behaves like a pure resistance. In the low frequency domain, the huge increase of the

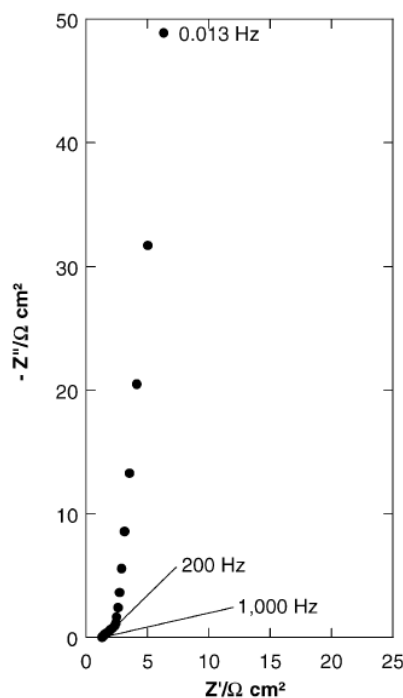


Figure I-20. Nyquist plot for 4 cm² cells assembled with electrodes constituted with activated carbon in 1.5M Net₄BF₄.¹¹⁵

imaginary part of the impedance corresponds to the capacitive behavior linked with the ion adsorption in the whole porous network, in this case BF₄⁻ anion. Finally, the authors considered that this part can be characterized by the extent of deviation from the 90° theoretical vertical line observed for an ideal capacitance.

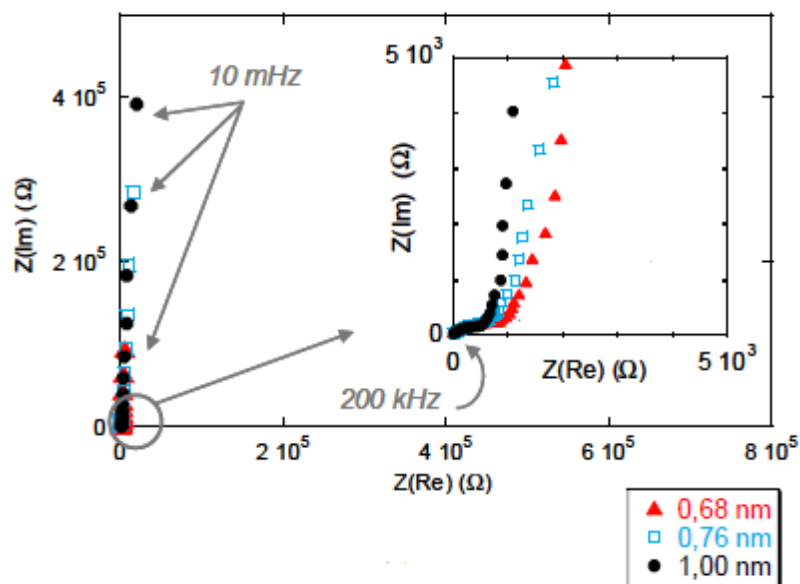


Figure I-21. Nyquist plots of the three CDC samples in AN + 1.5 M Net₄BF₄ electrolyte at an applied voltage of 0.5V/Ref which concerns the anion and cation electro-adsorption, respectively. A zoom at high frequencies is shown in the onsets.⁴⁰

I-2.2. Structural and Morphological Analysis: XRD, SEM, TEM, EDX and BET

This section will discuss five different techniques for structural and morphological analysis:

(i) X-Ray Diffraction (XRD), (ii) Scanning Electron Microscopy (SEM), (iii) Transmission Electron Microscopy (TEM), (iv) Energy-Dispersive X-ray Spectroscopy (EDX), and (v) nitrogen physisorption (Brunauer Emmett and Teller (BET)).

I-2.2.1. X-Ray Diffraction (XRD)

XRD is a fruitful characterization technique used to obtain structural information such as the crystal size, the crystallographic structures, the interlayer spacing, the structural strain, the crystal orientation *etc.*¹¹⁷⁻¹¹⁹ In addition, detailed information of the electron density distribution can be accessed.¹²⁰

Dall'Agnese *et al.*¹²¹ have used XRD to study the mechanism of Na^+ intercalation in Two-Dimensional Vanadium Carbide (MXene) (V_2CT_x) for Sodium-Ion Capacitor applications. Figure I-22 shows *ex. situ* XRD patterns of V_2CT_x recorded at different voltages. The authors observed that the (002) peak shifts continuously and reversibly from 9° to 12° during cycling between 1 and 3.5V versus Na^+/Na . In this potential range, the change is perfectly reversible, thus demonstrating that there are no undesired side reactions. During sodiation, the c-lattice parameter increases with the amount of Na^+ stored. The authors conclude that the V_2CT_x material stores energy through intercalation of Na ions in between the layers.¹²¹

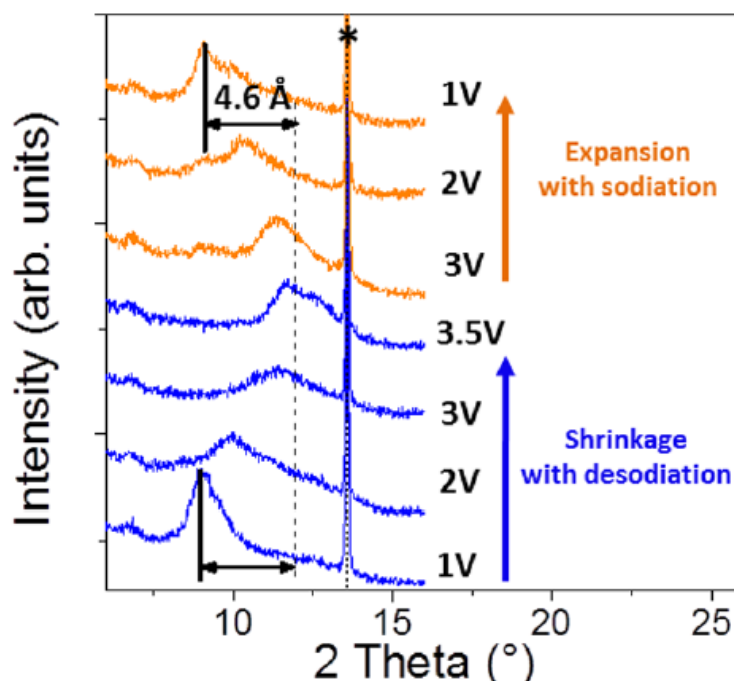


Figure I-22. XRD patterns at different potentials. (*) Peak of unreacted V_2AIC .¹²¹

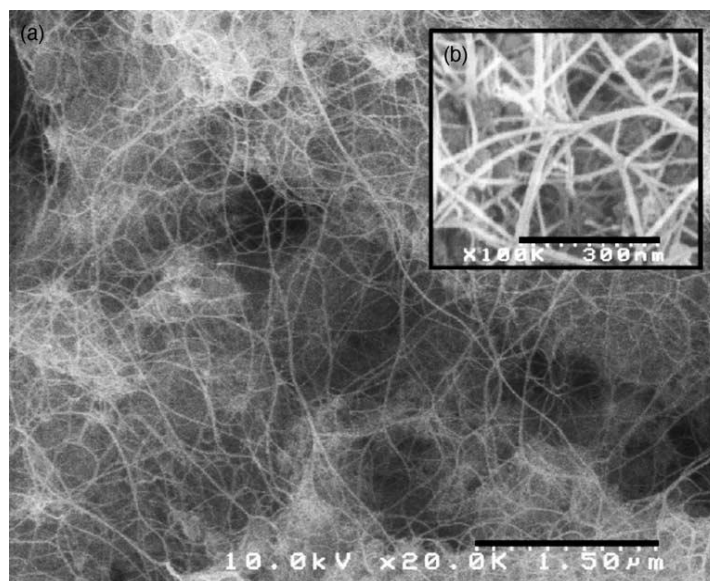


Figure I-23. (a) FEG-SEM image of the raw sample of DWCNTs. Inset (b) shows a higher magnification image of the bundles of DWCNTs.¹¹⁵

I-2.2.2. Scanning Electron Microscopy (SEM) and FEG-SEM

The scanning electron microscopy (SEM) can be used for the characterization and the exploration of the surface topography.^{36,122} SEM forms images from signals produced by the complex interactions between a primary electron beam and the sample, for example, a specimen of CNTs.

There are various types of electron guns. In comparison to thermionic electron guns, field emission guns (FEGs) provide enhanced electron brightness (approximately x 100) and longer lifetime. Furthermore, because of the lower electron energy spread (0.3 eV), the chromatic aberration is significantly reduced and probes smaller than 2 nm can be formed, thus, providing much higher resolution for SEM images.¹²² An example is shown in Fig I-23,¹¹⁵ which represents a FEG-SEM image of the raw CNT samples (before removal of the catalyst), revealing an important density of bundles of CNTs with extensive branching.¹¹⁵

Hui Pan *et al.*⁸⁵ have reported that the effects of shape engineering can greatly improve the capacitance and power density in CNTs. When compared with activated carbon cells, the high-density packed and aligned SWCNTs showed higher capacitance, less capacitance drop at high-power operation and better performance for thick electrodes. The SEM images in Figure I-24 show that the SWCNTs are high-densely packed after shape engineering.⁸⁵

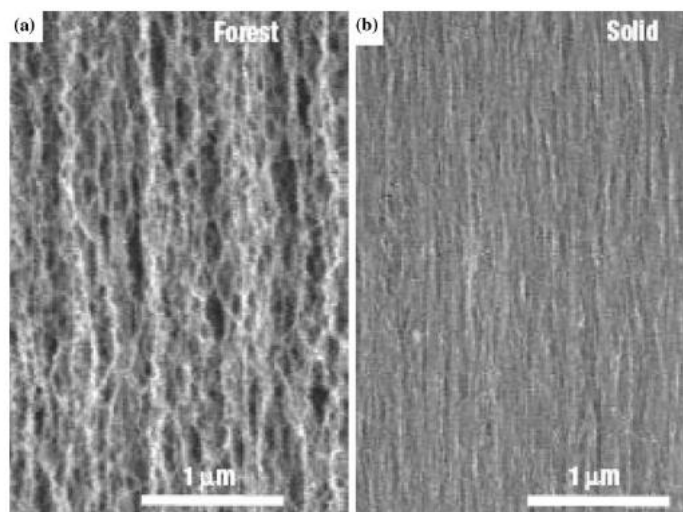


Figure I-24. SEM images of (a) the as-grown forest and (b) shape-engineered SWCNTs.⁸⁵

I-2.2.3. Transmission Electron Microscopy (TEM or HRTEM)

Transmission Electron Microscopy (TEM) is a characterization method for the visualization of the structural aspects (size and shape) of a sample. In its classic mode, the resolution is in the order of a few nanometers and, in its high resolution mode, so-called High Resolution Transmission Electron Microscopy (HRTEM), the resolution is about a tenth of nanometers.

Su, D. S. *et al.*¹²³ have reported that texture is an essential aspect in CNT type materials with regard to their application in Li-ion batteries. An example is shown Figure I-25, which compares the microstructure of a defect rich CNT (Figure I-25a) with a CNT with well-ordered graphitic wall (Figure I-25b). The authors conclude that a higher density of defects increase the Li-storage capacitance. Treatments (*e.g.* ball-milling the CNTs) that increase defect density and reduce the length of CNTs can change the performance of electrode materials.¹²³

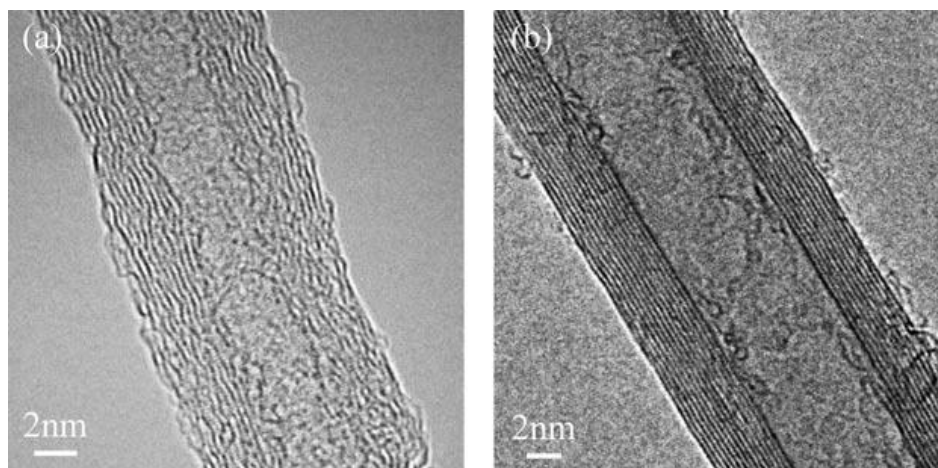


Figure I-25. HRTEM of CNTs with a) defect-rich surface and walls, and b) well-ordered graphitic walls.¹²³

I-2.2.4 Energy-Dispersive X-ray Spectroscopy (EDX)

Scanning Electron Microscopy (SEM) or Transmission Electron Microscopy (TEM) is generally combined with the Energy-Dispersive X-ray Spectroscopy (EDX or EDS)¹¹⁹ to quantify the elements present in a sample. Also, the elemental mapping of samples and image analysis can be obtained.

The EDX technique is based on the detection of X-rays emitted due to the interaction between electrons and sample atoms. Depending on the transmitter element, the energy of the electrons is different, which allows the identification of the elements present in the sample with the possibility of a quantitative analysis by measuring a known standard for each element.^{124,125}

Nossol, E, *et al.* have performed EDX analysis of CNT/Prussian Blue nanocomposite films, which is shown in Figure I-26. The authors conclude that the formation of Prussian Blue (PB) (Figure I-26a) also reveals the presence of both C and Fe. Figure 1-26b shows the EDX data after 150 cycles of the potential. The presence of N confirms the PB formation on the CNTs. In addition, an increase in the Fe/C peak ratio, from 0.08 to 0.22, has been found.¹²⁶

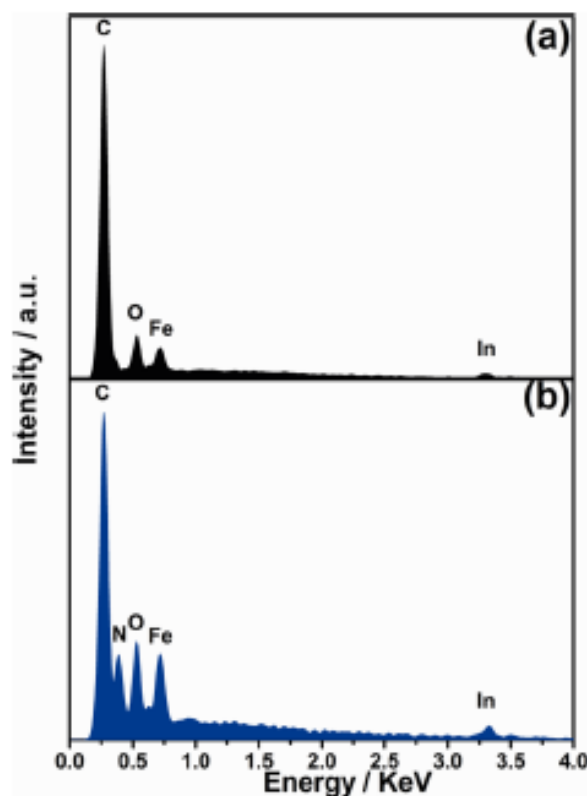


Figure I-26. EDX analysis of a CNT film before (a) and after (b) the formation of PB.¹²⁶

I-2.2.5. Brunauer Emmett and Teller (BET)

In the literature,^{34,45} it is very often assumed that the specific surface area estimated through the BET approach is equivalent to the specific surface area of the electrode/electrolyte interface. Therefore, some proportionality should exist between the estimated gravimetric capacitance and the BET specific surface area measured by nitrogen adsorption at 77°K. In Figure I-27, an example for a series of nanoporous carbons obtained by KOH activation of bituminous coal pyrolyzed at 520°C-1000°C is shown.¹²⁷ The proportionality is observed only for the low values of the BET specific surface area. Above 2000 m² g⁻¹, the observed values may be caused by an overestimation of the values of the specific surface area by the BET model.

In another work, Frackowiak *et al.*¹²⁸ have studied the effects of structures and diameters of CNTs, and microtexture and elemental composition of the materials on the capacitance. Table I-9 shows that the capacitance increases with increased specific surface area. The smallest value is obtained in CNTs with closed tips and graphitized carbon layers, where the mesopore volume for the diffusion of ions and the active surface area for the formation of the electrical double layer are very limited. The nanotubes with numerous edge planes, either due to herringbone morphology (A900Co/Si) or due to amorphous carbon coating (A700Co/Si), are the most efficient materials for the collection of charges. Quite moderate performance is given by straight and rigid nanotubes of large diameter (P800A1) despite a relatively high specific surface area.

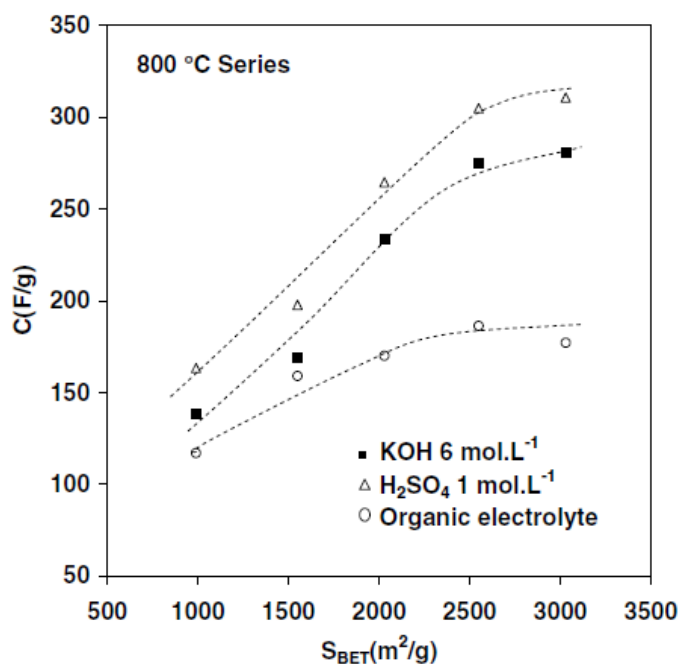


Figure I-27. Gravimetric capacitance in various electrolytes (1 mol L⁻¹ H₂SO₄, 6 mol L⁻¹ KOH and 1 mol L⁻¹ TEABF₄ in acetonitrile) vs BET specific surface area for a series of bituminous coal-derived carbons activated by KOH at 800°C.¹²⁷

Table I-9. BET specific surface area, mesopore volume, percentage of oxygen, and capacitance of the analyzed nanotubes.

Type of nanotubes	A700Co/Si	A900Co/Si	A600Co/NaY	P800/Al
V _{meso} (cm ³ STP/g)	435	381	269	643
SBET (m ² /g)	411	396	128	311
Oxygen (mass %)	10.8	4.6	0.8	<0.3
Capacitance (F/g)	80	62	4	36

However, the diameter of the central canal is too large in comparison to the size of the solvated ions. On the other hand, this particular behavior could also be due to a very hydrophobic character of these tubes, as suggested by the very small value of oxygen content (Table I-9).^{111,128}

I-2.3. Classical Electrogravimetric Investigations: Quartz Crystal Microbalance Based Methods

The most used electrogravimetric method for mass analysis and current changes is the EQCM (Electrochemical Quartz Crystal Microbalance), which will be discussed in this section.

Electrochemical Quartz Crystal Microbalance (EQCM) is a method where a Quartz Crystal Microbalance (QCM) is coupled with an electrochemical measurement.^{129,130} This method is also called cyclic electrogravimetry.^{131,132}

The EQCM is capable of quantitatively measuring small mass changes occurring at the electrode surface during an electrochemical process. It is able to detect mass changes in the order of 1 nanogram.¹³³ This method has been used to investigate diverse phenomena, for example, metal electrodeposition,¹³⁴⁻¹³⁶ electrocrystallization,¹³⁷ electrochromic reactions,¹³⁸ intercalation,^{131,139} and adsorption and mass changes associated with electrolyte-ion movement.¹⁴⁰⁻¹⁴²

The EQCM allows the investigation of the capacitive properties by analyzing the capacitive current and the resulting mass changes of the film. The operation principle of the EQCM will be discussed in further detail in Chapter II.

Reviewing the literature, only a limited number of works employing EQCM to study carbon materials can be found.^{2,143} Barisci *et al.* monitored the mass changes of carbon nanotube films as a function of the applied potential in both aqueous and non-aqueous solutions (Figure I-28).¹⁴³ The authors reported that the mass changes as a function of the applied potential are not directly proportional to the cation mass but they are associated with double-layer charging. The mass changes of nanotube films in acetonitrile solutions are similar to those observed for aqueous electrolytes (Figure I-28a) when the cation is tetrabutylammonium (Figure I-28b). However,

solutions of Li^+ cause a substantial increase in the nanotube film mass associated with cation insertion, which is not readily reversed, thus reflecting slow Li^+ expulsion (Figure I-28c). The authors concluded that the movements of anions, cations, and solvent molecules in the pores of the carbon nanotube films during potential sweeping involve complicated mechanisms.¹⁴³

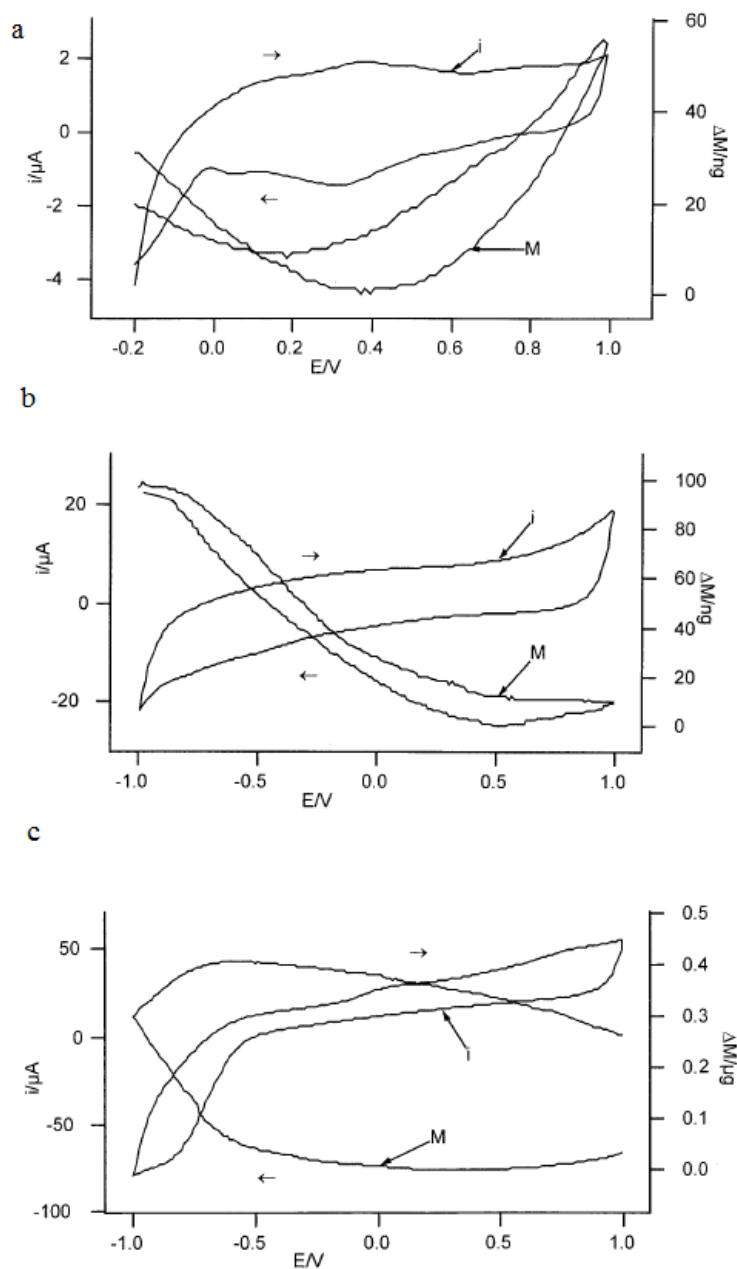


Figure I-28. Current-potential and mass-potential curves for a CNT film in (a) 0.1 M H_2SO_4 , (b) 0.1M TBATFB/acetonitrile and (c) 0.1M LiClO_4 /acetonitrile. Scan rate 50mV s^{-1} (reference electrode Ag/Ag^+).¹⁴³

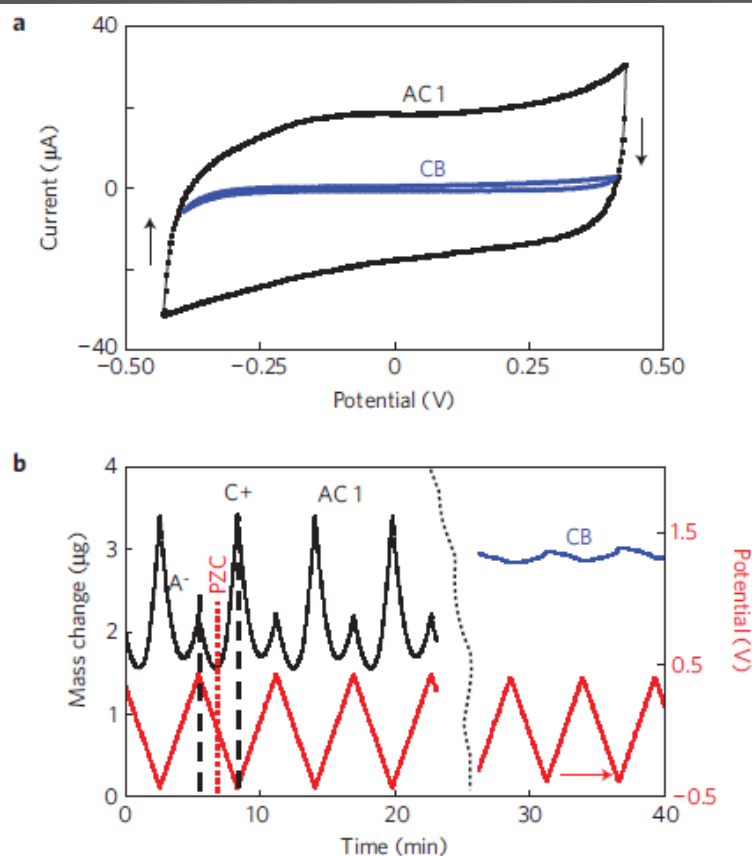


Figure I-29. (a) Cyclic voltammetry curves measured at a scan rate of 5 mV s^{-1} Ag/AgCl in aqueous 0.5M CsCl. (b) Simultaneously measured QCM responses. The red straight lines relate to the potential-time dependencies; the black and the blue curves represent the related mass changes of the cations (C^+) and anions (A^-) during potentiodynamic cycling of the electrodes.²

Maier *et al.* studied EQCM responses of typical microporous activated carbons. The periodic mass change during cycling was found to be much higher than that of the non-porous carbon-black electrode, proving the sorption of both anions and cations in relation to the microporous volume of the electrode² (Figure I-29).

Also, Maier *et al.* have studied the effect of specific adsorption of cations and their size on the charge-compensation mechanism in carbon micropores. This material was tested in 0.5 M NH_4Cl solution using the EQCM technique.¹⁴⁴ The authors reported that this technique reveals a complicated interplay between the adsorption of NH_4^+ cations and desorption of Cl^- anions inside carbon micropores at low surface charge densities, which results in failure of their permselectivity. Higher negative surface charge densities induce complete exclusion (desorption) of the Cl^- co-ions, which imparts purely permselective behavior on the carbon micropores (Figure I-30).¹⁴⁴

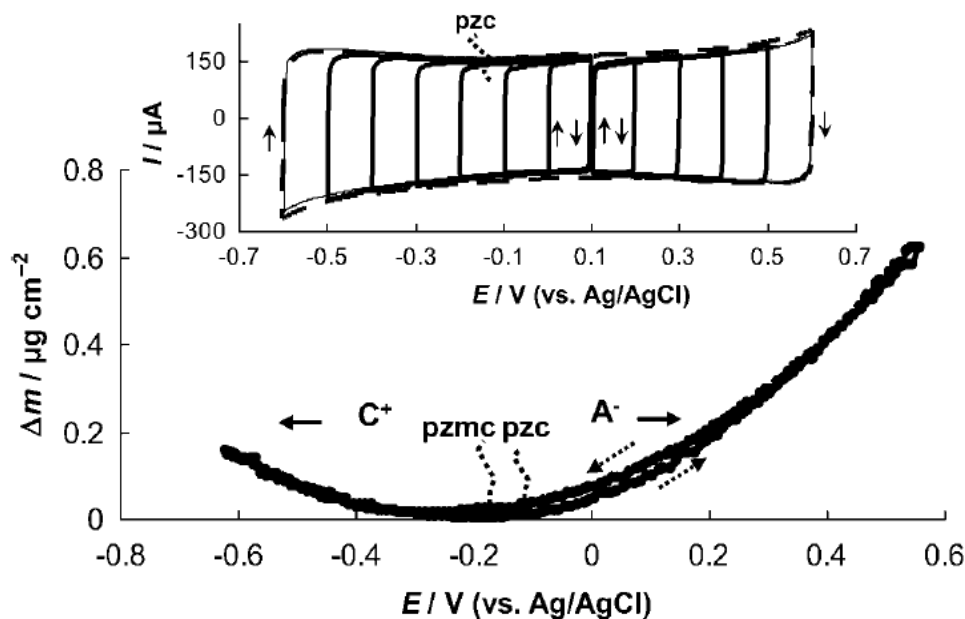


Figure I-30. Mass change of the carbon electrode in a 0.5M aqueous solution of NH_4Cl (scan rate = 20 mVs^{-1}) measured simultaneously with the CV of the largest 1.2V amplitude (see inset, broken line). The inset also shows a series of CVs measured with different potential amplitudes.¹⁴⁴

In order to quantitatively correlate the mass changes of the adsorbed ions and solvent molecules with the potential-induced variation of the electrode charge density, two terms are introduced by the authors: the potential of zero charge (pzc) and the potential of zero mass change (pzmc). The pzmc should coincide with the pzc, since, according to a conventional point of view, adsorption of anions and cations into carbon micropores occurs at $Q > 0$ and $Q < 0$, respectively. However, the pzmc obtained from the EQCM does not necessarily coincide with the pzc of the electrode, since the former may depend on the dynamics of formation of the ionic part of the electric double layer (EDL), that is, on the relation between the fluxes of counterions (anions at $Q > 0$ and cations at $Q < 0$) and co-ions (cations at $Q > 0$ and anions at $Q < 0$).

Recently, Tsai *et al.* reported that the combination of the CV and EQCM techniques offers a great opportunity for the understanding of ion transport and extent of solvation in porous materials, thus, enabling the design of optimized porous materials for the next generation of high energy density supercapacitors.¹⁴²

The authors obtained EQCM results from a sample of carbide-derived carbon with a pore size of 1 nm (CDC-1 nm) tested in 2 M EMI-TFSI AN solution (Figure I-31). From the frequency responses, the authors observed that the electrode mass increased during cation/anion adsorption and decreased during cation/anion desorption.¹⁴²

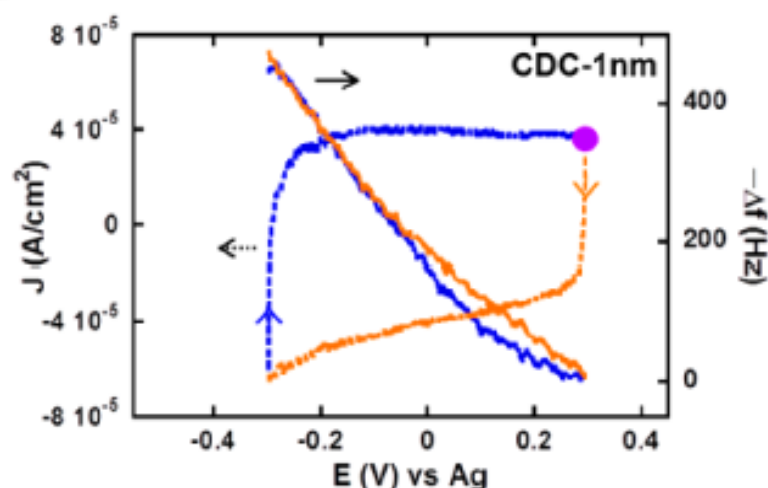


Figure I-31. CV and QCM frequency responses of CDC-1 nm films in 2 M EMI-TFSI/AN.¹⁴²

In fact, according to a classical approach, adsorption of anions is expected when the CDC electrode surface is positively charged, whereas the adsorption of cations should take place when the surface is negatively charged.¹³⁹

Regarding these previous studies, EQCM provides only a global response of the carbon film and kinetic information cannot really be obtained. Therefore, in these previous studies, an unambiguous identification of the species transferred and the determination of the free solvent contribution were not possible. To overcome these limitations, possible alternative methods should be sought.

I-3. The Scope and Objectives of the Ph.D. Thesis

Ionic transfer and transport phenomena largely influence the performance of the electrode materials for energy storage applications. Some studies suggest the use of microbalances as a means to characterize ion fluxes and transport phenomena for electrodes based on carbon. It has been demonstrated that the response of the microbalance allows an *in situ* estimation of the ionic flux, which strongly depends on the point of zero charge (PZC), of the pore size and of the size of the ions. Unfortunately, subtleties or more fair explanations cannot be reached through this classical technique.

In this Ph. D. thesis, coupled electrochemical and gravimetric methods, resolved at temporal level, specifically the electrochemical impedance spectroscopy (EIS) coupled with fast quartz microbalance (QCM) (*ac*-electrogravimetry), have been used to study the capacitive behavior of carbon based electrodes.

The use of *ac*-electrogravimetry provides very relevant information: kinetics and identification of the species transferred to the electrode/electrolyte interface, separation of the

contribution of different species and change of the relative concentration of species within the material. More precisely, all the species involved in the charge storing process can be identified by their atomic mass *via* a reversible adsorption of ions in the thin carbon films. Consequently, *ac*-electrogravimetry appears to be an attractive tool for studying the nature of the ionic flux at the electrode/electrolyte interface.

In this study, carbon nanotubes (CNTs), graphene and CNTs/polypyrrole, CNTs/Prussian blue nanocomposites have been selected due to their unique set of characteristics suitable for electrode materials in electrochemical devices (EDLCs as well as pseudocapacitors and hybrid capacitors). To achieve these objectives, new models, taking into account of non-redox processes and the combination of redox and non-redox processes, have been developed.

Chapter II. Experimental Part

CHAPTER II

Experimental Part

Chapter 2 begins with a detailed description of sample preparation. Three kinds of samples were prepared: Carbon nanotubes (CNTs), Carbon Nanocomposites and Electrochemically Reduced Graphene Oxides (ERGO). Thereafter follows a description of the methods used for the structural and morphological characterization of samples, particularly, the principle of operation of the methods, the type of instruments used and under which conditions the experiments were performed. Finally, the electrochemical characterization techniques applied in this Ph.D. thesis will be presented.

II-1. Preparation Procedure of Carbon Based Thin Film Electrodes

Materials such as Carbon Nanotubes (CNTs), Carbon Nanocomposites and Graphene Oxides were used for producing carbon based thin films on gold-patterned quartz substrates of 9 MHz as working electrodes. The reason for using the gold-patterned quartz substrates of 9 MHz as working electrodes (WE) is twofold: (i) it allows the EQCM and *ac*-electrogravimetric measurements to be realized, and (ii) it permits the recording of the frequency of the quartz resonator before and after the deposition of the CNTs or Graphene Oxide which is related to the deposited film mass using Sauerbrey's equation which will be detailed in the following.

II-1.1. Preparation of Carbon Nanotube (CNT) Based Thin Film Electrodes (Single Wall CNT, Double Wall CNT, Multi Wall CNT)

To achieve nanostructured electrodes, three types of carbon nanotubes: Single Wall CNT (755117-1G, length: 300-2300 nm and diameter: 0.7-1.1 nm), Double Wall CNT (755141-1G, length: 3 μm and diameter: 3.5 nm) and Multi Wall CNT (75517-1G, length: 1 μm and diameter: 9.5), acquired in Sigma Aldrich Company were chosen due to their tailorable pore dimensions and variety of specific surface areas. The preparation of CNT films was carried out according to the method described in the literature.^{2,140} CNTs were deposited by the "drop-casting" method on a gold electrode (effective surface area of 0.20 cm^2) of a quartz crystal resonator (9 MHz -AWS, Valencia, Spain), from a solution of carbon containing 90% CNT powder and 10% PVDF-HFP (Poly(vinylidene fluoride-hexafluoropropylene)) polymer binder in N-methyl-2-pyrrolidone. Around 8 μL of this solution was deposited on the gold electrode of the QCM. Then, the carbon films were subjected to a heat treatment at 120 $^{\circ}\text{C}$ for 30 minutes, with a heating rate of $\sim 5^{\circ}\text{C min}^{-1}$ to evaporate the residual solvent and improve the adhesion properties of the films on gold electrode (Figure II-1). The film thickness was estimated to be around 500 nm (based on FEG-SEM measurements).

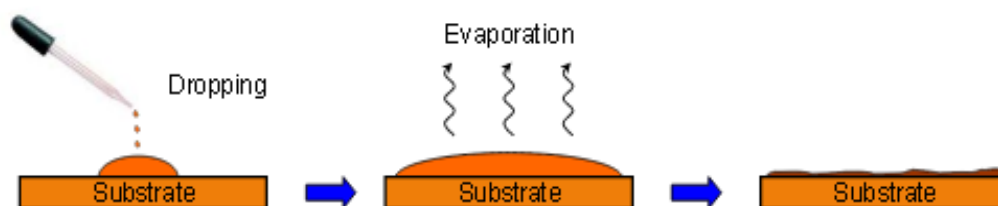


Figure II-1. Schematic representation of CNT Film Preparation.

Thereafter, EQCM and *ac*-electrogravimetric measurements were realized in 0.5 M aqueous solutions containing Li^+ , Na^+ , K^+ and Cl^- ions such as LiCl, NaCl and KCl (at different pH values). Moreover, measurements were realized in propylene carbonate containing 0.5 M LiClO_4 .

I-1.2. Elaboration of Nanocomposite Structures

Particularly, nanocomposite electrodes of CNTs and conducting polymers have been intensively studied the last few years to improve the specific capacitance of the supercapacitors.^{85,145,146} In this Ph.D. thesis, Prussian Blue (PB) and Polypyrrole were chosen to elaborate nanocomposite structures, because of their interesting properties and applications found in the literature.^{126,145,147,148} The elaboration of such thin film nanocomposite electrodes is explained below.

II-1.2.1. SWCNT/Prussian Blue Thin Film Electrodes

The preparation of SWCNT/PB nanocomposite films was carried out according to the method described in the literature¹²⁶. The procedure consists of cycling the SWCNT film in a solution containing 1×10^{-3} M $\text{K}_3\text{Fe}(\text{CN})_6$ and 0.1 M KCl, without the addition of Fe^{3+} ions, at a scan rate of 0.05 V s^{-1} in a potential range from -0.2 V to 0.8 V *vs.* Ag/AgCl during 15 cycles. Then, electrochemical studies were realized in an aqueous solution of 0.5 M KCl, at pH 3.

II-1.2.2. SWCNT/Polypyrrole Thin Film Electrodes

The elaboration of the SWCNT/Polypyrrole nanocomposite films was established following a method described in the literature⁴. The procedure consists of cycling the SWCNT film, previously prepared in a solution containing 0.1 M pyrrole (previously distilled) and 0.05 M sodium dodecylsulphate (NaDS), at a scan rate of 0.01 V s^{-1} in a potential range from 0 V to 0.675 V *vs.* Ag/AgCl during 2 cycles. The chemicals NaDS (436143-25G) and pyrrole were acquired from Sigma Aldrich. EQCM and *ac*-electrogravimetric measurements were realized in a 0.5 M aqueous solution of CsCl.

II-1.3. Elaboration of Electrochemically Reduced Graphene Oxide (ERGO) Thin Film Electrodes

First, a GO thin film was prepared by depositing a GO suspension (GO powder in double-distilled water) on a gold-patterned quartz resonator as shown in Figure II-1. A 1 mg/ml GO suspension was prepared from GO powder in double-distilled water. This suspension was then placed in an ultrasonic bath for 3 hours. Then, 20 μL of GO suspension was deposited on the gold electrode of the quartz resonator. To do this in a controlled manner, a laboratory-made mask (proving the exposure of the gold electrode only) was used to prevent the solution to spread out on to the whole surface of the quartz resonators. A GO film was formed after drying in an oven at 70°C for 1h. The film thickness was estimated to be around 50 nm based on FEG-SEM measurements.

After the GO was successfully deposited on the quartz, the sample was electrochemically reduced to obtain ERGO. The electrochemical reduction was carried out by chronoamperometry at -1.1 V *vs.* Ag/AgCl during 5 minutes with a Biologic SP-200 potentiostat under the Ec-Lab software.

II-2. Structural and Morphological Investigation Methods

This section is dedicated to the various structural and morphological methods for characterization of carbon based materials. Particularly, the principle of operation of the methods, the type of instruments and the preparation of the samples for the experiments will be explained.

II-2.1. Scanning Electron Microscopy (SEM)

Figure II-2 shows a schematic description of a SEM set-up. The electron gun generates a primary electron beam in a vacuum. The beam is collimated by electromagnetic condenser lenses, focused by an objective lens, and scanned across the surface of the sample by electromagnetic deflection coils.¹⁴⁹ As a consequence of the sample/primary beam interaction, secondary electrons are emitted from the sample.¹²² The secondary electrons are selectively attracted towards the secondary electron detector through a grid held at a low positive potential with respect to the sample.¹⁴⁹ There, the secondary electrons are counted (number of electrons arrived/unit time) and the count rate is translated into an electrical signal,¹⁴⁹ which can be used for a visualization of the sample.¹²² The resulting image reflects the surface topology, since the number of electrons that are collected from each point is dependent on surface topology. In shallow surfaces, fewer electrons escape the surface and reach the detector resulting in darker areas, while at the edges and at convex surfaces, more electrons escape and reach the detector resulting in brighter areas. However, charge

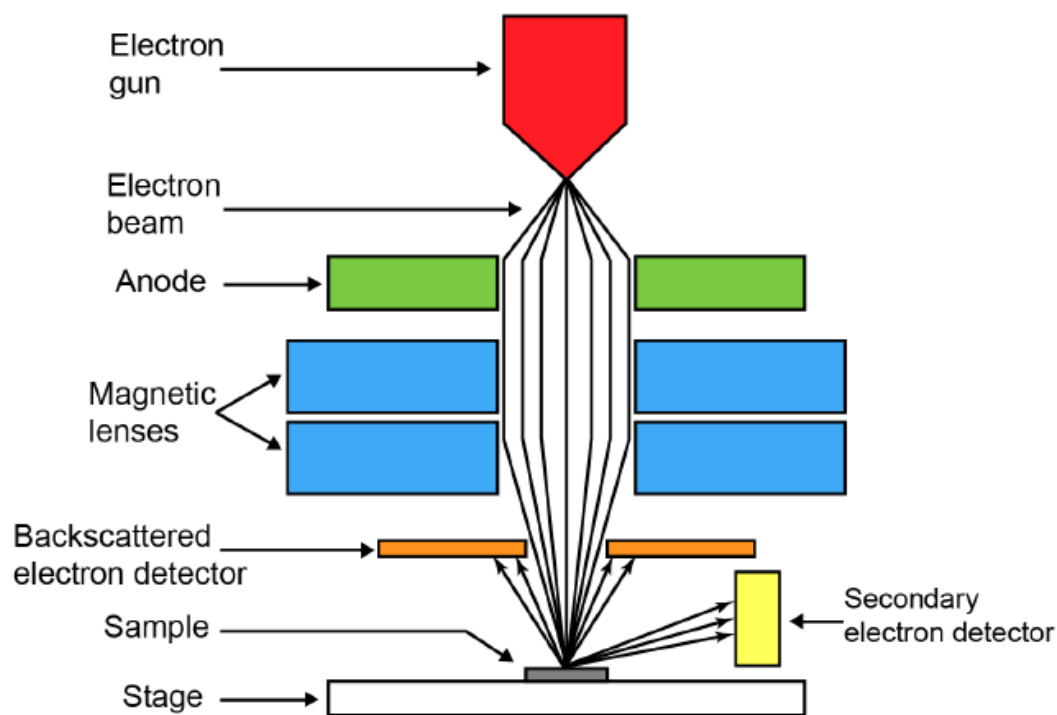


Figure II-2. Schematic description of a SEM set-up.¹⁵⁰

is built up on the sample surface by the electron bombardment of the primary beam and, in the case of non-conductive samples, this charge cannot be dissipated, which results in images that are bright throughout the sample. To avoid this, samples can be sputtered with a very thin layer of metals such as gold or gold/palladium as a part of the sample preparation.¹⁴⁹

There are various types of electron guns. In comparison to thermionic electron guns, field emission guns (FEGs) provide enhanced electron brightness (approximately $\times 100$) and longer lifetime. Furthermore, because of the lower electron energy spread (0.3 eV), the chromatic aberration is significantly reduced and probes smaller than 2 nm can be formed, thus, providing much higher resolution for SEM images.¹²²

In this Ph.D. thesis, the morphology and the thickness of the films were investigated by FEG-SEM (Zeiss, Supra 55). Before the analysis, the samples were fixed onto an aluminum stub with a conductive carbon tape and sputter-coated with gold (“JEOL JFC-1300 Auto fine coater”).

II-2.2. Transmission Electron Microscopy (TEM)

Figure II-3 shows a schematic presentation of a TEM set-up. The electron gun generates a primary electron beam either by thermoionic emission (using a heated filament as the cathode, *e.g.* LaB₆) or by field emission (using a fine tungsten tip as the cathode). The primary electron beam is focused by lenses into a thin, coherent beam, which hits the sample, resulting in various kinds of interaction between the electrons and the sample, *i.e.* absorption, diffraction, and elastic or inelastic scattering. The scattering processes are a result of the interaction between electrons and the nuclei of the sample. Therefore, heavy elements lead to higher scattering, which means that fewer electrons reach the image plate. Since the brightness of the image depends on the number of electrons reaching the image plate, sample regions containing heavy elements, *i.e.* fewer electrons, appear dark. Conversely, areas that contain only light elements, *e.g.* organic compounds, appear bright due to a limited scattering of electrons.

After hitting the sample, the transmitted portion of the beam is focused by an objective lens. The beam can be restricted by objective and select area apertures; the former enhances contrasts by blocking out high-angle diffracted electrons, the latter enables the examination of the periodic diffraction of electrons by ordered arrangements of the atoms in the sample. Thereafter, the electron beam passes magnetic lenses for magnification. Finally, the beam strikes a fluorescent screen coated with CdS and ZnS and the resulting irradiation is recorded by a CDD camera.¹⁴⁹ TEM can be operated in two modes: classic mode and high resolution mode (HR-TEM). In comparison to the classic mode, HR-TEM uses a much larger objective aperture (if any at all) to transfer high spatial frequencies. Then, the directly transmitted beam may interfere with one or more diffracted beams causing a contrast across the image (*i.e.* the bright-field image), which depends on the relative phases of the various beams.

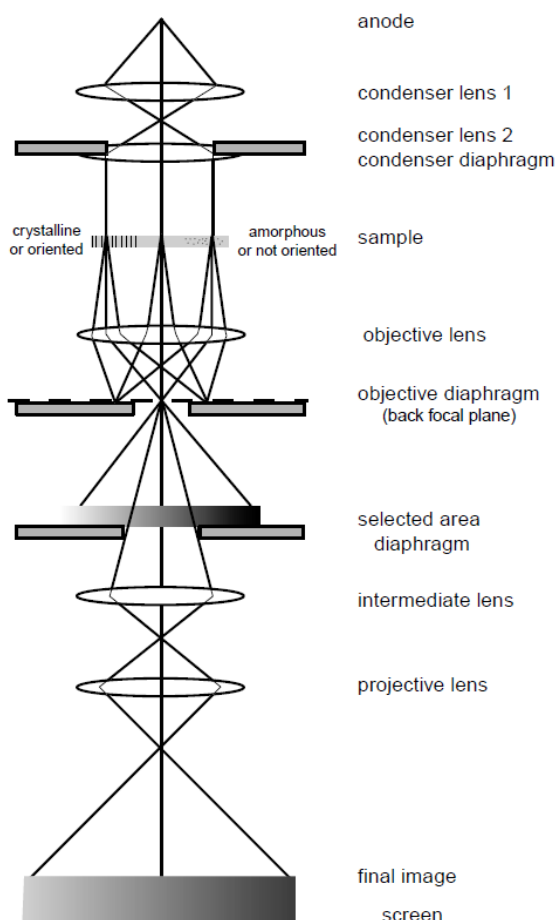


Figure II-3. Schematic description of a TEM/HRTEM set-up.¹⁵¹

Therefore, this technique is also called phase-contrast imaging. HR-TEM can be used to resolve crystalline lattices or columns of atoms, or for sub-Ångström imaging of the lattice and single atoms.¹⁵²

In this Ph.D. thesis, High Resolution Transmission Electron Microscopy (HR-TEM) analyses were performed using a JEOL 2010 UHR microscope operating at 200 kV equipped with a TCD camera. The samples were scraped off the substrate and ultrasonicated in ethanol before being placed on copper TEM grids.

II-2.3. Energy Dispersive X-rays (EDX)

Normally, EDX is associated to SEM or TEM. When the electron beam of the SEM is scanned across the sample, it causes excitation of characteristic x-rays from the atoms in the top few microns. The energy of each x-ray is specific to the atom from which it escaped. The EDX system collects the x-rays, sorts them by energy and displays the number of x-rays versus their energy. This qualitative EDX spectrum is captured electronically for display and processing (Figure II-4).

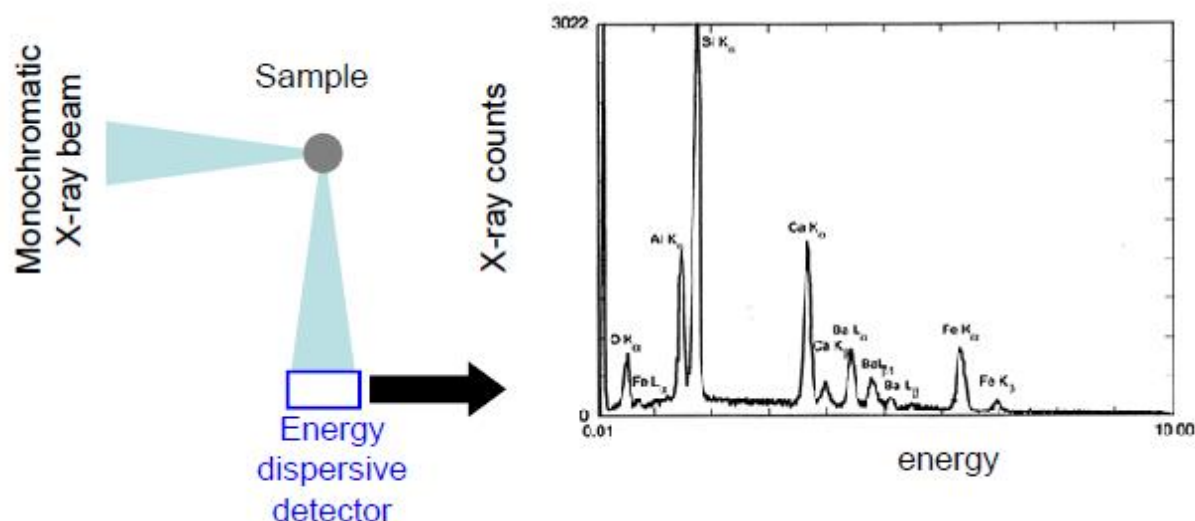


Figure II-4. Schema showing the working principle of an EDX detector.

In this Ph.D. thesis, the elemental analysis was performed with an energy dispersive X-ray (EDX) detector associated to the FEG-SEM.

II-2.4. X-ray Diffraction

The definition of X-rays is short-wavelength electromagnetic radiation produced either by the deceleration of high-energy electrons or by electronic transitions involving electrons in the inner orbitals of atoms. X-rays are produced in a vacuum tube containing two electrodes: an anode (usually of copper) and a cathode (usually a tungsten filament). First, the cathode is heated to provoke the emission of electrons and then, a high voltage is applied across the electrodes, resulting in streams of electrons (cathode rays) that are accelerated from the cathode to the anode and induce the emission of X-ray radiation from the anode. X-ray diffraction can be used to investigate crystal structures. Ideally, crystal structures consist of the infinite repetition of identical structural units in space, which can be either a single atom (such as in copper, silver or gold) or various atoms or molecules.¹⁴⁹ When investigating crystal structures by X-ray diffraction, Bragg's Law is the most basic and important principle (Figure II-5). Positive interference only occurs if the phase shift of the two rays is a multiple of the wavelength of the X-rays (λ). Since the phase shift is $2 d \sin\theta$, the Bragg equation^{120,149,153,154} is:

$$n\lambda = 2d \sin \theta \quad (\text{II-1})$$

In this Ph.D. thesis, the crystal structure of the samples were analyzed by using an Empyrean Panalytical X-ray diffractometer (Cu K α radiation, $\lambda = 1.541\,84\text{ \AA}$) operated at 60 kV.

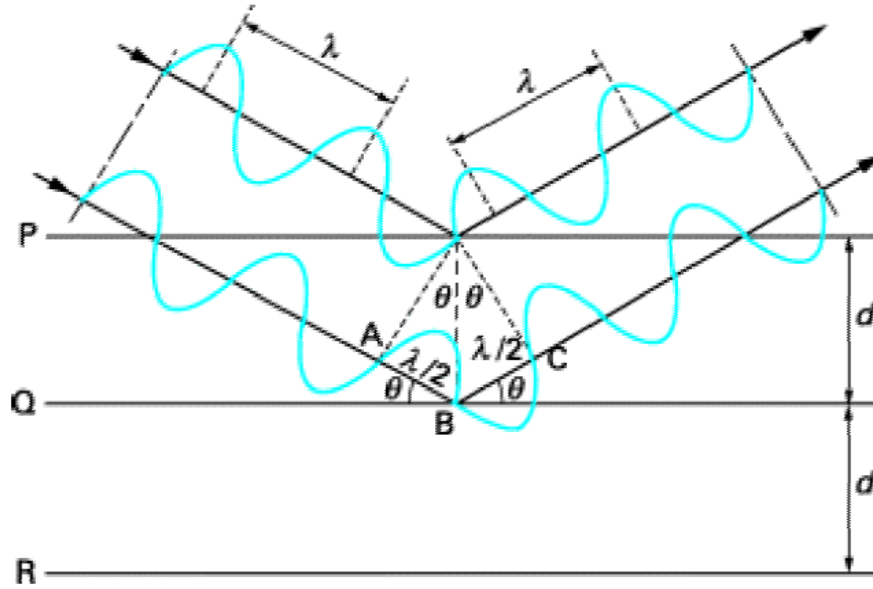


Figure II-5. Schematic diagram for determining Bragg's Law.³⁶

II-2.5. Nitrogen Physisorption and BET Surface Area Determination

Nitrogen Physisorption: Physical adsorption of gases on solid surfaces is caused by the attractive van der Waals interactions (*i.e.* dispersion forces) between gas molecules (adsorptive) and a solid (adsorbent). The interaction energy $U_s(z)$ of a gas molecule at a distance z from a solid surface is approximately:

$$U_s(z) = -\frac{(\pi/6)C_{sf}\rho_s}{z^3} \quad (\text{II-2})$$

where C_{sf} denotes the strength of attractive fluid-wall interactions and ρ_s the solid density. At sufficiently low temperatures (typically at and below the normal boiling temperature of the adsorptive), the adsorption of gases can be analyzed in terms of a two-phase model in which an adsorbed phase (adsorbate) coexists with the bulk phase. This is the typical situation encountered for nitrogen adsorption at the temperature of liquid nitrogen (ca. 77.35 K). The amount of adsorbed fluid can be expressed by the adsorbed mass of gas or volume (often given in STP per unit mass; STP: standard temperature and pressure, 273.15 K and 1.01325×10^5 Pa, respectively).¹⁴⁹

BET Surface Area Determination: The specific surface area can be calculated by the Brunauer, Emmett, and Teller (BET) method. In a relative pressure range between $P/P_0 = 0.05$ -0.35, the monolayer capacity n_m can be determined applying the BET equation:

$$\frac{P}{n(P_o - P)} = \frac{1}{n_m C} + \frac{C-1}{n_m C} x \frac{P}{P_o} \quad (\text{II-3})$$

where P and P_o are the equilibrium and the saturation pressure of adsorbates at the temperature of adsorption, n is the adsorbed gas quantity and C is the BET constant,

$$C = \exp\left(\frac{E_1 - E_L}{RT}\right) \quad (\text{II-4})$$

where E_1 is the heat of adsorption for the first layer and E_L is the heat of adsorption for the second and higher layers and is equal to the heat of liquefaction.

The specific surface area S_{BET} (m^2/g) is obtained from the monolayer capacity by applying the following equation:

$$S_{BET} = n_m \sigma_m N_A * 10^{-8} (\text{m}^2 \text{g}^{-1}) \quad (\text{II-5})$$

where N_A is the Avogadro constant and σ_m is the so-called cross-sectional area (the average area occupied by each molecule in a complete monolayer). The BET equation is applicable for surface area analysis of nonporous and mesoporous materials consisting of pores of wide pore diameter ($> 4\text{nm}$), but, in a strict sense, it is not applicable to microporous adsorbents. In addition, it seems that the BET method is inaccurate for estimating the surface area of mesoporous molecular sieves of pore widths $< \text{ca. } 4 \text{ nm}$, because pore filling is observed at pressures very close to the pressure range where monolayer-multilayer formation on the pore walls occurs, which may lead to a significant overestimation of the monolayer capacity.¹⁵⁵⁻¹⁵⁷

The BJH¹⁵⁸ method for calculating pore size distribution (PSD) is based on a model of the adsorbent as a collection of cylindrical pores. The theory accounts for capillary condensation in the pores using the classical Kelvin equation, which in turn assumes a hemispherical liquid-vapor meniscus and a well-defined surface tension, γ , of the bulk fluid, the densities of the coexistent liquid ρ^l and gas ρ^g ($\Delta\rho = \rho^l - \rho^g$) and the contact angle θ of the liquid meniscus against the pore wall. For cylindrical pores the modified Kelvin equation is given by:

$$\ln(P/P_o) = -2\gamma \cos\theta / RT\Delta\rho(r_p - t_c) \quad (\text{II-6})$$

where R is the universal gas constant, P is the Pressure, P_o is the saturation vapor pressure at the adsorption temperature, r_p the pore radius and t_c the thickness of an adsorbed multilayer film; which is formed prior to pore condensation.

In this Ph.D. thesis, Nitrogen adsorption-desorption isotherms of the samples were recorded at 77 K (temperature of liquid N₂) using a BELSORP-max high performance surface area and porosity analysis instrument. Samples were previously degassed at 250 °C and 0.397 μPa. The specific surface area and pore size distribution (PSD) were calculated according to the BET and BJH method.

II-3. Electrochemical and (Electro)gravimetric Techniques

II-3.1. Quartz Crystal Microbalance (QCM)

II-3.1.1. Piezoelectricity

The name Piezoelectricity derives from the Greek words, *piezein*, which means to press¹⁵⁹⁻¹⁶¹ and *elektron*¹⁶¹ or in other words, this term means “electricity by pressure”.¹⁶⁰ The piezoelectric effect was first reported by the Curie brothers in 1880^{24,160,162-169} and, a year later, the name “piezoelectricity” was proposed by Hankel^{160,164}. Furthermore, Lippmann predicted the converse effect based on thermodynamic considerations^{162,165,167,170}, which was verified by the Curies the same year. The piezoelectric effect is a property of certain materials (without a center of symmetry) that become electrically charged when a mechanical stress is applied (direct effect). Conversely, these materials can be deformed under the action of an external electrical field (converse effect).^{109,167} That is to say, the applied potential creates a reorientation of the dipoles in the acentric material causing its shear deformation¹⁶³ (Figure II-6). This is the basic principle of the microbalance operation.

The direct and converse piezoelectric effect can be applied in several areas. The direct effect is used in sensor applications,^{109,165,171} while the converse effect is used in ultrasound and communication techniques such as measuring the speed of sound, transmitting signals, remote controlling of equipment *etc.* Another important application is the field of actuators such as loudspeakers, piezoelectric motors, inkjet printers^{109,165,171-173} *etc.*

Of all the piezoelectric materials existing in nature or made industrially, quartz is one of the most commonly used. This material is insoluble in water and can resist to temperatures up to 573°C without losing its piezoelectric properties¹⁷⁴. The quartz (empirical formula is SiO₂) has trigonal-trapezohedral crystal symmetry resulting from its hexagonal prism structure with six cap faces at each end, which are shown in Figure II-7a.¹⁷⁵

The Z axis of quartz is called the optic axis. This axis of symmetry of order 3 is in an orthogonal X (electrical axis), Y (mechanical axis) coordinate system (Figure II-7c).^{176,177} The cutting of the quartz crystal, with respect to its crystallographic axes, determines the mode of vibration and its frequency domain.

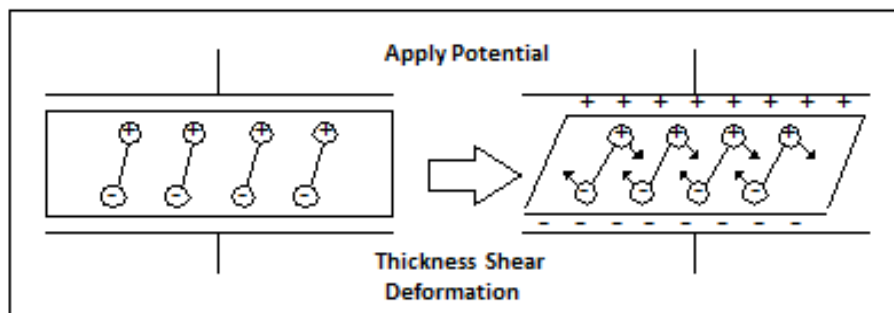


Figure II-6. Schematic representation of the deformation of a polarized quartz material. ^{163,178}

As shown in Figure II-7b, the BT, CT and DT cuttings correspond to a shear face mode having a resonant frequency around 1 MHz.¹⁰⁹

The main vibration modes include flexion vibration, longitudinal vibration, face shear vibration and thickness shear vibration.¹⁷⁸ The thickness shear vibration associated with the AT-cut orientation of $35^{\circ} 12'$ with respect to the Z axis is commonly used for quartz microbalance sensors.

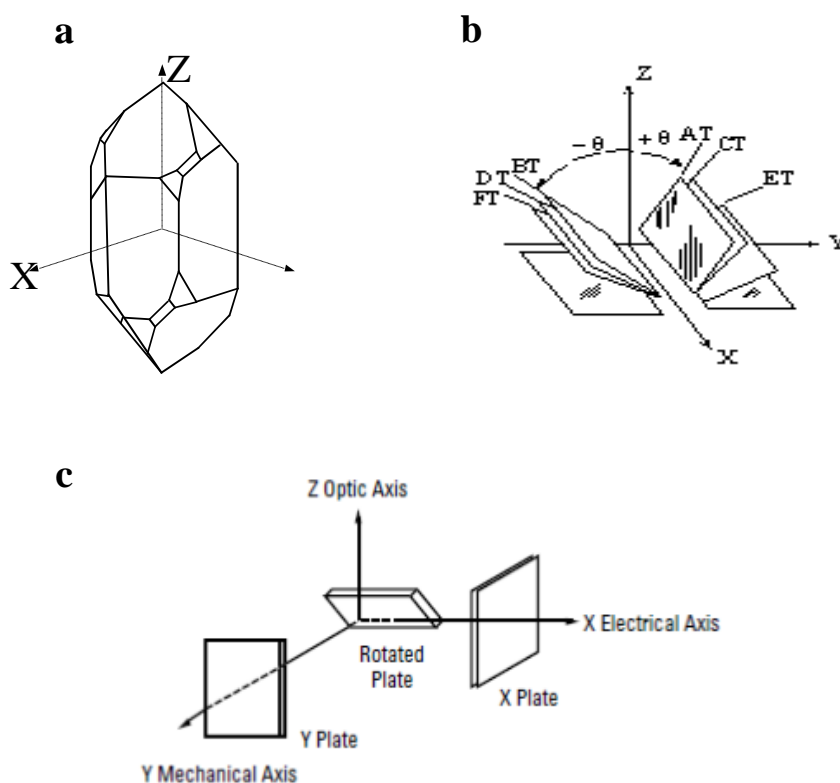


Figure II-7. Representation of the different sections of a quartz crystal with respect to the principal axes.

The crystal cut in the form of a thin disk with a diameter of 14 mm is used in this Ph.D. thesis (Figure II-8).

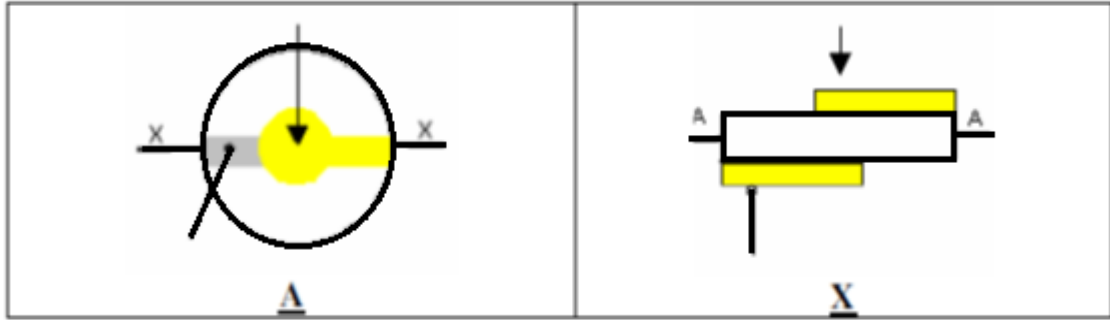


Figure II-8. Quartz disk face (A) and cross-sectional (X) carrying the two gold electrodes¹⁰⁹

The thickness of the quartz determines its resonant frequency. On each side of the disk, a gold electrode is deposited by vacuum evaporation. Each electrode is in the form of a disk, 5 mm in diameter, extended by a "leg" for the electrical connection. In practice, a sub-layer of chromium is sandwiched between the crystal surface and the gold electrode to have better adhesion. In general, the gold electrode has a thickness of 100 to 200 nm and the sub-layer of chromium is about ten times finer. The piezoelectric effect can take place in the area defined by the two gold electrodes that are placed opposite to each other, the so-called active area. Figure II-8 shows schematically a quartz disk with gold electrodes, seen from the front (A) and sectional (X). The first arrow indicates the active portion corresponding to the electrodes. The second arrow, circular nozzle, shows the leg electrodes, useful for making electrical connections.¹⁰⁹

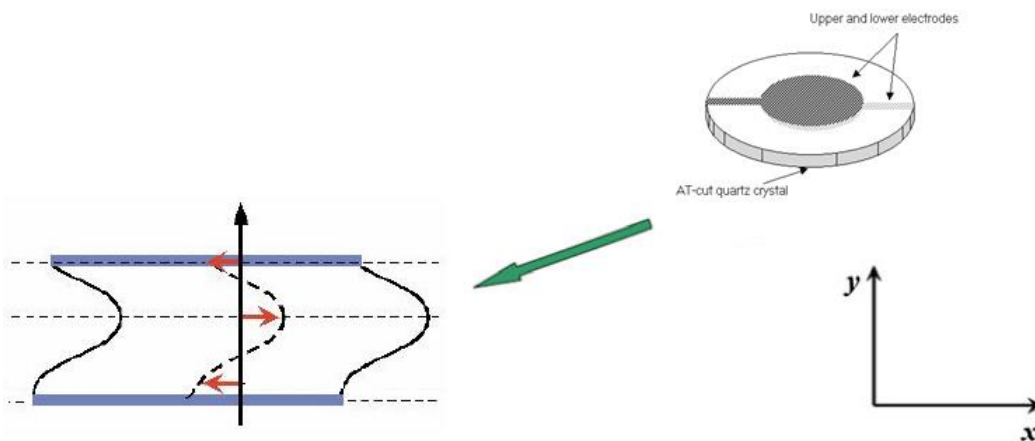


Figure II-9. Schematic illustration of a thickness shear mode quartz resonator.

When an alternating voltage is applied between a pair of gold electrodes, the upper and the lower faces of the active zone resonate (parallel to each other), which is shown in Figure II-9. A stationary acoustic wave is generated throughout the quartz crystal. The frequency of this wave is called the resonant frequency of the quartz resonator.^{109,178}

II-3.1.2. Working Principle of QCM

The quartz crystal can convert a mechanical stress into an electrical signal, which can be used to make a transducer or a sensor.¹⁷⁸ The piezoelectric transducer is a device that transforms an interaction at the modified electrode/liquid interface into a measurable electrical signal.¹⁰⁹ The piezoelectric transducer, also called quartz crystal microbalance¹⁷⁹ (QCM), is an attractive tool for gravimetric measurements. Applications can be found in many research fields such as chemical sensors^{179,180} and biosensors.¹⁸¹ This device permits the measurement of a mass sample deposited on the surface of a piezoelectric crystal through the change of its resonant frequency characteristics.^{133,138,163,177,182,183}

The QCM is based on a thin quartz crystal linked to an electrical circuit that is strong enough to create vibrational motion of the crystal at its resonant frequency (crystal oscillator).^{163,178,184} The microbalance frequency may be followed over time, the precision depending on the measuring parameters and the stability of the microbalance.¹⁸⁵⁻¹⁸⁷

The QCM is a high precision instrument which permits the determination of the mass variations of the quartz surfaces by measuring the changes of the resonance frequency of the quartz resonator.

In 1959, Sauerbrey¹⁸⁸ was the first to establish an equation (II-7) showing the relationship between the mass and frequency changes. When a rigid, purely elastic and electroacoustically thin layer is deposited on the quartz, the relationship between the mass of the material and the quartz crystal frequency change is:

$$\Delta f_m = -k_s x \Delta m = - \left(\frac{2f_o^2}{Sn\sqrt{\rho_q\mu_q}} \right) \Delta m \quad (\text{II-7})$$

where Δf_m is the frequency change of the microbalance, Δm is the mass change of the microbalance active surface (g), ρ_q is the quartz density (2.648 g.cm⁻³), μ_q is the shear modulus of a shear AT quartz crystal (2.947 x 10¹¹ g cm⁻¹ s⁻²), f_o is the fundamental resonant frequency of the

quartz (Hz), S is the active surface on the quartz corresponding to the metal electrode deposited on it (cm^2), n is the overtone number and k_s is the theoretical sensitivity factor ($\text{Hz g}^{-1} \text{cm}^2$).

With a QCM operating at 9 MHz, the theoretical sensitivity factor calculated from the Sauerbrey equation is equal to $18.3 \times 10^7 \text{ Hz g}^{-1} \text{cm}^2$. Bizet *et al.*¹⁸⁹ have determined the sensitivity coefficients by electrodeposition of copper for QCMs operating at 6, 9 and 27 MHz. Frequency changes of these three transducers were followed as a function of time during copper electrodeposition at different electrical current values. For resonators operating at 9 MHz, the experimental mass sensitivity factor found is equal to $16.31 (\pm 0.32) 10^7 \text{ Hz g}^{-1} \text{cm}^2$ at an imposed current of 0.5 mA, a value which is in fairly good agreement with the theory. This experimental mass sensitivity factor is used throughout the present Ph.D. thesis.

The experimental procedure for estimating k_s^{exp} is as follows: A cathodic current is applied to the gold electrode deposited on the quartz surface in a Cu^{2+} containing solution. This results in the reduction of Cu^{2+} ions to Cu^0 and, therefore, leads to the electrogeneration of copper on the gold electrode ($\text{Cu}^{2+} + 2e^- \rightarrow \text{Cu}$). The deposit is accumulated on the microbalance electrode, thus, causing a resonant frequency decrease due to the augmentation of mass during the electrodeposition. The current applied is controlled through a galvanostat and the mass change, Δm , is calculated by assuming that the efficiency of the reduction reaction of copper is equal to 100%. The experimental mass sensitivity factor is determined according to the following equation (II-8):

$$k_s^{\text{exp}} = \frac{\Delta f_m}{\Delta m} \times S = \frac{\Delta f}{\Delta t} \times \frac{\Delta t}{\Delta m} \times S \quad (\text{II-8})$$

where Δt is the time variation. By plotting the frequency vs time, the ratio $\frac{\Delta f}{\Delta t}$ is experimentally determined. The ratio $\frac{\Delta t}{\Delta m}$ is calculated using Faraday's law, assuming a 100% efficiency. The charge variation, Δq , is given by equation (II-9):

$$\Delta q = i \times \Delta t \quad (\text{II-9})$$

where i is the current.

The number of moles of Cu deposited is calculated from:

$$n_{\text{Cu}} = \frac{\Delta q}{n_{e^-} \times F} = \frac{i \times \Delta t}{n_{e^-} \times F} \quad (\text{II-10})$$

The mass change of the copper deposited is defined by:

$$\Delta m = n_{Cu} \times M = \frac{i \times \Delta t}{n_{e^-} \times F} \quad (\text{II-11})$$

Dividing equation (II-11) by Δt , it comes:

$$\frac{\Delta m}{\Delta t} = \frac{j \times M}{n_{e^-} \times F} = \frac{j \times \Delta t}{n_{e^-} \times F} \times S \quad (\text{II-12})$$

where J corresponds to the current density (A cm^{-2}), M is the molar mass of copper (63 g mol^{-1}), F is Faraday's constant (96500 C mol^{-1}) and n_{e^-} is the electron number. Therefore, by inserting $\Delta f/\Delta t$ and $\Delta m/\Delta t$ in equation (II-8), k_s^{exp} can be estimated.

II-3.1.3. Experimental Set-Up

The quartz crystal and its electrodes make up a piezoelectric resonator: surface changes (in mass, mechanical stress *etc.*) are transformed into electrical signals. The resonant frequency of the quartz resonator varies under the effect of surface changes,^{109,178} viscoelastic changes¹⁹⁰ and viscosity of the solution¹⁹¹. However, in the literature, it has been reported that at a certain frequency of QCM, the viscosity of the solution is not affected.¹⁹²

In this Ph.D. thesis, the set-up used for measuring mass/frequency change is a lab made microbalance developed at the LISE laboratory. A gold-patterned 9 MHz quartz crystal resonator (AWS, Spain or TEMEX, France) is inserted in an electrochemical cell (AWS Company, Spain, used for the first time in this Ph.D. thesis) and connected to a specific electronic circuit, the whole system being called an oscillator (Figure II-10). Thus, it is possible to monitor the evolution of microbalance frequency, f_m , in real time through the FRQM software developed at LISE.

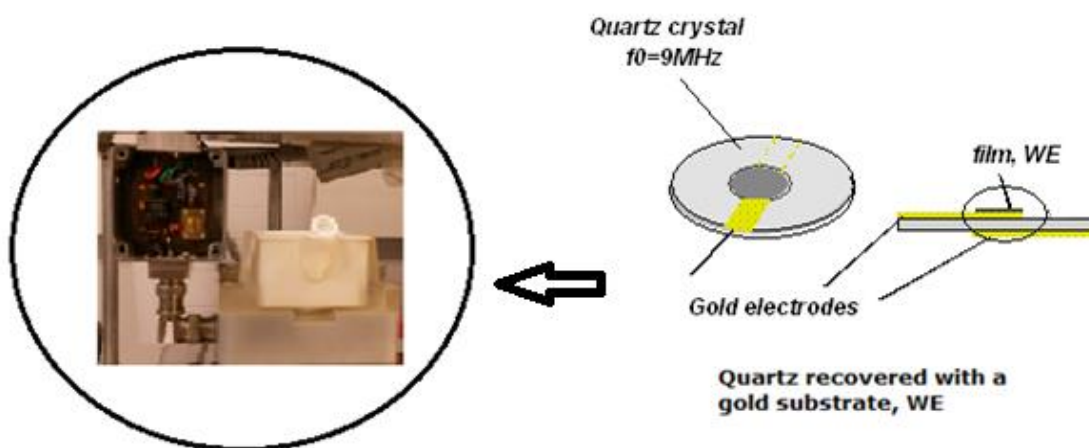


Figure II-10. Set-up of the electrochemical device used in this work.

II-3.2. Cyclic Electrogravimetry (EQCM)

As mentioned previously, cyclic electrogravimetry, also commonly called EQCM, is a method based on the coupling between cyclic voltammetry (CV) and gravimetric measurements through a QCM device. Using this method, information on the mass changes of the electrode (calculated from Sauerbrey's equation) during an electrochemical process can be obtained.

II-3.2.1. Principle

In cyclic voltammetry (CV), the electrochemical measurements are carried out in a classical three electrode configuration. The principle consists in applying two inverse successive potential scans between the working electrode (*e.g.* the gold electrode of the QCM) and the reference electrode, and in measuring the current changes resulting from the experiment. By using the gold electrode of the QCM as a working electrode in a CV experiment, it is also possible to measure simultaneously the frequency variations of quartz, which constitutes the basic principle of an EQCM experiment. The resonant frequency change can be converted into the electrode's mass changes according to the Sauerbrey equation given previously, Equation II-7.¹⁸⁸ Therefore, mass changes taking place on the QCM active electrode can be monitored.

An example of EQCM results from a sample of Single Wall CNT films tested in aqueous solution 0.5 M NaCl at 100mV/s, 50mV/s and 25mV/s from -0.45 V to 0.45 V vs Ag/AgCl is presented in Figure II-11.

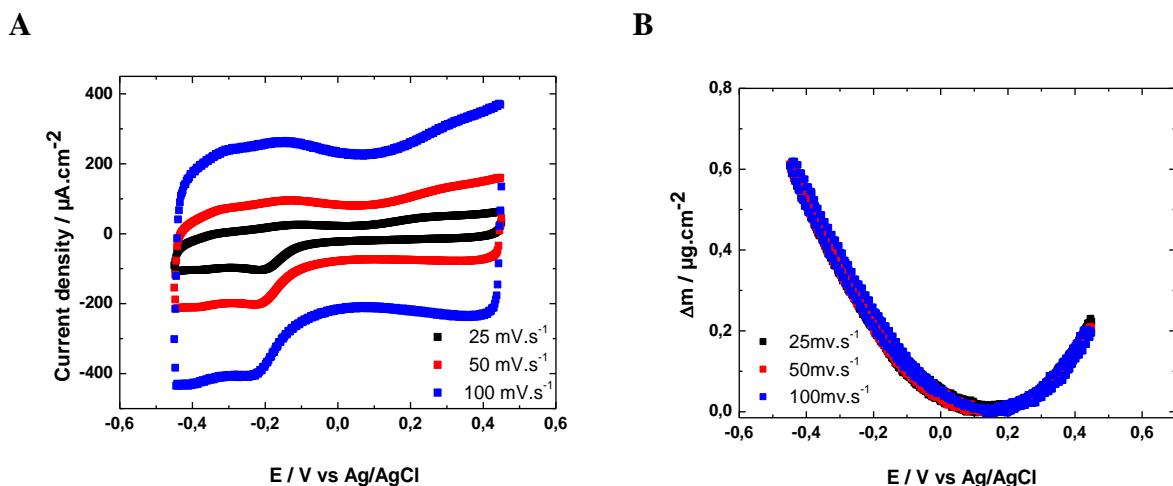


Figure II-11. The EQCM results of Single Wall CNT thin films current vs potential (A) and mass variation vs potential (B) profiles measured in aqueous electrolyte 0.5 M NaCl.

II-3.2.2. Experimental Set-Up

The experimental set-up is composed of an electrogravimetric cell (AWS, Spain) with three electrodes: a working electrode, *WE*, (a gold electrode deposited on a quartz resonator, 0.5 cm in diameter and an effective surface area of 0.2 cm²), a reference electrode, *RE*, in silver/silver chloride (Ag/AgCl) and a counter electrode, *CE*, a platinum grid. This cell is connected to a potentiostatic system (Biologic SP200 or Autolab PG stat 100), a frequency-meter (Yokogawa), the QCM and a computer (Figure II-12).

In this Ph.D. thesis, EQCM is utilized to analyze (i) the electrodeposition process of electroactive films, and (ii) the insertion and/or electroadsorption process of super- and/or pseudo-capacitive electrode materials.

The QCM electrode that operates as the working electrode is in contact with the electrolyte. For example, metallic cations may be dissolved in an acidic solution. By applying a negative potential to the working electrode, the cations can be deposited onto the electrode surface as metal atoms and the deposited mass is determined using the QCM. Moreover, the current during the deposition is also monitored and, by integration, the charge per surface unit can be measured. If all the charges are used for the deposition, the charge-to-mass ratio can be determined. This relation between the charge transfer and the mass deposited on the *WE* can be used as an alternate method for evaluating the thickness of a deposited layer.¹⁹³ Assuming that *the number of moles of the substance deposited on the electrode equals the number of moles of electrons interchanged during the reaction*, and knowing the density of the material deposited onto the quartz electrode, the thickness of the layer can be estimated as follows:

$$h_1 = \frac{q}{nFS} \frac{M}{\rho_1} \quad (\text{II-13})$$

where *S* is the surface where the substance is deposited, *q* is the charge involved in the process, *n* is the number of electrons interchanged in the reaction, *F* is Faraday's constant, *M* is the molecular weight and ρ_1 is the density of the substance.

In the case of supercapacitor studies, the mass change, according to Sauerbrey's equation, will produce a resonant frequency shift of the quartz resonator controlled *via* a circuit oscillator.^{194,195} This frequency is monitored by the frequency meter and, at the same time, the resulting current is measured by the potentiostat. These measurements are registered in a central computer.

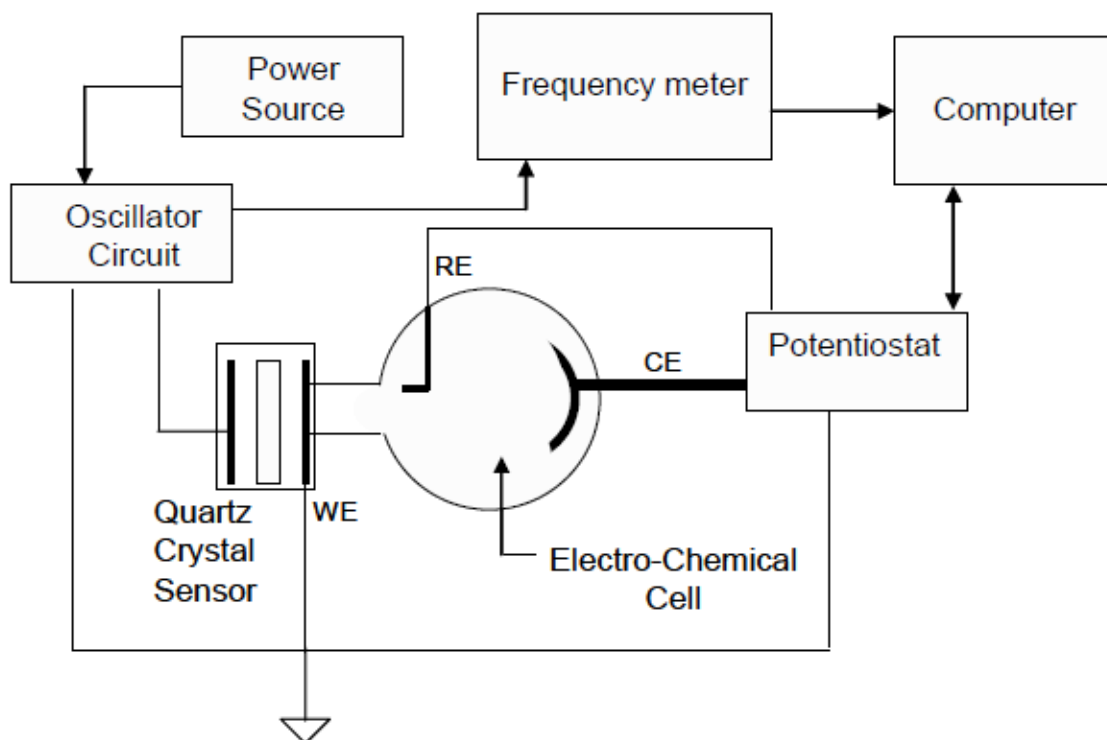


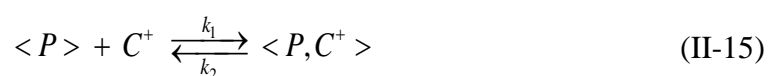
Figure II-12. Experimental set-up of an EQCM¹⁹³

II-3.2.3. Calculation of the $F(dm/dq)$ Function

The analysis of EQCM data by means of the $F(dm/dq)$ function gives the mass/charge ratio values at each applied potential during a voltammetric scan, which provides the information on the apparent mass of the ions, M , involved in the charge compensation.^{133,177} The instantaneous value of this ratio at each potential needs a prior evaluation of the dm/dt curve. For this calculation, mass, m , and current values, i , need to be previously filtered by a numerical procedure based on the fast Fourier transform and then, smoothed through Savitzky–Golay procedure. Then, Fdm/dq can be evaluated as:

$$M = F \frac{dm}{dq} = F \frac{dm/dt}{dq/dt} = F \frac{dm/dt}{i} \quad (\text{II-14})$$

where F is the Faraday constant ($\text{C} \cdot \text{mol}^{-1}$), dm is the mass variation, dq is the charge variation and M is the global molar mass. A proof of this relation is given by considering the insertion reaction of a monovalent cation:



where, $\langle P \rangle$ is the free site in the film, C^+ is the monovalent cation and $\langle P, C^+ \rangle$ is the site associated with a monovalent cation.

When a potential variation, ΔE , is applied to the electrochemical system, mass and charge variations may occur according to the relation:

$$F = \frac{dq}{dn} = \frac{dq}{dm} M_{C^+} \quad (\text{II-16})$$

$$\Rightarrow M_{C^+} = F \frac{dm}{dq} \quad (\text{II-17})$$

where dq is the charge variation during the insertion of C^+ and dn the variation of the number of moles of C^+ .

This proof was made considering only one cation contribution. The calculation is similar when only one anion is involved in the electrochemical process. If there is another species participating, the limitation of this method appears as only a global molar mass that represents the contribution of both species can be estimated. Under such circumstances, it is impossible to discriminate between the contributions of different species, solely based on the cyclic electrogravimetry (EQCM) approach.

II-3.3. Electrochemical Impedance Spectroscopy (EIS)

Electrochemical reactions can be composed of a succession of steps with different kinetics. To better understand the detailed mechanism of an electrochemical system, an appropriate method of separation of each reaction is necessary. However, conventional techniques do not always allow the distinction between these elementary steps to be done. Therefore, electrochemical impedance spectroscopy (EIS) can be useful as it often provides the information necessary to distinguish one reaction step from the other. In general, electrochemical impedance has been used to study the reaction mechanisms occurring at the electrode/electrolyte interface.^{196,197} Also, EIS has been employed in different domains such as: corrosion,¹⁹⁸ energy^{39,113,115} and biosensors.¹⁷⁹

II-3.3.1. Principle

EIS measurements are often performed under potentiostatic regulation. The basic principle of EIS is to apply a low amplitude sinusoidal perturbation, at a certain frequency, given around a stationary potential. The electrochemical system is under stable condition and the low level of disturbance associated with frequency modulation should help to separate the different reactions with different kinetics: fast phenomena occur at high frequencies while the slower phenomena are visible at lower frequencies.^{37,40,198,199} In general, electrochemical systems have a nonlinear current-voltage $I=f(V)$ characteristic curve (Figure II-13). However, working only on a small portion of the so-called Lissajous curve, the relationship between ΔV (low amplitude sinusoidal perturbation

imposed around the stationary potential) and ΔI (low amplitude sinusoidal response in current) may be considered as linear (Figure II-13).

Therefore, by applying a low amplitude sinusoidal perturbation, ΔV , to the system around a stationary potential, V_s , the current response will also be sinusoidal in shape, and with a small amplitude, ΔI , around a stationary value I_s .

The concept of impedance is a generalization of the concept of resistance, applicable to sinusoidal functions (there is a Fourier transform to all the functions).

The transfer function $\Delta V/\Delta I(\omega)$, called the electrochemical impedance $Z(\omega)$, can be defined with $\omega = 2\pi f$ corresponding to the pulsation.

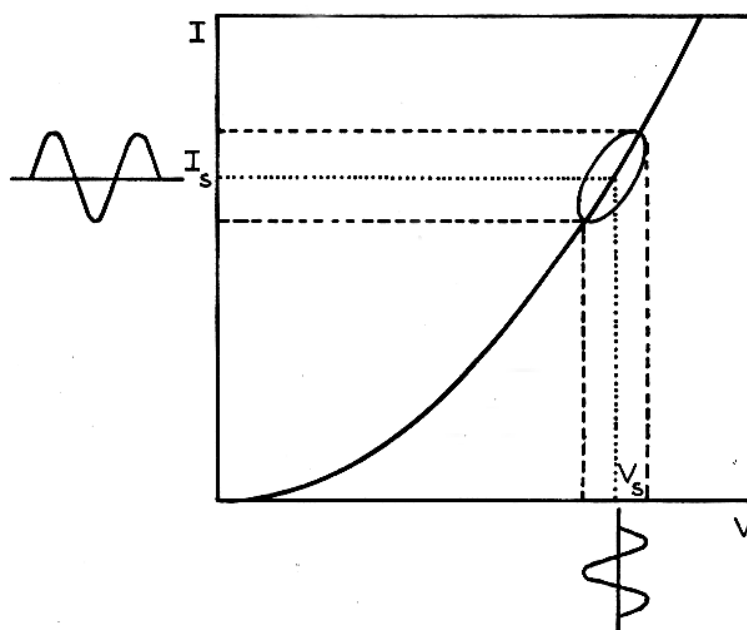


Figure II-13. Linear current response to a low amplitude sinusoidal perturbation potential around a stationary value.

The electrochemical impedance $Z(\omega)$ is a complex number that can be represented either in polar coordinates ($|Z|, \varphi$), or Cartesian coordinates ($\text{Re } Z, \text{Im } Z$) :

$$Z(\omega) = |Z| \exp j\varphi = \text{Re } Z + j \text{Im } Z \quad (\text{II-18})$$

The relationship between these quantities are:

-on the one hand,

$$|Z|^2 = (\text{Re } Z)^2 + (\text{Im } Z)^2 \quad (\text{II-19})$$

$$\varphi = \arctan \frac{\text{Im } Z}{\text{Re } Z} \quad (\text{II-20})$$

-on the other hand,

$$\operatorname{Re} Z = |Z| \cos \varphi \quad (\text{II-21})$$

$$\operatorname{Im} Z = |Z| \sin \varphi \quad (\text{II-22})$$

where $|Z|$ is the impedance modulus, ratio of amplitudes between ΔV and ΔI ; $\operatorname{Re} Z$ and $\operatorname{Im} Z$ are the real and imaginary parts of $Z(\omega)$, Φ is the phase angle between ΔV and ΔI , and j is the complex number ($j^2 = -1$). A basic example of the classical equivalent circuit used for characterizing the electrochemical interface and based on two parallel arms, one dedicated to the capacitive effect and the other, related to the faradic process is shown in Figure II-14

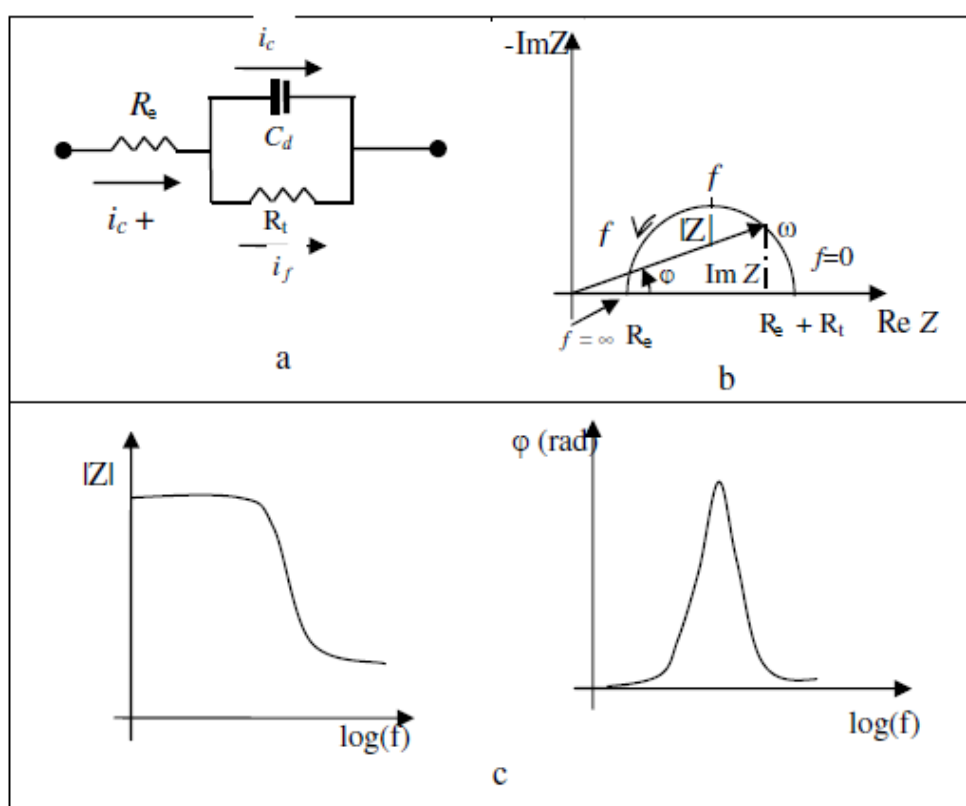


Figure II-14. (a) Equivalent electrical circuit. Plots of impedance of an electrochemical cell in (b) the Nyquist diagram and in (c) the Bode diagram.¹⁹⁹

A resistance corresponding to the electrolyte resistance is in series with the two previous components. The Nyquist diagram (Figure II-14b) illustrates a set of points where each corresponds to a certain frequency. The high frequency limit (HF) corresponds to the high-frequency resistance, often equal to the resistance of the electrolyte. The low frequency limit (BF), if obtained, corresponds to the polarization resistance. The Bode plot (Figure II-14c) illustrates separately the module $|Z|$ and φ the phase as a function of the logarithm of the frequency, $\log f$, (where $f = \omega/2\pi$).

When applying a low amplitude sinusoidal perturbation potential to an electrochemical cell, the total current obtained is the sum of Faraday's current, i_f , and the capacitive current, i_c . The faradic process characterizes the transfer of electrons at the electrode/electrolyte interface. The double layer defines the electrical charge at the interface and is characterized by a capacitance, C_d . Therefore, it is possible to model in a classical manner an electrochemical cell by an equivalent circuit comprising a double layer capacitance in parallel with a transfer resistance, R_t , and introducing in series an electrolyte, R_e , (Figure II-14a).^{109,199,200}

Consequently, the electrochemical impedance of the equivalent circuit is as follows:

$$Z(\omega) = R_e + \frac{1}{\frac{1}{R_t} + j\omega C_d} \quad (\text{II-23})$$

II-3.3.2. Experimental Set-Up

The experimental set-up used in this Ph.D. thesis is shown in Figure II-15. It consists of:

- A SOLETEM-PGSTAT100 potentiostat that works under potentiostatic mode, and imposes a given stationary potential, V_s .
- A frequency generator, included in the Frequency Response Analyzer (FRA 1254, Solartron), that delivers the low amplitude sinusoidal perturbation, ΔV .
- A three-electrode cell.

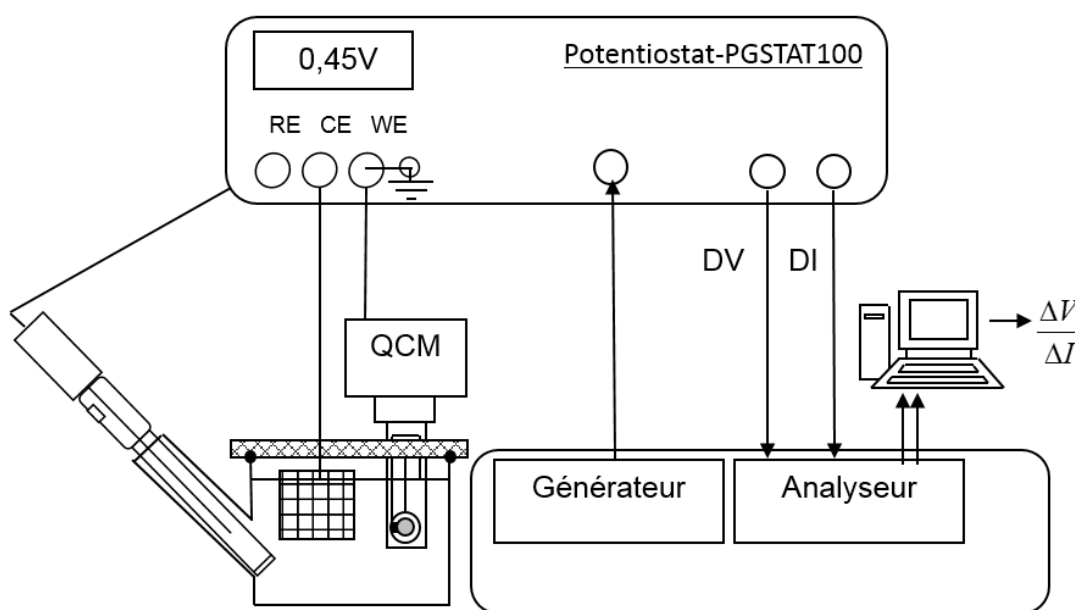


Figure II-15. Experimental set-up for electrochemical impedance measurements.

II-3.4. Ac-Electrogravimetry - A Fast Electrogravimetric Method

As mentioned previously, the *ac*-electrogravimetry consists of coupling EIS measurements with a fast response quartz crystal microbalance (QCM) used in dynamic mode. This technique was first proposed by Gabrielli *et al.*²⁰¹ at the LISE laboratory in France and it can be used to discriminate the activity of the different species involved in the charge transfer during an electrochemical process. More precisely, it provides access to relevant information on the kinetics of species transferred at the electrode/electrolyte interface and their transport in the bulk of the materials, the nature of these species as well as their relative concentration within the material. Consequently, *ac*-electrogravimetry appears to be an attractive tool for studying the nature of the ionic flux at the electrode/electrolyte interface.

II-3.4.1. Principle

The principle of *ac*-electrogravimetry is analogous to the principle of the electrochemical impedance described in the previous section. A low amplitude sinusoidal perturbation, ΔV , applied to an electrochemical system, can lead to changes in the mass of the film placed on the microbalance surface, Δm , allowing the measurement of the electrogravimetric transfer function $\frac{\Delta m}{\Delta E}(\omega)$. Using the gold electrode of the quartz resonator as a working electrode, two distinct transfer functions can be obtained simultaneously: an electrochemical impedance $\frac{\Delta E}{\Delta I}(\omega)$ and an electrogravimetric or mass/potential transfer function $\frac{\Delta m}{\Delta E}(\omega)$.^{4,131,202}

The measurements are made with the same three-electrode cell as described in Section II-3.2.2. When the low amplitude sinusoidal perturbation, ΔV , is applied to the film deposited on the gold electrode of the QCM, some of the charged species in the solution participate in the charge compensation process within the electroactive material. This insertion/removal of species into/from the film, driven by the potential values, is detectable through the microbalance frequency change, Δf_m . Using the Sauerbrey equation (Equation II-7), the mass changes of the film, Δm , can be estimated.

The modulation frequency of the perturbation signal provides additional information, *i.e.* it allows the separation of the kinetics of different species involved in the charge compensation of the film. The measurements are controlled by a computer using FRACOM software, a software developed at the LISE laboratory. Figure II-16 shows the principle of the measurement of the electrogravimetric transfer function, $\Delta m/\Delta E(\omega)$.

For these transfer function measurements, a multi-channel FRA-Solartron 1254 was used, permitting the simultaneous determination of two main transfer functions: the electrochemical impedance $\Delta E/\Delta I(\omega)$ and the corresponding mass/potential transfer function $\Delta V_f/\Delta V$. Through the latter, the electrogravimetric transfer function, $\Delta m/\Delta E(\omega)$, may be obtained. In fact, $\Delta m/\Delta E(\omega)$, is not directly measurable. Instead, a frequency/voltage converter must be used in order to convert the microbalance frequency signal, Δf_m , into a measurable voltage signal, ΔV_f . However, in order to extract a few Hz modulation on a carrier signal to 9 MHz, to perform effectively this demodulation

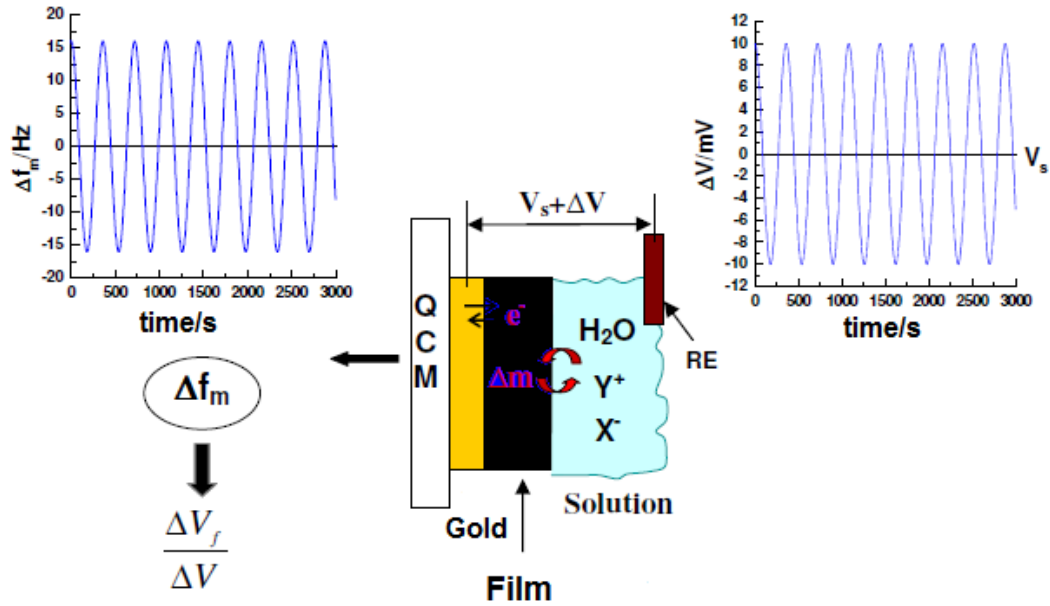


Figure II-16. Principle of measuring the electrogravimetric transfer function $\Delta V_f/\Delta V$.

frequency, the carrier is reduced to a few hundred Hertz to increase accuracy. To do this, a frequency synthesizer (Marconi-2023) and an electronic module that allow differentiation to reduce this carrier within the range of a few hundred Hertz are used. Then, it is possible to extrapolate Δm from the ΔV_f signal for a given configuration and type of measurement. This is achieved by calibrating the system before the measurement. Figure II-17 shows the method implemented to achieve these electrogravimetric transfer functions $\frac{\Delta m}{\Delta E}(\omega)$.

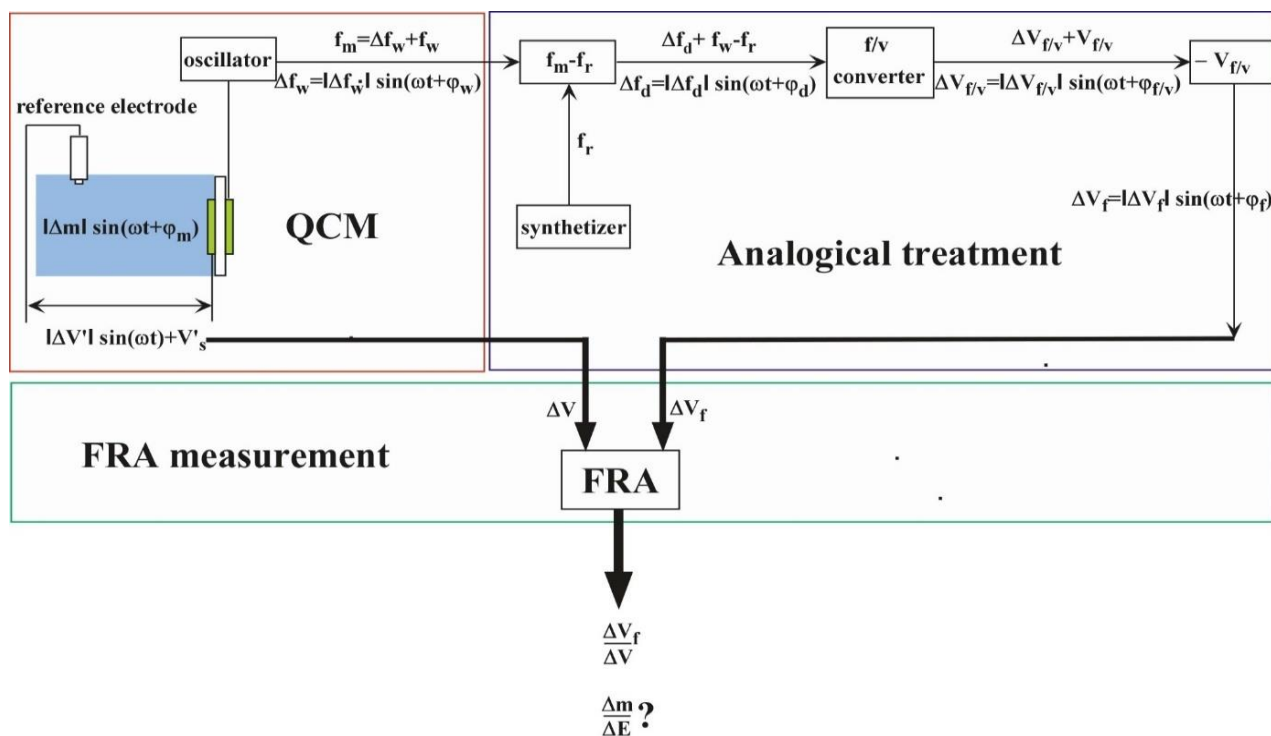


Figure II-17. Scheme of the principle of electrogravimetric transfer function measurements.

II-3.4.2. Experimental Method: $\Delta V_f / \Delta V$

The experimental method is shown in Figure II-18. It consists of:

- An electrochemical cell with three electrodes and the QCM. The reference electrode is silver/silver chloride (Ag/AgCl), the counter electrode is platinum and the working electrode is one of the gold electrodes deposited on the faces of the quartz resonator,
- A SOTELEM PG-STAT 100 potentiostat,
- A FRA Solartron 1254, comprising a voltage generator ($\Delta V'$),
- A Marconi 2023 reference frequency synthesizer,
- A frequency/voltage converter developed at LISE.

The QCM working electrode is polarized by the potentiostat at a chosen potential. Then, the Solartron 1254 generator delivers a low amplitude sinusoidal perturbation, $\Delta V'$, at a modulation frequency, f . This signal is superimposed on the polarization potential supplied by the potentiostat, V'_s .

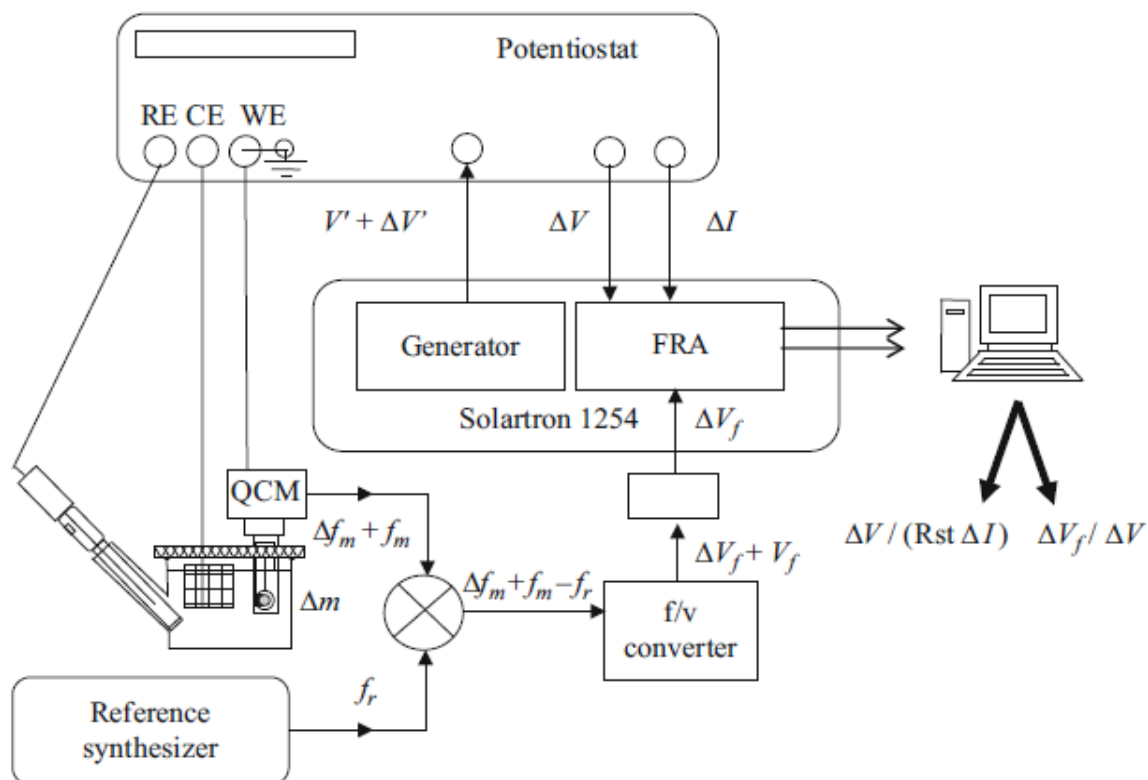


Figure II-18. Ac-electrogravimetric set-up²⁰³

The signal from the microbalance, f_m , is detected by means of a lab made frequency/voltage converter,^{204,205} which subtracts a reference signal, f_r , close to the frequency of the microbalance issued by the Marconi 2023 frequency synthesizer. Then, the $f_m - f_r$ signal is converted into voltage, V_f : if f_m varies from the Δf_m , the converter delivers a voltage variation, ΔV_f . The resulting signal, ΔV_f , and the current response, ΔI , of the working electrode are simultaneously sent to the FRA-Solartron 1254, which allows the two transfer functions, $\Delta V_f / \Delta V(\omega)$ and $\Delta V / R_t \Delta I(\omega)$, to be determined (Figure II-19). ΔV is the raw potential response, which takes into account the electrolyte resistance, and R_t is the resistance in the counter electrode circuit, which allows the current, ΔI to be measured. Usually, a 10^{-3} Hz to 60 kHz frequency range is used to measure these transfer functions.^{109,203}

II-3.4.3. Calibration and Corrections of the Ac-Electrogravimetry System

Firstly, the experimental electrochemical impedance $\frac{\Delta E}{\Delta I}(\omega)$ must be estimated from the raw transfer function $[\Delta V / (R_t \times \Delta I)](\omega)$ as:

$$\frac{\Delta E}{\Delta I}(\omega) = \left[\frac{\Delta V}{(\Delta I \times R_t)} \times R_t \right] - R_e \quad (\text{II-24})$$

where R_t is the resistance used in the counter electrode circuit, incorporated in the potentiostat for measuring the current, and R_e is the electrolyte resistance taken from the high frequency value of $(\Delta V/\Delta I)(\omega)$.

As mentioned previously, the raw transfer function given by the 1254 FRA, $\frac{\Delta V_f}{\Delta V}(\omega)$, must

be corrected to obtain the final mass/potential transfer function $\frac{\Delta m}{\Delta E}(\omega)$,

$$\frac{\Delta m}{\Delta E} = \frac{\Delta m}{\Delta f_m}(\omega) \frac{\Delta f_m}{\Delta V_f}(\omega) \frac{\Delta V_f}{\Delta V}(\omega) \frac{\Delta V}{\Delta E}(\omega) \quad (\text{II-25})$$

Four different transfer functions can be distinguished, as described below:

- $\frac{\Delta m}{\Delta f_m}(\omega)$ is related to the Sauerbrey equation (II-6) and is equal to $-1/k_s^{theor}$ or $-1/k_s^{exp}$ where

k_s^{exp} is the experimental mass/microbalance frequency factor. At 9 MHz, k_s^{exp} is equal to $16.3 \times 10^{-7} \text{ Hz g}^{-1} \text{ cm}^2$ as justified previously.¹⁸⁹

- $\frac{\Delta f_m}{\Delta V_f}(\omega)$ is the inverse of the f/v converter sensitivity and can be estimated by using the

following equation:

$$\frac{\Delta f_m}{\Delta V_f} = \frac{\Delta f_m}{\Delta e}(\omega) \frac{\Delta e}{\Delta V_f}(\omega) \quad (\text{II-26})$$

where $\Delta f_m / \Delta e(\omega) = \Delta f_s / \Delta e(\omega)$ is the sensitivity of the reference synthesizer by assuming $\Delta f_m = \Delta f_s$.

$\Delta e / \Delta V_f(\omega)$ is the inverse of the global calibration transfer function, $(\Delta V_f / \Delta e)(\omega)$. It has been observed that the voltage perturbation during a calibration is $\Delta e = |\Delta e| \cdot \sin(\omega t)$. Furthermore, the sensitivity of the converter is given by $\Delta V_f / \Delta f_s$.¹⁰⁹

- $\frac{\Delta V_f}{\Delta V}(\omega)$ is the raw experimental transfer function obtained from the 1254 FRA.

- $\frac{\Delta V}{\Delta E}(\omega)$ allows the Ohmic drop correction to be done by taking into account the electrolyte

resistance R_e . The following relation is used by incorporating the experimental electrochemical impedance $(\frac{\Delta E}{\Delta I}(\omega))$ determined in equation (II.24)

$$\frac{\Delta V}{\Delta E}(\omega) = \frac{R_e}{\left(\frac{\Delta E}{\Delta I}\right)(\omega)} + 1 \quad (\text{II-27})$$

II-3.4.3.1. Transfer Function of the Frequency/Voltage Converter: $(\Delta V_f/\Delta e)(\omega)$

This transfer function is determined by replacing the microbalance device by a frequency synthesizer (Agilent 33205A) which can modulate the frequency as shown in Figure II-18. The rest of the assembly is identical to that shown in Figure II-19 except that the electrochemical part disappears. The signal, Δe , coming from the generator FRA 1254 permits the modulation of the frequency of the synthesizer Agilent 33205A and, also, the simulation of the response of a microbalance on which sinusoidal mass variations might be observed.

A global calibration transfer function, $(\Delta V_f/\Delta e)(\omega)$, has been determined by Gabrielli *et al.*²⁰³ to evaluate the sensitivity of the frequency/voltage converter, to determine the linear frequency range and also, to measure the calibration file. Figure II-20 shows the modulus and the phase of the global calibration transfer function, $(\Delta V_f/\Delta e)(\omega)$. At low frequencies, the phase shift of $(\Delta V_f/\Delta e)(\omega)$ is close to 0 and the modulus, $|\Delta V_f/\Delta e|$, is equal to 0.57. This result means that the dynamic sensitivity $(\Delta V_f/\Delta f_s)_{\text{dynamic}}$ of the system is 29 mV Hz^{-1} which is explained in Section II-3.4.3.2.

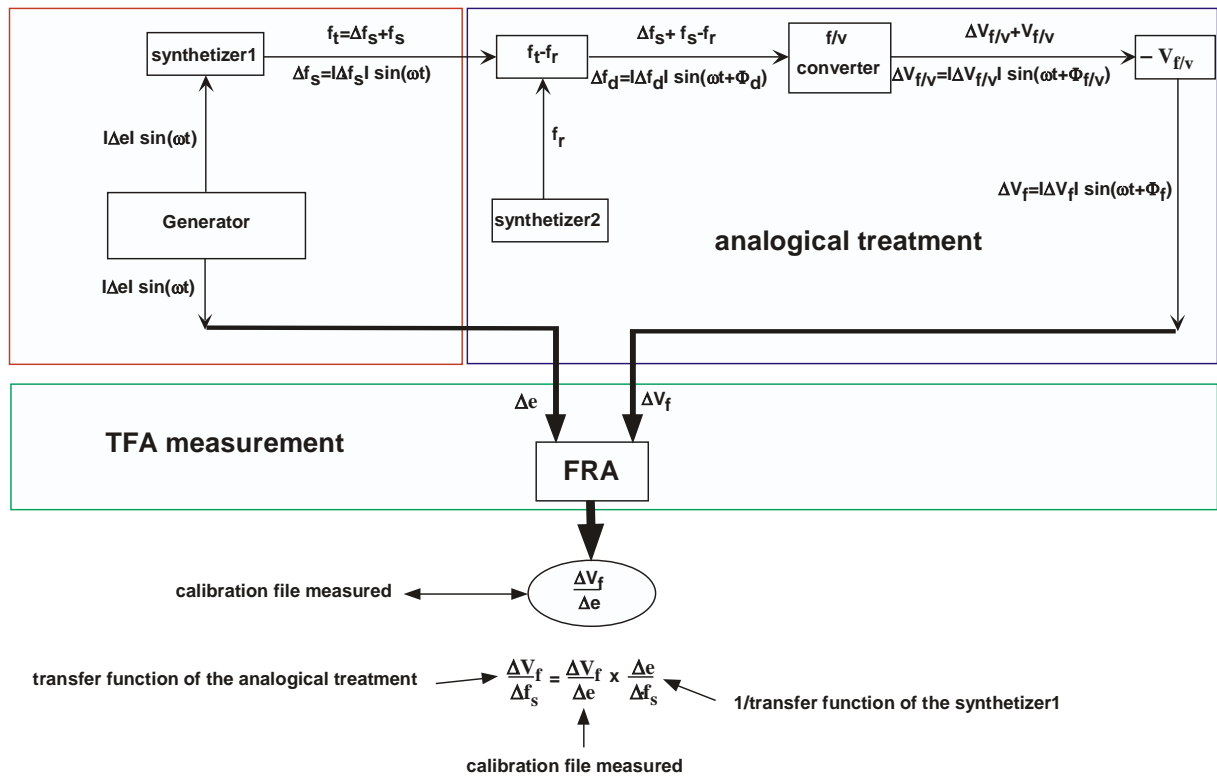


Figure II-19. Scheme of the calibration of the frequency/voltage converter for determining the transfer function $\Delta V_f/\Delta e(\omega)$.

The useable frequencies, that is, where the system can be used without any correction, ranges from low frequencies to 1 Hz for this particular configuration. If measurements are expected above 1 Hz, a modulus and phase shift correction is necessary by using calibration curves such as those given in Figure II-20.

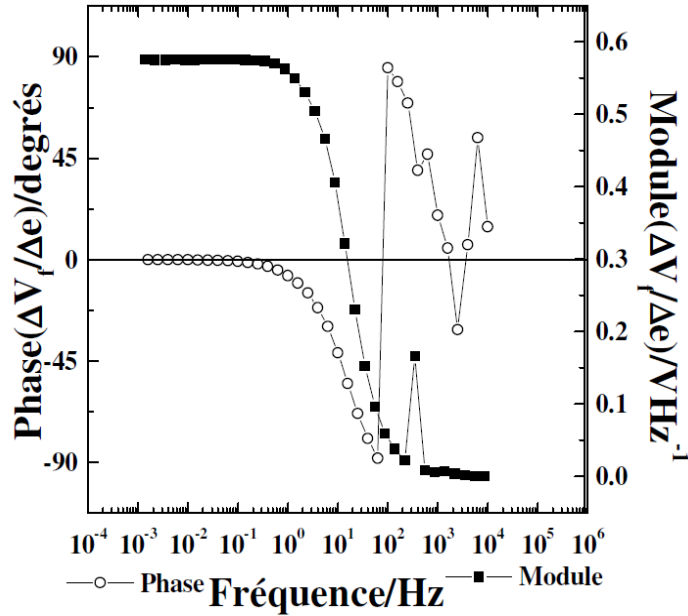


Figure II-20. Modulus and phase of the global calibration of the frequency/voltage converter.²⁰³

II-3.4.3.2. Calibration of Synthesizer: $\Delta f_s/\Delta e$

To Thi Kim¹⁰⁹ has proposed a method to determine the transfer function $\Delta f_s/\Delta e$ of the Agilent 33250A synthesizer used to simulate the QCM during the calibration procedure given previously. To determine the transfer function of the synthesizer, the FRA 1254 generator must impose a fixed sinusoidal perturbation frequency, f , in order to vary the amplitude, Δe . The Agilent 33250A synthesizer was adjusted to a 9.0 MHz carrier frequency equivalent to the frequency of the QCM used. Then, different tests were performed for three levels of modulation depth around the carrier frequency (FM mode) available on the Agilent 33250A: 10 Hz, 100 Hz and 300 Hz.

A plot in Origin[®] allows the determination of Δe and Δf_s in a precise way at a given frequency modulation and, by selecting the three settings of modulation depth available on the synthesizer, three values for the transfer function $\Delta f_s/\Delta e$ can be obtained (Figure II-21).

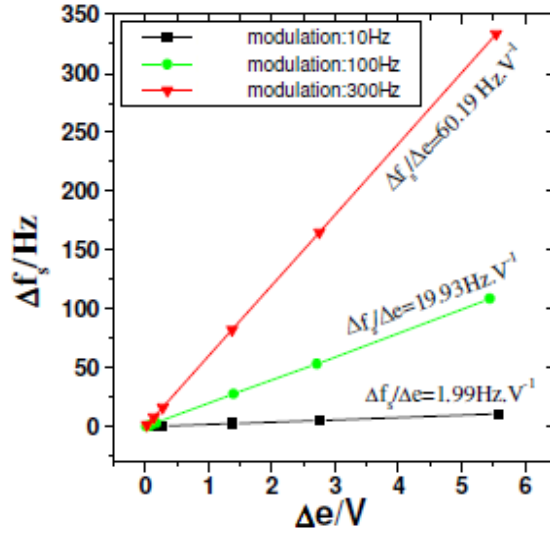


Figure II-21. Measurements of the transfer function $\Delta f_s/\Delta e$ from the Agilent 33250A-synthesizer for three settings depth modulation (FM): 10 Hz, 100 Hz, 300 Hz.

In this Ph.D thesis, the value $\Delta f_s/\Delta e = 19.93 \text{ Hz.V}^{-1}$ is used and the dynamic sensitivity $(\Delta V_f/\Delta f_s)_{\text{dynamic}}$ is calculated as:

$$\left| \frac{\Delta V_f}{\Delta f_s} \right|_{\omega \rightarrow 0}^{\text{dynamic}} = 0.57 \times \frac{1}{19.9} = 28,6 \text{ mV Hz}^{-1} \quad (\text{II-28})$$

II-3.5. Data Treatment of Ac-Electrogravimetry

II-3.5.1. Experimental data

From the experimental data, the following transfer functions are calculated and are taken into account in the fittings in II-3.5.2 as follows:

Using the electrochemical impedance and the relation $\Delta I = j\omega \Delta q$, the charge/potential TF can be estimated:

$$\left. \frac{\Delta q}{\Delta E} \right|_{\text{exp}} = \frac{1}{j\omega} \left. \frac{\Delta I}{\Delta E} \right|_{\text{exp}} \quad (\text{II-29})$$

The disturbance causes a charge compensation within the film: species come and go at the discretion of the disturbance signal. Physically, this corresponds to a variation of mass.

From the experimental electrogravimetric transfer function, it is possible to calculate the experimental partial transfer functions, eliminating the contribution of an anion or a cation, where four species are taken into account: cation1 (c1), cation 2 (c2), anion (a) and solvent (s). For

example, if the contribution of the cation 2 is extracted, the contribution of the cation 1, the solvent and the anion is calculated according to the following equation:

$$\left. \frac{\Delta m}{\Delta E} \right|_{\text{exp}}^{\text{c1as}} = \left. \frac{\Delta m}{\Delta E} \right|_{\text{exp}} + \frac{m_{c2}}{F} \left. \frac{\Delta q}{\Delta E} \right|_{\text{exp}} \quad (\text{II-30})$$

Furthermore, if the contribution of the cation 1 is extracted, it comes:

$$\left. \frac{\Delta m}{\Delta E} \right|_{\text{exp}}^{\text{c2as}} = \left. \frac{\Delta m}{\Delta E} \right|_{\text{exp}} + \frac{m_{c1}}{F} \left. \frac{\Delta q}{\Delta E} \right|_{\text{exp}} \quad (\text{II-31})$$

and if the contribution of the anion is extracted, it comes :

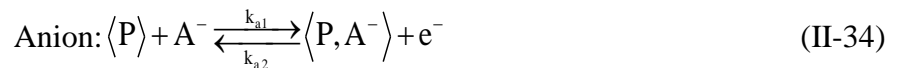
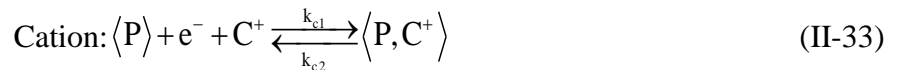
$$\left. \frac{\Delta m}{\Delta E} \right|_{\text{exp}}^{\text{c1c2s}} = \left. \frac{\Delta m}{\Delta E} \right|_{\text{exp}} - \frac{m_a}{F} \left. \frac{\Delta q}{\Delta E} \right|_{\text{exp}} \quad (\text{II-32})$$

II-3.5.2. Fitting from Mathcad Simulation Data

The fitting of the experimental TFs with the theoretical TFs (which will be described in the following) by using Mathcad software (PTC Mathcad 15.0) allows the pertinent information on the charge compensation process to be obtained.

Specifically, the fitting of the data (at each potential perturbation applied) is performed *via* Mathcad software by calculating the electrochemical impedance, the charge/potential transfer function, the global and partial mass/potential transfer functions at different modulation frequencies with different values of the parameters. The fitting procedure respects the strict criteria that a good agreement between the experimental and the theoretical function in terms of shape and frequencies was achieved. This provides relevant information on the ions transfer characterized by the K_i and G_i parameters and identifies the nature of the species involved by their molar mass, m_i .

Let us consider the following electroadsorption/desorption mechanism which intervenes in our electrochemical system:



where $\langle P \rangle$ is the free site "in" the film, $\langle P, C^+ \rangle$ is the site occupied with a monovalent cation and $\langle P, A^- \rangle$ is the site occupied with a monovalent anion. The k_i are related to the transfer kinetic rates. Then, the instantaneous flux of each species, J_i , can be written as follows:

For a cation:

$$J_c = -d_f (k_{c1} (C_{C^+, \max} - C_{C^+}) [C^+]_{sol} - k_{c2} (C_{C^+} - C_{C^+ \min})) \quad (II-35)$$

For an anion:

$$J_a = -d_f (k_{a1} (C_{A^-, \max} - C_{A^-}) [A^-]_{sol} - k_{a2} (C_{A^-} - C_{A^- \min})) \quad (II-36)$$

where $C_{i, \max}$ is the maximum concentration of P sites occupied in the film by cations or anions, C_i is the concentration in the film of cations or anions associated to the P sites and $C_{i, \min}$ is the minimum concentration of P sites occupied in the film by cations or anions.

Under the effect of a sinusoidal potential perturbation, ΔE , imposed on the film/electrolyte interfaces, sinusoidal concentration fluctuations, ΔC_i and the flux, ΔJ_i , are observed (a: anion, c: cation, s: solvent), in the following form:

$$\Delta J_i = -d_f \frac{d(\Delta C_i)}{dt} \quad (II-37)$$

where d_f is the film thickness (m), ΔJ_i is the variation of the flux related to the species i crossing the film/electrolyte interface ($\text{mol.m}^{-2}.\text{s}^{-1}$) and ΔC_i is the variation of the concentration in the film (mol.m^{-3}).

In dynamic regime, the flux change ΔJ_i is a function of the potential E and the concentration of the species, ΔC_i , can also be written as:

$$\Delta J_i = \frac{\partial J_i}{\partial C_i} \Delta C_i + \frac{\partial J_i}{\partial E} \Delta E = K_i \Delta C_i + G_i \Delta E \quad (II-38)$$

Then, the $\left. \frac{\Delta C_i}{\Delta E} \right|_{th} (\omega)$ transfer function can be calculated using the equations (II-37) and (II-38):

$$\left. \frac{\Delta C_i}{\Delta E} \right|_{th} (\omega) = \frac{-G_i}{j\omega d + K_i} \quad (II-39)$$

where $\omega = 2\pi f$ is the pulsation, f is the frequency of potential modulation and K_i and G_i are the partial derivatives of the flux with respect to the concentration and the potential, respectively.

$$K_i = \left(\frac{\partial J_i}{\partial C_i} \right)_E \text{ and } G_i = \left(\frac{\partial J_i}{\partial E} \right)_{C_i} \quad (\text{II-40})$$

Then, the “virtual” transfer function given in equation (II-39) allows the calculation of all the other measured transfer functions. Thus, the following theoretical expressions have been used to fit all the experimental transfer functions. From the equation (II-39) and considering four species involved in the electrochemical process: cation 1, $c1$, cation 2, $c2$, anion, a , and solvent, s , the following equations can be listed:

$\frac{\Delta C_{c1}}{\Delta E} \Big _{th} (\omega) = -\frac{G_{c1}}{(j\omega d_f) + K_{c1}} \quad (\text{II-41})$	$\frac{\Delta C_{c2}}{\Delta E} \Big _{th} (\omega) = -\frac{G_{c2}}{(j\omega d_f) + K_{c2}} \quad (\text{II-42})$
$\frac{\Delta C_a}{\Delta E} \Big _{th} (\omega) = -\frac{G_a}{(j\omega d_f) + K_a} \quad (\text{II-43})$	$\frac{\Delta C_s}{\Delta E} \Big _{th} (\omega) = -\frac{G_s}{(j\omega d_f) + K_s} \quad (\text{II-44})$

II-3.5.2.1. Charge/Potential Transfer Function

The charge/potential transfer function, $\frac{\Delta q}{\Delta E} \Big|_{th} (\omega)$, calculated for the adsorption/desorption of two cations, $c1$ and $c2$, and an anion, a , using the Faraday number, F can be written as follows :

$$\frac{\Delta q}{\Delta E} \Big|_{th} (\omega) = -d_f F \left(\frac{\Delta C_{c1}}{\Delta E} + \frac{\Delta C_{c2}}{\Delta E} - \frac{\Delta C_a}{\Delta E} \right) \quad (\text{II-45})$$

Replacing the equations (II-39) with the equation (II-45) gives:

$$\frac{\Delta q}{\Delta E} \Big|_{th} = d_f F \left(\frac{G_{c1}}{(j\omega d_f) + K_{c1}} - \frac{G_{c2}}{(j\omega d_f) + K_{c2}} - \frac{G_a}{(j\omega d_f) + K_a} \right) \quad (\text{II-46})$$

II-3.5.2.2. Electrochemical Impedance

The theoretical electrochemical impedance can be calculated as follows:

$$\frac{\Delta q}{\Delta E} \Big|_{th} (\omega) = \frac{1}{j\omega} \frac{\Delta I}{\Delta E} = d_f F \left(-\frac{\Delta C_{c1}}{\Delta E} - \frac{\Delta C_{c2}}{\Delta E} + \frac{\Delta C_a}{\Delta E} \right) \quad (\text{II-47})$$

Replacing the equation (II-39) with the equation (II-47) gives:

$$\left. \frac{\Delta E}{\Delta I} \right|_{th}(\omega) = \frac{1}{j\omega d_f F \left(\frac{G_{c1}}{j\omega d_f + K_{c1}} + \frac{G_{c2}}{j\omega d_f + K_{c2}} - \frac{G_a}{j\omega d_f + K_a} \right)} \quad (\text{II-48})$$

In theory, if faradic reactions are present, the theoretical Faradaic impedance $Z_F|_{th}(\omega)$ should be taken into account.

II-3.5.2.3. Electrogravimetric Transfer Function

The theoretical electrogravimetric transfer function, $\left. \frac{\Delta m}{\Delta E} \right|_{th}(\omega)$, can be calculated, taking into account the charged/uncharged species contribution:

$$\left. \frac{\Delta m}{\Delta E} \right|_{th}(\omega) = d_f \left(m_{c1} \frac{\Delta C_{c1}}{\Delta E} - m_{c2} \frac{\Delta C_{c2}}{\Delta E} + m_a \frac{\Delta C_a}{\Delta E} + m_s \frac{\Delta C_s}{\Delta E} \right) \quad (\text{II-49})$$

Then, replacing the equation (II-39) with the equation (II-49) results in:

$$\left. \frac{\Delta m}{\Delta E} \right|_{th}(\omega) = d_f \left(m_{c1} \frac{\Delta G_{c1}}{(j\omega d_f) + K_{c1}} + m_{c2} \frac{\Delta G_{c2}}{(j\omega d_f) + K_{c2}} + m_a \frac{\Delta G_a}{(j\omega d_f) + K_a} + m_s \frac{\Delta G_s}{(j\omega d_f) + K_s} \right) \quad (\text{II-50})$$

where m_{c1} , m_{c2} , m_a and m_s are the atomic weight of involved species.

From the theoretical overall electrogravimetric transfer function (II-50), it is possible to calculate the theoretical partial transfer functions by removing the c2 contribution, calculating

$\left. \frac{\Delta q}{\Delta E} \right|_{th}^{c1as}(\omega)$; or the c1 contribution, calculating; $\left. \frac{\Delta q}{\Delta E} \right|_{th}^{c2as}(\omega)$ or the anion contribution, calculating

$\left. \frac{\Delta q}{\Delta E} \right|_{th}^{c1c2s}(\omega)$; as shown in the following equations:

$$\left. \frac{\Delta m}{\Delta E} \right|_{th}^{c1as}(\omega) = -d_f \left[(m_{c1} - m_{c2}) \frac{\Delta C_{c1}}{\Delta E} + (m_a - m_{c2}) \frac{\Delta C_a}{\Delta E} + m_s \frac{\Delta C_s}{\Delta E} \right] \quad (\text{II-51})$$

$$\left. \frac{\Delta m}{\Delta E} \right|_{th}^{c2as}(\omega) = d_f \left[(m_{c2} - m_{c1}) \frac{\Delta C_{c1}}{\Delta E} + (m_a - m_{c1}) \frac{\Delta C_a}{\Delta E} + m_s \frac{\Delta C_s}{\Delta E} \right] \quad (\text{II-52})$$

$$\left. \frac{\Delta m}{\Delta E} \right|_{th}^{c1c2s}(\omega) = d_f \left[(m_{c1} - m_{c2}) \frac{\Delta C_{c1}}{\Delta E} + (m_{c2} - m_{c1}) \frac{\Delta C_{c2}}{\Delta E} + m_s \frac{\Delta C_s}{\Delta E} \right] \quad (\text{II-53})$$

Chapter III. Ion Dynamics in SWCNT Based Thin Film Electrodes

CHAPTER III

Ion dynamics in SWCNT Based Thin Film Electrodes

In this chapter the *Ac*-electrogravimetry is chosen as a characterization methodology due to its ability to give very relevant information such as: kinetics and identification of species transferred at the electrode/electrolyte interface, separation of the contribution of different species and determination of the relative concentration changes of the species in the electrode. The aim of this part is to contribute to the clarification of the mechanism of the ion transfer of carbon based electrodes. It will provide a better understanding of the charge storage mechanisms and validate the positive impact of using nanostructured electrodes in energy storage devices. Here, a pertinent example is presented and detailed to demonstrate the power of our approach for SWCNT films tested in NaCl electrolyte. At the end, a key question about the possibility to deconvolute the classical EQCM responses is raised, and the dynamic and gravimetric aspects of this global response are discussed.

III-1. Structure and Morphology of the SWCNT Powders and Prepared Thin Film Electrodes

The surface morphology of the SWCNT thin films deposited on the gold electrode of the quartz resonators were characterized by FEG-SEM. Prior to the thin film preparation, the SWCNT powders were characterized by HRTEM, XRD and N₂ sorption.

SWCNT thin films were prepared directly on the gold electrode surface using the PVDF-HFP as a polymer binder according to the protocol given in the experimental part (See Chapter II Section

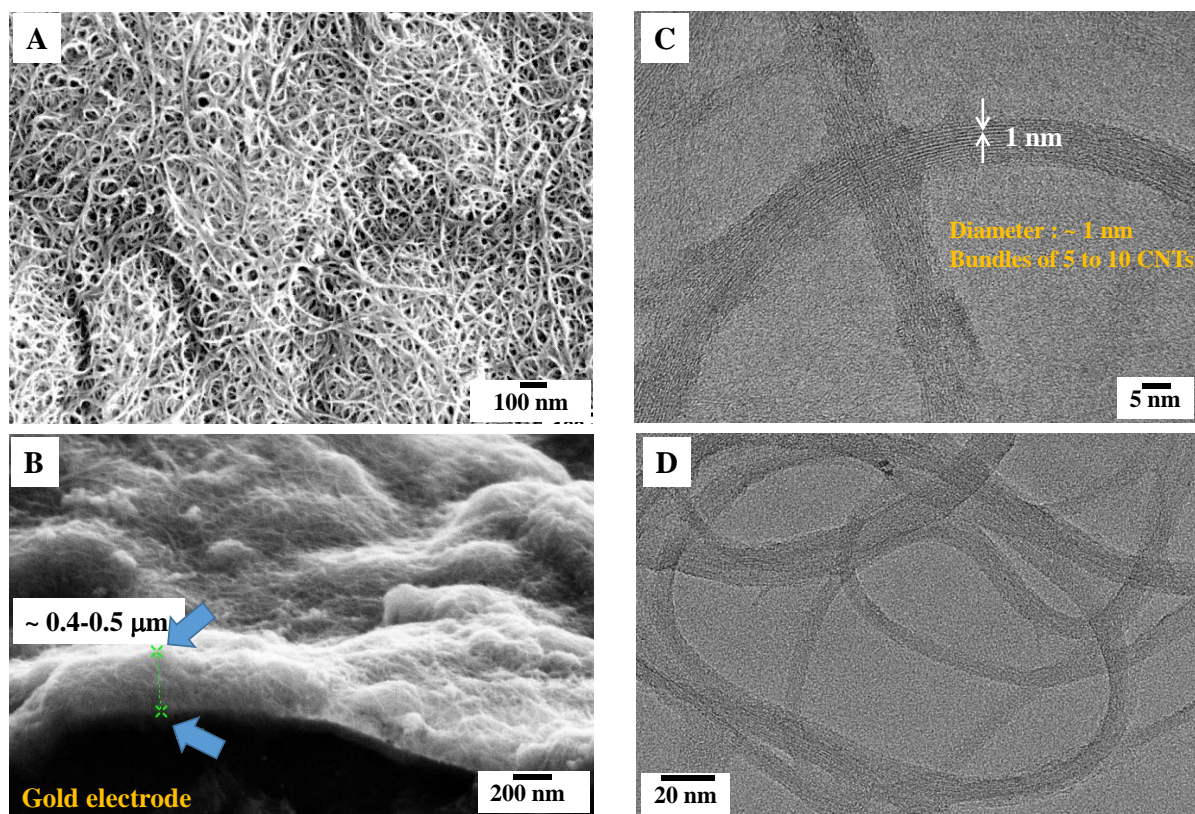


Figure III-1. FEG-SEM of an SWCNT based thin film deposited on the gold electrode of a quartz resonator (A), cross section (B) and HRTEM images of the SWCNTs (C) and (D).

1.1). Figure III-1A shows a representative FEG-SEM image of the SWCNT based thin film electrode, revealing an important density of CNT bundles around 10 nm. The cross-section of the SWCNTs shown in Figure III-1B permits the estimation of the film thickness. The films are electroacoustically thin ($\sim 0.4\text{-}0.5\ \mu\text{m}$) which assures the gravimetric regime; consequently, the Sauerbrey Equation applies.

The SWCNTs constituting the composite electrode in figure III-1A and 1B were also characterized by HRTEM. The images in Figure III-1C and 1D indicate that the diameter of the SWCNTs is $\sim 1\text{-}2\ \text{nm}$ and present bundles of at least 5 to 10 CNTs together. These dimensions are in good agreement with the values for similar structures reported in the literature.^{113,115}

Figure III-2A and 2B depicts the XRD pattern of the SWCNTs. The strongest diffraction peak related to the SWCNT structure at the angle (2θ) of $\sim 25^\circ$ can be indexed as the (002) reflection of the hexagonal graphite structure similar to the structures reported in the literature.²⁰⁶ The sharpness of the peak at the angle (2θ) of 25° is related to the graphitic structure and a slight broadening in Fig. III-2A and 2B indicates the presence of a certain disorder in their structure in agreement with the HRTEM investigations.

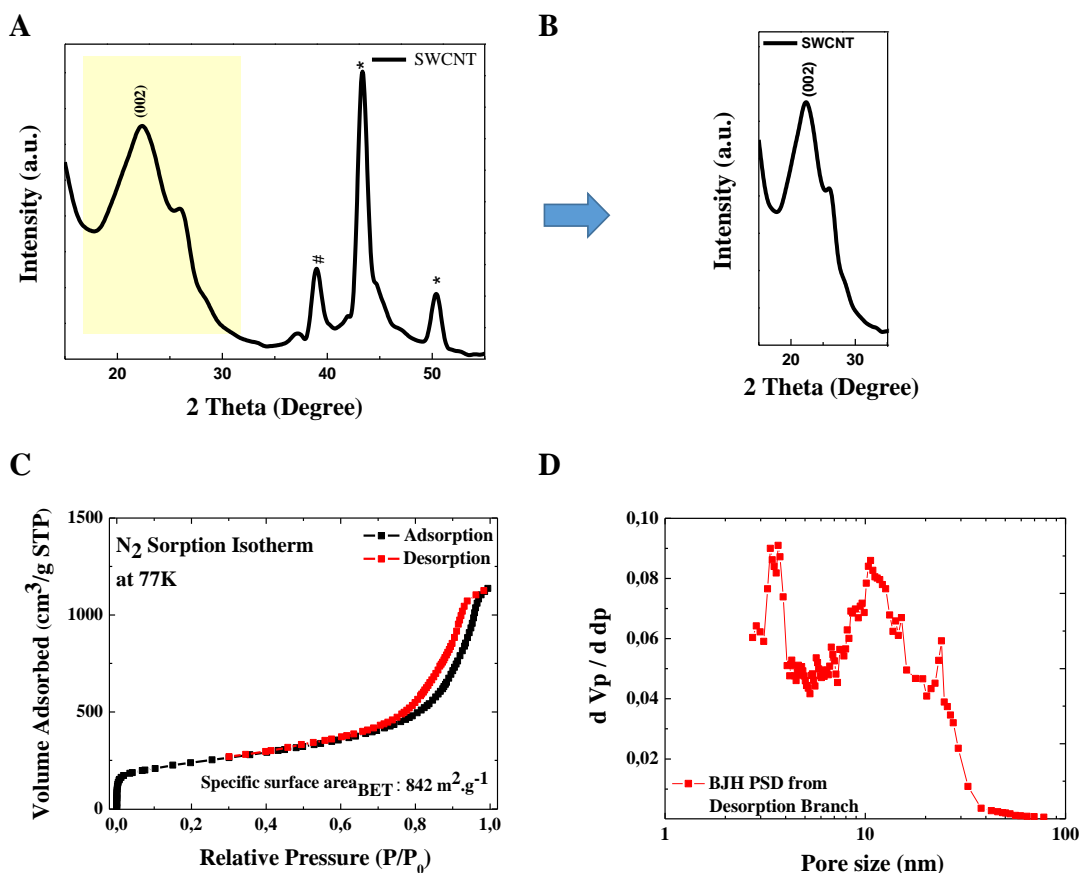


Figure III-2. XRD spectra (A) and (B) of SWCNTs (the 2 theta region related to SWCNTs are shown in (B) and # and * are related to the sample holder). Nitrogen sorption isotherm (C) and the pore size distribution (PSD) of SWCNTs.

The pore and specific surface area characteristics of the SWCNTs were studied by nitrogen sorption measurements. Figure III-2C shows the nitrogen adsorption-desorption isotherm of the SWCNTs. The shape of the isotherms can be considered as type-IV curves²⁰⁷ (characteristic for mesoporous adsorbents) with a slight hysteresis loop at high relative pressures (P/P₀) between 0.8-1. The Brunauer-Emmett-Teller (BET) method was applied for the specific surface area determination of the SWCNTs and was estimated to be $\sim 842 \text{ m}^2.\text{g}^{-1}$. Furthermore, the nitrogen sorption isotherm was used to estimate the pore size distribution (PSD) of the SWCNTs and shown in Fig. III-2D. The PSD presents two main peaks centered at $\sim 2\text{-}3 \text{ nm}$ and $\sim 10 \text{ nm}$ which can be attributed to the diameter of the SWCNTs and the voids formed between the CNT bundles, respectively. The presence of several pore dimensions is in agreement with the HRTEM images shown in figure III-1C and 1D. The structural characterization based on microscopic, spectroscopic and gas adsorption methods indicates that the SWCNT based electrodes have pertinent physical and morphological attributes to study the supercapacitive charge storage behavior (*e.x.* high specific surface area of $\sim 842 \text{ m}^2.\text{g}^{-1}$).

III-2. Classical Electrogravimetric Study of SWCNT Thin Film Electrodes in Aqueous NaCl Electrolyte

III-2.1. EQCM measurements on SWCNT Thin Film Electrodes

EQCM responses from a sample of SWCNT films tested in aqueous solution 0.5 M NaCl at 100mV/s, 50mV/s and 25mV/s from 0.45V to -0.45 V vs Ag/AgCl are presented in Figure III-3.

A growing capacitive current is observed when the scan rate increases. Purely capacitive materials exhibit perfect rectangular-shaped cyclic voltammetry responses. In this study, the SWCNT thin films show quasi-rectangular shaped responses indicating that the charge storage is mainly due to the reversible electroadsorption of electrolyte ions (Figure III-3A).

The slight distortion from a perfect rectangular shape is due to the presence of a slight faradic contribution to the charge storage. This small faradic contribution can be due to several reactions such as (i) the reduction of the protons present in the electrolyte, (ii) the reduction of remaining surface functional groups on SWCNTs and/or (iii) catalyst remaining after purifying carbon nanotubes. A fairly large number of publications related to the carbons with oxygen-containing surface functional groups have been found in the literature.²⁰⁸⁻²¹³ The corresponding mass variations is followed by simultaneous QCM measurements as a function of potential. In Figure III-3B, the mass change of the SWCNT electrode presents a change in slope ($\frac{\Delta m}{\Delta E} < 0$ for the transfer of cations and $\frac{\Delta m}{\Delta E} > 0$ for anions), around 0.1 V vs Ag/AgCl. It indicates that the point of zero charge (pzc) is around this value.

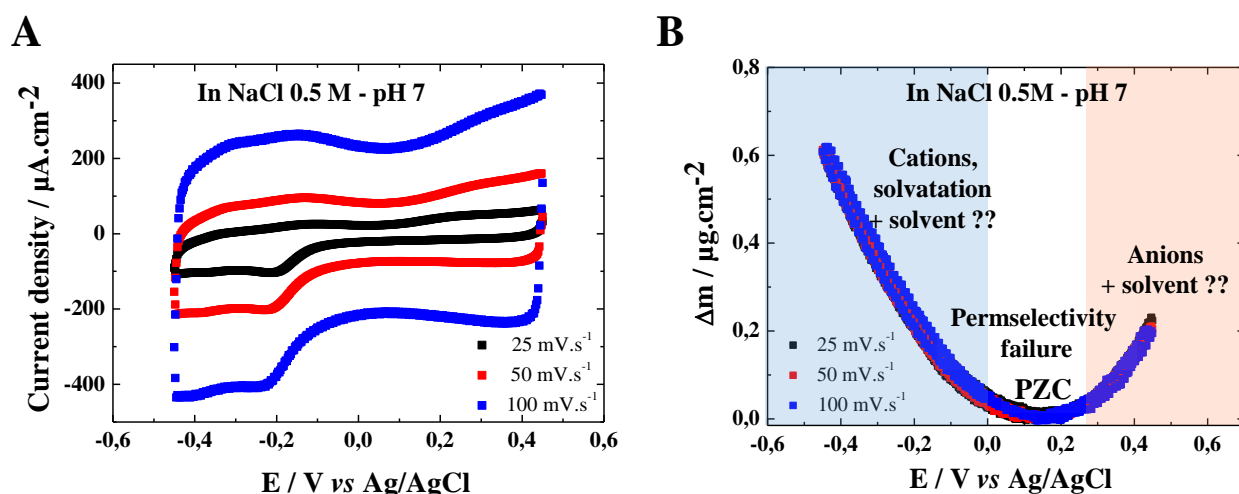


Figure III-3. EQCM results of SWCNT thin films - the CV curves (A) and the simultaneously obtained mass changes (B) measured in aqueous 0.5 M NaCl electrolyte at pH=7.

According to electrostatic considerations, ions contributing to the charge compensation should be the cations and anions at a potential below and above the pzc, respectively. Indeed, when a more cathodic potential than pzc is applied to the electrode, the electrons generated at SWCNT film/electrolyte interface are compensated mainly by the cations present in the electrolyte *via* an electroadsorption process: the global mass of the electrode increases and this effect is determined real time with the sufficiently sensitive EQCM device. On the contrary, when a more anodic potential than pzc is applied to the electrode, the anions are expected to be electroadsorbed to charge compensate the positive charges generated at the SWCNT film/electrolyte interface. To obtain indications on the nature of the transferred species, the $F \times \frac{\Delta m}{\Delta q} = F \frac{\Delta m / \Delta t}{\Delta Q / \Delta t}$ function was calculated over the whole potential range, as explained previously (Chapter II, Section 3.2.3.).

III-2.2. Fdm/dq Function Calculations

Figure III-4 shows the Fdm/dq values which are equivalent to the molecular mass of the electroadsorbed species at a given scan rate.¹⁰⁹

The values are calculated as a function of the potential in NaCl electrolyte (See Chapter II for details of calculation). The Fdm/dq shows a value between -40 to -23 g.mol⁻¹ for potentials in the range of the 0.05 V to -0.4 V *vs* Ag/AgCl, particularly at 100 mV.s⁻¹ scan rate. It is important to note here that the negative and positive molar mass values correspond to the cations and anions, respectively.¹⁰⁹ Absolute values of the Fdm/dq function is considered for discussion. The molecular mass at 23 g.mol⁻¹ may correspond to the cation contribution and the molar mass higher than 23 g.mol⁻¹ may indicate the presence of hydrated cations and/or hydrated cations accompanied by free solvent molecules in the same flux direction during the transfer. In the anodic part, higher molar mass values than the respective anion in the electrolyte are observed especially at high scan rates. Therefore, a concomitant transfer of the anions with free solvent can be expected. Additionally, a strong scan rate dependence of the Fdm/dq function is observed at more anodic potentials.

The contribution of (i) counter ions solely, (ii) counter ions and solvent or (iii) both counter- and co-ions (without solvent) in carbon based electrodes were intensively investigated by Levi and Aurbach *et al.*¹⁴⁴, and similar cases were considered in doped conducting polymers and conventional redox systems by Bruckenstein and Hillman *et al.*²¹⁴⁻²¹⁷

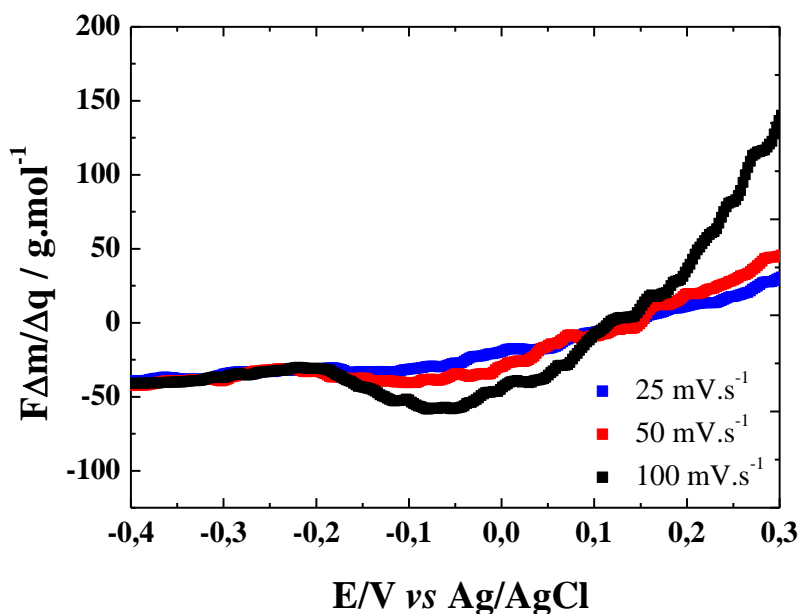


Figure III-4. The $F\Delta m/dq$ as a function of the applied potential, obtained from the reduction branch of the EQCM results measured in 0.5 M NaCl at pH=7 (Fig.III.3) for SWCNT based thin film electrodes.

Our findings and the literature results strongly suggest that the EQCM data envelops the subtleties of the supercapacitive charge storage. This global EQCM response, measured at a certain scan rate cannot give an easy access to the details related to the capacitive charge storage mechanism. Therefore, an *ac*-electrogravimetric study is conducted for the deconvolution of the global EQCM response into distinct contributions with a resolution at the temporal level.

Before going into the details of the *ac*-electrogravimetric study, the specific capacitance of the SWCNT based thin film electrodes are briefly discussed below.

III-2.3. Specific Capacitance Calculations

The specific capacitance values were calculated by using the following relation:

$C_{\text{specific}} (F/g) = \frac{I (Ampere)}{v_s (volt/second) \times \text{electrode mass (g)}}$ where C is the specific capacitance, I is the measured current and v_s is the scan rate used.

By using the data presented in Figure III-3A, the specific capacitance values are estimated to be around 25 F.g⁻¹ at 100 mV s⁻¹ scan rate (Figure III-5). The normalization of the capacitance values could be done with precision thanks to the exact mass determination using the QCM. These values are in the same order of magnitude as the reported values found in the literature by authors.⁸⁵ The specific capacitance values are dependent on the scan rate, which indicates the kinetics of the

species play a role in the charge compensation mechanisms. This aspect will be scrutinized with an *ac*-electrogravimetric study.

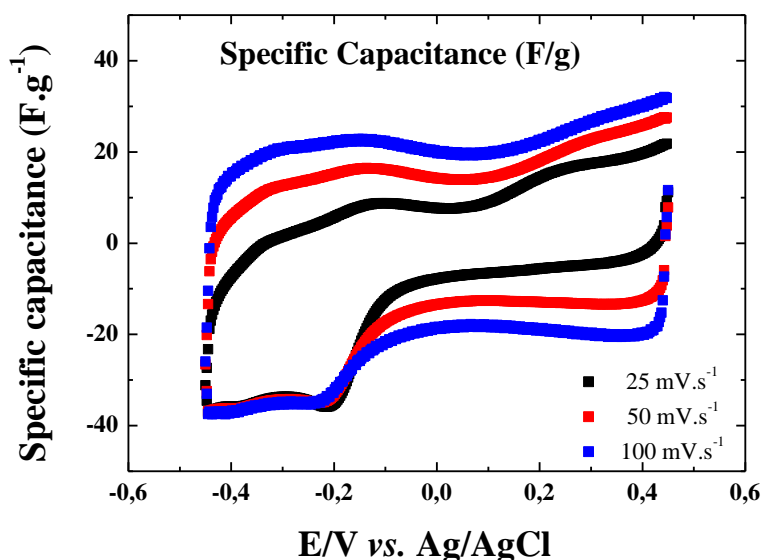


Figure III-5. Specific capacitance values of SWCNT thin films (calculated from Figure III-3A) as a function of potential, estimated at selected scan rates for 0.5 M NaCl pH=7.

III-3. *Ac*-Electrogravimetric Studies of SWCNT Thin Film Electrodes in Aqueous NaCl Electrolyte

The supercapacitive charge storage behavior was studied by *ac*-electrogravimetry in aqueous NaCl, at stationary potential values in the range of -0.45 V to 0.45 V vs Ag/AgCl. For the sake of clarity, the methodology of data interpretation at a selected potential will be given which allows the model used here to be justified. Then, an extension to other potentials and pertinent parameters can be obtained from this approach will be examined. At the end, the deconvolution of the classical Δm -E curves (obtained from EQCM responses) will be our center of focus using the key results given by the *ac*-electrogravimetry. For the latter, the aim is to reach a deconvolution both at a gravimetric and a kinetic level.

III-3.1. EQCM *versus* *Ac*-Electrogravimetry

Ac-electrogravimetric results presented below were performed at -0.4 V vs Ag/AgCl. This part is dedicated to a step-by-step clarification of our *ac*-electrogravimetry experimental data analysis with different examples.

In Figure III-6A and B, the two main experimental TFs are presented: $\frac{\Delta q}{\Delta E}(\omega)$ and $\frac{\Delta m}{\Delta E}(\omega)$. In the former, two loops can be observed with a reasonable frequency separation, the high frequency loop being twice as high in diameter as the low frequency one.

At this stage, it is impossible to unambiguously attribute these two loops to two different ionic responses. For the second experimental TF, $\frac{\Delta m}{\Delta E}(\omega)$, a large semi-circle was seen in the third quadrant. It indicates the contribution of cations mainly but without a fair separation of the different responses. For that, several configurations were tested using the models described in Chapter II-3.5 with the strict criteria that a good agreement between the experimental and the theoretical functions in terms of shape and frequencies was achieved. For the theoretical functions, the equations presented in Chapter II are adapted based on the number of species considered in the different hypothesis considered (*i.e.* Eq II-46 for $\frac{\Delta q}{\Delta E}(\omega)$, Eq. II-50 for $\frac{\Delta m}{\Delta E}(\omega)$ and Eqs. II.51-53 for partial mass/potential transfer functions).

(i) Hypothesis I: Considering Two Species: Solvated Na^+ and H_2O

In Figure III-6, the theoretical transfer functions were calculated taking into account a single cation ($\text{Na}^+\cdot\text{H}_2\text{O}$) and free solvent (H_2O) molecules. It is evident that the charge/potential TF cannot be fitted with this consideration.

It appears that for low frequencies another charged species is involved as can be seen in the $\frac{\Delta q}{\Delta E}(\omega)$ TF (Fig. III-7A). It should be underlined that in this case the theoretical $\frac{\Delta m}{\Delta E}(\omega)$ TF fits very well the experimental data by using the free solvent contribution (Fig. III-6B). Nevertheless, the fitting of several other functions including $F \frac{\Delta m}{\Delta q}(\omega)$ is not appropriate. Therefore, this configuration was discarded.

A second phase of simulation has been realized with the involvement of two cations. No anion contribution is expected at -0.4 V vs Ag/AgCl.

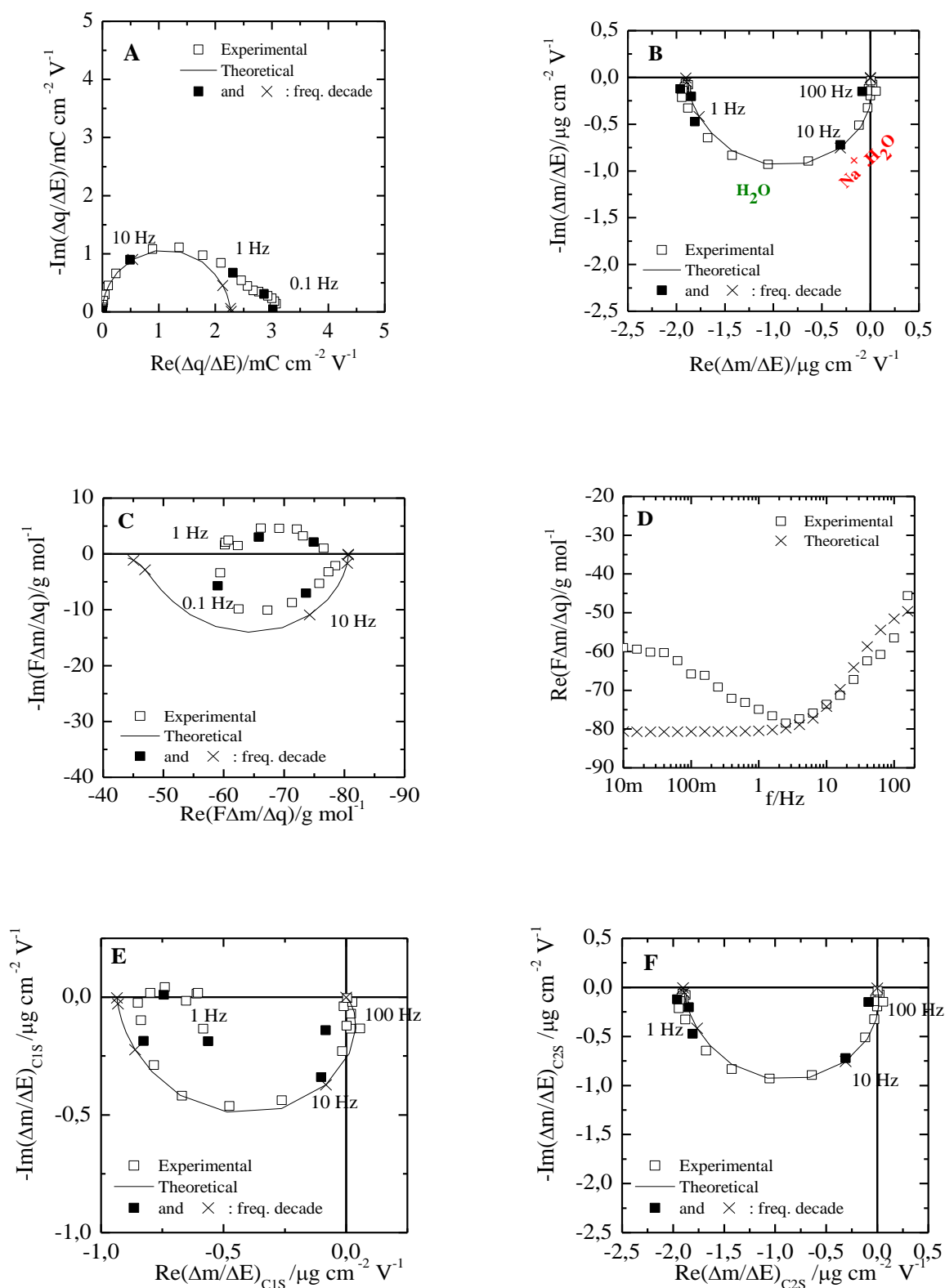


Figure III-6. Experimental and theoretical transfer functions at -0.4 V vs Ag/AgCl in 0.5 M NaCl. The theoretical functions were calculated taking into account only one cation (Na^+ , H_2O) and free solvent (H_2O). Theoretical functions were calculated with the following parameters: $d_f = 0.4 \mu\text{m}$, $K_{c2} = 6.91 \times 10^{-3} \text{ cm s}^{-1}$, $G_{c2} = 4.01 \times 10^{-6} \text{ mol s}^{-1} \text{ cm}^{-2} \text{ V}^{-1}$, $K_s = 3.14 \times 10^{-3} \text{ cm s}^{-1}$, $G_s = 4.08 \times 10^{-6} \text{ mol s}^{-1}$, $m_{c2} = 23+18 \text{ g mol}^{-1}$, $m_s = 18 \text{ g mol}^{-1}$.

(ii) Hypothesis II: Considering Two Charged Species: Solvated Na⁺ and H⁺

In a second hypothesis, the theoretical transfer functions were calculated taking into account of two cations: Na⁺.H₂O and H⁺ as shown in Figure III-7. Although this configuration fits the charge/potential transfer function (Fig. III-7A), it does not lead to a good agreement with the other experimental data, above all the $\frac{\Delta m}{\Delta E}(\omega)$ TF (Fig. III-7B). It seems that free solvent molecules may also be involved indirectly in the charge compensation mechanism of the thin film SWCNT based electrodes.

(iii) Hypothesis III: Considering Three Species: Solvated Na⁺, H⁺ and H₂O

Finally, the theoretical transfer functions were calculated taking into account three species: Na⁺.H₂O, H⁺, and H₂O and the results are presented in Figure III-8. With this configuration, figure III-8A permits the observation of two loops in the diagram of the transfer function $\frac{\Delta q}{\Delta E}(\omega)$ where a good agreement between the experimental and theoretical functions are achieved. In this figure, each loop corresponds to one charged species involved in the electrochemical process of the film (the electroadsorption of ions on the surface of the SWCNT). It may be that two cations or two anions or one cation and one anion are involved, because this function does not allow a direct identification of ions. The identification of the species can be achieved with the electrogravimetric transfer function. The electrogravimetric transfer function $\frac{\Delta m}{\Delta E}(\omega)$ shows one loop which is actually fitted by considering Na⁺.H₂O, H⁺ and free H₂O contributions (Figure III-8B). To have a cross-check of this configuration involving three species (c1, c2 and s), all the other transfer functions are regarded in detail (Figures III-8-C-D-E and F). The partial mass/potential TFs were analyzed to validate our hypothesis involving three different species; they are estimated, for example by removing the c2 contribution, calculating $\left. \frac{\Delta m}{\Delta E} \right|_{th}^{c1s}$ or by removing the c1 contribution, calculating $\left. \frac{\Delta m}{\Delta E} \right|_{th}^{c2s}$ (Fig. III-8E and 8F). A good fit appears as well as for all the other transfer functions shown in Figures III-9-C-D-E and F in terms of shape and frequency distribution. The hydrated Na⁺ appears at high frequency (fast process) whereas the protons participate at low frequency (slow process). The kinetics of the free solvent molecules is close to that of hydrated Na⁺ species suggesting that polar water molecules are electrodragged together with hydrated Na⁺.²¹⁸

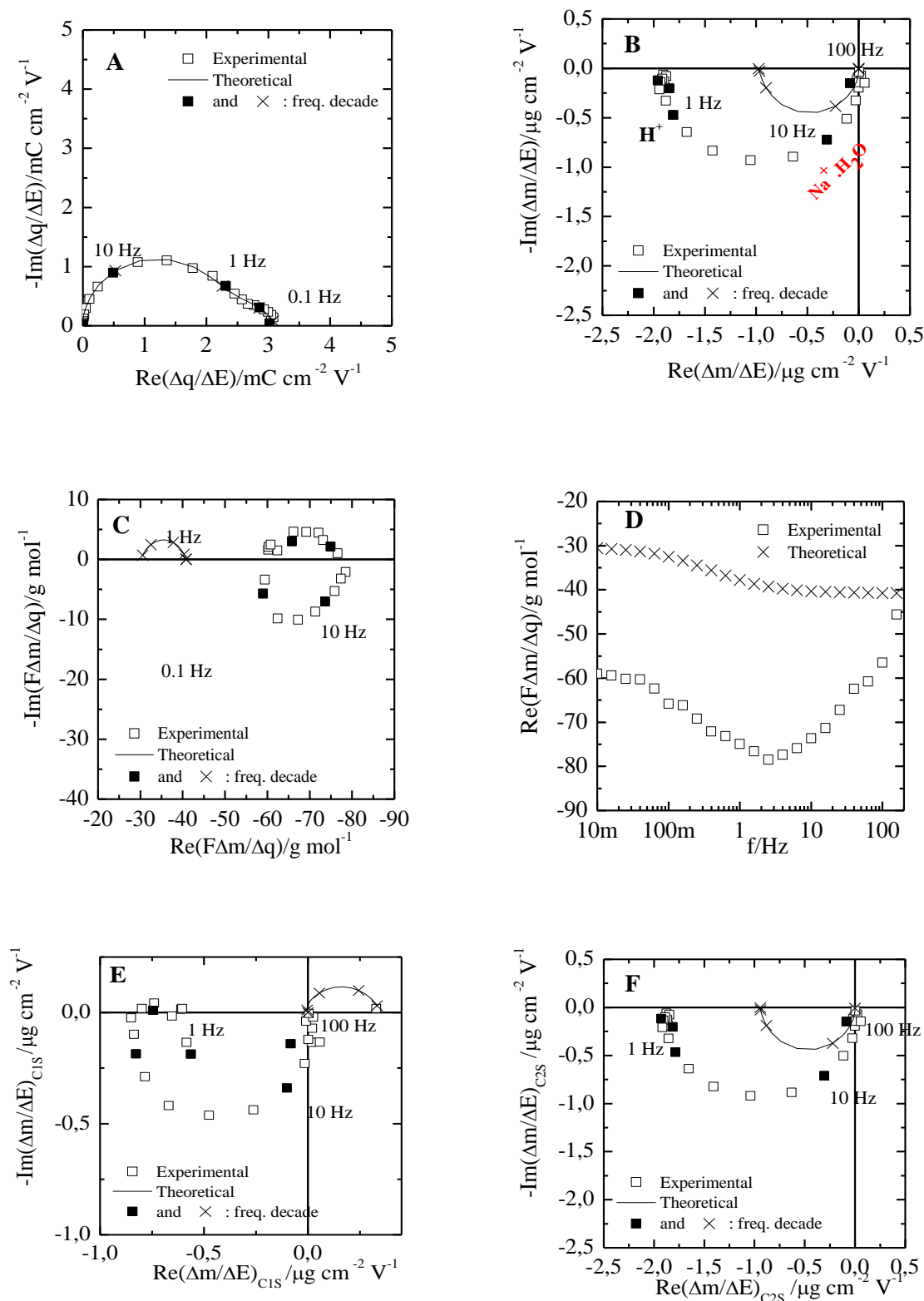


Figure III-7. Experimental and theoretical transfer functions at -0.4V vs Ag/AgCl in 0.5 M NaCl. The theoretical functions were calculated taking into account of two cations (Na^+ , H_2O) and (H^+). Theoretical functions were calculated with the following parameters: $d_f = 0.4 \mu\text{m}$, $K_{c1} = 5.40 \times 10^{-5} \text{ cm s}^{-1}$, $G_{c1} = 1.19 \times 10^{-8} \text{ mol s}^{-1} \text{ cm}^{-2} \text{ V}^{-1}$, $K_{c2} = 6.91 \times 10^{-3} \text{ cm s}^{-1}$, $G_{c2} = 4.08 \times 10^{-6} \text{ mol s}^{-1}$, $m_{c2} = 23+18 \text{ g mol}^{-1}$, $m_{c1} = 1 \text{ g mol}^{-1}$.

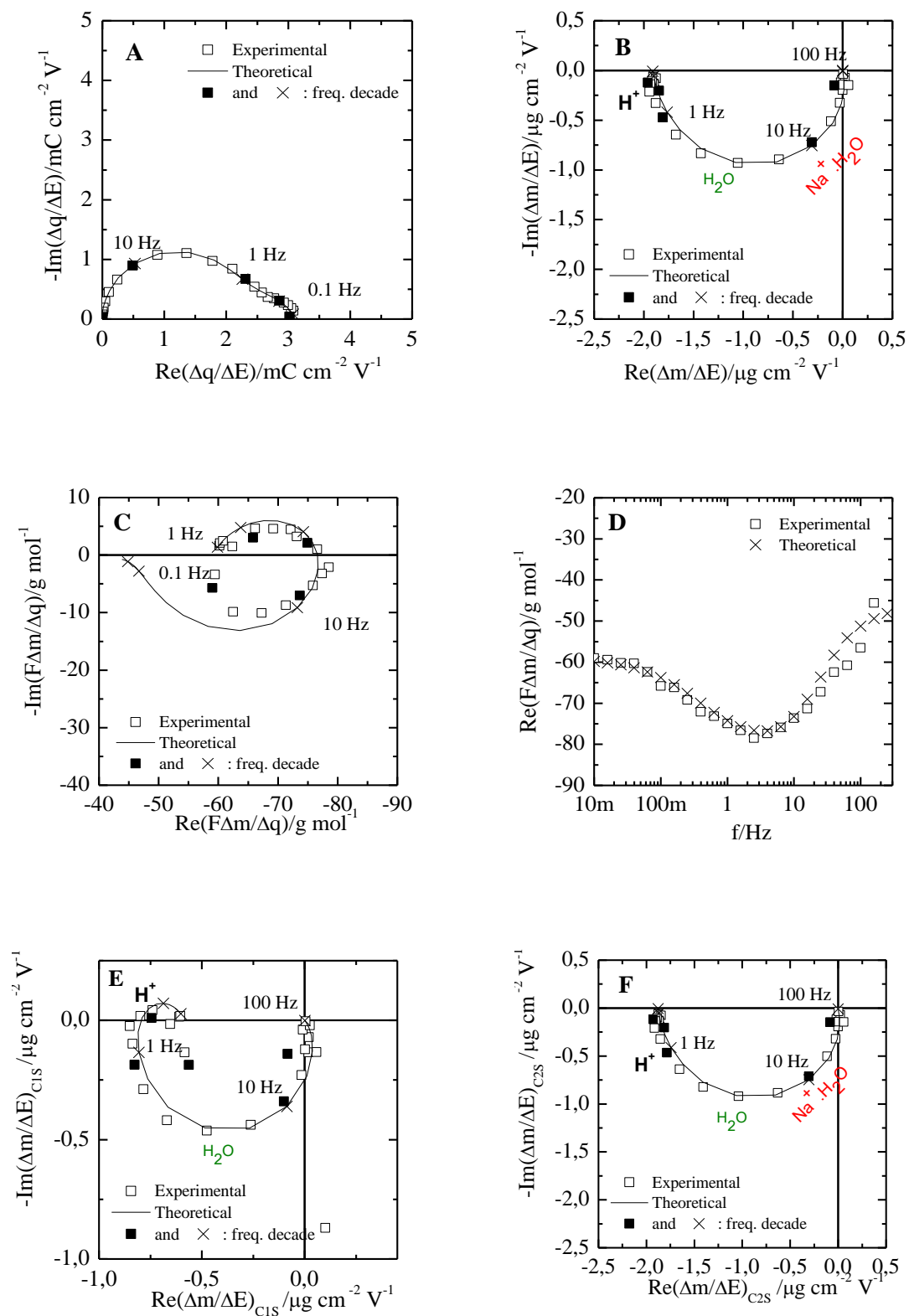


Figure III-8. Experimental and theoretical transfer functions at -0.4V vs Ag/AgCl in 0.5 M NaCl. The theoretical functions were calculated taking into account two cations (Na^+ , H_2O) and (H^+) and free solvent (H_2O). Theoretical functions were calculated with the following parameters: $d_f = 0.4 \mu\text{m}$, $K_{c1} = 5.40 \times 10^{-5} \text{ cm s}^{-1}$, $G_{c1} = 1.19 \times 10^{-8} \text{ mol s}^{-1} \text{ cm}^{-2} \text{ V}^{-1}$, $K_{c2} = 6.91 \times 10^{-3} \text{ cm s}^{-1}$, $G_{c2} = 4.08 \times 10^{-6} \text{ mol s}^{-1}$, $K_s = 3.14 \times 10^{-3} \text{ cm s}^{-1}$, $G_s = 4.08 \times 10^{-6} \text{ mol s}^{-1}$, $m_{c2} = 23+18 \text{ g mol}^{-1}$, $m_{c1} = 1 \text{ g mol}^{-1}$.

It is important to highlight a delicate point in our *ac*-electrogravimetric analysis. Figure III-8E shows a small contribution at low frequencies in the fourth quadrant. Characteristically, this should correspond to a response of an anion.¹⁰⁹ In fact, this contribution is that of a cation of which atomic mass is smaller than the fastest cation. This is evident from Equation II-51 in Chapter II where the response is multiplied by $m_{c1}-m_{c2}$. As $c1$ corresponds to H^+ and $c2$ corresponds to $Na^+.H_2O$, $m_{c1}-m_{c2}$ value is negative which makes it appear as a “*virtual anion*”. These partial electrogravimetric transfer functions (Fig. III-8E and F) provides a crosscheck for validating the hypothesis involving three different species and a better separation of the various contributions.

At this selected potential (-0.4 V *vs* Ag/AgCl), the hydrated Na^+ appears at high frequency (fast process) whereas the protons participate at low frequency (slow process). The kinetics of the free solvent molecules is close to that of hydrated Na^+ species suggesting that polar water molecules are electrodragged together with hydrated Na^+ .²¹⁸

(iv) Evolution of the Different Parameters over the Applied Potentials-the Nature and the Kinetics of the Species

Above discussion was based on the detailed analysis of the *ac*-electrogravimetric data at a selected potential. Such measurements and data analysis were performed at different stationary potential values in the range of -0.45 V to 0.45 V *vs* Ag/AgCl. The nature of the species and the corresponding K_i (kinetics of transfer) and G_i (related to the ease or difficulty of interfacial transfer) parameters were estimated as a function of potential. The G_i parameter was used to estimate the

transfer resistance, $Rt_i = \frac{1}{FG_i}$, of the species at the film/electrolyte interface.

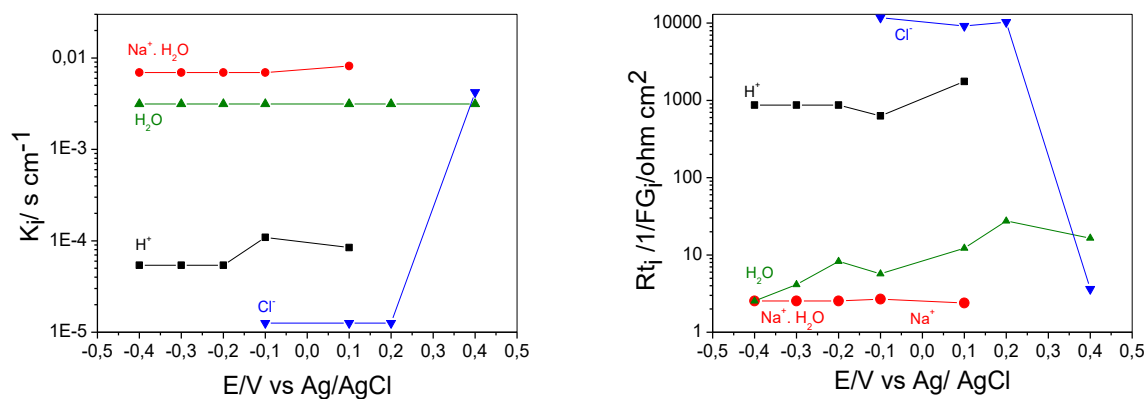


Figure III-9. Kinetic transfer rates K_i (A), and transfer resistances Rt_i (B) for all species estimated from the fitting of the *ac*-electrogravimetry data measured in 0.5 M NaCl pH=7.

Figure III-9 shows the evolution of kinetic transfer rates, K_i , and the transfer resistances, R_{t_i} , of the species as a function of the applied potential. It is easier to discuss this curves in two regions, corresponding to the more cathodic and more anodic potentials with respect to the pzc of the SWCNT based thin films. In agreement with the EQCM data in Fig. III-3, the pzc can be considered to be around 0.1 V vs Ag/AgCl.

Two different cationic species and free water molecules were detected in the potential range from -0.4 V to 0.1 V (no major anions contribution in that region). The hydrated Na^+ ions are persistently the fastest species, *i.e.* $K_i(\text{Na}^+.\text{H}_2\text{O}) > K_i(\text{H}^+)$ (Fig. III-9A). The R_{t_i} (transfer resistance) parameter which can explain the ease or the difficulty in the transfer at the electrode/electrolyte interface present the following order: $R_{t_i}(\text{H}^+) > R_{t_i}(\text{Na}^+.\text{H}_2\text{O})$ (inverse of the K_i) (Fig. III-9B). Furthermore, the transfer kinetics of free water molecules are somewhat close to the values of the $\text{Na}^+.\text{nH}_2\text{O}$. Additionally, these water molecules have the same flux directions as the cations, suggesting that it might be the water molecules that accompany the transfer of $\text{Na}^+.\text{nH}_2\text{O}$, most likely due to an electrodragging effect as previously discussed at -0.4V vs Ag/AgCl..

These findings strongly suggest that $\text{Na}^+.\text{H}_2\text{O}$, although formally larger than H^+ , are faster and easier to be electroadsorbed at the SWCNT/electrolyte interfaces. This, a priori anomalous behavior can be discussed in terms of cation concentration or of the relationship between the dehydration energy and the ion size. For the former, the proton concentration is lower compared to the sodium and can affect the kinetics of transfer.

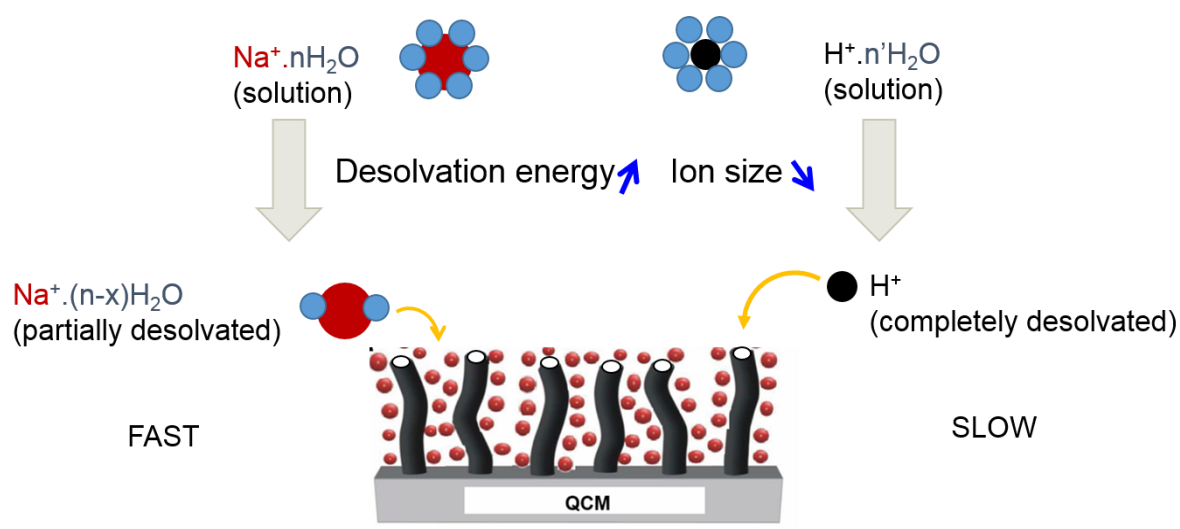


Figure III-10. Schematic representation of the interaction of ions with carbon nanotube based electrodes on gold electrodes of the quartz resonator in aqueous 0.5 M NaCl at pH=7.

For the latter, the smaller ions are more tightly bound to their water molecules such that it exists an inverse relationship between the dehydration energy and the ion size (Fig. III-10). Sodium species (completely or partially dehydrated) require less energy to get rid of their water molecules (compared to protons), which probably confers a rapid (faster transfer kinetics, K_i) and an easy transfer (low transfer resistance R_{ti}) characteristics on sodium species (Fig. III-10). The literature results agree that ions with higher charge density have higher number of tightly bound water molecules.²¹⁸⁻²²⁰ Here, this phenomenon has been shown to play a role in the capacitive charge storage behavior of SWCNT electrodes. Additionally, the possibility that electroadsorption occurs in two different sites; directly on the surface (sites more accessible for the hydrated sodium) or inside the nanotubes (sites less accessible for the dehydrated protons) can be suggested (Fig. III-10).

The participation of the anions (Cl^-) to the electroadsorption process was also detected at around the pzc (Fig. III-9) probably due to the permselectivity failure of the SWCNT films around this value leading to the mixed adsorption.¹³⁹ Their transfer resistance is high around pzc which decreases at more anodic potentials *i.e.* 0.4 V vs Ag/AgCl (Fig. III-9).

(v) Deconvolution of the Global EQCM Mass Response by *Ac*-electrogravimetry

A major advantage of *ac*-electrogravimetry is the estimation of the relative concentration change with respect to the individual species.

Therefore, to quantify the role of each species, $\left. \frac{\Delta C_i}{\Delta E} \right|_{\omega \rightarrow 0} = -\frac{G_i}{K_i}$ has been calculated (from

Fig.III-9) as a function of the applied potential. The integration of the $\left. \frac{\Delta C_i}{\Delta E} \right|_{\omega \rightarrow 0}$ against potential

gives the relative concentration change, $(C_i - C_0)$ as depicted in Figure III-11A. The $(C_i - C_0)$ values of the $\text{Na}^+ \cdot n\text{H}_2\text{O}$ are significantly higher than the $(C_i - C_0)$ values of the H^+ at cathodic potentials. It is noteworthy that despite the slow kinetics and high transfer resistance of the protons, their contribution to the charge storage is still not negligible. For more anodic potentials (when the SWCNT surface is positively charged), the electroadsorption of anions occurs keeping the electroneutrality of the electrode/electrolyte interface.

Furthermore, the $(C_i - C_0)$ values of the free solvent is close to the $\text{Na}^+ \cdot n\text{H}_2\text{O}$ at cathodic potentials and close to the Cl^- at anodic potentials which is coherent with the hypothesis explained previously (electrodragging).

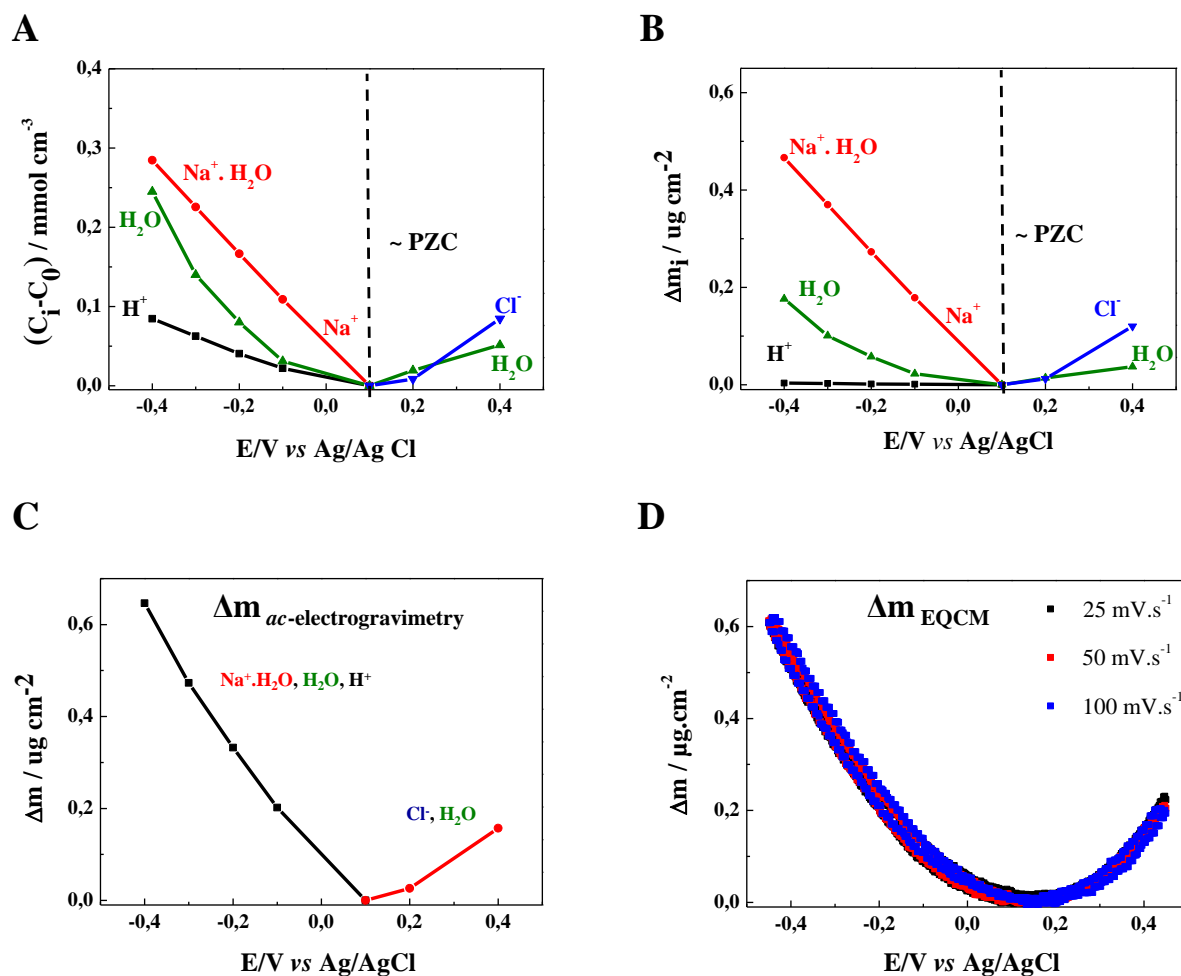


Figure III-11. Relative concentration variation, $C_i - C_0$ (A), relative mass variation (B) (calculated from A) of respective species in the SWCNT based electrode, measured in 0.5 M NaCl at pH=7. Total mass variation reconstructed from *ac*-electrogravimetry (C) is compared with the EQCM data (D).

It was mentioned earlier that one of the main problems with the EQCM is the interpretation of the global mass changes offered by this technique. As shown previously,^{1,2,142} a clear identification of various species which may contribute to the charge compensation process and their dynamics of transfer are rather hard to be understood using this classical approach.

By using the results of *ac*-electrogravimetry of our study, it was possible to recalculate the mass changes of the film *versus* the applied potentials. The concentration variation of individual species ($C_i - C_0$) obtained from the *ac*-electrogravimetry are converted into their respective mass variations (Figure III-11B) by using the atomic weight of each species involved in the electrochemical process. Subsequently, the total mass response of the SWCNT based electrode is reconstructed by addition of the individual contributions (Figure III-11C). This total mass response reconstructed from *ac*-electrogravimetry is in very good agreement with the global mass response

obtained from EQCM method (Figure III-11D) (*i.e.* $\Delta m_{ac-electrogravimetry} = 0.65 \mu g.cm^{-1}$ and $\Delta m_{EQCM} = 0.62 \mu g.cm^{-1}$ for the cathodic potentials). It is further highlighted that *ac*-electrogravimetry results are obtained from individual measurements at stationary potentials and the reconstructed mass response is in good agreement with the EQCM data from cyclic voltammetry. This is highly significant since it evidences that the *ac*-electrogravimetry result in Figure III-11B is indeed a deconvolution of the global EQCM mass response into distinct contributions. Since *ac*-electrogravimetry provides additional information on the kinetics of the respective species, then it is legitimate to call it a gravimetric and dynamic deconvolution.²¹⁸

III-4. *Ac*-Electrogravimetric Study of SWCNT Thin Films in Organic Electrolytes

Up to now, in this chapter, we have presented the detailed analysis of ions interactions with the SWCNT based electrodes in aqueous electrolytes. As mentioned previously in Chapter I-1.2.3, one of the most commonly used organic electrolytes in energy devices are solvents based on propylene carbonate (PC). To explore the possibility to extend *ac*-electrogravimetry methodology to organic electrolytes, we have tested SWCNT based electrodes in in 0.5M LiClO₄/PC propylene carbonate.

Ac-electrogravimetric measurements realized at a selected potential (at -0.4V vs Ag/AgCl) are discussed below. The theoretical transfer functions were calculated taking into account of three species (identified as Li⁺, H₃O⁺, and PC) and the results are presented in Figure III-12.

One loop is observed in the charge/potential transfer function $\frac{\Delta q}{\Delta E}(\omega)$ (Fig. III-12A). This function does not allow a direct identification and a fair separation of ions to be achieved. The electrogravimetric transfer function, $\frac{\Delta m}{\Delta E}(\omega)$, is more informative: two loops are obtained, at high frequency (HF) a small loop in the first quadrant, associated to the cation and at medium and low frequency (LF) loop in the second and third quadrant, correlated to solvent and cation, respectively (Figure III-12B).

The nature of the ions and uncharged species is estimated by their molar mass thanks to the electrogravimetric transfer function. Li⁺ ions and free solvent (PC) participate at HF and medium frequencies, respectively, while H₃O⁺ participates at LF.

It is noted that the free solvent molecules (PC) has the opposite flux direction with respect to the cations, probably providing space to the electroadsorption of the cations at the electrode/electrolyte interfaces.

It is important to note that the HF cation response is very small and not clearly visible. Indeed, the molar mass of Li^+ is relatively small and leads to this small contribution. Among the several configurations tested, the Li^+ ions contribution was absolutely necessary to fit the experimental data.

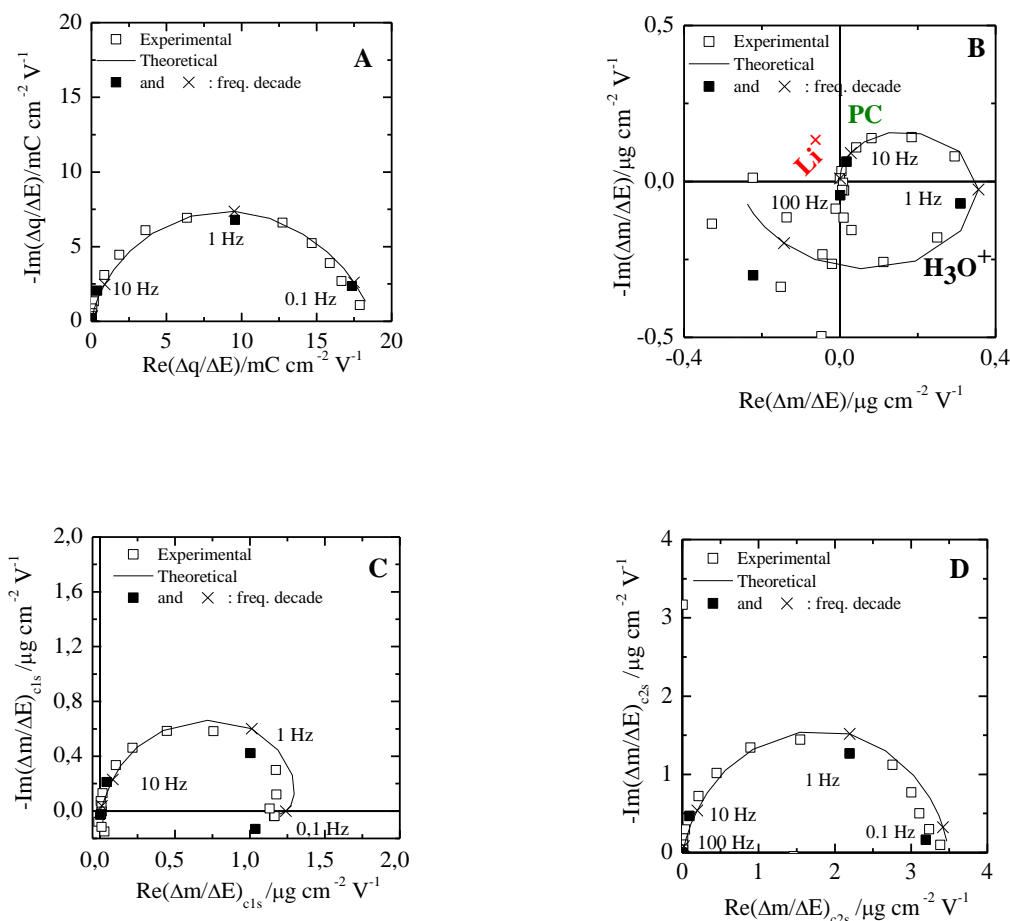


Figure III-12. Experimental and theoretical ac-electrogravimetric data of the SWCNT thin film in 0.5

M LiClO_4 measured at -0.4V vs Ag/AgCl. (A) $\frac{\Delta q}{\Delta E}(\omega)$, (B) $\frac{\Delta m}{\Delta E}(\omega)$, (C) $\frac{\Delta m}{\Delta E}\bigg|^{c1s}(\omega)$, (D) $\frac{\Delta m}{\Delta E}\bigg|^{c2s}(\omega)$.

Theoretical functions were calculated with the following parameters: $d_f = 0.4\mu\text{m}$, $K_{c1} = 9.43 \times 10^{-5} \text{ cm s}^{-1}$, $G_{c1} = 1.08 \times 10^{-7} \text{ mol s}^{-1} \text{ cm}^{-2} \text{ V}^{-1}$, $K_{c2} = 2.07 \times 10^{-3} \text{ cm s}^{-1}$, $G_{c2} = 7.26 \times 10^{-6} \text{ mol s}^{-1} \text{ cm}^{-2} \text{ V}^{-1}$, $K_s = 1.86 \times 10^{-3} \text{ cm s}^{-1}$, $G_s = -7.25 \times 10^{-7} \text{ mol s}^{-1}$, $m_{c1} = 19 \text{ g mol}^{-1}$, $m_{c2} = 7 \text{ g mol}^{-1}$, $m_s = 102 \text{ g mol}^{-1}$.

The presence of H_3O^+ along with the Li^+ species is related to the measurement conditions, which are not performed in a glove-box, leading to a certain amount of water in PC especially in the presence of LiClO_4 salt.

The presence of three different species (estimated by fitting the experimental data) was further confirmed by carefully analyzing the partial electrogravimetric transfer functions (Figures III-12C

and D). All these latter transfer functions exhibited good agreement between the experimental and theoretical curves as well, strengthening our hypothesis concerning the nature and the kinetics of the species.

The *ac*-electrogravimetry experiments are performed at different stationary potential values (in the electrochemical window of interest) and the identity of the species and the associated kinetic and thermodynamic parameters are estimated.

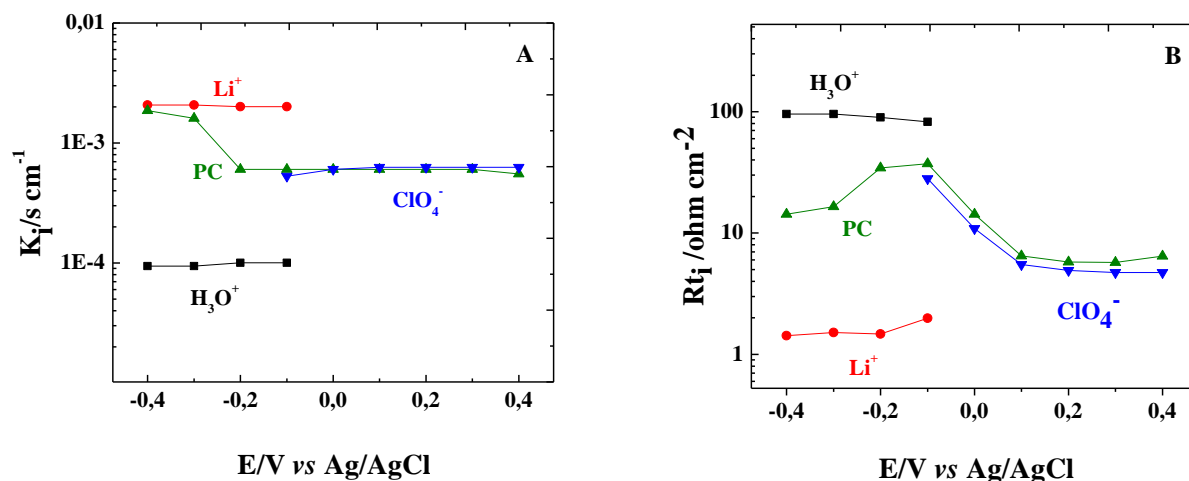


Figure III-13. The kinetic transfer rates K_i (A), and transfer resistances R_{ti} (B) parameters for all species estimated from the fitting of the *ac*-electrogravimetric data measured in 0.5M LiClO_4/PC .

For the more anodic potentials, we have detected the anionic species contribution which was not the case for the results at -0.4 V vs Ag/AgCl.

Figure III-13 shows the evolution of transfer kinetic rates, K_i , and the transfer resistance, R_{ti} , of the species as a function of the applied potential. Based on the K_i values presented in Figure III-13A, the Li^+ ion is the fastest of the four species present. Furthermore, the transfer rates of the free solvent in the Figure III-13A are somewhat close to the Li^+ ion and the ClO_4^- ion, probably due to the exclusion phenomenon. It is noted that the PC has persistently the opposite flux direction with the ionic species.

Considering the transfer resistance values of the ions, R_{ti} , the Li^+ is the easiest species to be transferred while the H_3O^+ is the most difficult to be transferred. This is in line with their kinetics and probably due to the lower concentration of the H_3O^+ compared to the Li^+ species in the electrolyte. Furthermore, the transfer resistance values of the free solvent are close to the ClO_4^- at anodic potentials. At cathodic potentials, the free solvent is first more difficult to be transferred compared to Li^+ but then approaches to the R_{ti} of the cations when the potential is even more cathodic (note the log scale) (Figure III-13B). This shows that both Li^+ and ClO_4^- transfers are coupled/influenced

to/by the free solvent motions at the electrode/electrolyte interface. The K_i and G_i parameters from the *ac*-electrogravimetry data at different potentials are used to calculate the $\left. \frac{\Delta C_i}{\Delta E} \right)_{\omega \rightarrow 0} = -\frac{G_i}{K_i}$ parameter. As explained previously, the integration of the $\left. \frac{\Delta C_i}{\Delta E} \right|_{\omega \rightarrow 0}$ against potential gives the relative concentration change, $(C_i - C_0)$ of each species over the applied potential (Figure III-14).

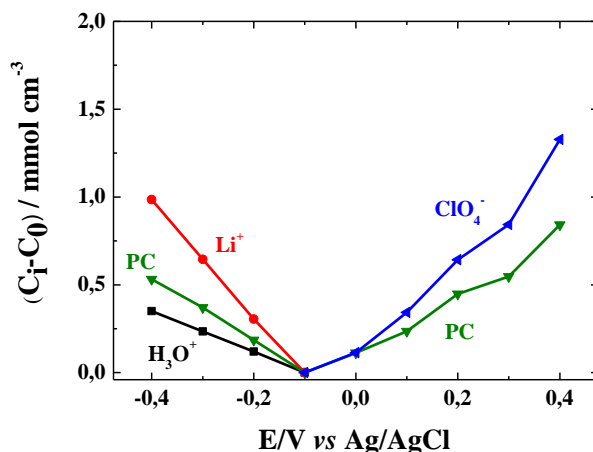


Figure III-14. Evolution of the relative concentration, $C_i - C_0$ of each species over the applied potential measured in 0.5M LiClO₄.

The $C_i - C_0$ values of the Li⁺ are more significant than that of the H₃O⁺ and free solvent at cathodic potentials. At anodic potentials, the $C_i - C_0$ values of the ClO₄⁻ is more significant than the $C_i - C_0$ values of the free solvent. Overall, the ClO₄⁻ is the most significant species in terms of relative concentration which is probably related to the pzc which has moved to more cathodic potentials compared to the aqueous media (different dielectric constants and ions present in the electrolyte). The *ac*-electrogravimetry results presented here showed the possibility to deconvolute the EQCM response into dynamic and gravimetric components even in organic electrolytes, and the viscosity of the media is low enough to allow the microbalance in our system to be functioned correctly.

III-5. Conclusions

SWCNT carbon-based electrodes were tested in aqueous and organic electrolytes. The results of pore morphology/structure and classic EQCM confirms that SWCNTs have interesting properties for energy storage applications.

From the traditional point of view, when the carbon electrode surface is negatively charged, one can expect the adsorption of the cationic species, and when the surface is positively charged, the adsorption of the anions should take place.

In this chapter, we have shown that this nominal or simplified presentation which assumes that one net charge stored on the electrode corresponds to one single ion adsorption does not take into account of several aspects.

Our *ac*-electrogravimetric study highlights the (i) the ion solvation effect, (ii) the possible presence of more than one ionic species which may favor/disfavor the kinetics of electroadsorption/desorption, and (iii) the influence of free electrolyte molecules that can interact, indirectly, with porous carbon/electrolyte interfaces.

Specifically, the chemical nature and the role of each species: anion, cation, solvated cation and free solvent, directly or indirectly involved in the charge storage, have been identified during the cathodic and anodic polarization by *ac*-electrogravimetric measurements. For example, in contact with an aqueous NaCl electrolyte, evidence was found that there are two types of cations ($\text{Na}^+ \cdot \text{H}_2\text{O}$ and H^+) electroadsorbed with different kinetics for cathodic potentials and the Cl^- ions for anodic potentials together with free water molecules. The reconstruction of the total mass response from independent *ac*-electrogravimetry measurements agrees perfectly well with the global EQCM response. Our findings reveal the unique sensitivity of the *ac*-electrogravimetry to provide a fair gravimetric and dynamic deconvolution of the global EQCM responses.

Chapter IV. Influence of the CNT Type, Structure and Electrolyte Properties on Ion Dynamics

CHAPTER IV

Influence of the CNT Type, Structure and Electrolyte Properties on Ion Dynamics

This chapter is dedicated to the study of the influence of the carbon nanotubes (CNT) types, structure and the electrolyte properties on ion dynamics and charge storage properties. For this kind of characterization, both structural and electrochemical methods such as SEM-FEG, HRTEM, XRD, N₂ sorption, EQCM and *ac*-electrogravimetry techniques were employed. The results of these different techniques are discussed to clarify the subtleties of charge storage behavior of different type of carbon nanotubes.

IV-1. Structure and Morphology of the DWCNT and MWCNT Powder and Thin Film Electrodes

Similar to the characterization methodology of SWCNTs in Chapter III, the morphology of the DWCNT and MWCNT based thin films deposited on the gold electrode of the quartz resonators were characterized by FEG-SEM. Prior to the thin film preparation, the DWCNT and MWCNT powders were characterized by HRTEM, XRD and N₂ sorption. CNT thin films were prepared directly on the gold electrode surface using the PVDF-HFP as a polymer binder according to the protocol given in the experimental part (See Chapter II Section 1.1).

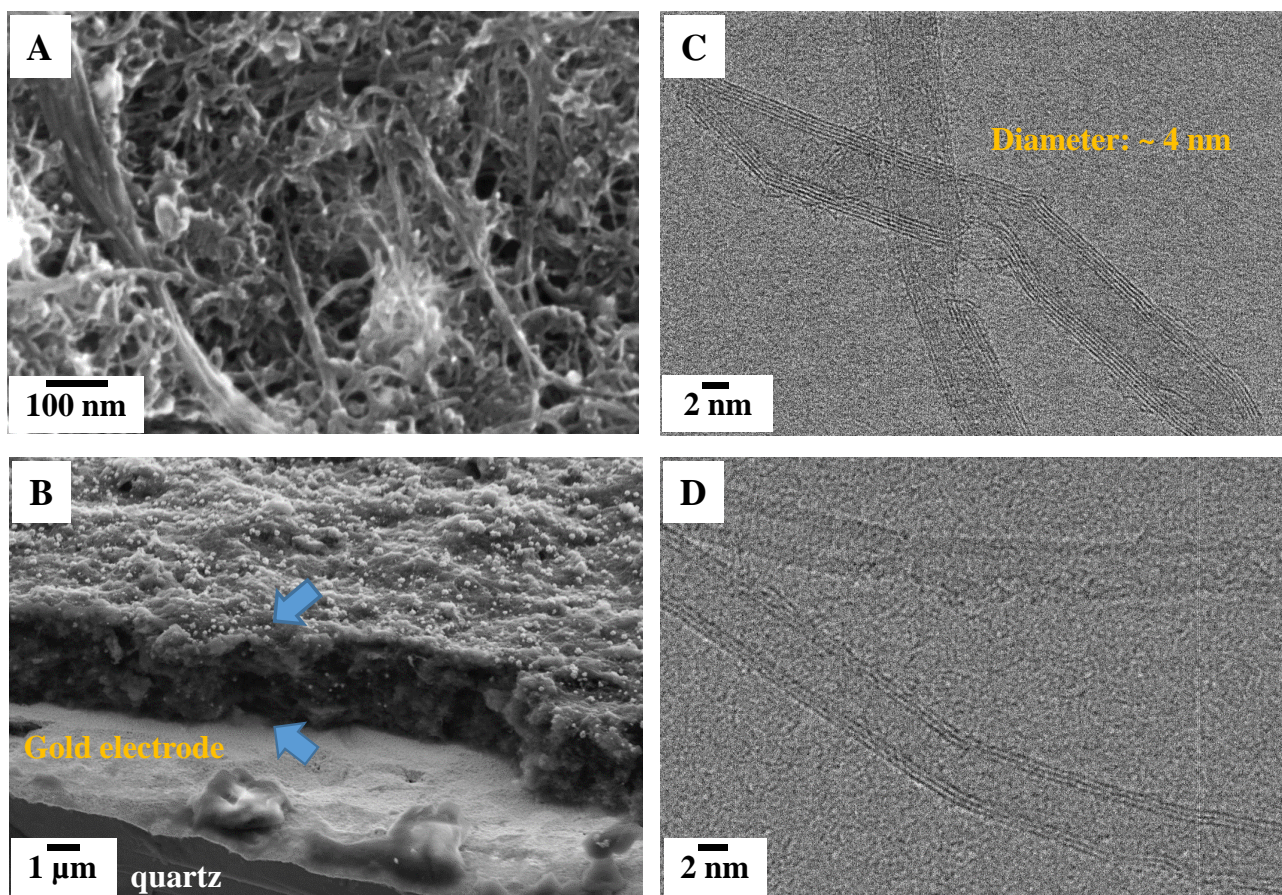


Figure IV-1. FEG-SEM of a DWCNT based thin film deposited on the gold electrode of a quartz resonator (A), cross section (B) and HRTEM images of the DWCNTs (C) and (D).

Figure IV-1A shows a representative FEG-SEM image of the DWCNT based thin film electrode surface, revealing the fact that CNT bundles are formed with an average thickness (or width) of 20 nm. The cross-section of the DWCNTs shown in Figure IV-1B permits the estimation of the film thickness. The film thickness deposited on the gold electrode of quartz resonators is limited to $\sim 1.5 \mu\text{m}$, to keep the gravimetric regime.

The inner diameter of the DWCNTs was estimated to be $\sim 4 \text{ nm}$ using the HRTEM technique (See Figure IV-1C). Our HRTEM images indicated that there is also a certain distribution of CNTs with more than two walls which is in line with the literature results. Indeed, DWCNTs are particular Multi-Wall CNTs (MWCNTs) since they have the smaller number of concentric walls. For this reason one can expect DWNTs to exhibit an intermediate behavior between SWNTs and MWNTs with number of walls higher than 2.^{113,115} Compared to the MWCNTs which will be introduced later in the chapter, the number of walls of CNTs presented in Fig. IV-1 is lower, and this sample is called DWCNT, thereafter.

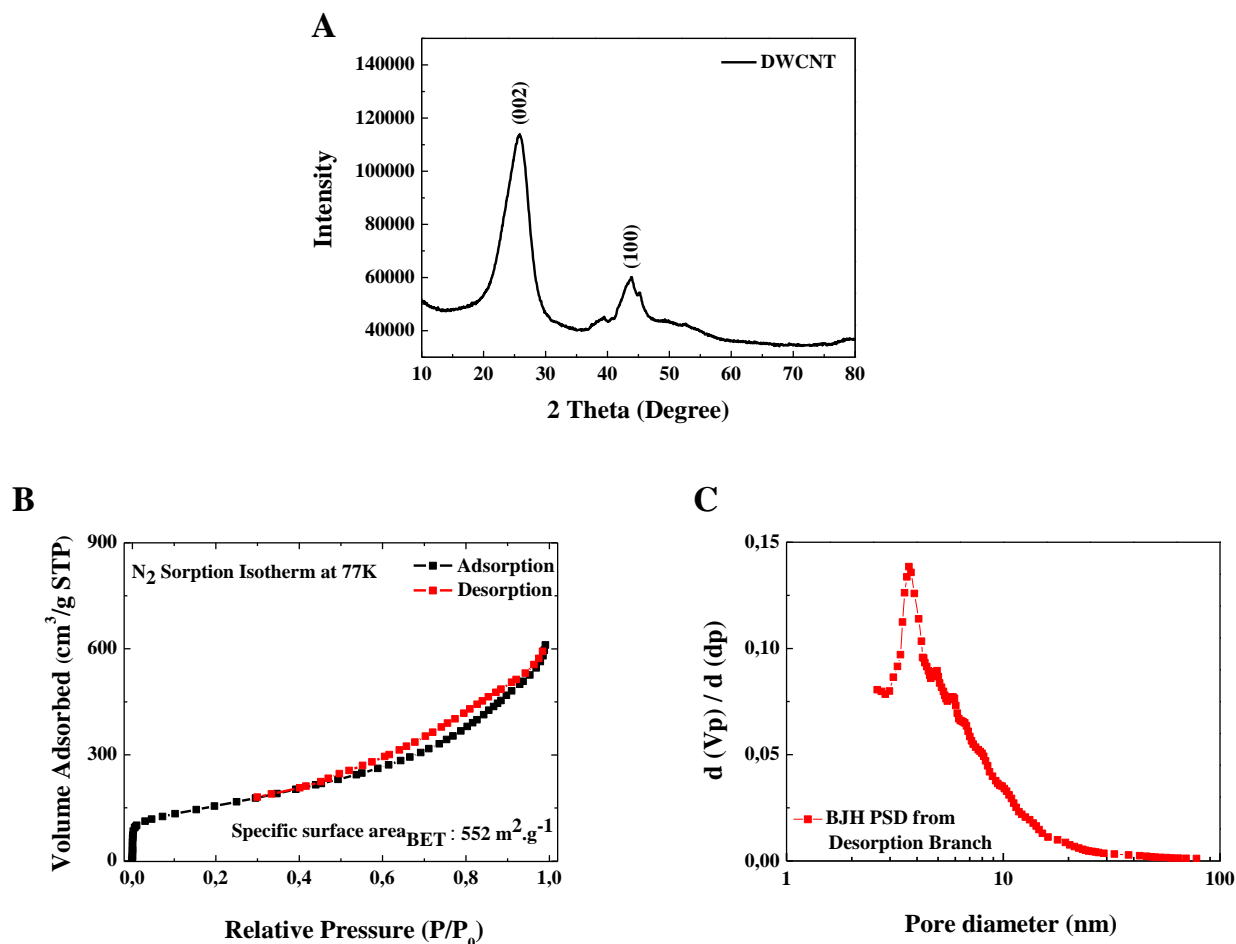


Figure IV-2. XRD spectra (A) of DWCNTs. Nitrogen sorption isotherm (B) and the pore size distribution (PSD) (C) of DWCNTs.

The crystalline structures of the DWCNT were evaluated by XRD (Figure IV-2A). The strongest diffraction peak related to the DWCNT structure at the angle (2θ) of $\sim 25^\circ$ and the peak at $2\theta \sim 42^\circ$ can be indexed as (002) and (100) reflections and are attributed to the hexagonal graphitic structure.²⁰⁶

The pore structure of the DWCNT was determined by nitrogen adsorption measurements. Figure IV-2B shows the nitrogen adsorption-desorption isotherms of the DWCNT. The shape of the isotherms can be considered as type-IV curves²⁰⁷ (characteristic for mesoporous adsorbents) with a slight hysteresis loop at high relative pressures (P/P_0) between 0.6-0.9. The Brunauer-Emmett-Teller (BET) method was applied for the specific surface area determination of the DWCNTs and was estimated to be $\sim 552 \text{ m}^2.\text{g}^{-1}$. Furthermore, the nitrogen sorption isotherm was used to estimate the pore size distribution (PSD) of the DWCNTs and shown in Fig. IV-2C. The PSD presents a main peak centered at $\sim 4 \text{ nm}$ which can be attributed to the inner diameter of the SWCNTs which is in agreement with the HRTEM images in Figure IV-1. However, the main peak in PSD presents a

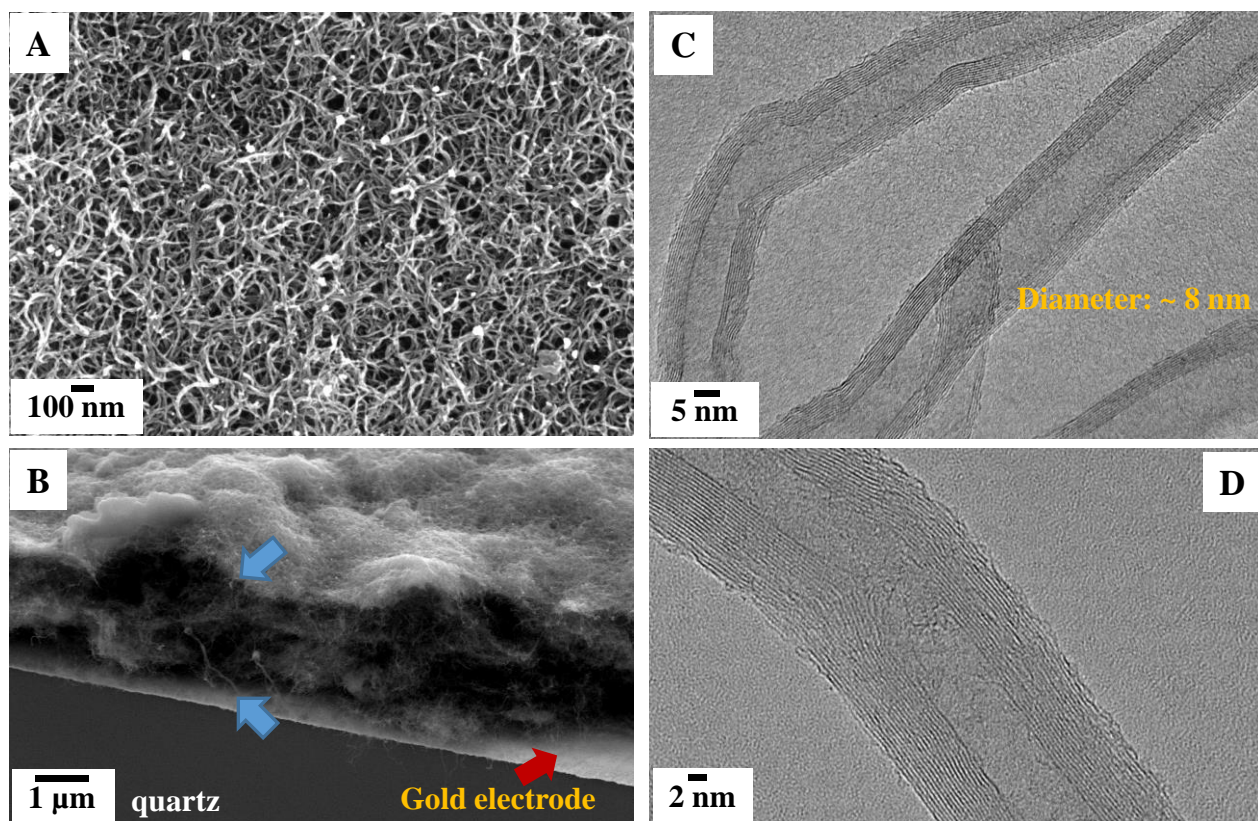


Figure IV-3. FEG-SEM of a MWCNT based thin film deposited on the gold electrode of a quartz resonator (A), cross section (B) and HRTEM images of the MWCNTs (C) and (D).

broad shoulder up to 15-20 nm, probably related to the voids between the nanotube bundles, as suggested by microscopy images.

Such structural and morphological characterizations were also performed for the MWCNTs. Figure IV-3A shows a representative FEG-SEM image of the MWCNT samples, revealing the fact that MWCNT bundles are slightly larger compared to SWCNT and DWCNTs, with a width of 30-40 nm (Figure IV-3A). The cross-section of the MWCNTs shown in Figure IV-3B permits the estimation of the film thickness. Similar to the DWCNTs, the film thickness deposited on the gold electrode of quartz resonators is limited to $\sim 1.5 \mu\text{m}$, to keep the gravimetric regime for further analysis with QCM based methods. The HRTEM in Figure IV-3C reveals a clear increase of the number of walls compared to DWCNTs and the multi wall structure of the CNTs. The inner diameter of the nanotubes varies and d_{average} is estimated as $\sim 8 \text{ nm}$ (Figure IV-3C and 3D).

The crystalline structures of the MWCNTs were evaluated by XRD (Figure IV-4A) and similar results to that of DWCNTs were obtained. The strongest diffraction peak related to the DWCNT structure at the angle (2θ) of $\sim 25^\circ$ and the peak at $2\theta \sim 42^\circ$ can be indexed as (002) and (100) reflections and are attributed to the hexagonal graphitic structure.²⁰⁶

The pore structure of the MWCNT was determined by nitrogen adsorption measurements. Figure IV-4B shows the nitrogen adsorption-desorption isotherms of the MWCNT. The increase in the diameter of the nanotubes is reflected as a decrease in the specific surface area which was estimated by BET approach as $300 \text{ m}^2 \text{ g}^{-1}$ (compared with DWCNT and SWCNT). The PSD of the MWCNTs (Figure IV-4C) is quite broad indicating the presence of several dimensions in the samples. The peak around 15-20 nm can be attributed to the outer diameter of the MWCNTs and the broad distribution centered at 40 nm can be attributed to the inter bundle voids of the MWCNTs, in agreement with the microscopy images in Figure IV-3C and 3D.

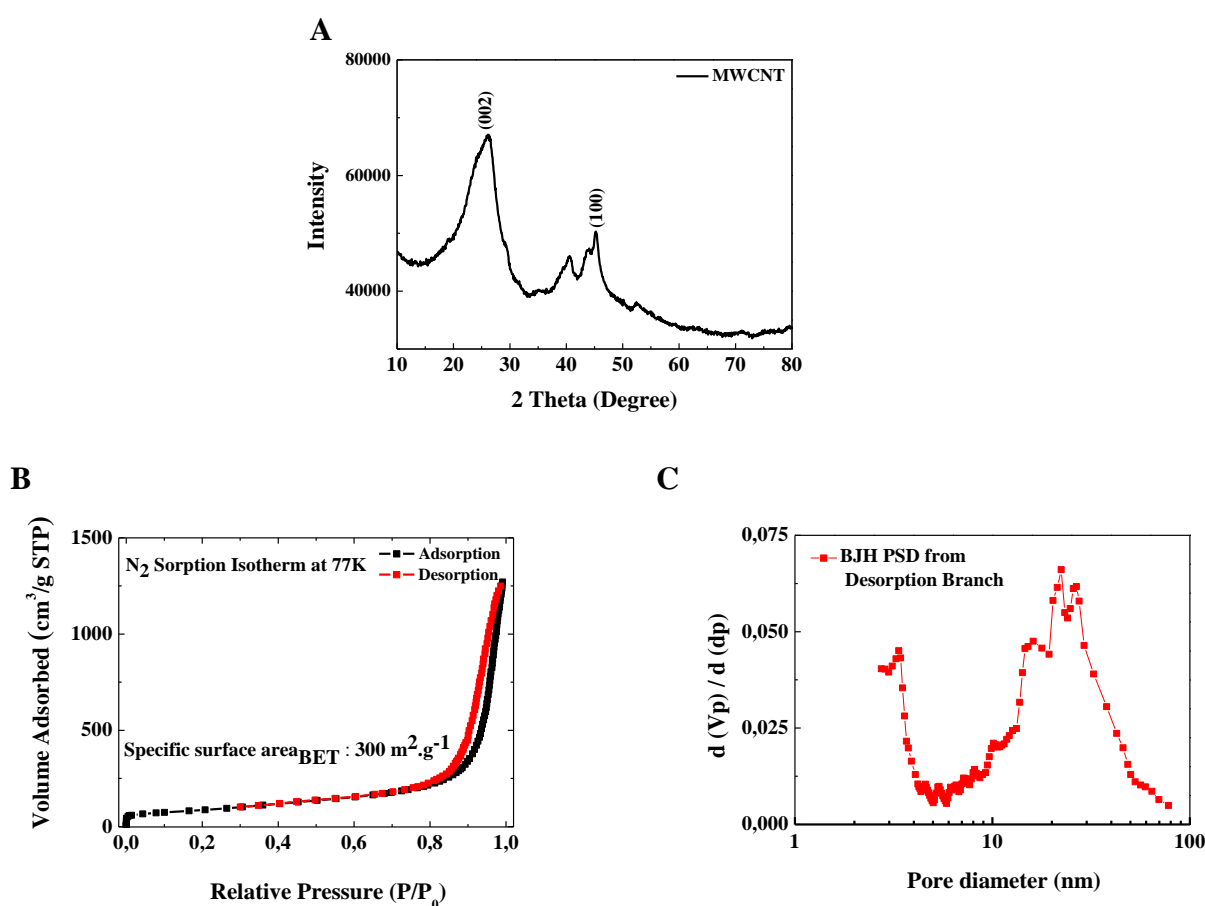


Figure IV-4. XRD spectra (A) of MWCNTs. Nitrogen sorption isotherm (B) and the pore size distribution (PSD) (C) of MWCNTs.

In the following part of this section, the CNT based thin films deposited on the quartz resonators are investigated by QCM based electrochemical methods. The main objective is to have a better understanding of the effect of structure, morphology and pore dimensions of the electrode as well as electrolyte properties on the charge storage mechanisms.

IV-2. Influence of the CNT Types**IV-2.1. EQCM Study of SWCNT, DWCNT and MWCNT in Aqueous NaCl Electrolyte**

Figure IV-5 shows the EQCM responses of CNT films obtained in aqueous electrolytes of 0.5M NaCl in a potential window of 0.45V to -0.45V *vs* Ag/AgCl. A growing capacitive current is observed when the scan rate increases (Figures IV-5 A, C and E). Furthermore, the capacitive current of the DWCNT is more significant than the capacitive current of the SWCNT and the MWCNT following the order: $i_{\text{DWCNT}} > i_{\text{SWCNT}} > i_{\text{MWCNT}}$. This difference in current is probably due to the pore structure of the materials and its accessibility to the electrolyte ions. In this study, the different CNT films show quasi-rectangular shaped responses indicating that the charge storage is mainly due to the reversible electroadsorption/electrodesorption of electrolyte ions. The slight distortion from a perfect rectangular shape is due to the presence of a slight faradaic contribution to the charge storage as already mentioned.

Concerning the mass changes, there is a difference between the responses of the SWCNTs, DWCNTs and MWCNTs following the same order as the current values, *i.e.*, $\Delta m_{\text{DWCNT}} > \Delta m_{\text{SWCNT}} > \Delta m_{\text{MWCNT}}$. Furthermore, the reversibility of the mass response is more evident in SWCNTs and DWCNTs than in MWCNTs (Figures IV-5 A, C and E) where a large hysteresis was observed. For the SWCNTs and DWCNTs, the mass change is more significant at cathodic potentials than at anodic potentials. In contrast, in MWCNTs, the mass change is slightly more significant at anodic potentials than at cathodic potentials (it is also noted that the pzc is shifted slightly towards more cathodic potentials (Figures IV-5 E). In other words, transfers of cationic species are more significant in DWCNTs and SWCNTs, while the transfers of anionic species are more important in MWCNTs in this potential range. This difference in behavior is probably related to the different adsorption sites of the species and different surface properties of the CNTs.

The Figures IV-5 B, D and F show the Fdm/dq values which can be considered equivalent to the molecular mass of the electroadsorbed species. The values are calculated as a function of the potential in NaCl electrolyte. The values vary in the range of 125 to -50 g.mol⁻¹, 50 to -35 g.mol⁻¹ and 180 to -70 g.mol⁻¹, for the SWCNT, DWCNT and MWCNT thin films, respectively.

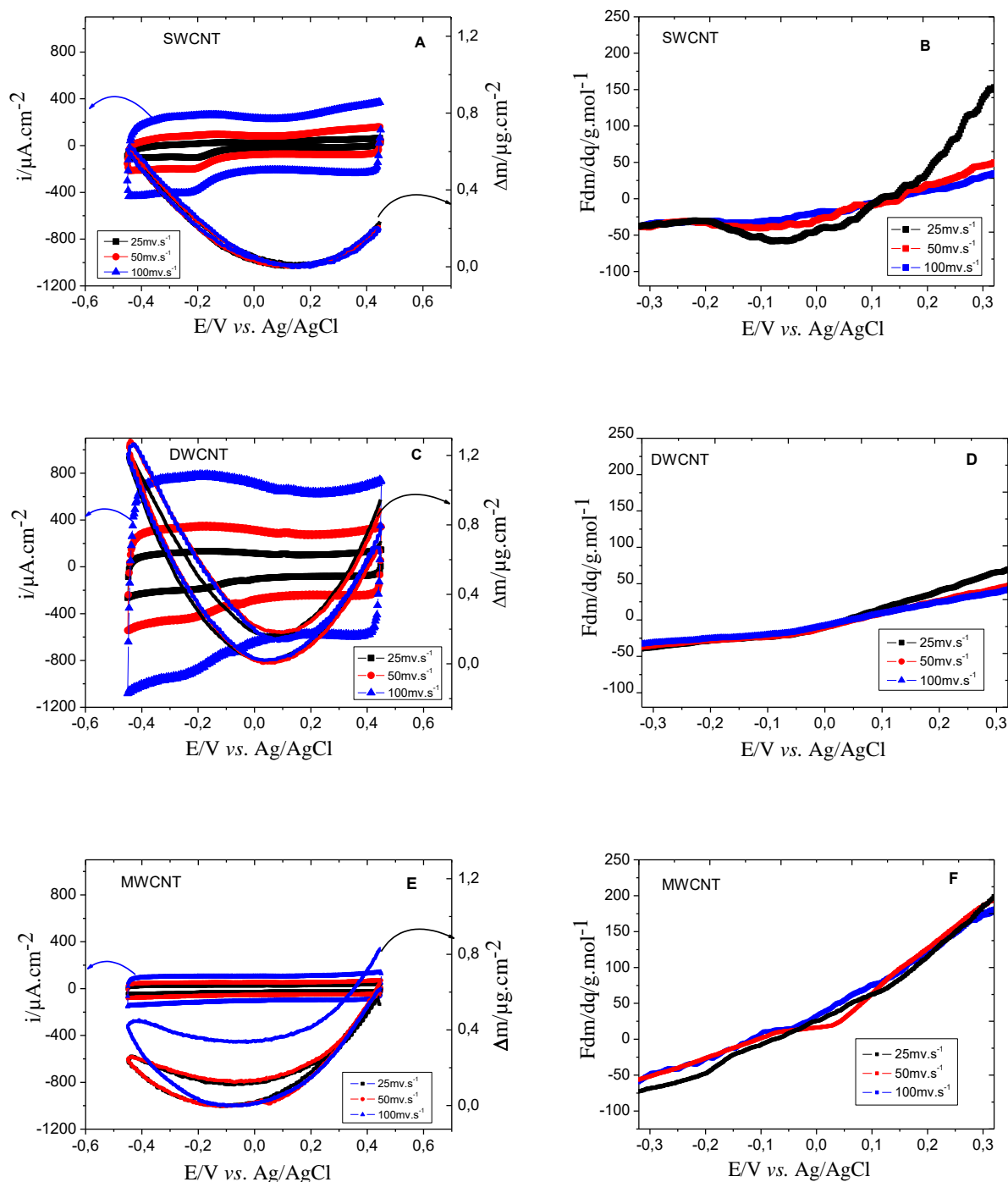


Figure IV-5. EQCM responses of SWCNT (A), DWCNT (C), and MWCNT (E) measured in 0.5 M NaCl aqueous electrolyte. The values corresponding to the average molecular weight, Fdm/dq , of the species involved in the charge compensation shown as a function of the potential and estimated for the three scan rates (obtained from the reduction branch of EQCM data presented in Figure IV 5 A, C and E).

From the three Figures IV-5B, D and F, it should be noted that for anodic potentials, positive Fdm/dq values are estimated which corresponds to anion contribution. As for cathodic potentials,

negative Fdm/dq values were calculated associated to cations. In all the cases, higher or lower atomic weight compared to Na^+ or Cl^- ions are found which indicates a complex ion transfer behavior. The observed higher values further indicate that the ions are hydrated and/or accompanied by free solvent molecules during their transfer. Particularly in MWCNTs, higher values at anodic potentials are observed which could correspond to anions accompanied by free solvent molecules.

The specific capacitance was calculated using the relation expressed in Chapter III Section 2.3. The measured capacitance values are around 25 F.g^{-1} , 26 F.g^{-1} , and 7 F.g^{-1} for the SWCNTs, DWCNTs and MWCNTs, respectively. These values are slightly lower especially for MWCNTs, but in the same order as the reported values in the literature.⁸⁵

IV-2.2. *Ac*-electrogravimetric Study of various CNT Thin Film Electrodes in Aqueous NaCl Electrolyte

Figures IV-6, IV-7 and IV-8 show an example of the experimental and theoretical transfer functions (TFs) obtained from *ac*-electrogravimetry of a SWCNT, DWCNT and MWCNT thin film in 0.5 M NaCl electrolyte at -0.4V vs Ag/AgCl . The measurements were performed each 100 mV in the range from 0.4V to -0.4V vs Ag/AgCl .

The experimental data were fitted according to the model presented in Chapter II. Figures IV-6-7-8 reveal a good agreement between experimental data and theoretical curves. First, the electrochemical impedance $\frac{\Delta E}{\Delta I}(\omega)$ responses (Figures IV-6A, V-7A and V-8A) present a distorted straight line at low frequencies, particularly in the SWCNTs, indicating that there is a multi-ion transfer contribution. The charge/potential transfer functions (TFs), $\frac{\Delta q}{\Delta E}(\omega)$, permit the separation of the ionic contributions, however, without any possibility to identify the ionic species involved. Figure IV-6B shows two loops with a small one at LF whereas in the case of DWCNTs and MWCNTs (Figures IV-7B and V-8B), only one big loop is observed. In these latter cases, it big loop can also be attributed to two species but with time constants not sufficiently different from each other. The global and partial mass /potential transfer functions are more informative to clarify these possibilities.

In the mass/potential transfer function, $\frac{\Delta m}{\Delta E}(\omega)$, one big loop appears in the third quadrant at high and medium frequencies (Figures IV-6C, IV-7C and IV-8C).

The loops in the third quadrant are characteristic for cation contributions or free solvent molecules following the same flux direction. The fitting of the experimental data by Mathcad

software, using Equations given in Chapter II Section 3.5, shows the presence of two charged species for the three films: $\text{Na}^+ \cdot n\text{H}_2\text{O}$ at higher frequencies and H^+ at lower frequencies. The loop at intermediate frequencies is attributed to the free solvent. Without this contribution it is impossible to fit correctly the experimental mass/potential TF.

The identification of these species was achieved by the determination of their molar mass using Equation II-50 in Chapter II and their respective kinetics of transfer were characterized by the K_i values. The presence of three different species estimated by simulating the experimental data was further confirmed by carefully analyzing the partial electrogravimetric transfer function, for example, by removing the cation 1, c1, contribution (Figures IV-6E, IV-7E and IV-8E) and calculating $\left. \frac{\Delta m}{\Delta E} \right|_{th}^{c2s}(\omega)$ or by removing the cation 2, c2, contribution (Figures IV-6D, IV-7D and IV-8D) and calculating $\left. \frac{\Delta m}{\Delta E} \right|_{th}^{c1s}(\omega)$ (Equations II-52 and 51). In Figures IV-6D and V-7D, a small contribution at low frequency is shown in the fourth quadrant.

Normally, this should match the response of an anion but in fact, this contribution is that of a cation whose atomic mass becomes negative due to the system of correction. This is evident from Equation II-51 that the response is multiplied by $m_{c1} - m_{c2}$. As c1 corresponds to H^+ and c2 corresponds to $\text{Na}^+ \cdot \text{H}_2\text{O}$, the value is negative. These partial electrogravimetric transfer functions provide a crosscheck for validating the hypothesis involving three different species and a better separation of the various contributions.

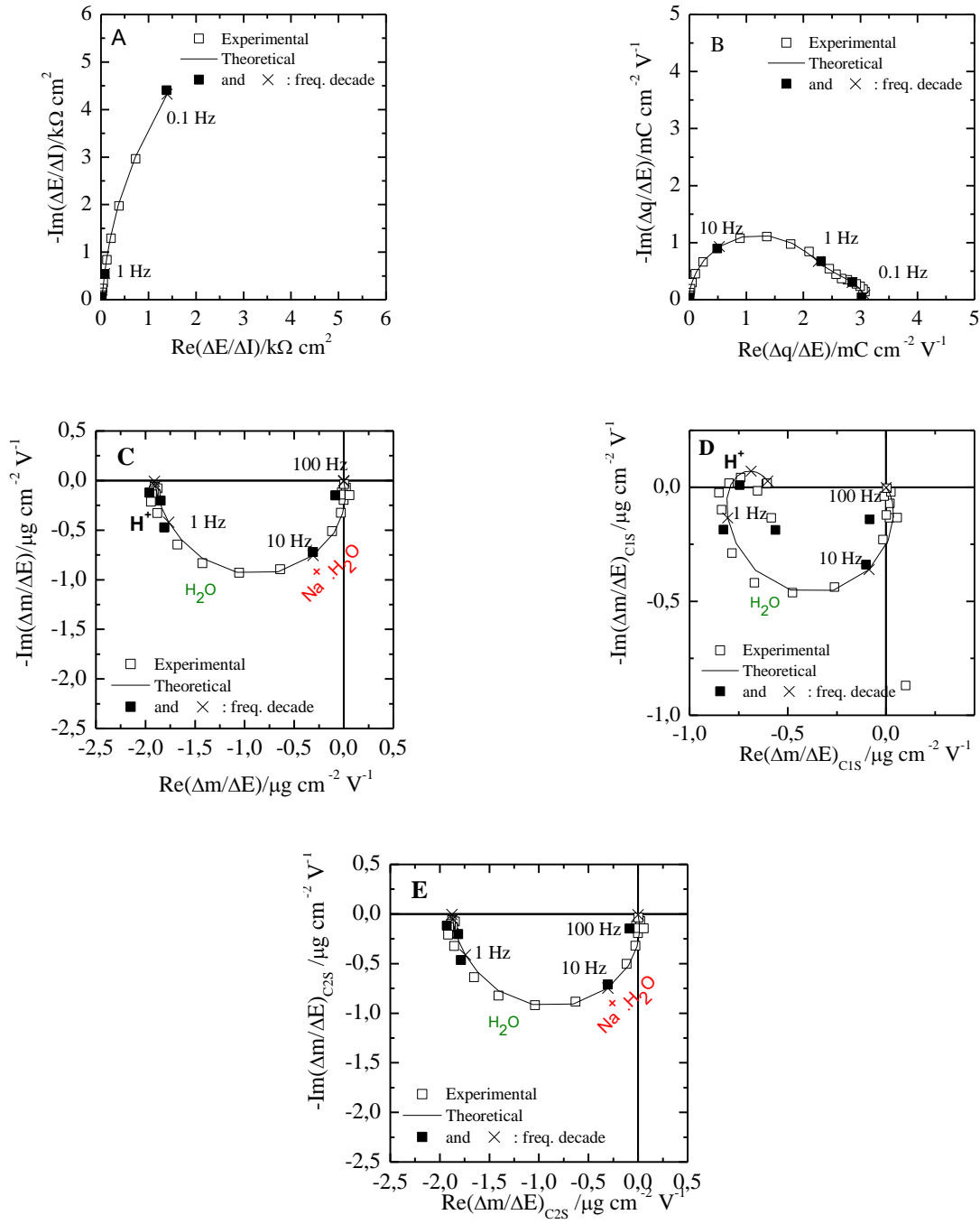


Figure IV-6. Experimental and theoretical *ac*-electrogravimetric data of the SWCNT thin film in

0.5 M NaCl measured at -0.4V vs Ag/AgCl. (A) $\frac{\Delta E}{\Delta I}(\omega)$, (B) $\frac{\Delta q}{\Delta E}(\omega)$, (C) $\frac{\Delta m}{\Delta E}(\omega)$, (D)

$\frac{\Delta m}{\Delta E}\bigg|^{c1s}(\omega)$, (E) $\frac{\Delta m}{\Delta E}\bigg|^{c2s}(\omega)$. Theoretical functions were calculated with the following parameters: $d_f = 0.4\mu\text{m}$, $K_{cl} = 5.04 \times 10^{-5} \text{ cm s}^{-1}$, $G_{cl} = 1.24 \times 10^{-8} \text{ mol.s}^{-1}.\text{cm}^{-2} \text{ V}^{-1}$, $K_{c2} = 6.91 \times 10^{-3} \text{ cm.s}^{-1}$, $G_{c2} = 4.01 \times 10^{-6} \text{ mol.s}^{-1} \text{ cm}^{-2}.\text{V}^{-1}$, $K_s = 3.14 \times 10^{-3} \text{ cm.s}^{-1}$, $G_s = 4.08 \times 10^{-6} \text{ mol.s}^{-1}$, $m_{cl} = 1 \text{ g.mol}^{-1}$, $m_{c2} = 23+18 \text{ g.mol}^{-1}$ and $m_s = 18 \text{ g.mol}^{-1}$.

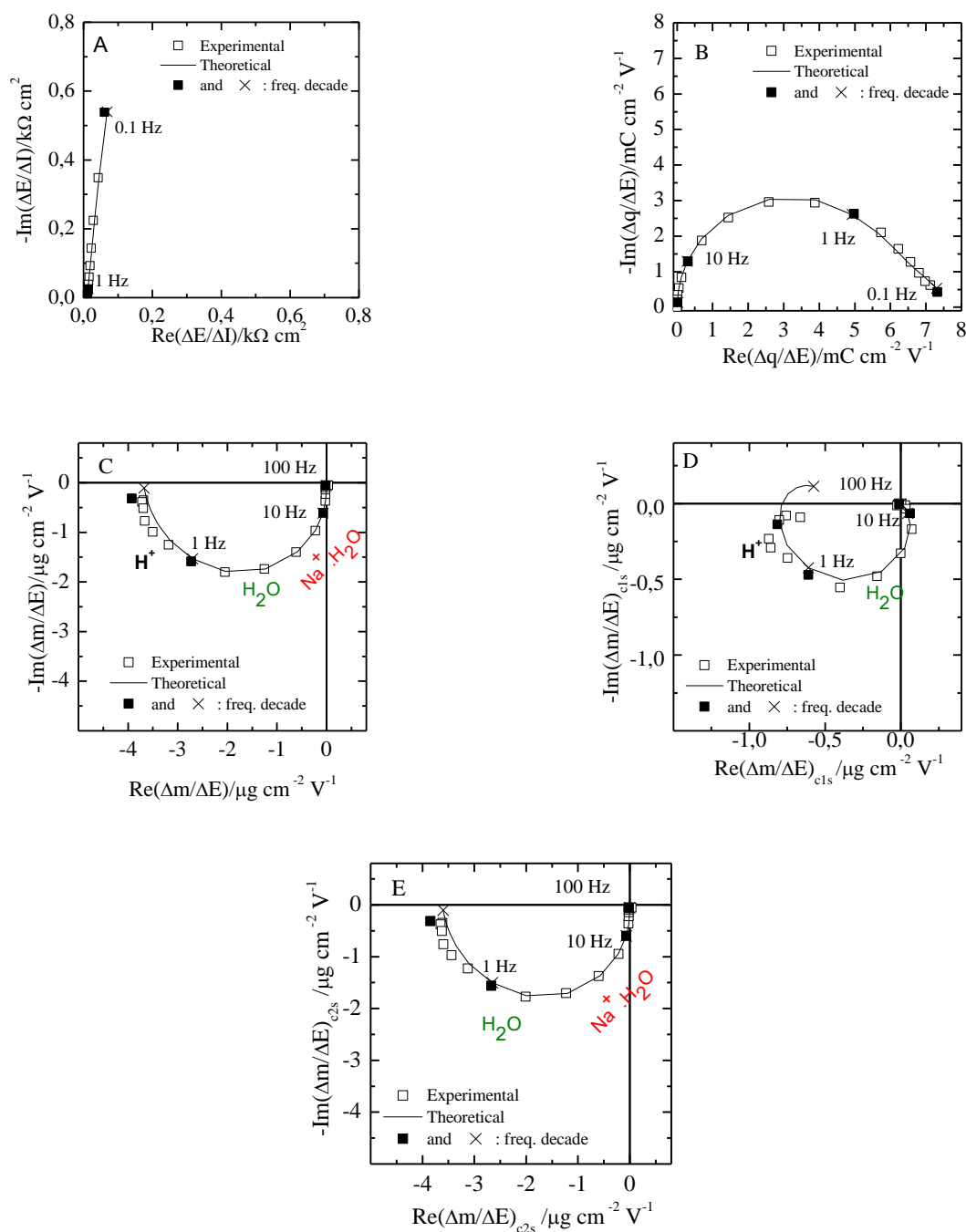


Figure IV-7. Experimental and theoretical *ac*-electrogravimetric data of the DWCNT thin film in

0.5 M NaCl measured at -0.4V vs Ag/AgCl. (A) $\frac{\Delta E}{\Delta I}(\omega)$, (B) $\frac{\Delta q}{\Delta E}(\omega)$, (C) $\frac{\Delta m}{\Delta E}(\omega)$, (D)

$\frac{\Delta m}{\Delta E}\bigg|^{c1s}(\omega)$, (E) $\frac{\Delta m}{\Delta E}\bigg|^{c2s}(\omega)$. Theoretical functions were calculated with the following parameters: $d_f = 0.4\mu\text{m}$, $K_{cl} = 3.64 \times 10^{-5} \text{ cm.s}^{-1}$, $G_{cl} = 1.39 \times 10^{-8} \text{ mol.s}^{-1}.\text{cm}^{-2}.\text{V}^{-1}$, $K_{c2} = 2.89 \times 10^{-3} \text{ cm.s}^{-1}$, $G_{c2} = 4.65 \times 10^{-6} \text{ mol.s}^{-1}.\text{cm}^{-2}.\text{V}^{-1}$, $K_s = 6.28 \times 10^{-4} \text{ cm.s}^{-1}$, $G_s = 9.11 \times 10^{-7} \text{ mol.s}^{-1}$, $m_{cl} = 1 \text{ g.mol}^{-1}$, $m_{c2} = 23+18 \text{ g.mol}^{-1}$ and $m_s = 18 \text{ g.mol}^{-1}$.

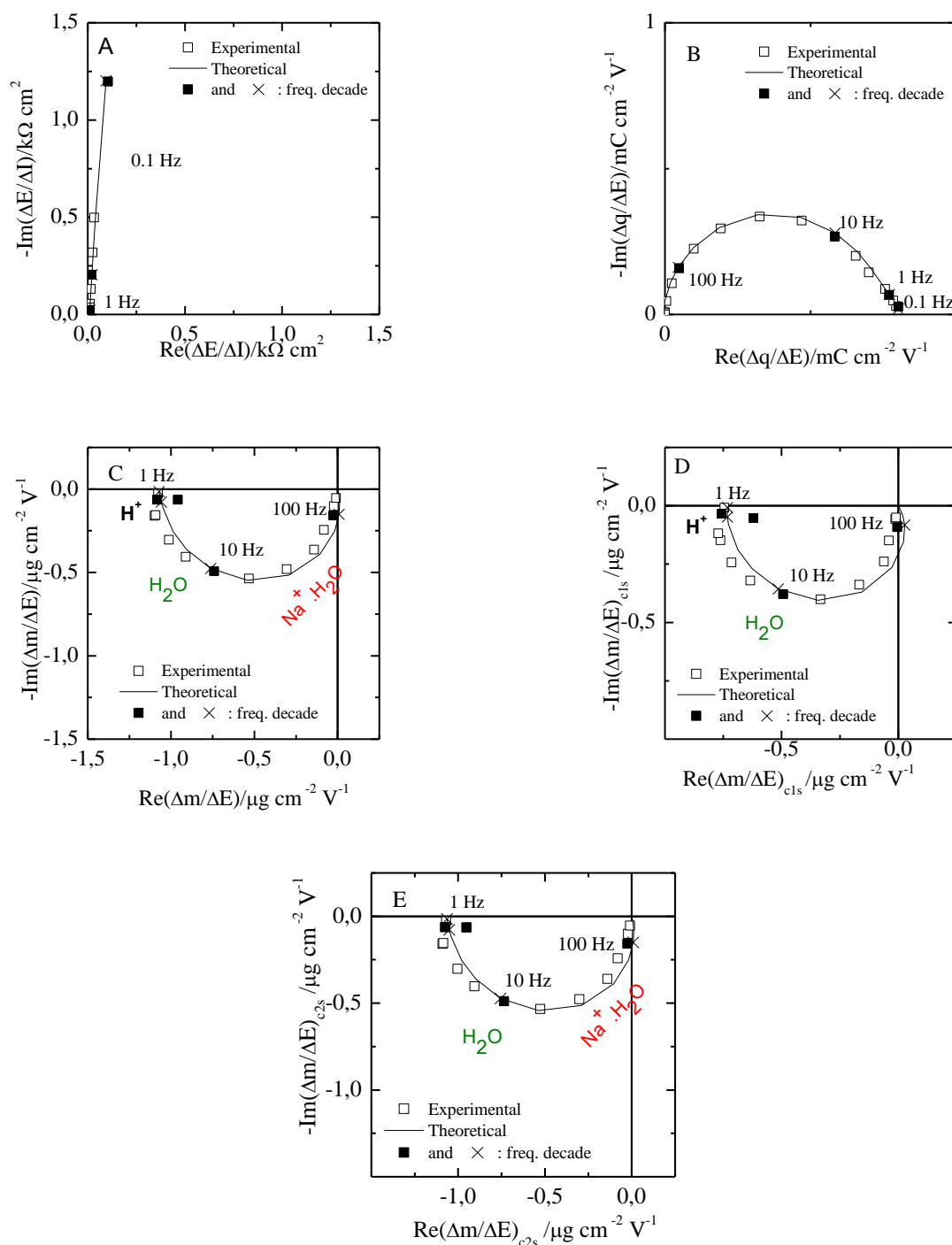


Figure IV-8. Experimental and theoretical *ac*-electrogravimetric data of the MWCNT thin film in

0.5 M NaCl measured at -0.4V vs Ag/AgCl. (A) $\frac{\Delta E}{\Delta I}(\omega)$, (B) $\frac{\Delta q}{\Delta E}(\omega)$, (C) $\frac{\Delta m}{\Delta E}(\omega)$, (D)

$\frac{\Delta m}{\Delta E}\bigg|^{c1s}(\omega)$, (E) $\frac{\Delta m}{\Delta E}\bigg|^{c2s}(\omega)$. Theoretical functions were calculated with the following parameters: d_f = 0.4 μm, K_{cl} = 2.39×10^{-4} cm.s⁻¹, G_{cl} = 3.58×10^{-9} mol.s⁻¹.cm⁻² V⁻¹, K_{c2} = 5.66×10^{-3} cm.s⁻¹, G_{c2} = 1.10×10^{-6} mol.s⁻¹.cm⁻².V⁻¹, K_s = 5.03×10^{-4} cm.s⁻¹, G_s = 5.23×10^{-6} mol.s⁻¹, m_{cl} = 1 g.mol⁻¹, m_{c2} = 23+18 g.mol⁻¹ and m_s = 18 g.mol⁻¹.

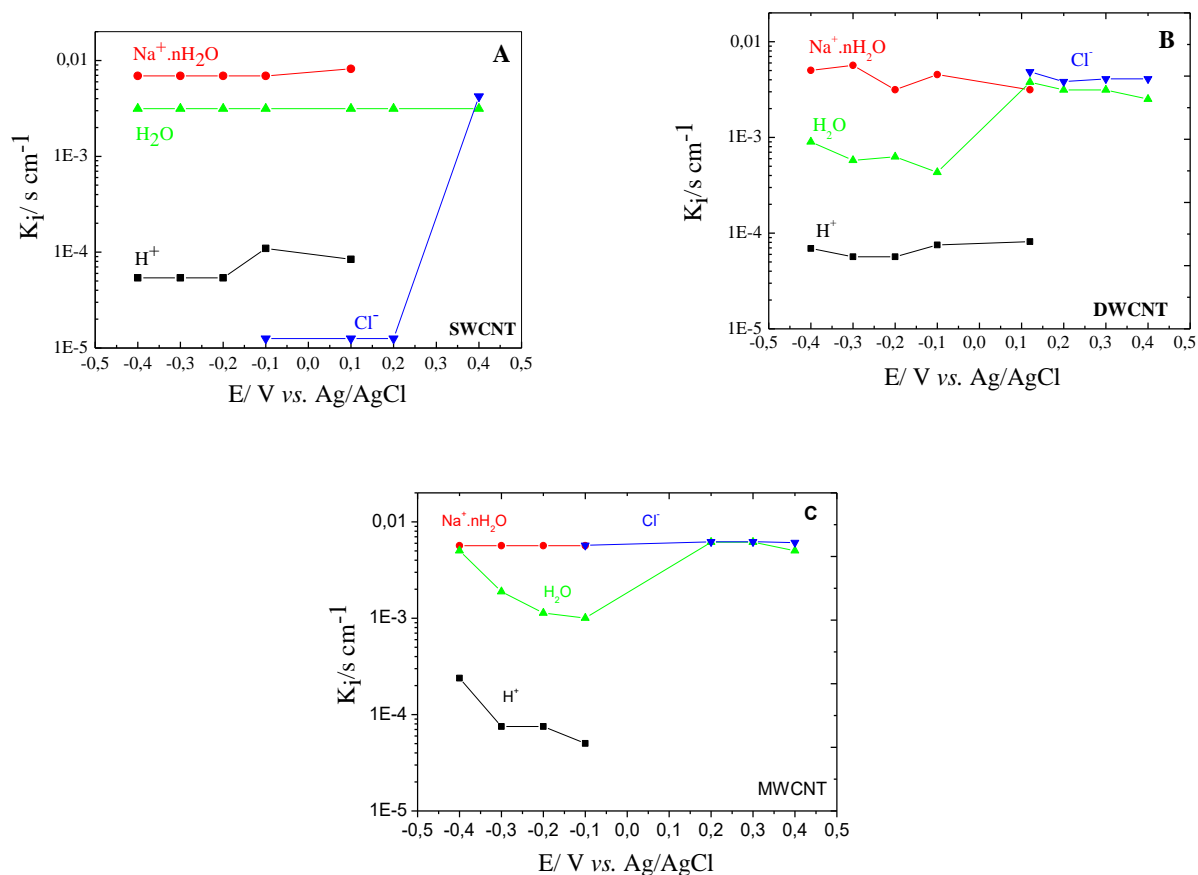


Figure IV-9. Constants of transfer kinetics, K_i , of SWCNT (A), DWCNT (B), MWCNT (C) estimated from the fitting of the *ac*-electrogravimetric data measured in aqueous 0.5M NaCl at pH7.

Figure IV-9 shows the evolution of the constant transfer kinetics, K_i , of the species as a function of the applied potential. Based on the K_i values presented in Figure IV-9, the $\text{Na}^+ \cdot n\text{H}_2\text{O}$ ion is the fastest of the three species in SWCNTs whereas (Fig. IV-9A), in DWCNTs and MWCNTs, the Cl^- ion is as fast as the $\text{Na}^+ \cdot n\text{H}_2\text{O}$ (Fig. IV-9 B and C). Furthermore, the transfer kinetics of free water molecules are somewhat close to the values of the $\text{Na}^+ \cdot n\text{H}_2\text{O}$ ion at cathodic potentials and to that of Cl^- ions at anodic potentials. Additionally, these water molecules have the same flux directions as the ions, suggesting that it might be the water molecules that accompany the transfer of $\text{Na}^+ \cdot n\text{H}_2\text{O}$ and Cl^- , most likely due to the an electrodragging phenomena. Finally, the H^+ ion is the slowest species at cathodic potentials for these three types of films (Figures IV-9A, B and C) showing K_i values in the same order of magnitude, this is in line with their substantially lower concentration in the media. If we compare the $\text{Na}^+ \cdot n\text{H}_2\text{O}$ dynamics if three different CNTs, hydrated sodium species are slightly faster to be transferred in SWCNTs compared to the other two types of CNTs.

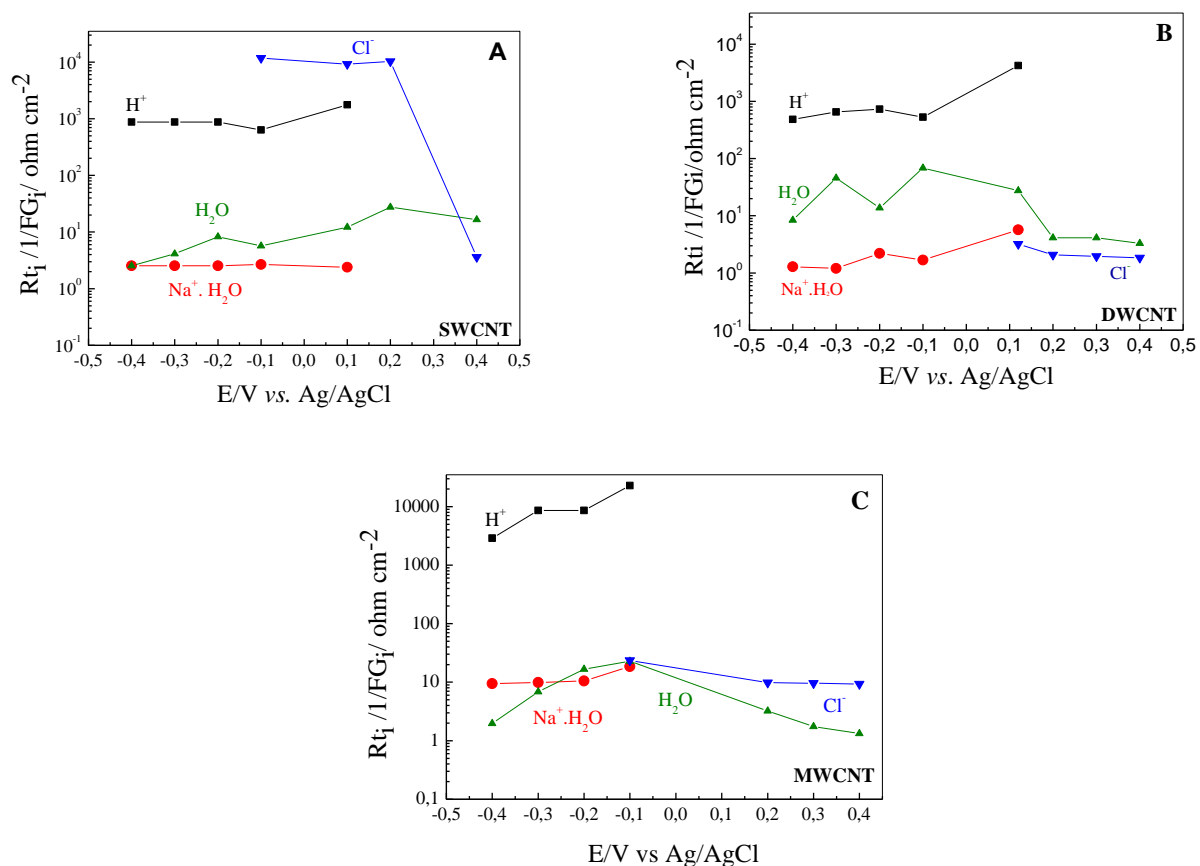


Figure IV-10. Transfer resistance, R_{ti} , of SWCNT (A), DWCNT (B), MWCNT (C) estimated from the fitting of the *ac*-electrogravimetric data measured in aqueous 0.5M NaCl at pH 7.

The transfer resistance, R_{ti} , values shown in Figure IV-10 reveal that the transfer of H^+ is more difficult than the transfer of the other species at cathodic potentials, which is correlated to the kinetic factors previously mentioned. The transfer of $Na^+.nH_2O$ and H^+ are more difficult in MWCNTs (Figure IV-10C) than in DWCNTs (Figure V-10B) and SWCNTs (Figure IV-10A) at cathodic potentials. The transfer of the Cl^- ion is more difficult in SWCNTs than in DWCNTs and MWCNTs at anodic potentials. Finally, the transfer resistance values of the free solvent are equivalent for these three types of films.

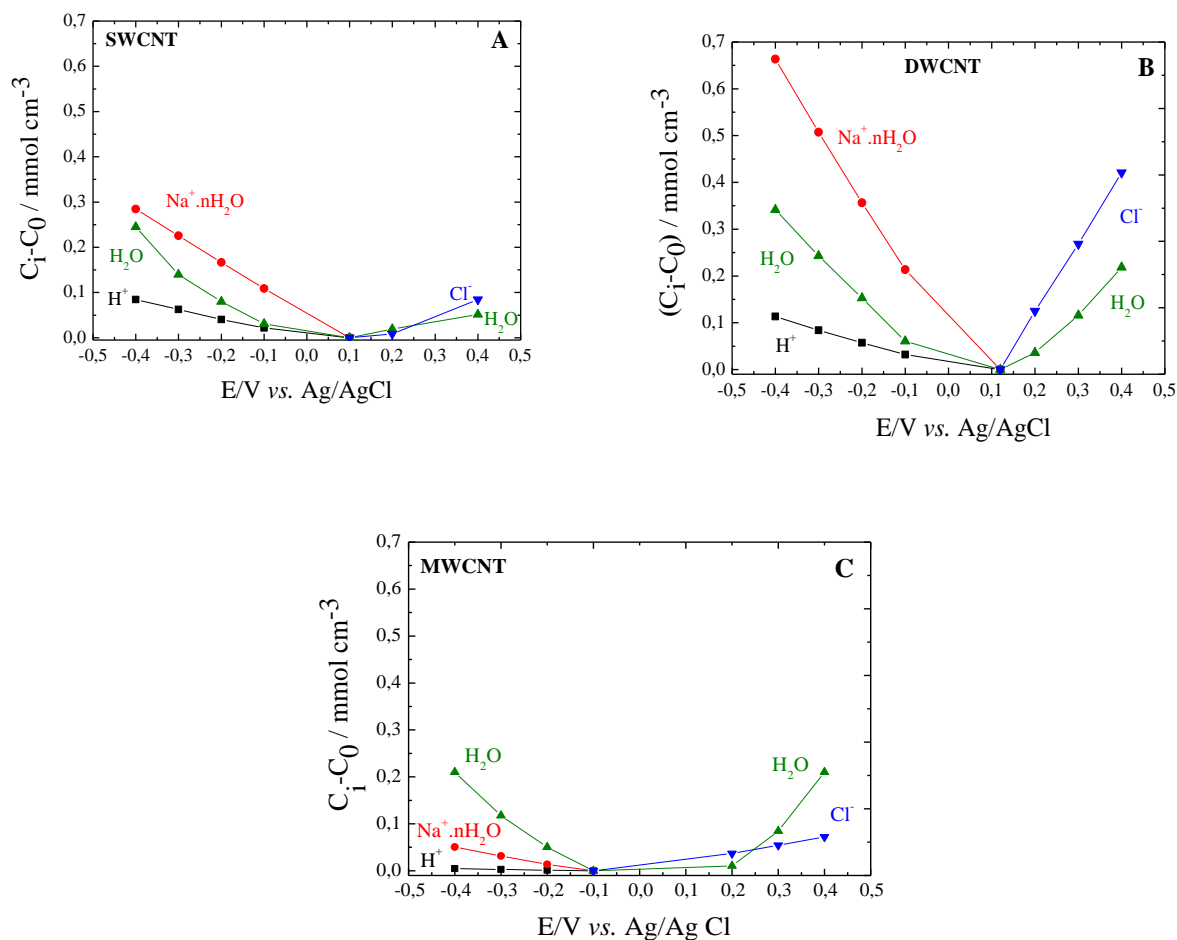


Figure IV-11. Evolution of the relative concentration, C_i-C_0 , for SWCNT (A), DWCNT (B), MWCNT (C) of the different species over the applied potential measured in aqueous 0.5M NaCl at pH 7.

In order to quantify the role of each species, $\left. \frac{\Delta C_i}{\Delta E} \right|_{\omega \rightarrow 0} = -\frac{G_i}{K_i}$ has been calculated as a function of the applied potential using the parameters estimated through *ac*-electrogravimetric fitting. The integration of $\left. \frac{\Delta C_i}{\Delta E} \right|_{\omega \rightarrow 0}$ against potential gives the relative concentration change, (C_i-C_0) of all the detected species as shown in Figure IV-11. The (C_i-C_0) values of the H_2O are significantly more important than the (C_i-C_0) values of the $Na^+.nH_2O$, Cl^- and H^+ for the MWCNTs (Figure IV-11C). Contrary to MWCNT, in SWCNTs and DWCNTs, the evolution of relative concentration of species presents a different trend. In comparison with the other species, the (C_i-C_0) values of the $Na^+.nH_2O$ are relatively more significant at cathodic potentials than the other species (Figures IV-11A and B). In conclusion, these results indicate that SWCNTs and DWCNTs appear to be the best

candidates for polarizable electrodes, since they can accommodate higher concentration of charged species compared to MWCNTs as shown in Figures IV-11A and B.

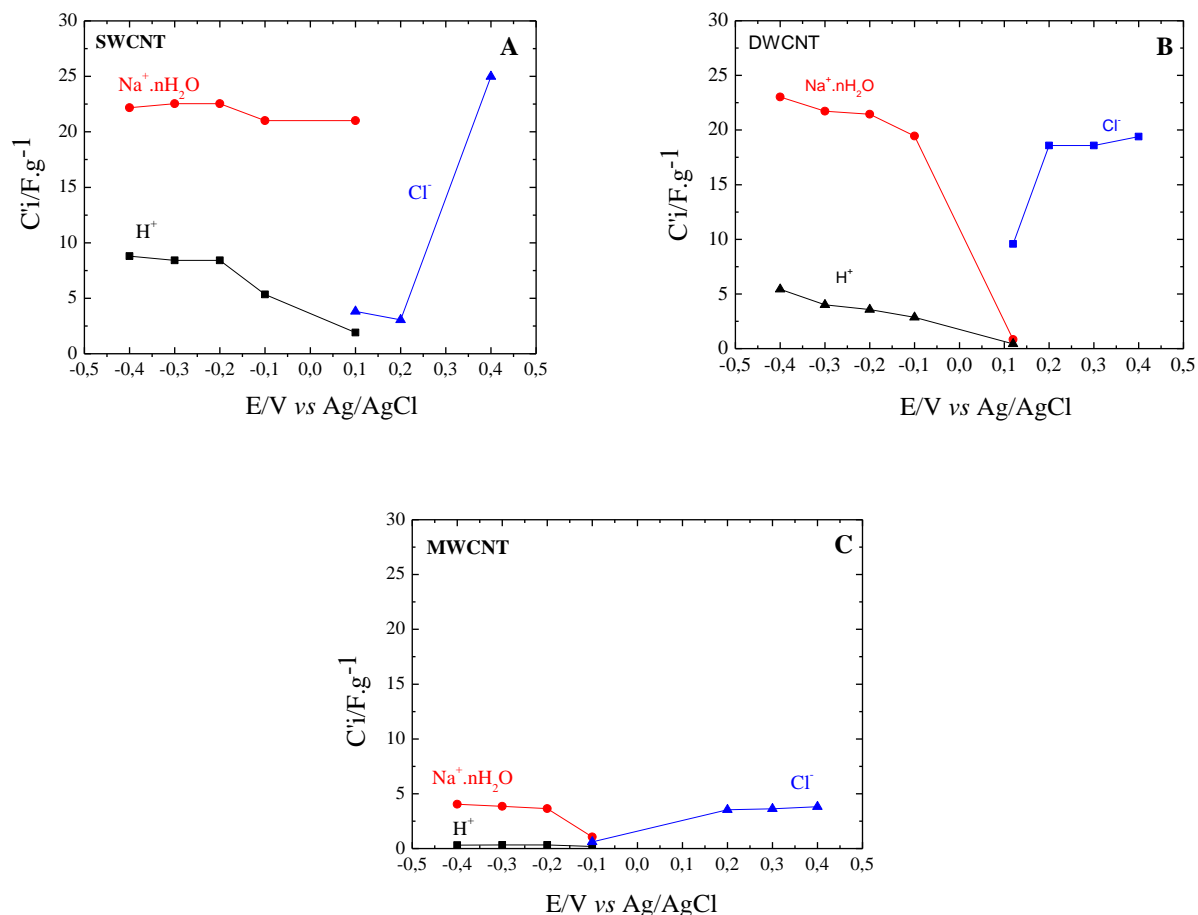


Figure IV-12. Instantaneous capacitance, C'_i , values of SWCNT (A), DWCNT (B) and MWCNT (C) thin films calculated from *ac*-electrogravimetric data.

Figure IV-12 shows the instantaneous capacitance values for each ion (C'_i) calculated as a function of the potential. These correspond to the capacitance attributed to each ions and the ability to take identified charges, which are the cations $\text{Na}^+.n\text{H}_2\text{O}$ and H^+ and the anion Cl^- , following a potential step. The instantaneous capacitance values for the SWCNT and DWCNT are equivalent for the two cations $\text{Na}^+.n\text{H}_2\text{O}$ and H^+ at cathodic potentials and for the anion Cl^- at anodic potentials (Figures IV-12A and B). Finally, the instantaneous capacitance values are lower in the MWCNT than in the SWCNT and DWCNT for all the species (Figure IV-12 C), which is coherent with the results of the relative concentration variations mentioned previously. This effect can be attributed to the lower specific surface determined in the case of the MWCNTs.

IV-3. Influence of the Electrolyte Properties**IV-3.1. EQCM Study of SWCNTs in Aqueous NaCl Electrolyte at different pH**

Figure IV-13 shows the EQCM results of SWCNT thin films obtained in aqueous electrolytes 0.5 M NaCl at pH 2, pH 7 and pH 10.

As mentioned previously, the CNT films show quasi-rectangular shaped responses and the slight distortions are pH-dependent. In the SWCNT film, the distortion is less evident at pH 2 than at pH 7 and pH 10 at cathodic potentials (Figures IV-13A, C and E).

Concerning the mass changes, anionic species are presented when the surface is positively charged (Figure IV-13A), whereas cationic species are presented when the surface is negatively charged (Figures IV-13C and E). Furthermore, the displacement of the PZC is pH-dependent.

Figure IV-13C, D and F show the variation of the Fdm/dq values, obtained from the reduction branch in the range 0.4V to -0.4V vs Ag/AgCl measured in 0.5M NaCl. The values vary in the range of 90 to -25 g.mol⁻¹, 140 to -50 g.mol⁻¹ and 70 to -40 g.mol⁻¹, for pH 2, pH 7 and pH 10, respectively. The observed higher values further indicate that the ions are hydrated and/or accompanied by free solvent molecules during their transfer. Nevertheless, the values obtained at pH 2 at cathodic potentials could correspond to Na⁺ or a low hydration level of Na⁺. The EQCM does not provide information on which of the possible scenarios that actually takes place such as hydrated or dehydrated species.

Therefore, an *ac*-electrogravimetric study is necessary in order to identify the ions that are involved in the electroadsorption/desorption mechanisms of the capacitive charge storage in SWCNT thin films.

The capacitance values were also calculated as a function of the applied potential for 0.5M NaCl at pH 2, pH 7 and pH 10. The measured capacitance values are around 25 to 35 F.g⁻¹ for all the pH values. Furthermore, the slight distortion from a perfect rectangular shape for pH 2, pH 7 and pH 10 was also observed and is due to the same phenomena (slight faradaic contribution) and is coherent with the EQCM results explained previously.

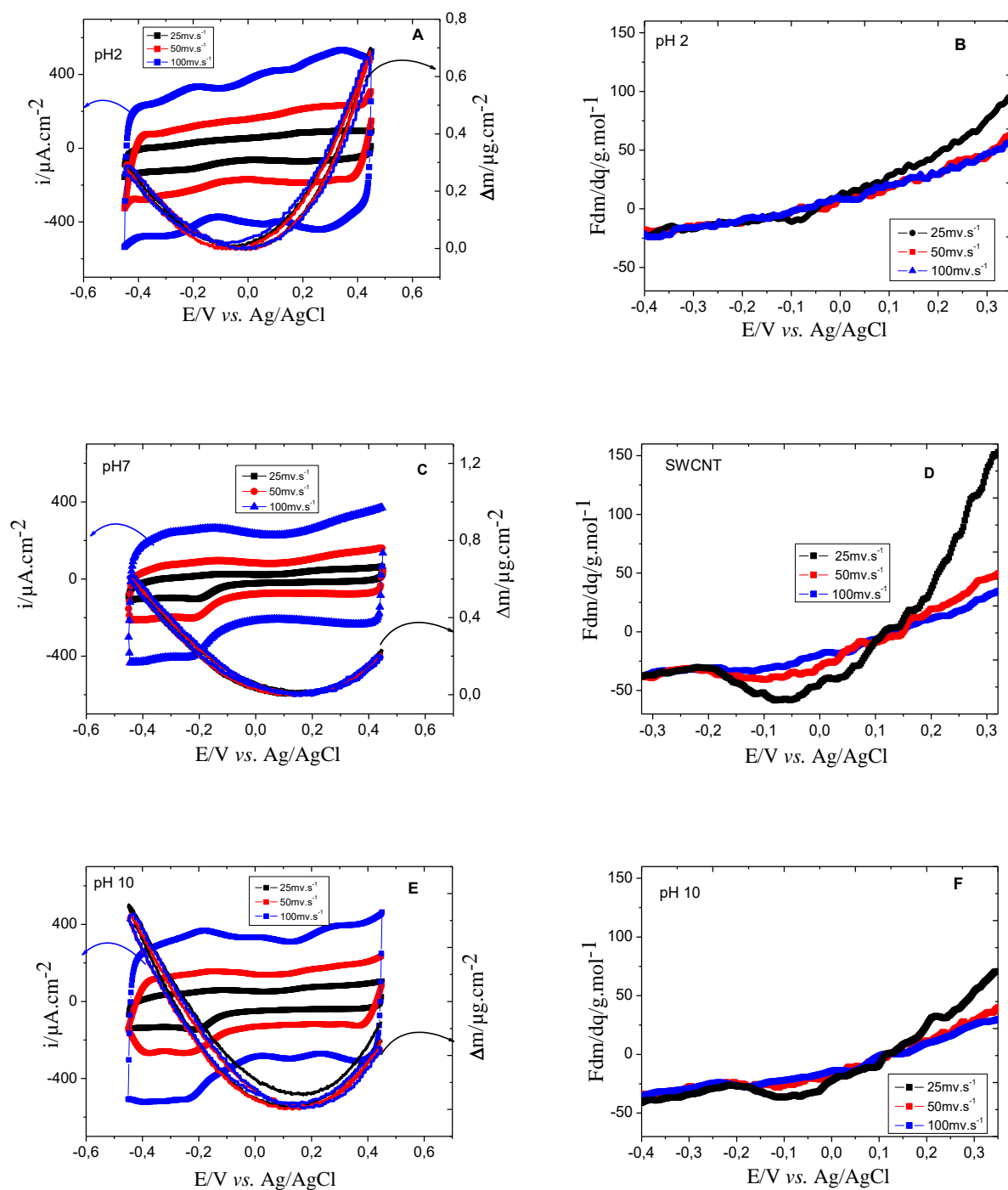


Figure IV-13. EQCM responses of SWCNT thin film measured in 0.5M NaCl at pH 2 (A) pH 7 (B) and pH 10 (C). The values corresponding to the average molecular weight of the species involved in the charge compensation shown as a function of the potential and estimated for the three pH values (obtained from the reduction branch of EQCM data presented in Figures IV 13 A, C and E).

IV-3.2. *Ac*-electrogravimetric Study of SWCNT Thin Film Electrode in Aqueous NaCl Electrolyte at different pH values.

In this part, a comparison and analysis of the *ac*-electrogravimetric responses of the SWCNT at pH 2, pH 7 and pH 10 will be presented (Figures IV-14, IV-6 and IV-15, respectively). First, the electrochemical impedance, $\frac{\Delta E}{\Delta I}(\omega)$, responses present a distorted straight line indicating that there is a multi-ion transfer contribution for the three pH values. Particularly at pH 2, the distortion is very important, which is probably due to the reduction of H^+ amplified by the high proton concentration in this case.

The charge/potential transfer functions (TFs), $\frac{\Delta q}{\Delta E}(\omega)$, show one main loop (Figures IV-14B, V-6B and V-15B), which can be attributed to one ionic species. At pH 7 and 10, a small loop appears at low frequencies. The size of the bigger loop is equivalent for all the pH values. Since the low frequency part of the $\frac{\Delta q}{\Delta E}(\omega)$ function is pH dependent, it may imply that these part of the response is related to the protons.

In the mass/potential transfer function, $\frac{\Delta m}{\Delta E}(\omega)$, one big loop appears in the third quadrant at high and medium frequencies (Figures IV-14C, IV-6C and IV-15C). This loop is bigger at pH 7 compared to pH 10 and pH 2. This variation in size is related to differences in the time constants (K_i , G_i) of the species transferred and also depends on the mass of the species involved. The loop in the third quadrant is characteristic of cation and free solvent molecules in the same flux directions. Here, it represents $Na^+ \cdot H_2O$ (c2) and H^+ (c1) for cations and free solvent (s) molecules in the same flux direction for all the pH values.

Partial transfer electrogravimetric transfer functions were also calculated and fitted for the three pH values in order to crosscheck the different hypothesis considered previously about the ions and solvent species involved. First, c2 contribution was removed from the global $\frac{\Delta m}{\Delta E}(\omega)$ TF and $\left. \frac{\Delta m}{\Delta E} \right|^{c1s}(\omega)$ was calculated and fitted as shown in Figures IV-14D, III-6D and IV-15D. At pH 7 and 10, the responses are quite similar with a big loop in the third quadrant at medium frequency (MF) corresponding to the free water and a small one at LF in the fourth quadrant. In this latter case, as explained previously, an anion like response is seen and it is due to the correction procedure where a $m_{c1}-m_{c2}$ is attributed to the proton response.

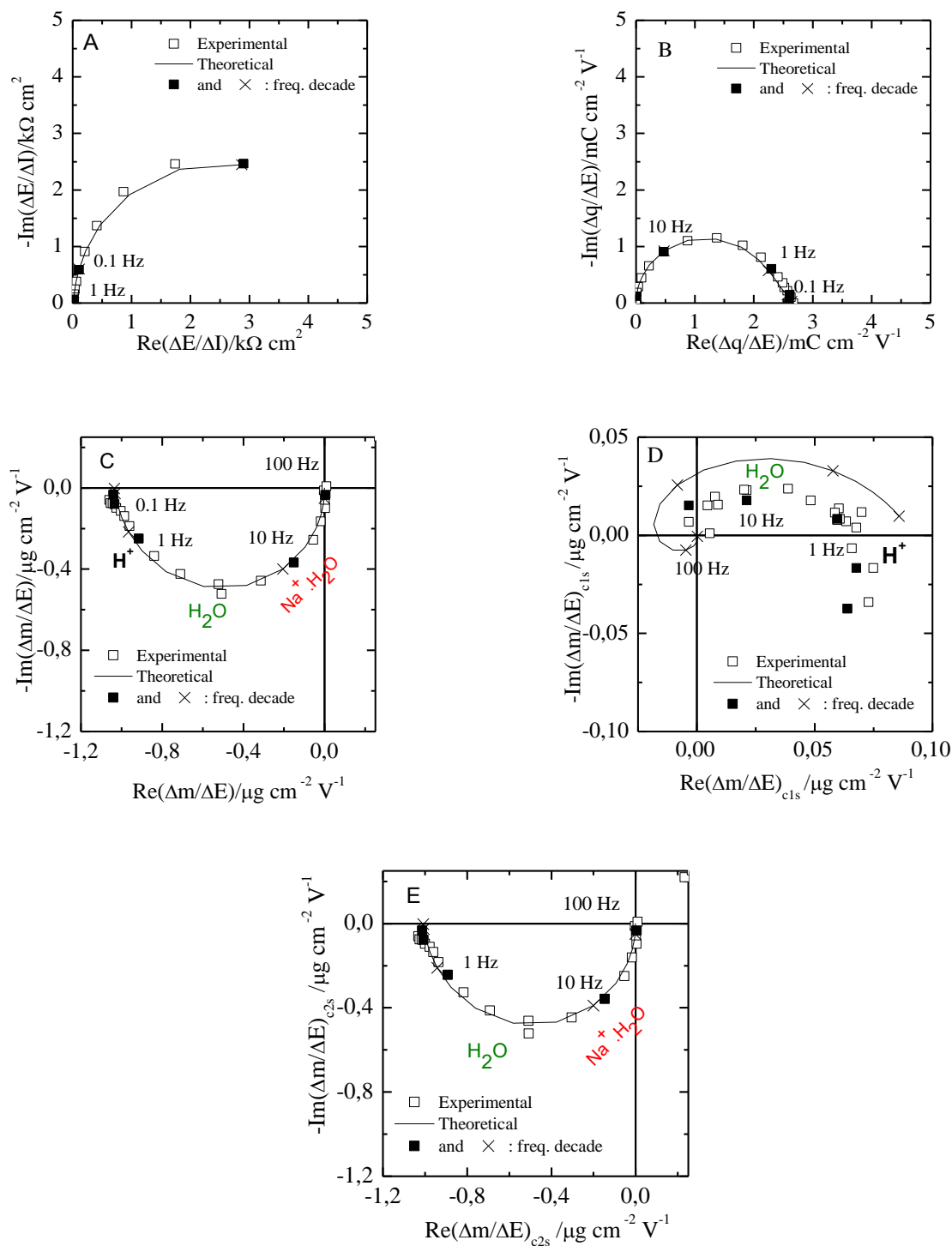


Figure IV-14. Experimental and theoretical *ac*-electrogravimetric data of the SWCNT thin film in 0.5 M NaCl measured at -0.4V vs Ag/AgCl pH 2. (A) $\frac{\Delta E}{\Delta I}(\omega)$, (B) $\frac{\Delta q}{\Delta E}(\omega)$, (C) $\frac{\Delta m}{\Delta E}(\omega)$,

(D) $\left. \frac{\Delta m}{\Delta E} \right|^{c1s}(\omega)$, (E) $\left. \frac{\Delta m}{\Delta E} \right|^{c2s}(\omega)$. Theoretical functions were calculated with the following

parameters: $d_f = 0.4 \mu\text{m}$, $K_{cl} = 6.16 \times 10^{-5} \text{ cm.s}^{-1}$, $G_{cl} = 4.93 \times 10^{-9} \text{ mol.s}^{-1}.\text{cm}^{-2} \text{ V}^{-1}$, $K_{c2} = 5.66 \times 10^{-3} \text{ cm.s}^{-1}$, $G_{c2} = 3.45 \times 10^{-6} \text{ mol.s}^{-1}.\text{cm}^{-2}.\text{V}^{-1}$, $K_s = 1.26 \times 10^{-3} \text{ cm.s}^{-1}$, $G_s = 6.28 \times 10^{-8} \text{ mol.s}^{-1}$, $m_{cl} = 1 \text{ g.mol}^{-1}$, $m_{c2} = 23+18 \text{ g.mol}^{-1}$ and $m_s = 18 \text{ g mol}^{-1}$.

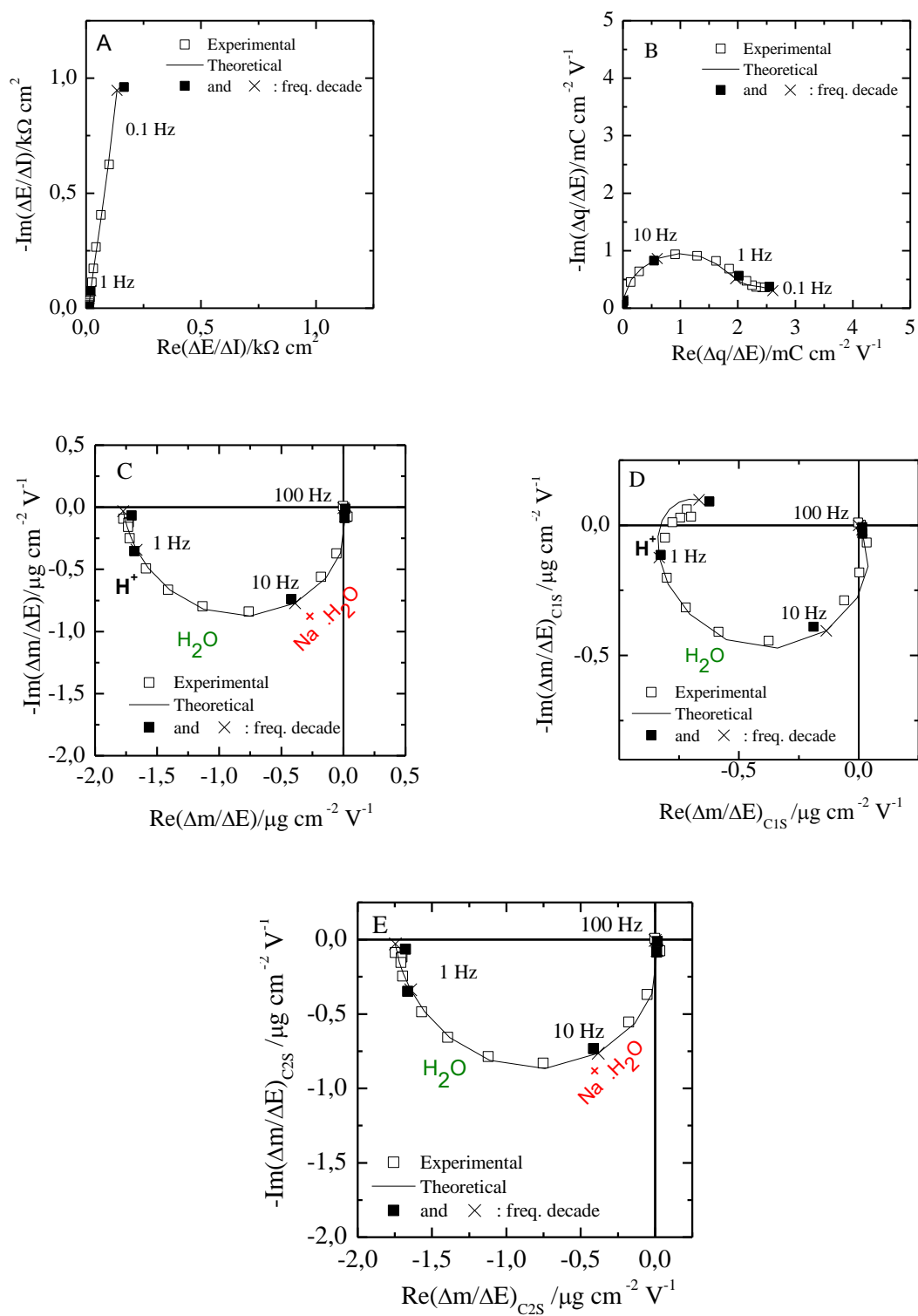


Figure IV-15. Experimental and theoretical *ac*-electrogravimetric data of the SWCNT thin film in 0.5 M NaCl measured at -0.4V vs Ag/AgCl pH 10. (A) $\frac{\Delta E}{\Delta I}(\omega)$, (B) $\frac{\Delta q}{\Delta E}(\omega)$, (C) $\frac{\Delta m}{\Delta E}(\omega)$,

(D) $\left. \frac{\Delta m}{\Delta E} \right|^{c1s}(\omega)$, (E) $\left. \frac{\Delta m}{\Delta E} \right|^{c2s}(\omega)$. Theoretical functions were calculated with the following

parameters: $d_f = 0.4 \mu\text{m}$, $K_{cl} = 1.63 \times 10^{-5} \text{ cm.s}^{-1}$, $G_{cl} = 1.96 \times 10^{-9} \text{ mol.s}^{-1}.\text{cm}^{-2} \text{ V}^{-1}$, $K_{c2} = 6.91 \times 10^{-3} \text{ cm.s}^{-1}$, $G_{c2} = 4.22 \times 10^{-6} \text{ mol.s}^{-1}.\text{cm}^{-2}.\text{V}^{-1}$, $K_s = 3.14 \times 10^{-3} \text{ cm.s}^{-1}$, $G_s = 4.71 \times 10^{-6} \text{ mol.s}^{-1}$, $m_{cl} = 1 \text{ g.mol}^{-1}$, $m_{c2} = 23+18 \text{ g.mol}^{-1}$ and $m_s = 18 \text{ g.mol}^{-1}$.

As m_{c2} is higher than m_{c1} , a negative value is thus found and leads to this atypical response. At pH 2, the water contribution decreases drastically as shown in Figure IV-14D. When the other partial electrogravimetric TF, $\left. \frac{\Delta m}{\Delta E} \right|^{c2s}(\omega)$, is calculated only the c1 and water contributions are seen as given in Figures IV-14E, III-6E and IV-15E.

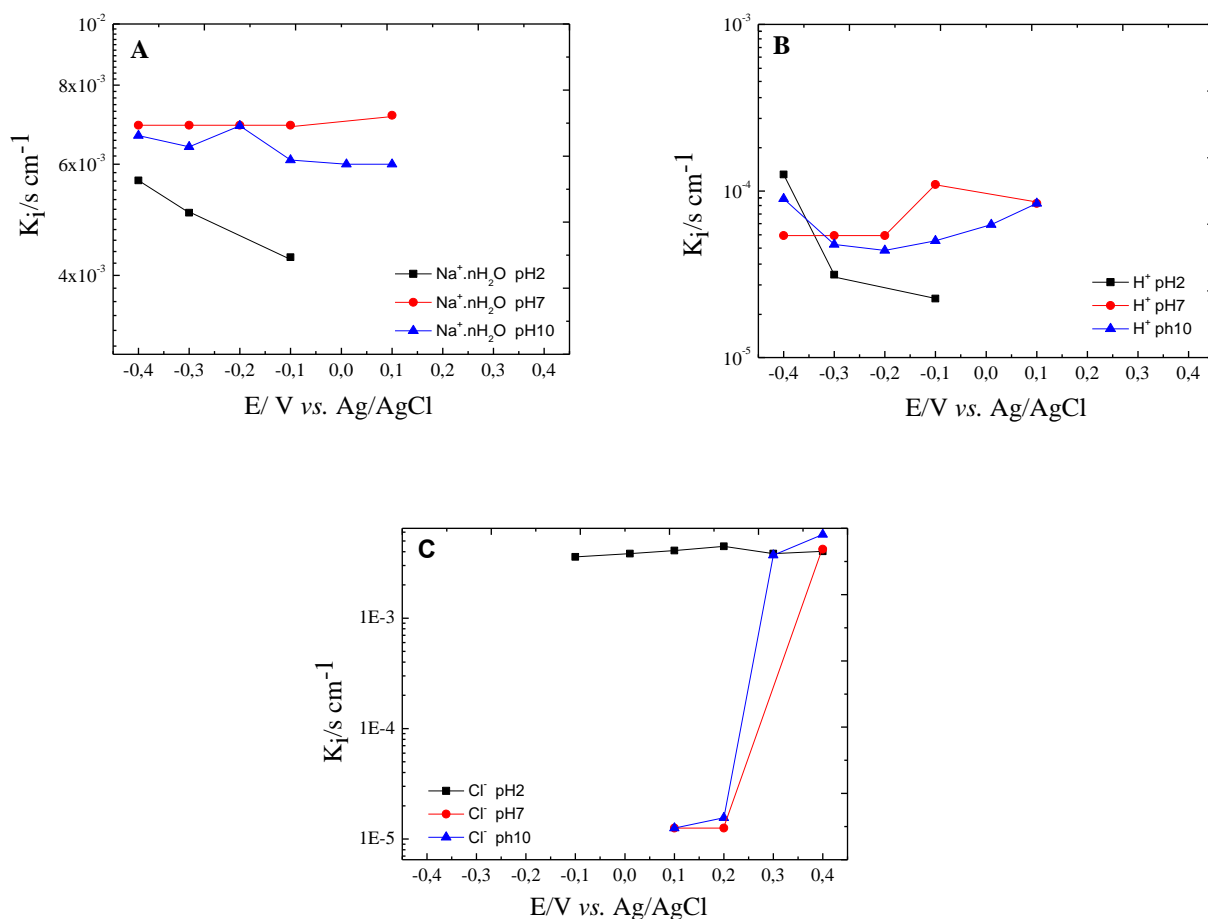


Figure IV-16. Constants of transfer kinetics, K_i , for ions (A) $\text{Na}^+ \cdot n\text{H}_2\text{O}$, (B) H^+ and (C) Cl^- estimated from the fitting of the *ac*-electrogravimetric data measured in 0.5M NaCl at different pH values.

Figure IV-16 shows the evolution of the constants of transfer kinetics, K_i , of the species as a function of the applied potential at different pH. Based on the K_i values presented in Figure IV-16A, ion transfer kinetics of the $\text{Na}^+ \cdot n\text{H}_2\text{O}$ at pH 7 and pH 10 are similar whereas the corresponding K_i values are lower at pH 2. The available (or measured) points of K_i for $\text{Na}^+ \cdot n\text{H}_2\text{O}$ at pH 2 are limited compared to the two other pH. This is due to the PZC value which is pH dependent and shifts to the more cathodic potentials at low pH values, therefore the contribution of cations is limited in this

potential range (important to remind that there is a V shaped behavior of the mass response around the PZC value, Figure IV-13A).

For the H^+ , the K_i values are in the same order of magnitude for all the pH, particularly at cathodic potentials (Figure IV-16B). Finally, the K_i values for Cl^- are the most significant at pH 2 and at cathodic potentials (Figure IV-16C). Indeed, the positive surface charge correlated to this pH favors the anion transfer.

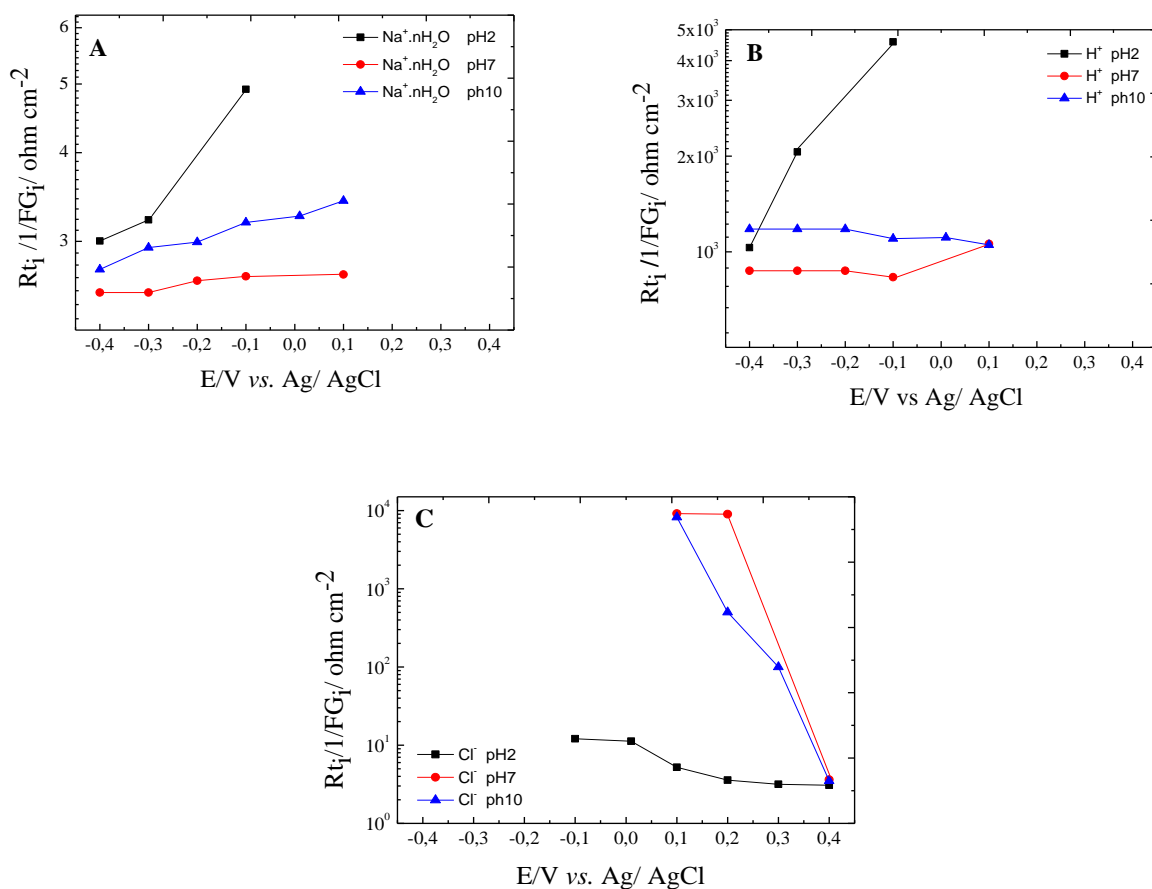


Figure IV-17. Transfer resistance, R_{ti} , for the different ions (A) $Na^+.nH_2O$, (B) H^+ and (C) Cl^- estimated from the fitting of the *ac*-electrogravimetric data measured in 0.5M NaCl at different pH values.

The transfer resistance, R_{ti} , values shown in Figures IV-17A and B characterize the ease of transfer of the $Na^+.nH_2O$ and H^+ cations. Results reveal that their transfers are more difficult at pH 2 than at pH 7 and pH 10 at cathodic potentials. The transfer of the Cl^- ion is easier at pH 2 than at pH 7 and pH 10 at anodic potentials (Figure IV-17C). These observations are directly correlated to the surface charge state and depends on the pH of the electrolyte.

Figure IV-18 shows the relative concentration change for the ionic species. The $(C_i - C_0)$ values of the $\text{Na}^+ \cdot n\text{H}_2\text{O}$ at pH 7 and pH 10 are significantly higher than the $(C_i - C_0)$ values of the other charged species (Figures IV-18B and C) regarding the same potential windows. In contrast, at pH 2, the $(C_i - C_0)$ values of the Cl^- are significantly higher than the $(C_i - C_0)$ values of the other species (Figure IV-18A) always keeping the same potential range. In other words, low pH values amplify the anion contribution whereas high pH values amplify the cationic response.

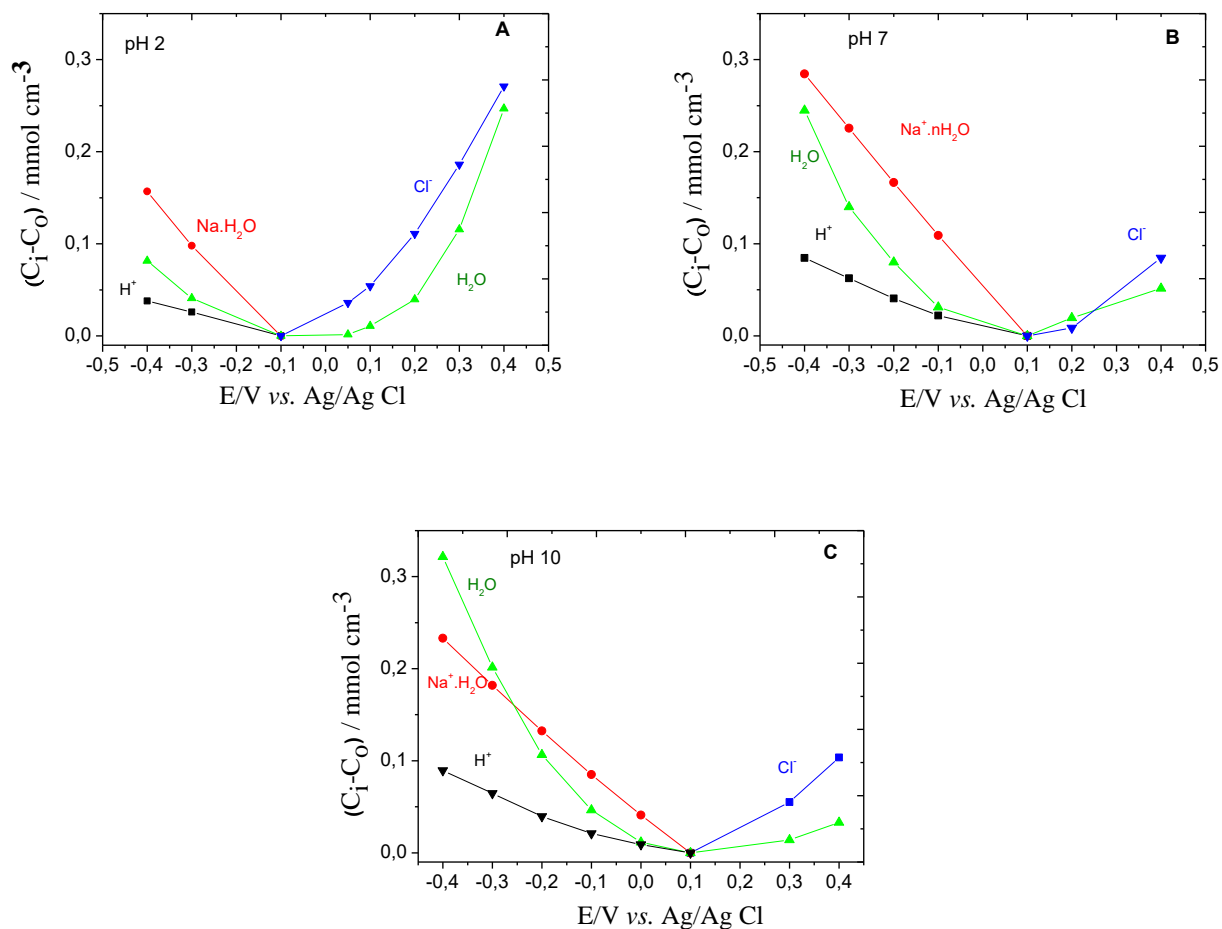


Figure IV-18. Evolution of the relative concentration, $C_i - C_0$, of each species over the applied potential measured in 0.5M NaCl at different pH: (A) pH 2, (B) pH 7 and (C) pH 10.

Nevertheless, regarding the concentration changes for exactly the same potential step, for example 0.3V around the PZC (in Figure IV-18A), $C_i - C_0$ values for $\text{Na}^+ \cdot n\text{H}_2\text{O}$ and Cl^- are completely equivalent; thus the pH shifts the $C_i - C_0$ curves only along the potential axis.

Finally, the $(C_i - C_0)$ values of the free solvent follow more or less the $(C_i - C_0)$ values of the $\text{Na}^+ \cdot n\text{H}_2\text{O}$ and Cl^- (Figures IV-18A, B and C) and this effect can be due to an electrodragging phenomena.

Figure IV-19 shows the instantaneous capacitance values of each ion, C'_i , calculated from *ac*-electrogravimetric data at different pH. These correspond to the capacitance attributed to the cations $\text{Na}^+ \cdot n\text{H}_2\text{O}$ and H^+ and the anion Cl^- . The capacitance concerning the cations $\text{Na}^+ \cdot n\text{H}_2\text{O}$ and H^+ are higher at pH 7 and pH 10 than at pH 2 (Figures IV-19A and 19B).

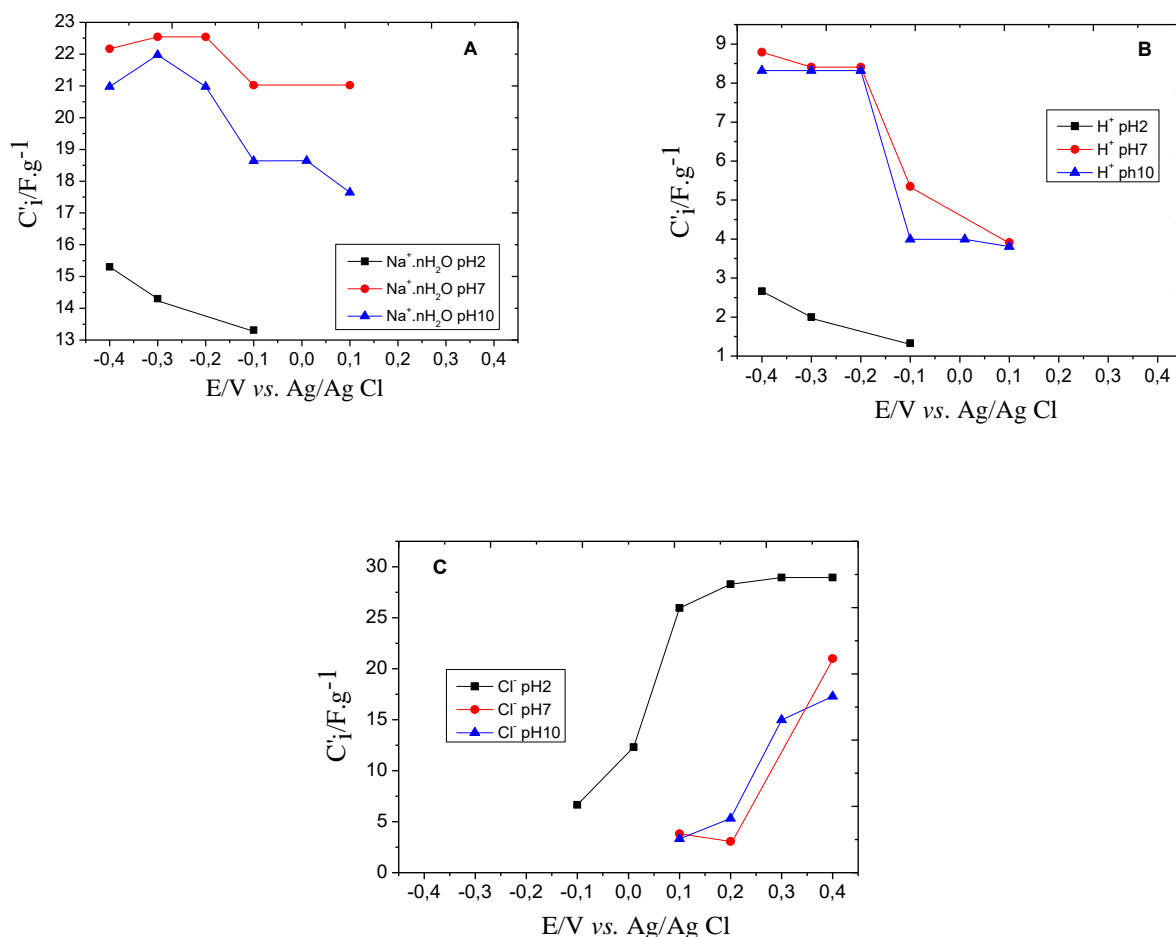


Figure IV-19. Instantaneous capacitance, C'_i , values of ions (A) $\text{Na}^+ \cdot n\text{H}_2\text{O}$, (B) H^+ and (C) Cl^- calculated from *ac*-electrogravimetric data at different pH.

In contrast, for the anion Cl^- , the instantaneous capacitance values are higher at pH 2 than at pH 7 and pH 10 (Figure IV-19C).

As a conclusion of this part, one can say that the pH value can drive completely the kinetics of transfer and the quantities inside the SWCNT film. Thus, it is possible to favor cations electroadsorption at high pH values and anion electroadsorption at low pH values.

IV-3.3. EQCM Study of SWCNT in Different Aqueous Electrolyte: Effect of the Cation Size

Up to now, the results presented concern only one type of electrolyte composition, *i.e.* 0.5 M aqueous NaCl at different pH values.

In this part, the influence of the cation size was investigated over the electrogravimetric response of the SWCNT films. Figure IV-20 shows the classical EQCM responses of SWCNT thin films obtained in three aqueous electrolytes 0.5 M LiCl, NaCl and KCl.

The mass changes of the SWCNT modified quartz resonators are determined simultaneously during the cyclic voltammetry in three different aqueous electrolyte. It can be noticed that current values decrease when the cation size increases. The mass changes follow the reverse order that is small for LiCl and at the maximum for KCl (Figures IV-20A, C and E). It indicates that the mass changes are not directly correlated to the charge variations or in other words, complex phenomena occur in terms of species transfer. In the light of previous results on CNTs, one can suggest that free water or solvated cations are certainly involved in these cases.

Figures IV-20 B, D and F show the Fdm/dq values obtained from the reduction branch of the EQCM results measured in different aqueous electrolytes. The values vary in the range of 150 to -25 g.mol⁻¹, 150 to -55 g.mol⁻¹ and 1500 to -90 g.mol⁻¹ in LiCl, NaCl and KCl, respectively. The observed higher values just confirm that the ions are hydrated and/or accompanied by free solvent molecules during their transfer.

Figure IV-21 show the capacitance curves as a function of the applied potential in 0.5M LiCl, NaCl and KCl, respectively. According to Figures IV-21A, B and C, the measured capacitance values are around 25 to 30 F.g⁻¹ for the three different electrolytes with homogeneous values. They are in the same order of magnitude as those reported in the literature.^{85,221} This confirms that SWCNT is an interesting candidate as supercapacitor electrode materials but the ions electroadsorption process is not straightforward and different electrolyte compositions may lead to different electrochemical properties.

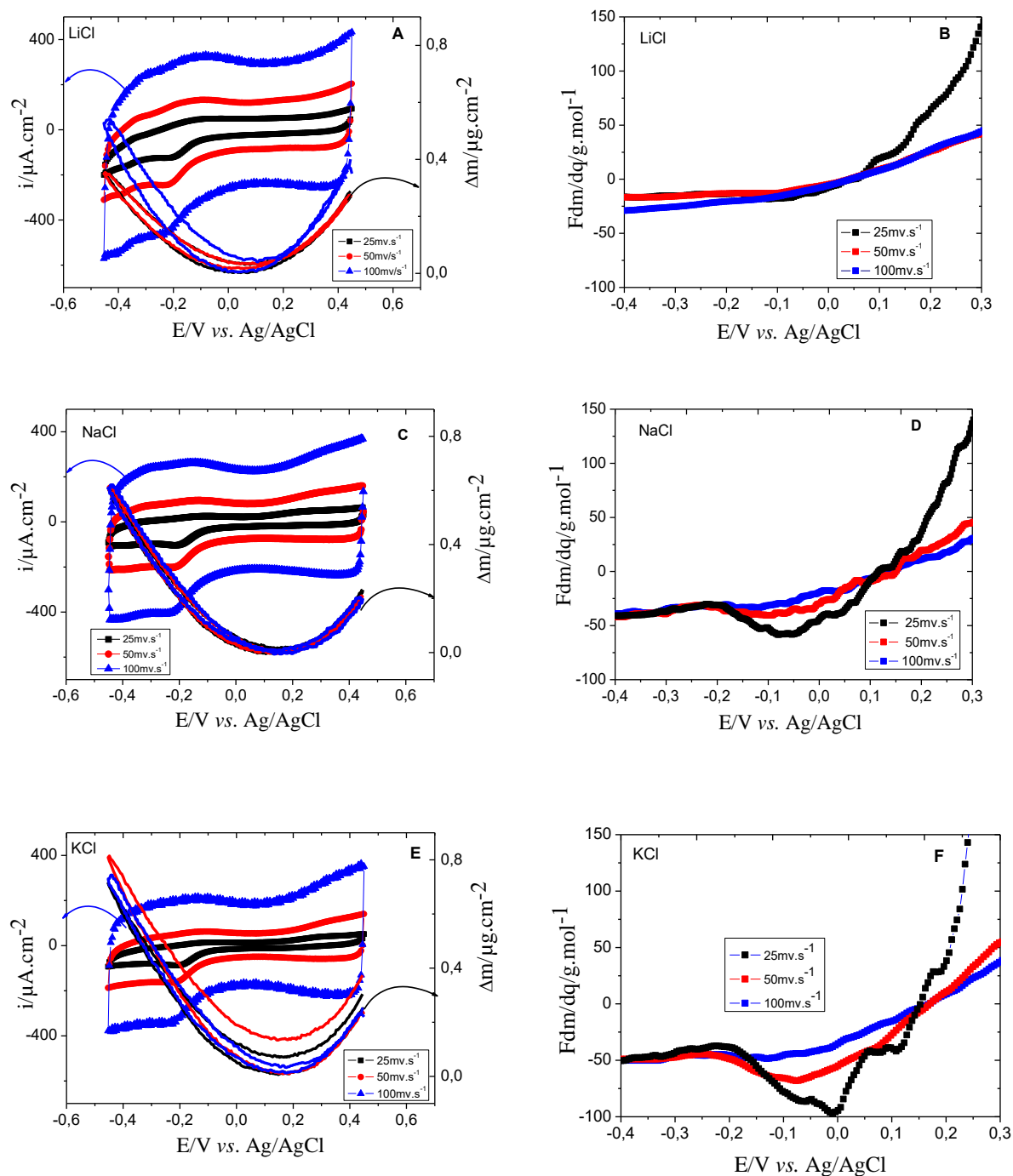


Figure IV-20. EQCM responses of SWCNT measured in different aqueous electrolyte 0.5 M LiCl (A), 0.5 M NaCl (C) and 0.5 M KCl (E). The values corresponding to the average molecular weight of the species involved in the charge compensation, F_{dm}/dq , are shown as a function of the potential and estimated for the three electrolytes (obtained from the reduction branch of EQCM data presented in Figure IV 20 A, C and E).

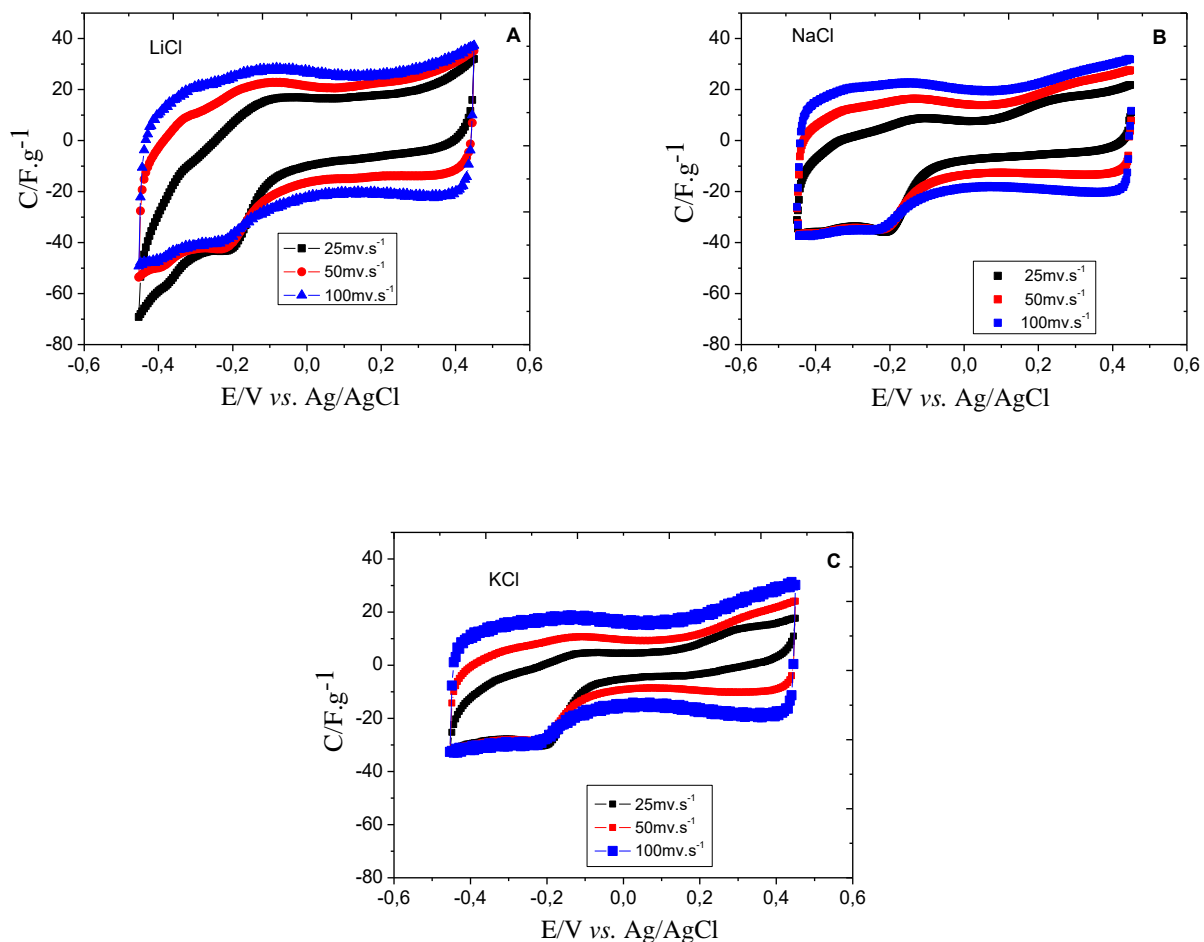


Figure IV-21. Specific capacitance, C , values (calculated from Figure IV-20) as a function of selected scan rates measured in 0.5M (A) LiCl, (B) NaCl and (5) KCl aqueous electrolyte.

Thus, it is necessary to understand the capacitive charge storage in these type of electrodes and to reach the subtleties of the transfer mechanism. With this perspective, *ac*-electrogravimetric experiments were performed in electrolytes with different cation size.

IV-3.4. *Ac*-electrogravimetric Study of various SWCNT Thin Film Electrodes in Different Aqueous Electrolytes: Effect of the Cation Size

In this part, a comparison and analysis of the *ac*-electrogravimetric responses of the SWCNT thin film measured in 0.5 M LiCl, NaCl, KCl aqueous electrolytes will be presented (Figures IV-22, IV-6 and IV-23). The results of the SWCNT in NaCl were previously shown in Figure IV-6.

First, the electrochemical impedance, $\frac{\Delta E}{\Delta I}(\omega)$, responses in LiCl, NaCl and KCl present a distorted straight line (Figures IV-22A, IV-6A and IV-23A), which is especially visible in NaCl. This distortion may be attributed to a multi-ion transfer contribution.

The charge/potential transfer function, $\frac{\Delta q}{\Delta E}(\omega)$, responses show one loop in the first quadrant (Figures IV-22B, IV-6B and IV-23B), which can be attributed to only one species or to two species, the latter is the case if the time constants of ions are not sufficiently different from each other. Nevertheless, at low frequencies and in all the electrolytes a small loop appears. In NaCl, this response is slightly amplified compared to those occurs in LiCl and KCl electrolytes.

The mass/potential transfer function, $\frac{\Delta m}{\Delta E}(\omega)$, responses of LiCl, NaCl, KCl show one big loop in the third quadrant from 100 Hz to 1 Hz (Figures IV-22C, IV-6C and IV-23C). These loops in the third quadrant are attributed to cation contributions ($\text{Li}^+ \cdot \text{H}_2\text{O}$, $\text{Na}^+ \cdot \text{H}_2\text{O}$ and K^+) at high frequencies, to free solvent molecules (H_2O) in the same flux direction at medium frequencies and to the H^+ at low frequencies. Furthermore, in KCl the cation at high frequencies participates freely without hydration, while in LiCl and NaCl the cations are hydrated. It means that three cations are electroadsorbed with different degrees of hydration. In fact, Li^+ and Na^+ can be more easily hydrated because of their small size, whereas the larger cations such as K^+ has a weaker interaction with water. In other words, Li^+ and Na^+ ion species are more tightly bonded to their water molecules in their hydration shell, thus it is possible to have a higher hydration level of the electroadsorbed lithium and sodium species than the potassium species, *i.e.* dehydration of K^+ is easier than the other Na^+ and Li^+ .^{219,222}

The presence of three different species were further confirmed by carefully analyzing the partial

electrogravimetric transfer functions, $\left. \frac{\Delta m}{\Delta E} \right|^{c1s}(\omega)$, (See Figures IV-22D, IV-6D and IV-23D) and

$\left. \frac{\Delta m}{\Delta E} \right|^{c2s}(\omega)$ (Figures IV-22E, IV-6E and IV-23E). Particularly in NaCl and KCl media, a small contribution is shown in the fourth quadrant at low frequencies (Figures IV-6D and IV-23D), which is due to the difference in molecular weight of the ions, as explained previously. In these partial TFs, the different ions contributions do not necessarily appear more clearly but a good agreement between the theoretical and experimental curves confirms the validity of our hypothesis.

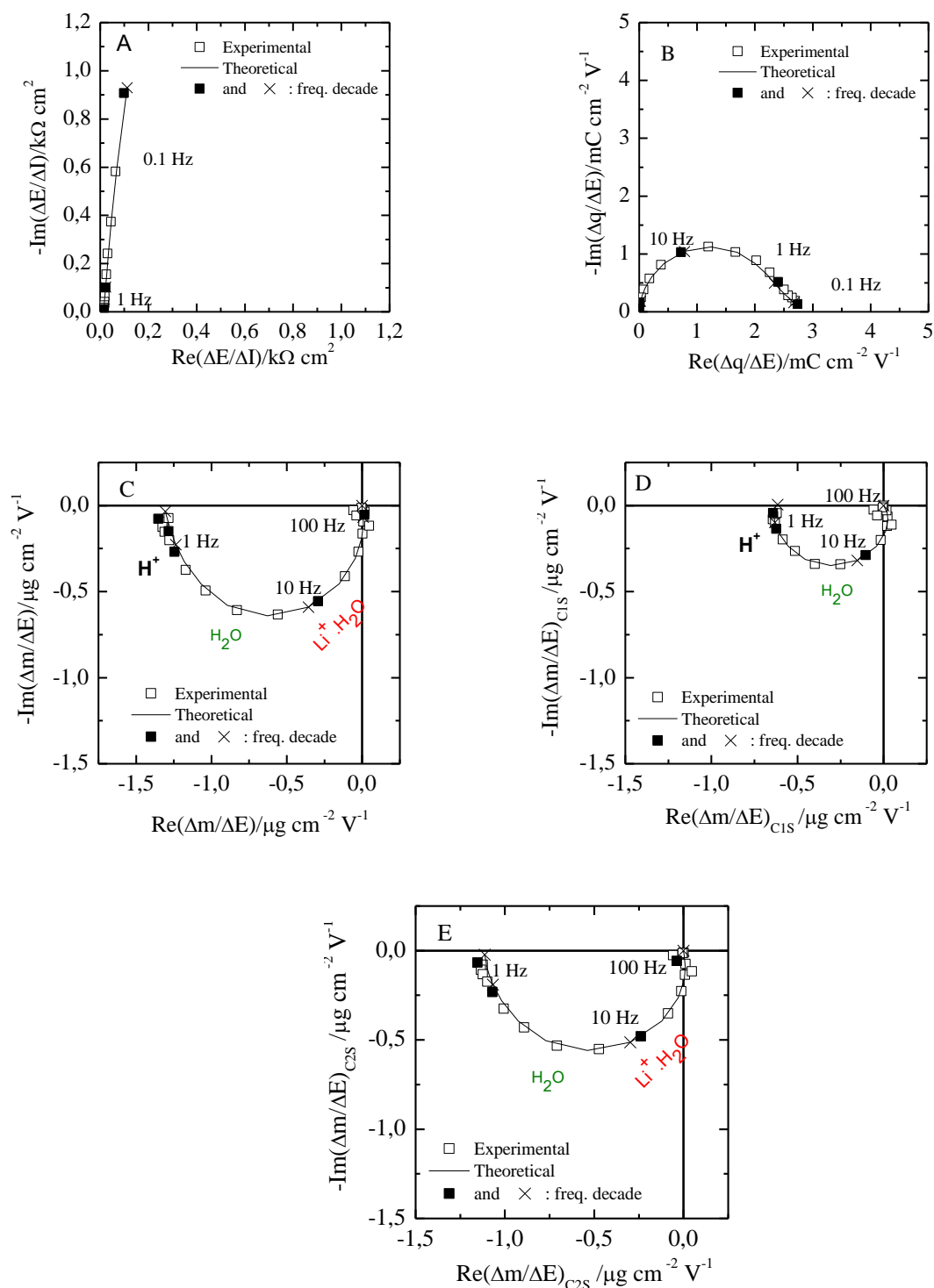


Figure IV-22. Experimental and theoretical *ac*-electrogravimetric data of the SWCNT thin film in

0.5 M LiCl measured at - 0.4V vs Ag/AgCl. (A) $\frac{\Delta E}{\Delta I}(\omega)$, (B) $\frac{\Delta q}{\Delta E}(\omega)$, (C) $\frac{\Delta m}{\Delta E}(\omega)$, (D) $\left. \frac{\Delta m}{\Delta E} \right|^{c1s}(\omega)$,

(E) $\left. \frac{\Delta m}{\Delta E} \right|^{c2s}(\omega)$. Theoretical functions were calculated with the following parameters: $d_f = 0.4 \mu\text{m}$,

$K_{cl} = 5.40 \times 10^{-4} \text{ cm s}^{-1}$, $G_{cl} = 7.03 \times 10^{-9} \text{ mol.s}^{-1} \text{ cm}^{-2} \text{ V}^{-1}$, $K_{c2} = 5.03 \times 10^{-3} \text{ cm.s}^{-1}$, $G_{c2} = 3.02 \times 10^{-6} \text{ mol.s}^{-1} \text{ cm}^{-2} \text{ V}^{-1}$, $K_s = 3.14 \times 10^{-3} \text{ cm.s}^{-1}$, $G_s = 2.99 \times 10^{-6} \text{ mol.s}^{-1}$, $m_{cl} = 1 \text{ g.mol}^{-1}$, $m_{c2} = 7+18 \text{ g.mol}^{-1}$ and $m_s = 18 \text{ g.mol}^{-1}$.

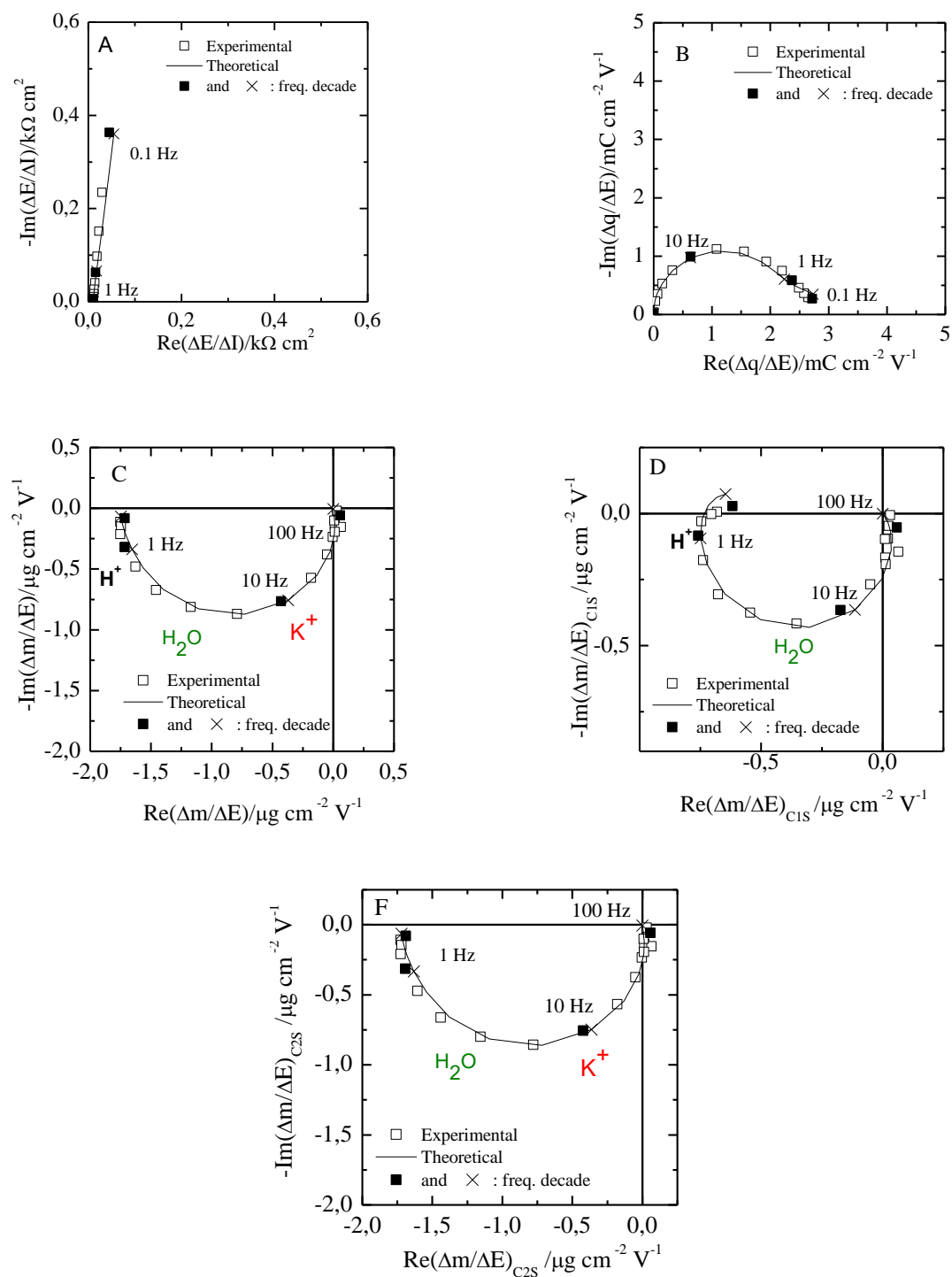


Figure IV-23. Experimental and theoretical *ac*-electrogravimetric data of the SWCNT thin film in 0.5 M KCl measured at - 0.4V vs Ag/AgCl. (A) $\frac{\Delta E}{\Delta I}(\omega)$, (B) $\frac{\Delta q}{\Delta E}(\omega)$, (C) $\frac{\Delta m}{\Delta E}(\omega)$, (D) $\frac{\Delta m}{\Delta E}\bigg|^{c1s}(\omega)$, (E) $\frac{\Delta m}{\Delta E}\bigg|^{c2s}(\omega)$. Theoretical functions were calculated with the following parameters: $d_f = 0.4 \mu\text{m}$, $K_{cl} = 3.90 \times 10^{-5} \text{ cm.s}^{-1}$, $G_{cl} = 1.91 \times 10^{-8} \text{ mol.s}^{-1} \text{ cm}^{-2} \text{ V}^{-1}$, $K_{c2} = 4.15 \times 10^{-3} \text{ cm.s}^{-1}$, $G_{c2} = 4.69 \times 10^{-6} \text{ mol.s}^{-1} \text{ cm}^{-2} \text{ V}^{-1}$, $K_s = 2.51 \times 10^{-3} \text{ cm.s}^{-1}$, $G_s = 1.23 \times 10^{-6} \text{ mol.s}^{-1}$, $m_{cl} = 1 \text{ g.mol}^{-1}$, $m_{c2} = 39 \text{ g.mol}^{-1}$ and $m_s = 18 \text{ g.mol}^{-1}$.

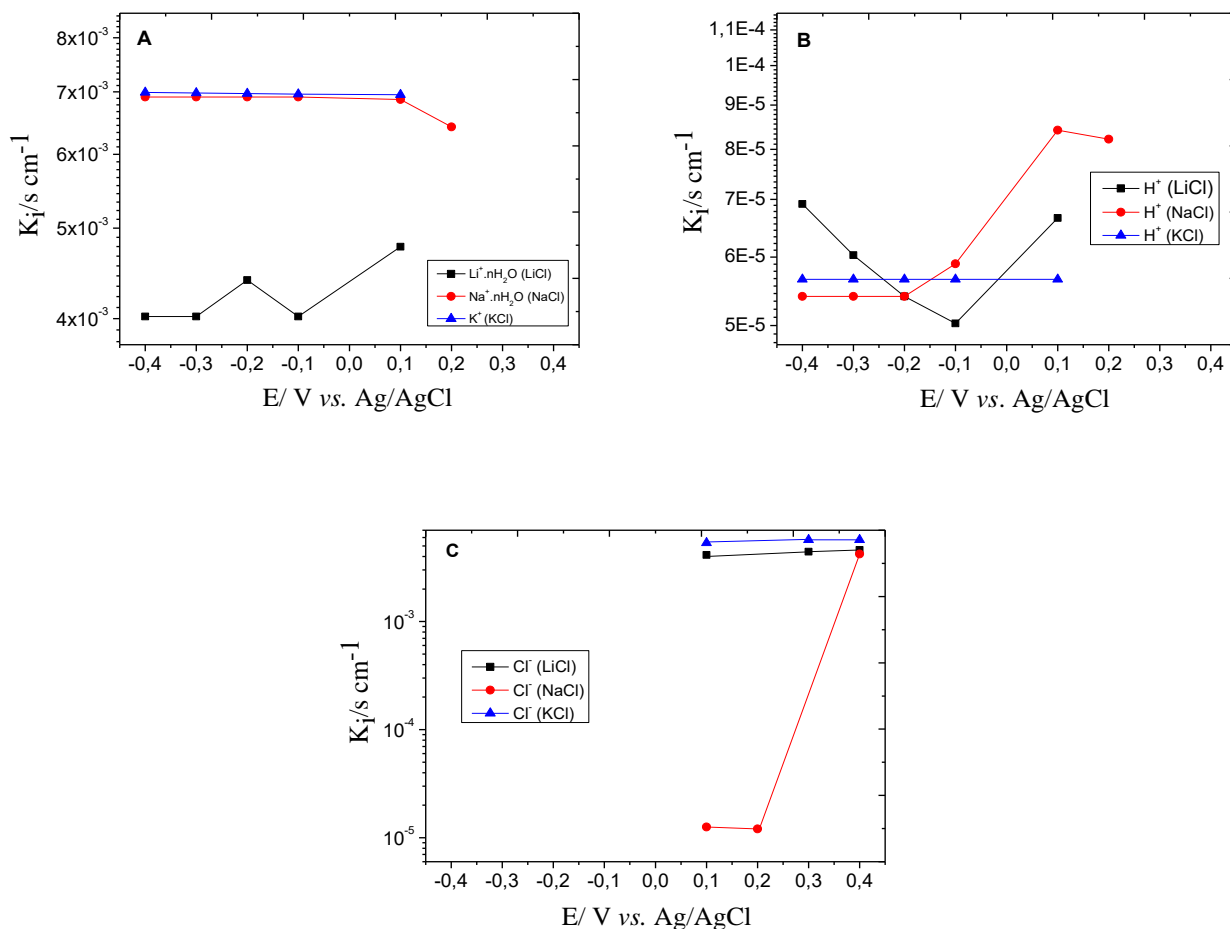


Figure IV-24. Constants of transfer kinetics, K_i , of ions (A) $\text{Li}^+.n\text{H}_2\text{O}$, $\text{Na}^+.n\text{H}_2\text{O}$, K^+ (B) H^+ and (C) Cl^- estimated from the fitting of the *ac*-electrogravimetric data measured in 0.5M LiCl, NaCl and KCl.

Figure IV-24 shows the evolution of the constant kinetic transfer, K_i , of the species as a function of the applied potential measured in different aqueous electrolytes. Based on the K_i values presented in Figure IV-24A, the transfer of $\text{Na}^+.n\text{H}_2\text{O}$ ion and K^+ ion is faster compared to that of $\text{Li}^+.n\text{H}_2\text{O}$ for cathodic potentials. For the H^+ , the K_i values are more or less equivalent in the three different media as shown in Figure IV-24B. This observation is in agreement with the ions size and the affinity for dehydration. K^+ ions due their completely dehydrated state, they probably become equivalent to partially dehydrated $\text{Na}^+.n\text{H}_2\text{O}$, in terms of kinetics.

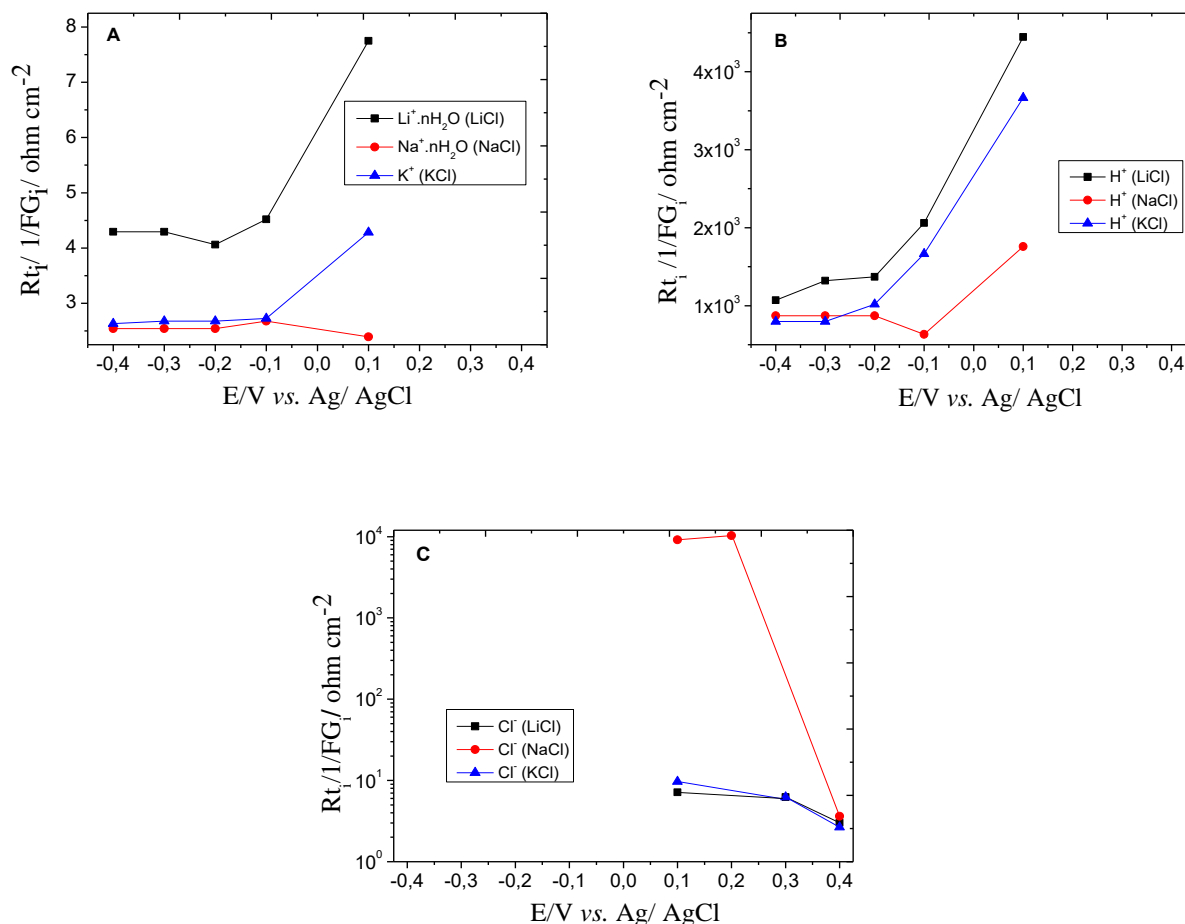


Figure IV-25. Transfer resistance values for three electrolytes (A) $\text{Li}^+.n\text{H}_2\text{O}$, $\text{Na}^+.n\text{H}_2\text{O}$, K^+ (B) H^+ and (C) Cl^- estimated from the fitting of the *ac*-electrogravimetric data measured in 0.5M LiCl, NaCl and KCl.

$\text{Li}^+.n\text{H}_2\text{O}$ ions dynamics is much lower since it is much more difficult for them to get rid of their hydration shell. It is important to note that the n is estimated as 1 in our simulations, for both $\text{Na}^+.n\text{H}_2\text{O}$ and $\text{Li}^+.n\text{H}_2\text{O}$ (Figures IV-6 and IV-22) and the bulk hydration numbers of these ions are much higher, *i.e.* these ions are only partially dehydrated. Figure IV-24B shows that H^+ has much lower kinetics than the other cations, which may be related to the fact that they are formally the smallest ions with more difficulty to dehydrate. Since their concentration is low in LiCl, NaCl and KCl electrolytes, they were not involved in the ion size/dehydration relationship discussion. Finally, for the Cl^- , the K_i values are higher for LiCl and KCl media than in NaCl at anodic potentials (Figure IV-24C).

Figure IV-25 shows the transfer resistance, R_{t_i} , values for charged species measured in the three different aqueous electrolytes: LiCl, NaCl and KCl. As shown in Figure IV-25A, the transfer of the Li^+ ion is more difficult than the transfer of the $\text{Na}^+.n\text{H}_2\text{O}$ and K^+ .

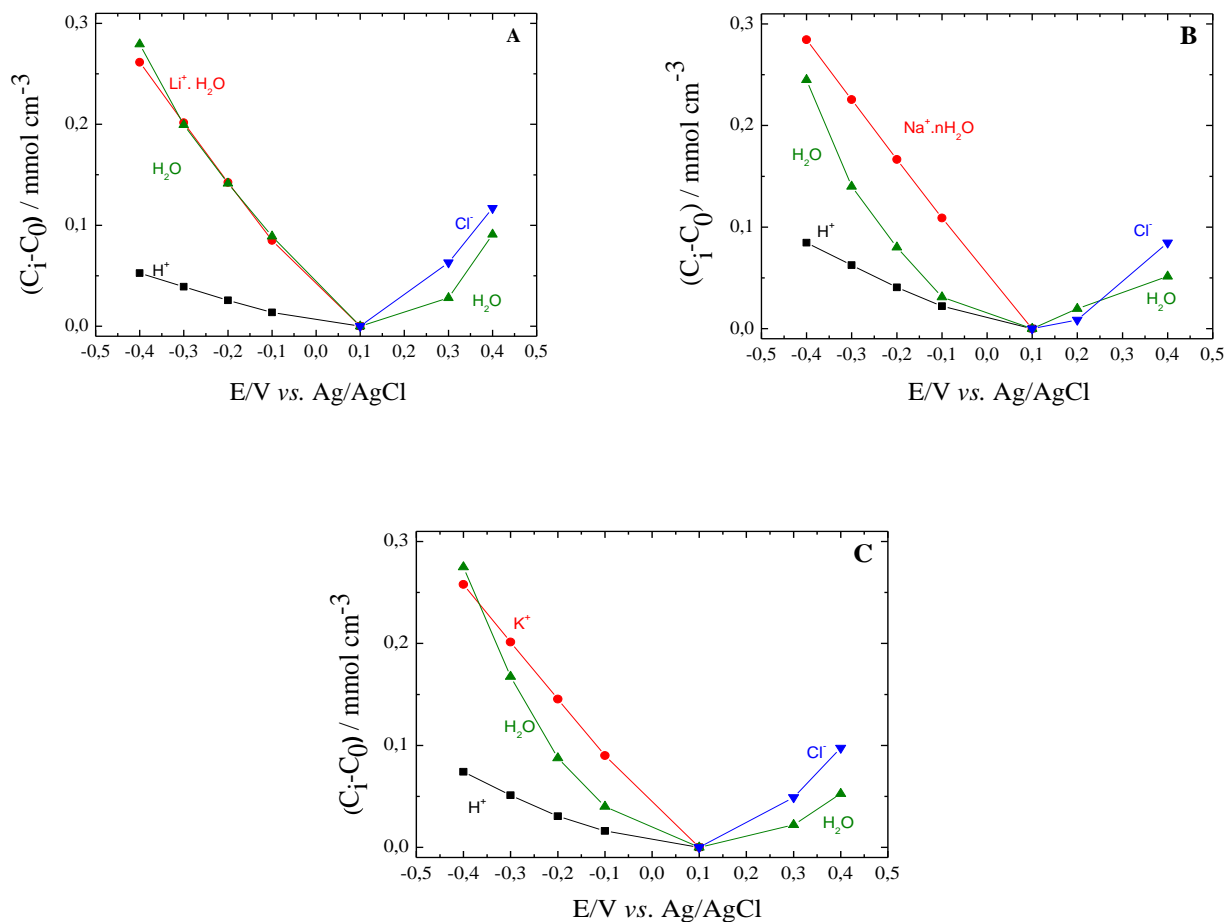


Figure V-26. Evolution of the concentration, $C_i - C_0$ of each species over the applied potential measured in 0.5M (A) LiCl, (B) NaCl, (C) KCl aqueous electrolytes.

For the H^+ ion, the transfer seems more difficult in LiCl and KCl media than in NaCl media, particularly at potentials closer to PZC (Figure IV-25B). Finally, the transfer of the Cl^- ion is more difficult in NaCl media than in KCl and LiCl media (Figure IV-25C). As expected, the transfer resistance of the species follows a reverse order of the kinetics of transfer of species, *i.e.* species with slower dynamics of transfer are more difficult to be transferred.

Figure IV-26 shows the relative concentration change for the ionic species. The $C_i - C_0$ values of the $Li^+.nH_2O$, $Na^+.nH_2O$ and K^+ are equivalent but significantly higher than the $C_i - C_0$ values of the H^+ for all the studied electrolytes. (Figures IV-26A, IV-26B and IV-26C) which is agreement with the lower concentrations of protons in the electrolyte at this pH. Earlier it was shown that the $Li^+.nH_2O$ ions presented slower dynamics and difficulty to be transferred (Figures IV-24A and 25A), but eventually similar amounts of species are transferred. This indicates that the concentration of electroadsorbed species depends majorly to the specific surface area of the electrode, here SWCNT electrodes.

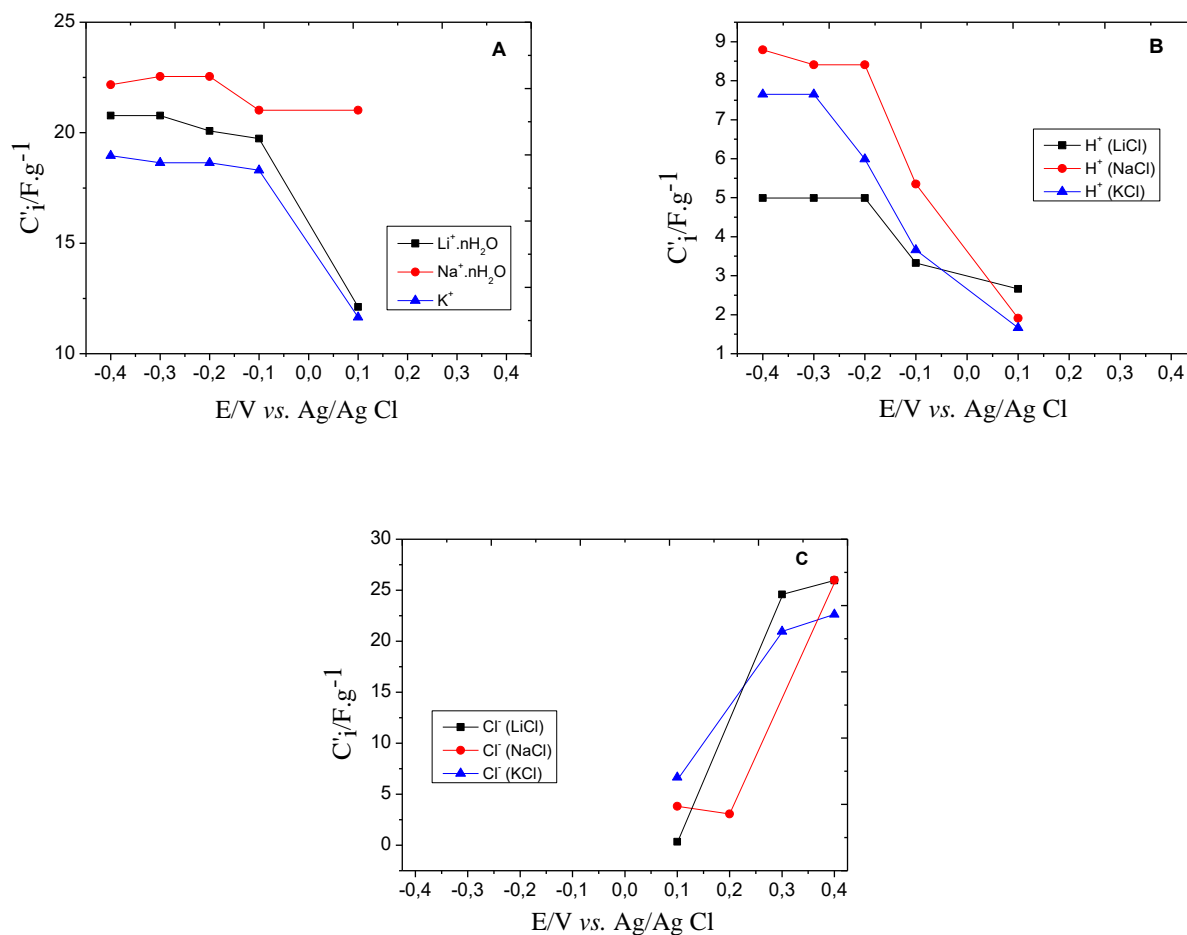


Figure IV-27. Instantaneous capacitance, C_i' , of ions (A) $\text{Li}^+ \cdot n\text{H}_2\text{O}$, $\text{Na}^+ \cdot n\text{H}_2\text{O}$, K^+ , (B) H^+ (C) Cl^- calculated from *ac*-electrogravimetric data in 0.5M LiCl, NaCl and KCl aqueous electrolytes.

At anodic potentials, the $C_i - C_0$ values of the Cl^- are slightly higher than the $C_i - C_0$ values of the free solvent for all the studied electrolytes (Figures IV-26A, IV-26B and IV-26C). Finally, the $C_i - C_0$ values of free solvent are close to the $C_i - C_0$ values of the cations at cathodic potentials, and close to the $C_i - C_0$ values of the anions at anodic potentials (Figures IV-26A, IV-26B and IV-26C), which is attributed to the *electrodragging* effect.

Figure IV-27 shows the instantaneous capacitance values for each ion, C_i' , calculated as a function of the applied potential. These values correspond to the capacitance attributed to each cation, $\text{Li}^+ \cdot n\text{H}_2\text{O}$, $\text{Na}^+ \cdot n\text{H}_2\text{O}$, K^+ , H^+ and the respective anion Cl^- of the three different electrolytes. The values of the instantaneous capacitance of the cations ($\text{Li}^+ \cdot n\text{H}_2\text{O}$, $\text{Na}^+ \cdot n\text{H}_2\text{O}$ and K^+) at cathodic potentials are presented as follows (in terms of the higher capacitance observed): $\text{Na}^+ \cdot n\text{H}_2\text{O} > \text{Li}^+ \cdot n\text{H}_2\text{O} > \text{K}^+$ (Figure IV-27A). This difference in capacitance between the cations is probably related to the phenomena of dehydration, differences of cation sizes adsorbed within the porous material and the accessibility of the porous structure by the ions. For the H^+ , the instantaneous capacitance values are more significant in NaCl and KCl aqueous electrolyte than in

LiCl (Figure 27B) which may indicate a competition between hydrated Li^+ ions and the protons for similar electroactive sites of the SWCNT film. Finally, at anodic potentials, the relative capacitance values of the Cl^- are equivalent in all the three electrolytes (Figure IV-27C) which indicates that the instantaneous capacitance of the anions is not effected by different *co-ions* such Li^+ , Na^+ and K^+ . It is important to highlight here the advantageous nature of *ac*-electrogravimetry which allows a separation of the global capacitance values to distinct contributions of each species to be obtained.

IV-4. Conclusions

SWCNT, DWCNT and MWCNT carbon-based electrodes were prepared on gold electrodes of the quartz resonators and their electrochemical charge storage behavior evaluated in aqueous electrolytes, *i.e.* 0.5 M NaCl at pH 2, pH 7 and pH 10 was presented. The cation size of the electrolyte was also varied from Li^+ , Na^+ to K^+ (in LiCl, NaCl and KCl), the results of SWCNTs were discussed in this chapter.

We have conducted a comparative study among different CNTs with different pore dimensions *via* an *ac*-electrogravimetric study and related the results to their structural and morphological characteristics. First of all, several species were detected to intervene to the electroadsorption process for all types of CNTs: there are two types of cations ($\text{Na}^+.\text{H}_2\text{O}$ and H^+) electroadsorbed with different kinetics for cathodic potentials and the Cl^- ions for anodic potentials together with free water molecules. When we compare the $\text{Na}^+.\text{nH}_2\text{O}$ dynamics (can be considered as the major cation detected) in three different CNTs, hydrated sodium species are slightly faster to be transferred in SWCNTs compared to the other two types of CNTs (Figure IV-9). In terms of the relative concentration changes DWCNTs also shows advantageous behavior (Figure IV-11), these results indicate that SWCNTs and DWCNTs appear to be better performance materials for polarizable electrodes, since they can accommodate higher concentration of charged species with relatively higher transfer dynamics as compared to MWCNTs. The relatively low performance of the MWCNTs is attributed to their lower specific surface area (the lowest among the three CNTs, Figure IV-4).

The effect of the electrolyte pH on the CNTs electroadsorption phenomena was evaluated by changing the pH of the NaCl solution to pH 2, pH 7 and pH 10 (presented for SWCNTs). In the same potential range, low pH values amplify the anion contribution whereas high pH values amplify the cationic response (Figure IV-18). Nevertheless, regarding the concentration changes for exactly the same potential step, for example 0.3V around the PZC (in Figure IV-18A), C_i-C_0 values for $\text{Na}^+.\text{nH}_2\text{O}$ and Cl^- are completely equivalent; thus the pH changes shifts the C_i-C_0 curves only along the potential axis. This means that it is possible to adjust the pH of the aqueous electrolyte to preferentially electroadsorb cations or anions in the same potential range.

The cation size dependence of the electrodeposition phenomena was studied by changing the electrolyte cation from Li^+ , Na^+ to K^+ and the results are shown for SWCNTs. The chemical nature and the role of each species, *i.e.* anion, cation, solvated cation, free solvent, directly or indirectly involved in the charge storage, have been identified during the cathodic and anodic polarization in *ac*-electrogravimetry measurements. The theoretical transfer functions have been calculated taken into account three different species ($\text{Li}^+ \cdot \text{H}_2\text{O}$, H^+ and H_2O), ($\text{Na}^+ \cdot \text{H}_2\text{O}$, H^+ and H_2O), (K^+ , H^+ and H_2O) for LiCl, NaCl and KCl electrolytes, respectively. Very good agreements between experimental and theoretical data for all functions of estimated transfers were obtained. Based on the K_i values presented in Figure IV-24A, the transfer of $\text{Na}^+ \cdot n\text{H}_2\text{O}$ ion and K^+ ion is faster compared to that of $\text{Li}^+ \cdot n\text{H}_2\text{O}$ for cathodic potentials. This observation is in agreement with the ions size and the affinity for dehydration. Li^+ and Na^+ can be more easily hydrated because of their small sizes, whereas the larger cations such as K^+ has a weaker interaction with water. In other words, Li^+ and Na^+ species are more tightly bonded to their water molecules in their hydration shell compared to the potassium species, *i.e.* dehydration of K^+ is easier than the other Na^+ and Li^+ . K^+ ions due their completely dehydrated state, they probably become equivalent to partially dehydrated $\text{Na}^+ \cdot n\text{H}_2\text{O}$, in terms of kinetics. $\text{Li}^+ \cdot n\text{H}_2\text{O}$ ions dynamics is much lower since it is much more difficult for them to get rid of their hydration shell making their transfer the slowest among the other cations. Our results clearly indicates that the dehydration affinity and the ions size plays a role in the electroadsorption dynamics of the species on the SWCNT based electrodes. However, although $\text{Li}^+ \cdot n\text{H}_2\text{O}$ ions presents slower dynamics and difficulty to be transferred (Figures IV-24A and 25A), our results indicated that eventually similar amounts of ions are transferred ($\text{Na}^+ \cdot n\text{H}_2\text{O}$, K^+ and $\text{Li}^+ \cdot n\text{H}_2\text{O}$). These findings strengthens the idea that the electroadsorption of these species takes place at different sites of the SWCNT electrodes, probably governed by the species size and dynamics of transfer and the accessibility of these sites to the species.

Chapter V. Composite Thin Film Electrodes and Beyond Carbon Nanotubes

CHAPTER V

Composite Thin Film Electrodes and Beyond Carbon Nanotubes

This chapter is dedicated to the interpretation of the results obtained from the study of SWCNT/Prussian Blue (PB) and SWCNT/Polypyrrole (PPy) composite and electrochemically reduced graphene oxide (ERGO) thin film electrodes. This approach was examined in order to increase the performances of the pure CNT films by functionalizing the CNT materials by redox films or by using alternative carbon based materials such as ERGO structures. Firstly, the results from the FEG-SEM, HRTEM, EDX and XRD studies of the structure and the morphology of the samples are presented and discussed. Thereafter follows the discussion of the results from the EQCM and the *ac*-electrogravimetry studies in order to thoroughly examine the electrochemical behavior of such layers.

V-1. Composite Thin Film Electrodes

V-1.1. SWCNT/Prussian Blue Thin Film Electrodes

V-1.1.1. Structure and Morphology of the SWCNT/PB Composites

The surface morphology of SWCNT/PB was characterized by FEG-SEM- as shown in Figure V-1. Prussian blue was deposited on the SWCNTs via cyclic voltammetry. After 15 cycles, nanosized cubes were formed and distributed along the thin layer of CNT films (Figure V-1A), which corresponds to PB (Prussian Blue).

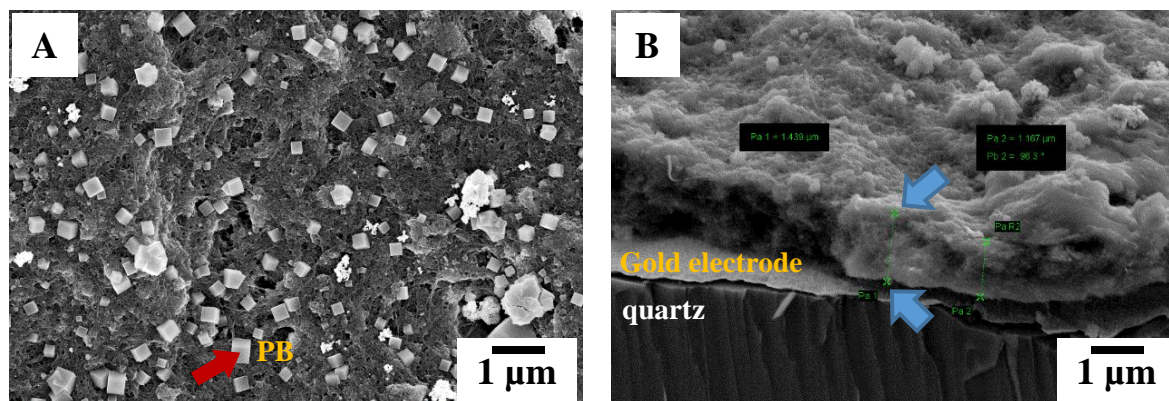


Figure V-1.FEG-SEM images of a SWCNT/PB nanocomposite film, surface (A) and cross-section (B).

The cross-section of the SWCNT/PB shown in Figure V-1B permits the determination of the film thickness. The thickness slightly inhomogenous along the thin film and presents a variation between 1.1 to 1.4 μm , which is in agreement with values found in earlier studies.¹²⁶ The electrodeposited PB component on the SWCNTs did not change the film thickness significantly and, the gravimetric regime is kept for the QCM based analysis.

The EDX analysis coupled with FEG-SEM observations indicates the presence of both C and Fe as constituents of the carbon nanotubes/PB composite (See Figure V-2). The presence of Au peaks is due to the gold electrode of the QCM. Furthermore, the presence of N further confirms the formation of PB on the CNTs where the PB structure is $\text{KFeFe}(\text{CN})_6$.

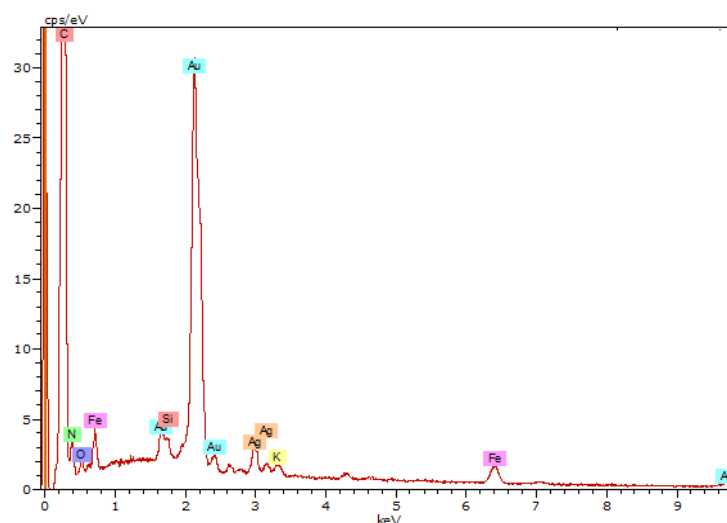


Figure V-2. EDX pattern of a SWCNT/PB nanocomposite film.

V-1.1.2. EQCM Study of the SWCNT/PB Composites

Figure V-3 shows the current and mass changes of the SWCNT/PB film when it is oxidized and reduced between -0.45V and 0.45V vs Ag/AgCl at a scan rate of 50 mV.s⁻¹ in a 0.5M KCl solution (pH 3).

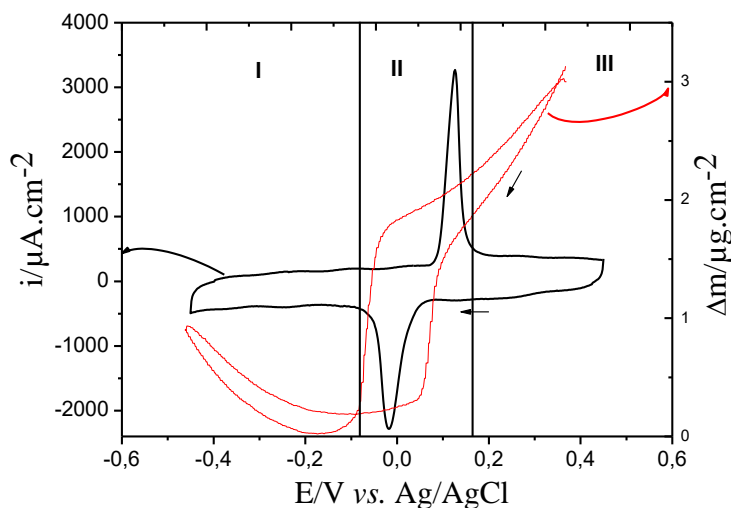


Figure V-3. The EQCM results of SWCNT/PB thin films: current vs. potential and mass variation vs. potential profiles measured in aqueous electrolyte 0.5 M KCl, scan rate is 50 mV.s⁻¹.

The cyclic voltammetry in Figure V-3 presents a capacitive behavior between -0.45V to -0.1V and 0.2V to 0.45V, which is typical of the electrochemical response of CNT films. In the range of ~0.05V to ~0.15V, peaks of oxidation/reduction are observed, which is characteristic of the PB redox response. The current responses are more significant than the current responses of PB film showed in the literature^{3,109,223} and more significant than SWCNT film (Figure III-3). Considering the mass response, the mass change of the SWCNT/PB electrode presents a particular behavior: a main contribution of cations in the zones of PB and CNTs from -0.45V to -0.15V and of anions between 0.2V to 0.45V by regarding the mass slope. The values of the mass changes are more significant than the values of the mass change of PB film shown in the literature^{3,109} and more significant than the values of the mass change of SWCNT film (Figure III-3). These results are corroborated by the calculation of the Fdm/dq function calculated instantaneously for each potential.

Figure V-4 shows the variation of Fdm/dq values as a function of the potential applied, obtained from the reduction branch, in the range 0.4V to -0.4V vs Ag/AgCl measured in 0.5M KCl. Three zones are defined.

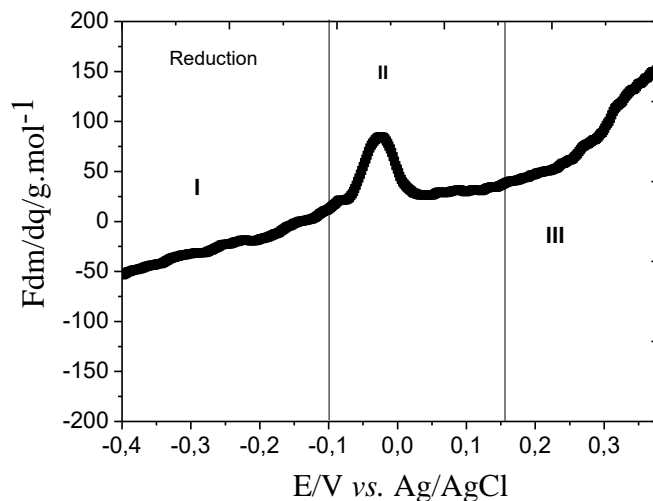


Figure V-4. The Fdm/dq values as a function of the potential applied, obtained from the reduction branch of the EQCM results measured in 0.5 M KCl with a scan rate of 50 mV.s⁻¹.

- ❖ Zone I, between -0.4V to 0.1V, the species involved could be the hydrated K⁺.
- ❖ Zone II, range -0.1V to 0.15 V, the species involved could be K⁺ and H₃O⁺ which is coherent with the PB response.
- ❖ Zone III, range 0.15V to 0.4V, the species involved could be Cl⁻ but the high values calculated indicate the contribution of free solvent.

Figure V-5 depicts the variation of capacitance values as a function of the potential applied in the same conditions as mentioned previously. The capacitance values are estimated to be around 25 F g⁻¹ in the zones III and I, which is in good agreement with the values obtained for SWCNTs described earlier in Chapter III. The capacitance value of the oxidation peak (zone PB) is estimated to be around 250 F g⁻¹.

However, another method for calculation of the capacitance adapted to faradaic process has been proposed using the following relation $C = \frac{\int_{E_2}^{E_1} i(E)dE}{2(E_2 - E_1)mv}$ where C is the specific capacitance

of electrode, E_1 and E_2 are the working voltage in cyclic voltammetry, and $\int_{E_2}^{E_1} i(E)dE$ is the total voltammetric charge in cyclic voltammetry, m is the mass of the film, and v is the scan rate. The value is estimated to be around 114 F g⁻¹ which is four times higher than the capacitance values obtained from SWCNT film (See Figure III-5). This improvement in capacitance is due to the faradaic process that occurring in the redox zone.

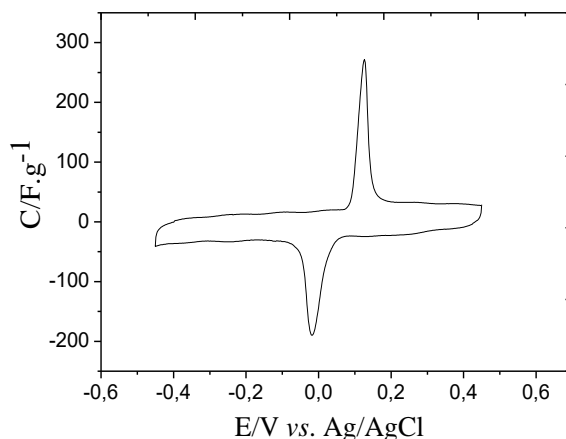


Figure V-5. Specific capacitance values (calculated from Figure VI-4) as a function of potential at a scan rate of 50 mV.s⁻¹ calculated for 0.5M KCl.

V-1.1.3. *Ac*-electrogravimetry Study of the SWCNT/PB Composites

The measurements are performed each 100 mV in the range from -0.4V to 0.4V *vs* Ag/AgCl. Figure V-6 shows an example of the experimental and theoretical transfer functions (TFs) obtained from *ac*-electrogravimetry of a SWCNT/PB thin film in 0.5 M KCl electrolyte at -0.4V *vs* Ag/AgCl. The experimental data were fitted according to the model presented in Chapter III. Figure V-6 reveals a good agreement between experimental data and theoretical curves. First, the electrochemical impedance $\frac{\Delta E}{\Delta I}(\omega)$ responses (Figure V-6A) present a slightly distorted straight line indicating that there is a multi-ion transfer contribution. Consequently, it is difficult to extract information. The experimental transfer function and the fitted data from the model (See Chapter II, Section 3.5) are reported on the same graphs.

However, it should be noted that there is no evident part with a slope equal to 45° or below in the electrochemical impedance response, therefore, the rate limiting step is not the mass transport in the films or in the solution, but rather ionic transfer between the solution and the film.³

The charge/potential transfer functions (TFs), $\frac{\Delta q}{\Delta E}(\omega)$ (Figure V-6B), permit the separation of the ionic contributions, however, without any possibility to identify the ionic species involved. Figure V-6B shows two loops, a big one for the high frequencies and a small one for the low frequencies. They can be attributed to any of the species present in the electrolyte and their time constants are sufficiently different from each other. Only the mass/potential TF permits this identification when associated to partial TFs.

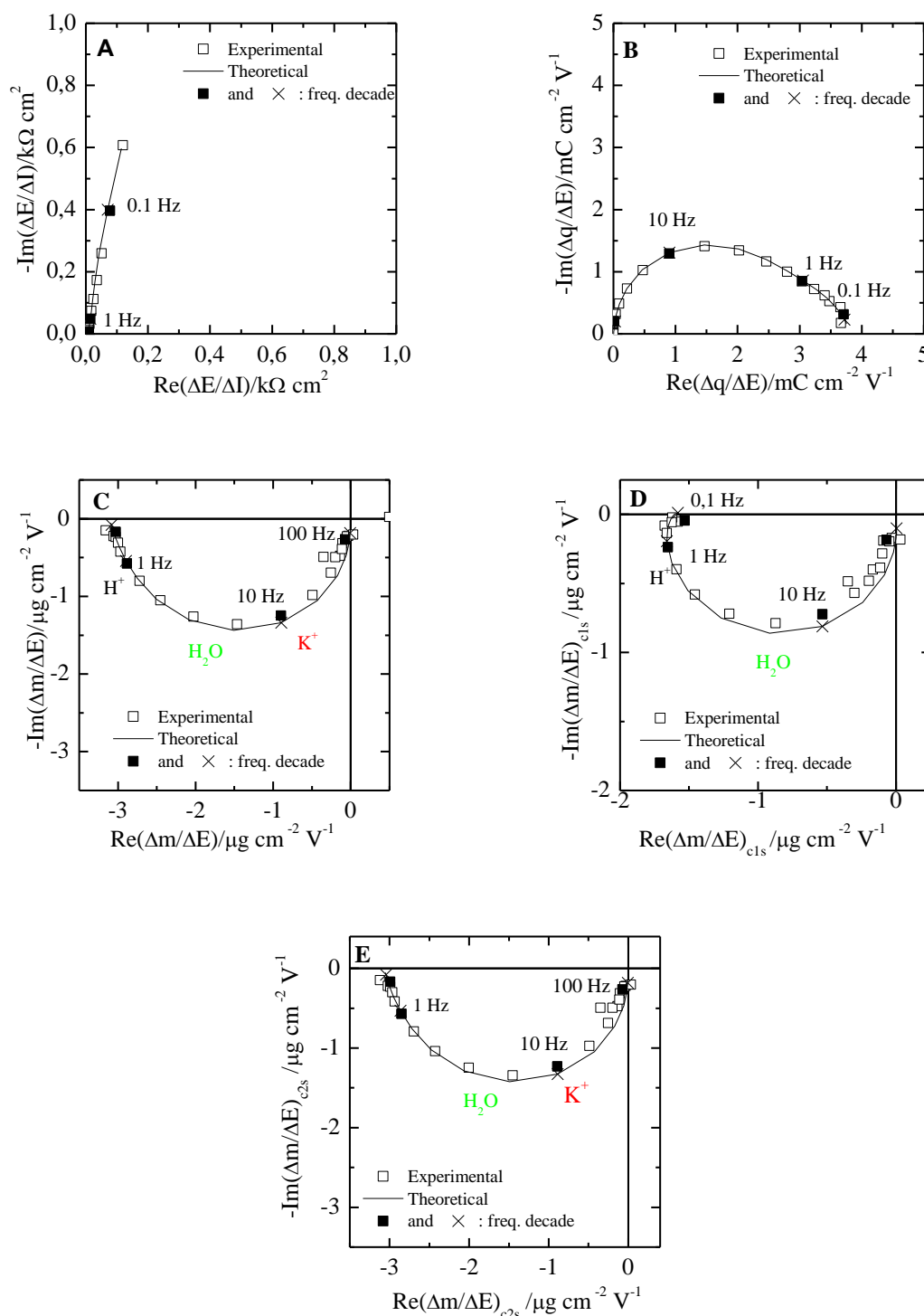


Figure V-6. Experimental and theoretical *ac*-electrogravimetry data of a SWNT-PB thin film in 0.5M KCl measured at - 0.4V vs Ag/AgCl. (A) $\frac{\Delta E}{\Delta I}(\omega)$, (B) $\frac{\Delta q}{\Delta E}(\omega)$, (C) $\frac{\Delta m}{\Delta E}(\omega)$, (D) $\left. \frac{\Delta m}{\Delta E} \right|^{c_{ls}}(\omega)$, (E) $\left. \frac{\Delta m}{\Delta E} \right|^{c_{2s}}(\omega)$. Theoretical functions were calculated with the following parameters: $d_f = 0.4 \mu\text{m}$, $K_{cl} = 1.51 \times 10^{-4} \text{ cm s}^{-1}$, $G_{cl} = 3.77 \times 10^{-8} \text{ mole s}^{-1} \text{ cm}^{-2} \text{ V}^{-1}$, $K_{c2} = 5.03 \times 10^{-3} \text{ cm s}^{-1}$, $G_{c2} = 3.72 \times 10^{-6} \text{ mole s}^{-1} \text{ cm}^{-2} \text{ V}^{-1}$, $K_s = 2.77 \times 10^{-3} \text{ cm s}^{-1}$, $G_s = 7.47 \times 10^{-6} \text{ mole s}^{-1}$, $m_{cl} = 1 \text{ g mole}^{-1}$, $m_{c2} = 39 \text{ g mole}^{-1}$, $m_s = 18 \text{ g mole}^{-1}$.

In the mass/potential transfer function $\frac{\Delta m}{\Delta E}(\omega)$, one big loop appears in the third quadrant at high and medium frequencies (See Figure V-6C). The loops in the third quadrant are characteristic for cation contributions or free solvent molecules in the same flux direction. Another contribution also appears at lower frequencies in the fourth quadrant (anions with opposite flux direction) highlighting the challenge in the exact identification of these two or three loops. The fitting of the experimental data by Mathcad software, using the equations given in Chapter II Section 3.5, showed the presence of two charged species: K^+ at higher frequencies and Cl^- at lower frequencies. The loop at intermediate frequencies is attributed to the free solvent. The identification of these species was achieved by the determination of their molar mass using Equation II-50 Chapter II. Their respective kinetics of transfer were determined by the K_i values. The presence of three different species estimated by simulating the experimental data was further confirmed on a fair analysis of the partial electrogravimetric transfer function, for example, by removing the c2 contribution and calculating $\frac{\Delta m}{\Delta E}\bigg|_{th}^{c1s}(\omega)$ or by removing the c1 contribution and calculating $\frac{\Delta m}{\Delta E}\bigg|_{th}^{c2s}(\omega)$ (Equations II-52 and 53). Figure V-7D and E exhibit a good agreement between the theoretical and experimental data. This partial electrogravimetric transfer function provides a crosscheck for validating the hypothesis involving three different species and allowing a better separation of the various contributions to be attained. The same fitting procedure and validation process was used for all the other potentials and the pertinent parameters for the ions transfer are estimated..

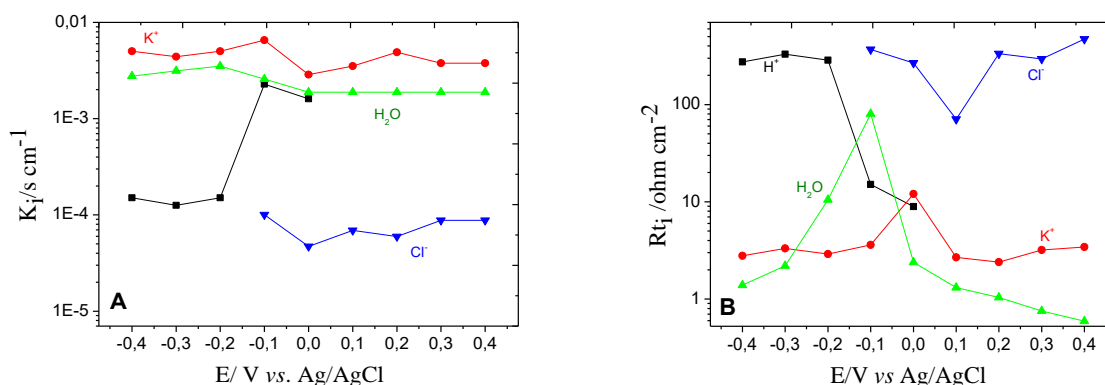


Figure V-7. The kinetic constants K_i (A), and transfer resistances R_{ti} (B) for all species estimated from the fitting of the *ac*-electrogravimetry data measured in 0.5M KCl.

Figure V-7 shows the evolution of transfer kinetics, K_i , and the transfer resistance, Rt_i , of the species as a function of the potential applied. This potential range corresponds to the conditions where the electroadsorption/desorption and insertion/expulsion process of the composite thin film are observed. Based on the K_i values presented in Figure V-7A, the K^+ ion is the fastest of the three species. Furthermore, the transfer kinetics of free water molecules are somewhat close to the values of the K^+ ion. Additionally, these water molecules have the same flux directions as the cations, suggesting that it might be the water molecules that accompany the transfer of K^+ , most likely due to the electrodragging. Chloride anions appear only for the more anodic potentials which indicates that the capacitive CNTs film behavior is dominant in this potential range. If we compare the K^+ ions kinetics of the composite film with that observed in pristine SWCNTs, one can say that the presence of PB on the surface of SWCNTs does not slow down the transfer dynamics of K^+ ions (similar K_i in SWCNTs, Figure IV-24A). Additionally, the contribution of potassium ions in the composite film is enlarged to the whole potential range (Figure V-7A).

The transfer resistance values shown in Figure V-7B reveal that K^+ is transferred easier than Cl^- , which is corroborated by the kinetic values previously mentioned. For free solvent molecules, the transfer resistance value is smaller for the extreme potential values but in the PB electroactivity domain, this value becomes higher: H_2O is more difficult to be transferred in the redox PB domain compared to potassium ions. Indeed, when only PB films are examined, free water molecules were not detected which is in line with the present observations.^{3,203}

The transfer kinetic rates of H^+ in the SWCNT/PB are more significant than the transfer kinetic rates of H^+ in SWCNT, probably due to the difference in pH (Figure IV-24B). The transfer kinetic rates of Cl^- in the SWCNT/PB are less significant than the transfer kinetic rates of Cl^- in the SWCNT (Figure IV-24C). Considering the transfer resistance values of Kt_i ions, the K^+ from the SWCNT-PB are equivalent to the K^+ from the SWCNT (Figure IV-25A). The H^+ from the SWCNT-PB are easier transferred than H^+ from SWCNT (Figure IV-25B). The Cl^- from SWCNT-PB are more difficult transferred than the Cl^- from the SWCNT (Figure IV-25C).

As mentioned previously, in SWCNT/PB the transfer kinetic rates of K^+ is equivalent to the transfer kinetic rates of K^+ from the SWCNT (Figure IV-24A), thus advantageously, the presence of PB does not hinder the electroadsorption process of cations.

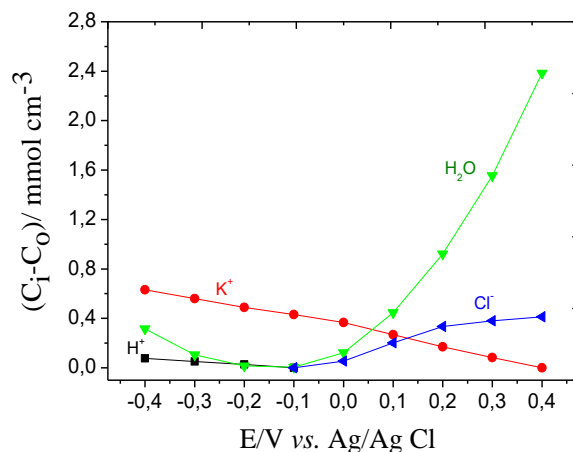


Figure V-8. Evolution of the relative concentration, $C_i - C_0$, of each species over the applied potential measured in 0.5M KCl.

In order to quantify the role of each species, $\left. \frac{\Delta C_i}{\Delta E} \right|_{\omega \rightarrow 0} = -\frac{G_i}{K_i}$ has been calculated as a

function of the applied potential. The integration of the $\left. \frac{\Delta C_i}{\Delta E} \right|_{\omega \rightarrow 0}$ against potential gives the relative

concentration change, $(C_i - C_0)$. Figure V-8 shows the relative concentration change for the ionic species involved in the electrochemical process. The $C_i - C_0$ values for H_2O are significantly higher than the $(C_i - C_0)$ values of K^+ and Cl^- , especially at more anodic potentials. Furthermore, all the species show different behaviors probably related to the composite structure: at more cathodic potentials, the concentration of K^+ increases in the studied potential window and the anions are not detected beyond -0.1V vs. Ag/AgCl. The potassium species are detected at all potentials indicating a collective effect of the composite structure, *i.e.* potassium species due to the redox of PB and the electroadsorption on SWCNTs. The anions are detected only at anodic potentials indicating that they are related to the electroadsorption process on SWCNTs. The free water molecules accompany the potassium ions at cathodic potentials, but at more anodic potentials, the concentration of H_2O and Cl^- increases. These behaviors are probably due to the mixed Faradaic and non-Faradaic mechanisms which occur in the film.

As a comparison, we have detected that the $C_i - C_0$ values of the species K^+ , Cl^- and free solvent are more significant in the composite SWCNT-PB thin films than in pristine SWCNT thin films. Furthermore, the $C_i - C_0$ values of the free solvent in the SWCNT-PB are also higher and equivalent, at anodic potentials, and cathodic potentials, respectively; as compared to the pristine SWCNT thin films (Figure IV-26C). These results indicate that the relative concentration of the species is

significantly increased in the case of the SWCNT/PB composite structure, which probably is the reason for the significantly higher specific capacitance values obtained in Figure V-5 (114 F g^{-1}). It is important to remind that this value is obtained from cyclic voltammetry and corresponds to a certain scan rate of the potential and may not be representative of all the species contributing with different kinetics. Therefore, we have calculated from the instantaneous capacitance values of each ion from *ac*-electrogravimetry data.

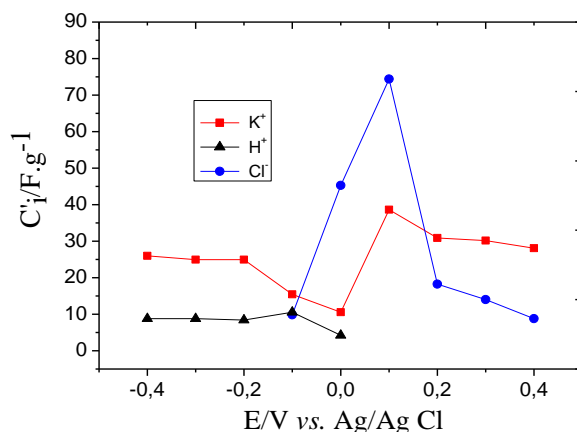


Figure V-9. Instantaneous capacitance values, C_i' , calculated from *ac*-electrogravimetry data.

Figure V-9 shows the instantaneous capacitance values of each ion, C_i' , calculated as a function of the potential. These correspond to the capacitance attributed to cation (K^+) and anion (Cl^-), respectively and calculated using the relation expressed previously. The capacitance values calculated from the *ac*-electrogravimetry data differ from that found from the cyclic voltammetry but they are in the same order of magnitude. This difference is due to the kinetics and ease/difficulty of each species to be inserted/electroadsorbed (K_i , Rt_i). *Ac*-electrogravimetry takes into account of these aspects and the capacitance contribution of two different species with different kinetic constants are separately calculated.

In comparison, the instantaneous capacitance values of the K^+ and H^+ are slightly higher for the SWCNT-PB than those for the SWCNT (Figures IV-27A and B). The instantaneous capacitance values of Cl^- are also more significant in the SWCNT-PB than in SWCNT (Figure IV-27C). These results further indicate the faradaic contribution to the charge storage process of the SWCNTs in the presence of PB.

V-1.2. SWCNT/Polypyrrole Thin Film Electrodes

V-1.2.1. Structure and Morphology of the SWCNT/PPy Composites

The surface morphology of SWCNT/Polypyrrole (PPy) thin films was characterized by FEG-SEM as shown in Figure V-10. After 2 cycles (cyclic Voltammetry) of electrodeposition of the PPy (dodecylsulphate doped (DS^-)) on the SWCNT based electrodes a typical cauli-flower-like structure was formed on the thin layer of CNT films which corresponds to polypyrrole.

The cross-section of the SWCNT/PPy shown in Figure V-10B permits the determination of the thickness of the composite thin films. The thickness slightly inhomogeneous along the thin film and presents a variation between 350 to 550 nm. The electrodeposited PPy component (only 2 cycles of electrodeposition) on the SWCNTs does not change the film thickness significantly and the gravimetric regime is kept for the QCM based analysis. It is important to note that the composite film thickness is mainly governed by the SWCNT layer under these experimental conditions.

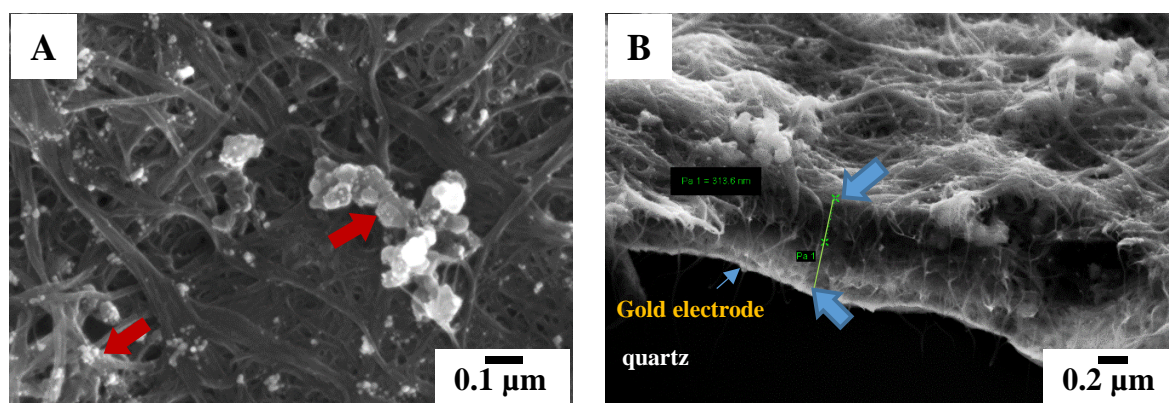


Figure V-10. SEM-FEG images of SWCNT/PPy nanocomposite film in surface (A) and in cross-section (B).

V-1.2.2. EQCM Study of the SWCNT/PPy Composites

Figure V-11A shows the current and Figure V-11B shows the mass changes of the SWCNT/PPy film when it is oxidized and reduced between 0.45V and -1.2V vs Ag/AgCl at three different scan rates of 25mV.s^{-1} , 50mV.s^{-1} and 100mV.s^{-1} in a 0.5M NaCl solution (pH 7). The slight contribution of the PPy component is evident in the CV responses (Figure V-11A), as compared to that of pristine SWCNTs. When the composite film was reduced, a mass increase was observed and when it was oxidized, a mass loss was observed. Indeed, when the polymer film was

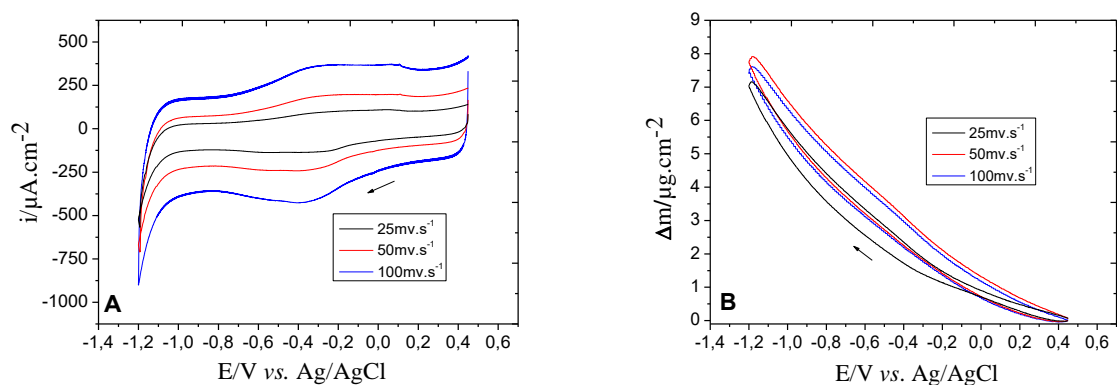


Figure V-11. The EQCM results of SWCNT/PPy thin films: (A) current vs. potential and (B) mass variation vs. potential profiles measured in aqueous electrolyte 0.5 M NaCl.

oxidized, a positive charge is created inside the film and positively charged species should be expelled to counterbalance the latter. Unfortunately, these analytical technique appear very limited, because the charge compensation can be due also to the concomitant insertion of anions or to solvated cations or to a mixture of these species. Consequently, only dynamics approaches can lead to a fair separation of these processes.

Figure V-12 shows the Fdm/dq function calculated from the EQCM data as a function of potential, which is equivalent to the global molecular mass of the species obtained from the reduction branch in the range 0.4V to -1.2V vs Ag/AgCl in 0.5M NaCl. At more cathodic potentials, the values of the molecular mass vary in the range of 50-200 g.mol^{-1} which could correspond to Na^+ with high number of hydration or Na^+ accompanied by free solvent. In anodic potentials, the values of the molecular mass vary in the range 0-50 g.mol^{-1} , which is also difficult to be attributed to a single ion contribution.

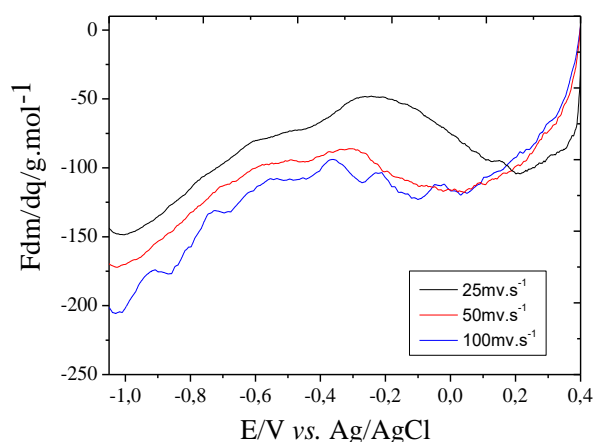


Figure V-12. The Fdm/dq values as a function of the applied potential, obtained from the reduction branch of the EQCM results measured in 0.5 M NaCl.

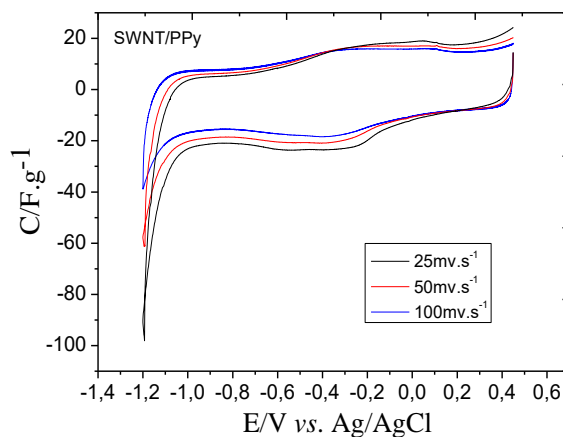


Figure V-13. Specific capacitance values (calculated from Figure V-4) as a function of potential at three selected scan rates, measured in 0.5M NaCl.

Figure V-13 depicts the variation of capacitance values as a function of the potential applied under the same conditions as mentioned previously. The capacitance values are estimated to be around 25 to 30 F g⁻¹ in the range from 0.45V to -1V vs. Ag/AgCl. These values of capacitance are in the same order of magnitude that pristine SWCNT thin film electrodes.

A small dependence to the scan rate values is observed (more pronounced in the Fdm/dq function in Figure V-12 but also in Figure V-13) which suggest that depending on the scan rate, different species may contribute to the electroadsorption and faradaic processes. Indeed, the information obtained from the EQCM is insufficient for a thorough explanation of the transfer mechanism of the different species. As *ac*-electrogravimetry was proven to be a strong complementary tool in the CNT study, the composite films were also analyzed with this methodology.

V-1.2.3. *Ac*-electrogravimetry Study of the SWCNT/PPy Composites

The measurements were performed each 200 mV in the range from 0.4V to -1.2V vs Ag/AgCl in 0.5M NaCl electrolyte. Figure V-14 shows an example of the experimental and theoretical transfer functions (TFs) obtained from *ac*-electrogravimetry of a SWCNT/PPy thin film in 0.5 M NaCl electrolyte at -0.4V vs Ag/AgCl.

The experimental data were fitted according to the model presented in Chapter II, Section 3.5. Figure V-14 reveals a good agreement between experimental data and theoretical curves. First, the electrochemical impedance $\frac{\Delta E}{\Delta I}(\omega)$ responses (Figure V-14A) present a slightly distorted straight line indicating that there is a multi-ion transfer contribution.

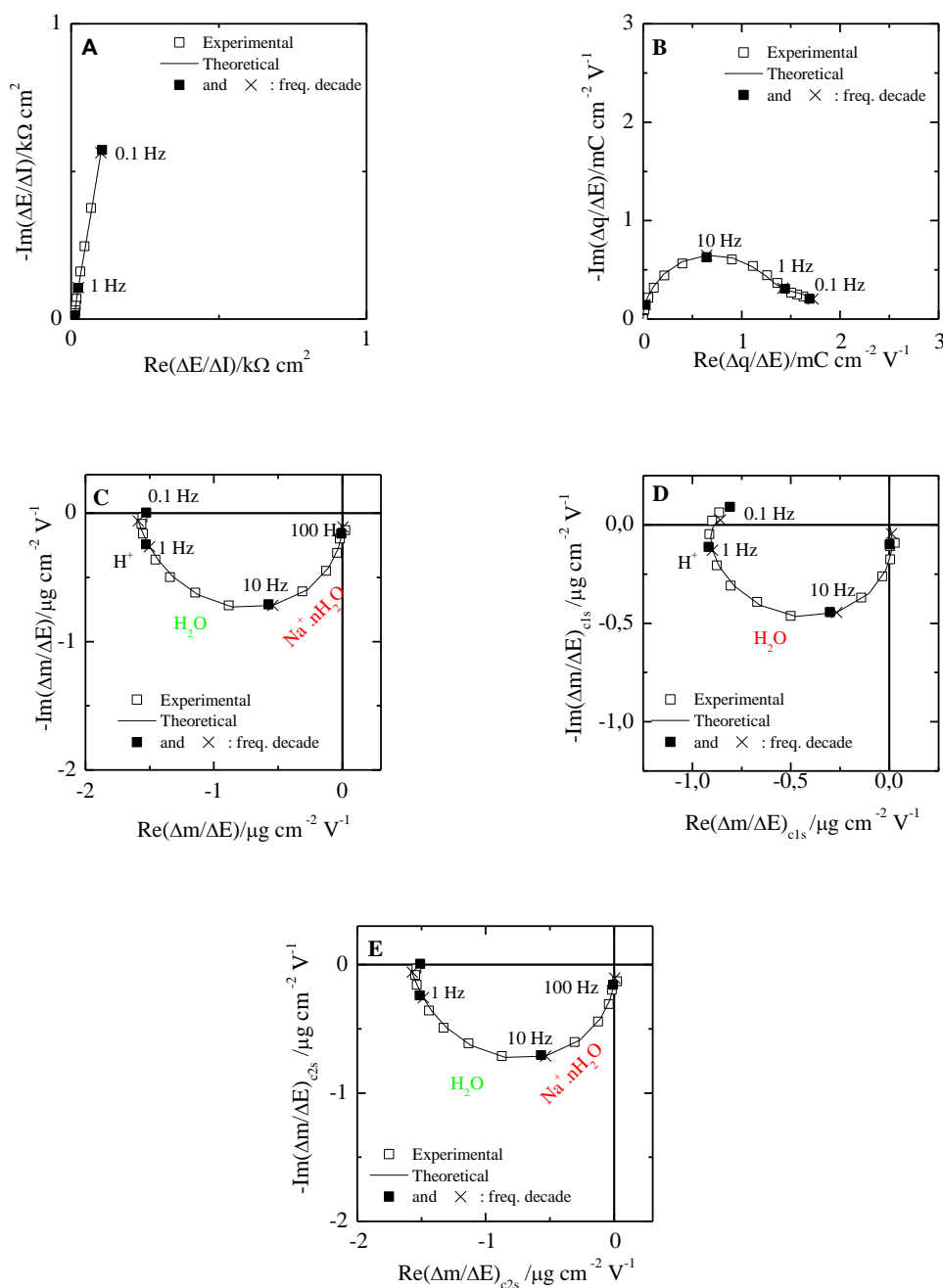


Figure V-14. Experimental and theoretical *ac*-electrogravimetric data of the SWNT-PPy thin film

in 0.5 M NaCl measured at -0.4V vs Ag/AgCl. (A) $\frac{\Delta E}{\Delta I}(\omega)$, (B) $\frac{\Delta q}{\Delta E}(\omega)$, (C) $\frac{\Delta m}{\Delta E}(\omega)$, (D)

$\frac{\Delta m}{\Delta E}\bigg|^{cls}(\omega)$, (E) $\frac{\Delta m}{\Delta E}\bigg|^{c2s}(\omega)$. Theoretical functions were calculated with the following parameters: $d_f = 0.4 \mu\text{m}$, $K_{c1} = 9.50 \times 10^{-5} \text{ cm s}^{-1}$, $G_{c1} = 7.98 \times 10^{-9} \text{ mol s}^{-1} \text{ cm}^{-2} \text{ V}^{-1}$, $K_{c2} = 3.46 \times 10^{-3} \text{ cm s}^{-1}$, $G_{c2} = 9.3 \times 10^{-7} \text{ mol s}^{-1} \text{ cm}^{-2} \text{ V}^{-1}$, $K_s = 1.97 \times 10^{-3} \text{ cm s}^{-1}$, $G_s = 1.99 \times 10^{-6} \text{ mol s}^{-1}$, $m_{c1} = 1 \text{ g mol}^{-1}$, $m_{c2} = 23+18 \text{ g mol}^{-1}$, $m_s = 18 \text{ g mol}^{-1}$.

Consequently, it is difficult to extract information from this transfer function. The charge/potential transfer functions (TFs), $\frac{\Delta q}{\Delta E}(\omega)$ (Figure V-14B), permit the separation of the ionic contributions, however, without any possibility to identify the ionic species involved. Figure V-14B shows one flattened loop, which can be attributed to at least two species, where their time constants are not sufficiently different from each other to obtain perfectly separated loops.

In the mass/potential transfer function $\frac{\Delta m}{\Delta E}(\omega)$, one big loop appears in the third quadrant involving contributions at high and medium frequencies (Figure V-14C). The loops in the third quadrant are characteristic for cation contributions or free solvent molecules in the same flux direction. The fitting of the experimental data by Mathcad software, using the equations given in Chapter II, showed the presence of two charged species: $\text{Na}^+ \cdot n\text{H}_2\text{O}$ at higher frequencies and H^+ at lower frequencies. The loop at intermediate frequencies is attributed to the free solvent. The identification of these species was achieved by the determination of their molar mass using Equation II-50 in Chapter II and their respective kinetics of transfer were illustrated by their K_i values. The presence of three different species estimated by simulating the experimental data was further confirmed by carefully analyzing the partial electrogravimetric transfer function, for example, by removing the cation 1 contribution and calculating $\left. \frac{\Delta m}{\Delta E} \right|^{c2s}(\omega)$ or by removing the cation 2 contribution and calculating $\left. \frac{\Delta m}{\Delta E} \right|^{c1s}(\omega)$ (Equations II-52 and 51). Figures V-14D and E exhibit a good agreement between the theoretical and experimental data. As mentioned for the other electrode systems presented earlier, these partial electrogravimetric transfer functions provide a crosscheck for validating the hypothesis involving three different species and a better separation of the various contributions. If the atomic masses chosen to identify the species are different than reality, a good agreement cannot be obtained. Given that we have a perfect agreement for all the TFs, we can say that our assumption is valid for modelling all the TFs at this potential (-0.4V vs Ag/AgCl).

For potentials more cathodic than -0.3 V vs Ag/AgCl, the contribution of only three species is found mixing the two cations, $\text{Na}^+ \cdot n\text{H}_2\text{O}$ and H^+ , and free solvent water following the same transfer direction. For more anodic potential values, the proton contribution disappears and chloride species is found at very low frequencies.

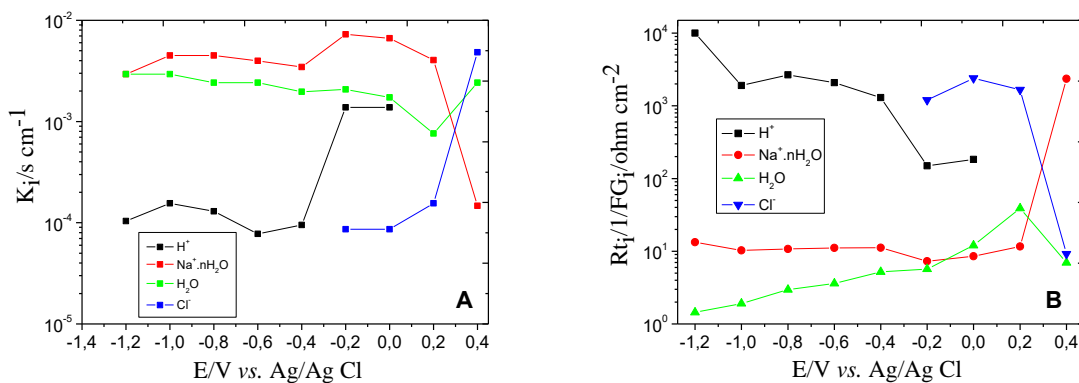


Figure V-15. The transfer kinetic constants, K_i (A), and transfer resistance, R_t (B) for all species estimated from the fitting of the *ac*-electrogravimetry data of SWCNT-PPy composite measured in 0.5M NaCl.

Figures V-15A and B show the evolution of the transfer kinetic rates, K_i , and the transfer resistance, R_t , of the species as a function of the potential applied. This potential range corresponds to the conditions where the electroadsorption/desorption or insertion/expulsion processes of the thin film are observed. Based on the K_i values presented in Figure V-15A, the $\text{Na}^+.n\text{H}_2\text{O}$ ion is the fastest of the four species. This observation may be correlated to the easier dehydration process of the sodium species compared to the protons where their transfer occurs at low frequencies. Additionally, the concentration of the protons in the electrolyte is much lower compared to that of sodium species at this pH. Furthermore, the transfer kinetic rates of free water molecules are somewhat close to the values of the $\text{Na}^+.n\text{H}_2\text{O}$ ions. Chloride ions appear only at low frequencies and at more anodic potentials.

In SWCNT/PPy composites, the transfer kinetic rates of $\text{Na}^+.n\text{H}_2\text{O}$ are only slightly lower than the K_i of the $\text{Na}^+.n\text{H}_2\text{O}$ in pristine SWCNTs and higher than the K_i of the Na^+ species detected in pristine PPy (a previous work from our group)²²⁴, measured under similar conditions. These results indicate that the composite structure does not hinder the sodium species transfer. Additionally, the contribution of the sodium species to the charge compensation process (both electrostatic and faradaic) is enlarged to the whole potential range, *i.e.* 0.4V to -1.2V vs Ag/AgCl (larger than that used for SWCNTs alone).

For the other species, the following trends were observed: (i) the transfer kinetic rates of the H^+ in the SWCNT/PPy are faster than the transfer kinetic rates of H^+ in the SWCNT and (ii) the transfer kinetic rates of the Cl^- in the SWCNT/PPy are more or less equivalent to the transfer kinetic rates of the Cl^- in the SWCNT (See Figure III-9 Chapter III) and more significant than the transfer kinetic rates of the Cl^- for pristine doped PPy.²²⁴

Considering the transfer resistance values of the R_{ti} ions, the $\text{Na}^+ \cdot n\text{H}_2\text{O}$ species from the SWCNT-PPy are slightly more difficult to be transferred compared with the $\text{Na}^+ \cdot n\text{H}_2\text{O}$ species in the SWCNT (10 ohm.cm^{-2} versus 2 ohm.cm^{-2}) (Figure V-15 and Figure III-9) The R_{ti} of H^+ in the SWCNT-PPy composite is more or less equivalent to that in pristine SWCNT. The R_{ti} of Cl^- in the SWCNT-PPy composite is comparable to that of obtained in pristine SWCNT (See Figure III-9 Chapter III) and that of found in doped PPy electrodes.²²⁴

Taking into consideration of the K_i and R_{ti} values of various species detected, one can suggest that there is no major hindrance of the ions transfer when doped PPy is deposited on the SWCNT electrodes. The species detected are related to the electroactivity of the two components. For example, at the anodic potentials, there is no cation contribution in pristine SWCNTs whereas it exists in the composite structure, due to the PPy.

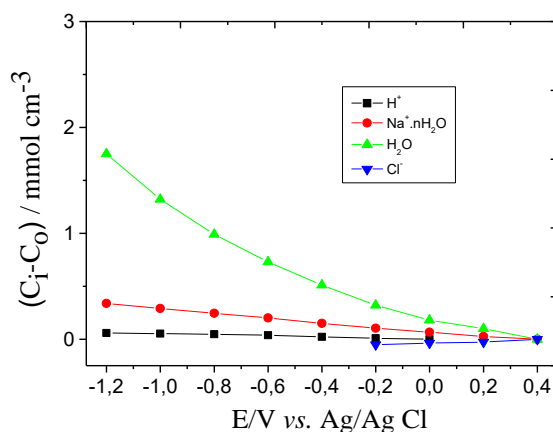


Figure V-16. Evolution of the relative concentration, $C_i - C_0$ of each species over the potential applied measured in 0.5M NaCl SWCNT-PPy.

Figure V-16 shows the relative concentration change for the ionic species. The $C_i - C_0$ values for H_2O are significantly higher than the $C_i - C_0$ values of $\text{Na}^+ \cdot n\text{H}_2\text{O}$, H^+ and Cl^- . The relative concentration change of the $\text{Na}^+ \cdot n\text{H}_2\text{O}$ in SWCNT-PPy are equivalent to the $C_i - C_0$ values of the $\text{Na}^+ \cdot n\text{H}_2\text{O}$ in pristine SWCNT. These values are also in good agreement with the $C_i - C_0$ values of Na^+ detected in doped PPy structures.²²⁴ The same trend was observed for H^+ and Cl^- anions, $C_i - C_0$ values of the H^+ and Cl^- did not change considerably in the SWCNT-PPy composite compared to SWCNTs alone (Figure III-11A Chapter III). The $C_i - C_0$ values of the free solvent in SWCNT-PPy composite are significantly higher than the $C_i - C_0$ values of the free solvent in the SWCNT. These values are rather equivalent to the that obtained for doped PPy thin films (based on earlier work in our group).²²⁴ This indicates that the water transfer is related to the doped PPy of the composite electrode.

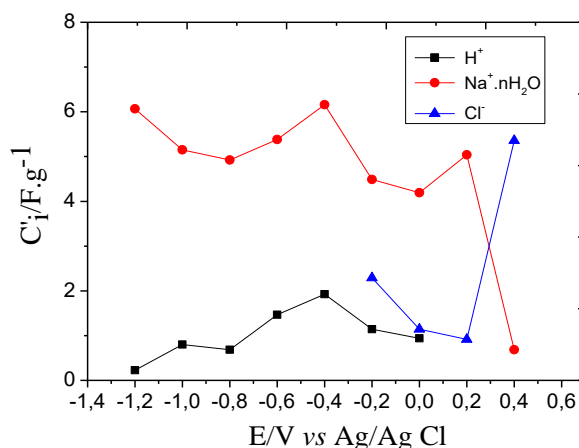


Figure V-17. The instantaneous capacitance values calculated from ac-electrogravimetry data SWCNT-PPY.

To evaluate the capacitance contribution of each species, the instantaneous capacitance values of each ion (C'_i) calculated as a function of the potential (Figure V-17). These correspond to the capacitance attributed to cation 1 (H^+), cation 2 ($Na^+.nH_2O$) and anion (Cl^-), respectively. The capacitance values calculated from the *ac*-electrogravimetry data slightly differ from that found from the cyclic voltammetry because it takes into account of dynamic aspects of ion transfer.

These instantaneous capacitance values of the $Na^+.nH_2O$, H^+ and Cl^- are lower than those obtained in the previous composite electrode with PB (SWCNT-PB, Figure IV-12A Chapter IV). Also, in the case of SWCNT-PB, we have detected that the C_i-C_0 values of the species K^+ , Cl^- and free solvent are more significant than in pristine SWCNT thin films. Consequently, the instantaneous capacitance values of the K^+ and H^+ are slightly higher for the SWCNT-PB than those for the SWCNT (Figures IV-27A and B). From these points of view, one can say that SWCNT-PB composites are more performant than the SWCNT-PPy composites. To reach a definite conclusion on this point, further studies for example by changing the SWCNT/PPy or SWCNT/PB ratios are required. Clearly, in both composites, cationic species contribution (sodium in the present study) to the charge compensation process (both electrostatic and faradaic) is enlarged to the whole potential window (larger than that used for SWCNTs alone). This can be considered as an advantage when they are used as capacitive electrodes.

V-2. Beyond Carbon Nanotube Based Electrodes

V-2.1. Electrochemically Reduced Graphene Oxide (ERGO) Thin Film Electrodes

The electrochemical reduction was performed in a 3-electrode electrochemical cell, as described previously in Chapter II. The reduction was achieved in aqueous 0.5M $NaNO_3$ solution.

Nitrogen bubbling was performed for 10 minutes to remove the dissolved oxygen in the solution. A platinum grid and an Ag/AgCl served as the counter electrode and the reference electrode, respectively.

V-2.1.1. Structure and Morphology of the ERGO Thin Film Electrodes

The surface morphology of GO and ERGO was characterized by FEG-SEM as shown in Figure V-18. Thin layers of GO sheets appear crumpled and folded into a typical wrinkled structure. This characteristic crumpled aspect remains after electrochemical reduction and is similar to that of GO sheets reduced chemically or thermally.²²⁵ This geometric wrinkling is caused by nanoscale interlocking of GO sheets, bringing good mechanical properties, surface roughness and a larger specific surface area.²²⁵ The cross-section of the GO layers, deposited on the QCM electrode surface, before and after reduction shown in Figure V-19 allows the determination of the thin film thickness (70 nm and 50nm for GO and ERGO, respectively).

The reduced thickness may indicate the removal of oxygen containing functional groups in the GO carbon plane due to the reduction process, which is in agreement with earlier studies.²²⁶ EDX results showed a decrease of the amount of oxygen on the surface.

According to Table V-1, the amount of oxygen declines from 36.1% to 20.6% during the reduction. Although not completely (lost oxygen), this result suggests that a substantial amount of the oxygen containing functional groups are removed during electrochemical reduction which resulting in a graphene-like material.

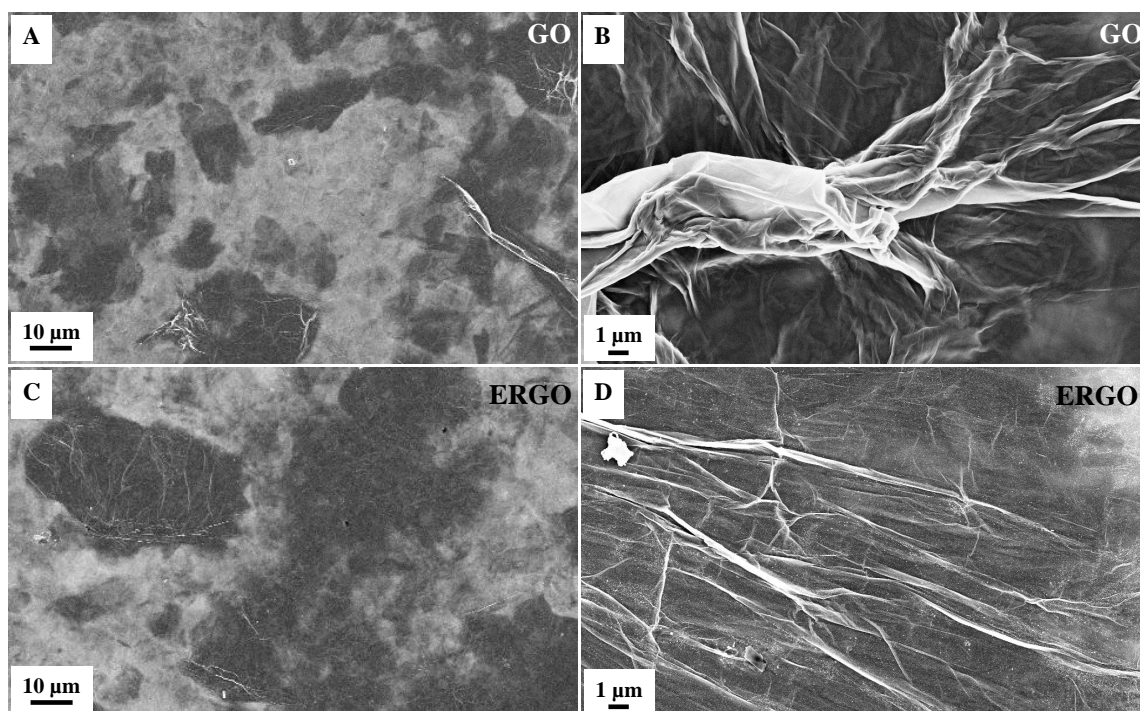


Figure V-18. FEG-SEM images of GO (A and B) and ERGO (C and D) thin films.

The thickness of the film was estimated to 70 nm and 50 nm for GO and ERGO, respectively.

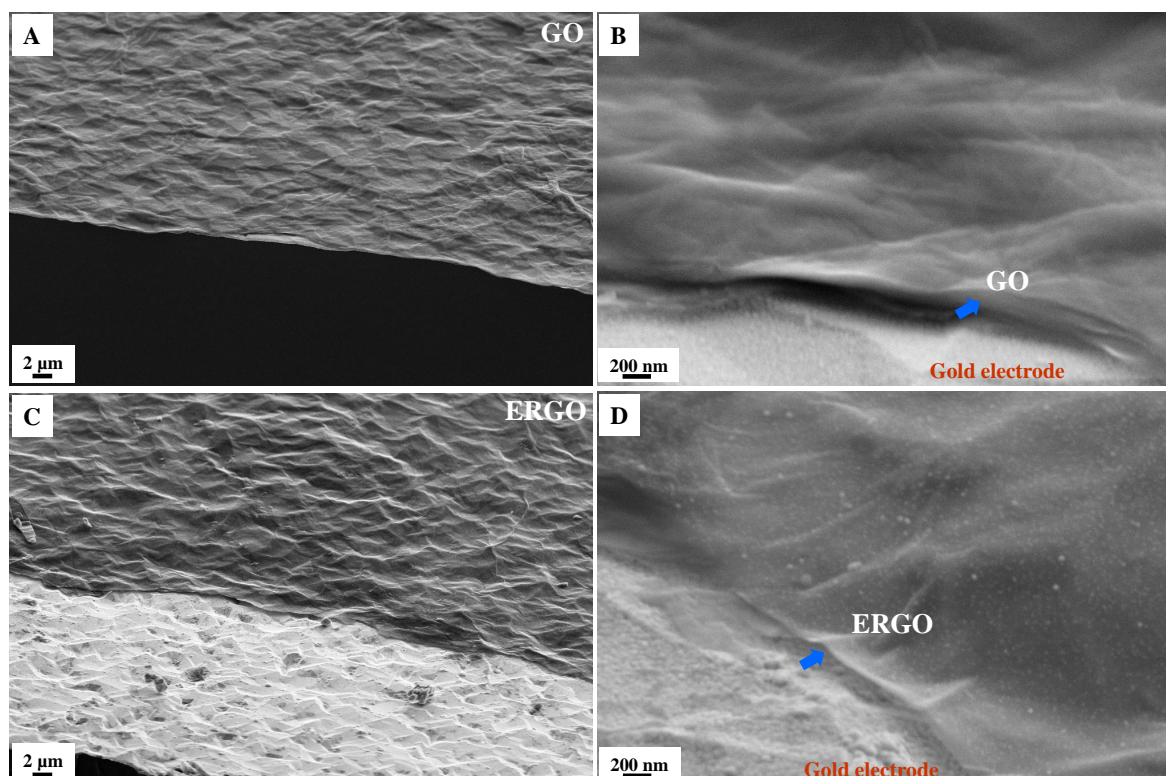
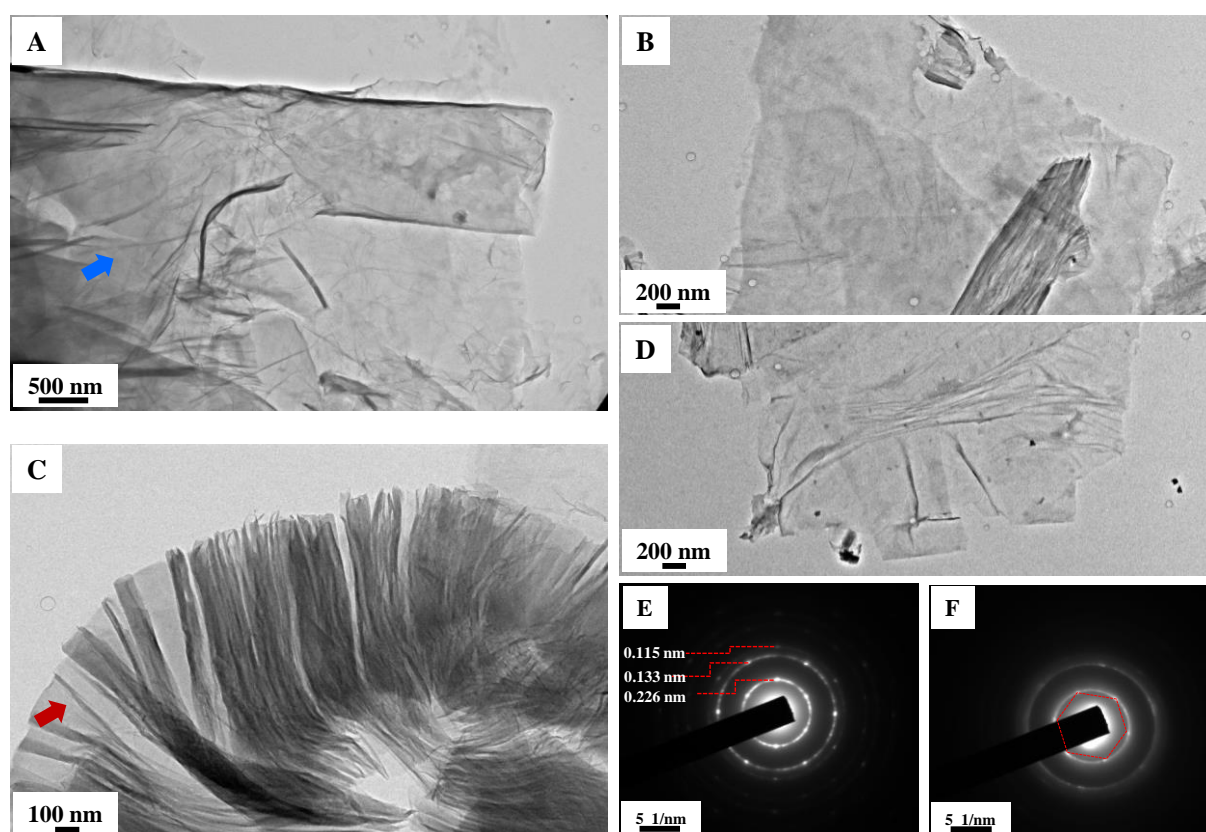


Figure V-19. FEG-SEM images of the cross-section of the ERGO thin films, revealing the thickness of the film before and after reduction.

Table V-1: EDX results of GO and ERGO thin films: carbon and oxygen amount in GO and ERGO.

	GO	ERGO
Average Carbon content (%)	63.9±1.5%	79.4±3.6%
Average Oxygen content (%)	36.1±1.5%	20.6±3.6%

**Figure V-20.** HR-TEM images of ERGO (A-D) and selected area electron diffraction patterns (SAED) (E and F taken from A and C, respectively).

The ERGO thin films were scraped off the substrate and ultrasonicated in ethanol before being placed on copper TEM grids. The HR-TEM images in Figure V-20 shows characteristic 2D nanosheets, (a few layers) bearing transparent and wrinkled features with corrugation. Such wrinkles are due to the sp^3 hybridized carbons within the network, which cause structure distortions.²²⁷ These nanosheets deform without a structural break-down (Figure V-20C), thus ERGO in the present study exhibits good mechanical properties of a graphene-like material. The SAED patterns taken from two different domains (shown by arrows on Figures V-20A and C) are presented in Figure V-20E and F, respectively. Both diffraction patterns show rings, but also

diffraction spots with the appearance of six-fold symmetry, which is an indication of crystalline order (the presence of graphene-like structures).²²⁸ However, the appearance of diffraction rings indicates that a portion of the ERGO is polycrystalline, *i.e.* no preferred stacking orientation between the ERGO monolayers. The six-fold symmetry is more obvious in the SAED pattern (Figure V-12E) taken from Figure V-12A (less number of layers of ERGO) suggesting that the layers of ERGO consist of conjugated domains with less structural defects in the sp^2 planes.

The crystalline structures of GO and ERGO were evaluated by XRD technique (Figure V-21). The diffraction peak of GO at 12.5° (002) (Figure V-21A) corresponds to an interlayering distance (d-spacing) of 0.70 nm.

Classically, graphite has a sharp peak at $2\theta=26.38^\circ$ representing the ordered organisation with an interlayer distance of 0.34 nm along (002) orientation.²²⁹ Increase in the d-spacing in the case of GO (Figure V-21A) is explained by the introduction of the oxygen containing functional groups and water molecules adsorbed between the layers. This observation is in good agreement with previous reports in literature.^{230,231} After electrochemical reduction, the peak located at 12.5° disappeared and a broad band appeared at around 25° , confirming the reduction of the GO (Figure V-21B).

The broad peak appearing at $2\theta=25^\circ$ corresponds to a d-spacing of 0.38nm. This decrease compared to that of GO (0.70 nm) is attributed to the oxygen removal.²³²

The electrochemical reduction of grapheme oxide was followed in situ using Raman spectroscopy. Figure V-22 shows the Raman spectra of pristine GO ($t = 0$ min) and ERGO ($t = 44$ min). These Raman spectra exhibit three particular bands: one of the most prominent feature around 1580 cm^{-1} is the so-called G mode (G as “graphitic”) due to the relative motion of sp^2 carbon atoms which appears around 1580 cm^{-1} ; the other one which appears around 1350 cm^{-1} is the D band (D as “defect”) and is due to the out-of-plane breathing mode of the sp^2 carbons.²³³ The small double band around 2700 cm^{-1} is the 2D mode (sometimes called G’ mode).

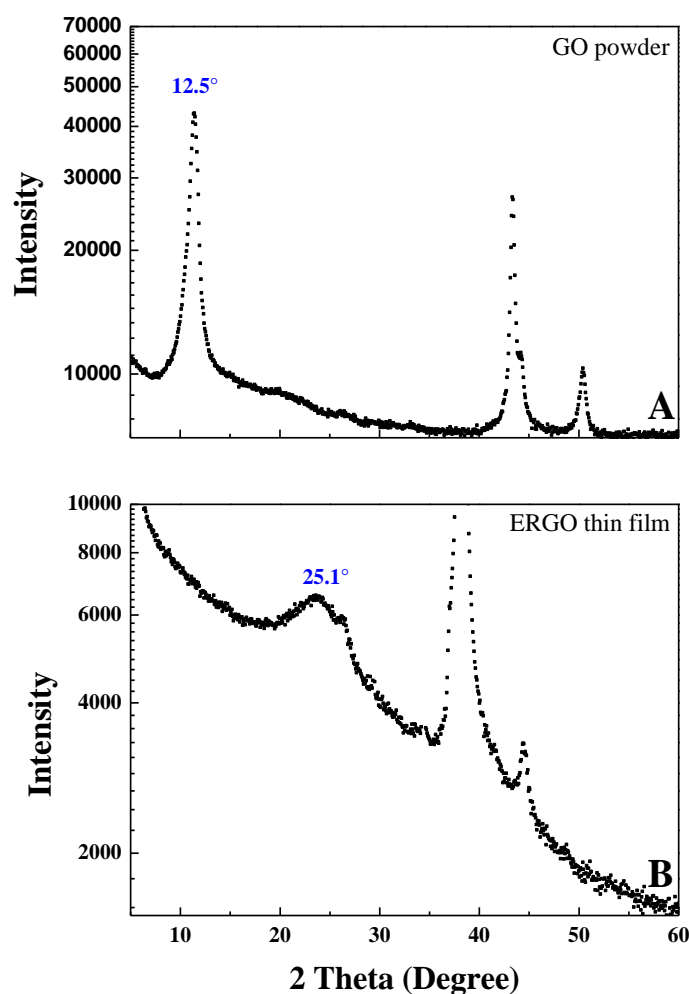


Figure V-21. XRD spectra of GO powder (A) and ERGO thin films deposited on quartz resonators (B). (Cu K α radiation ($\lambda = 1.541\ 84\ \text{\AA}$), main peaks for GO and ERGO are indexed, residual peaks are due to the substrate).

The D mode is usually related to a forbidden transition, however in the presence of disorder the symmetry is broken and the transition becomes allowed. As first reported on amorphous carbon⁶⁵ and then, on graphene^{234,235}, this band appears for example on the edge of graphite and also on the basal planes if sp^3 defects break the sp^2 lattice in case of covalent modification of graphene surface. It was demonstrated that Raman spectroscopy and especially the study of the relative intensities or areas of the D and G bands could provide quantitative information about the amount of sp^3 -type defects in sp^2 lattice.²³⁶

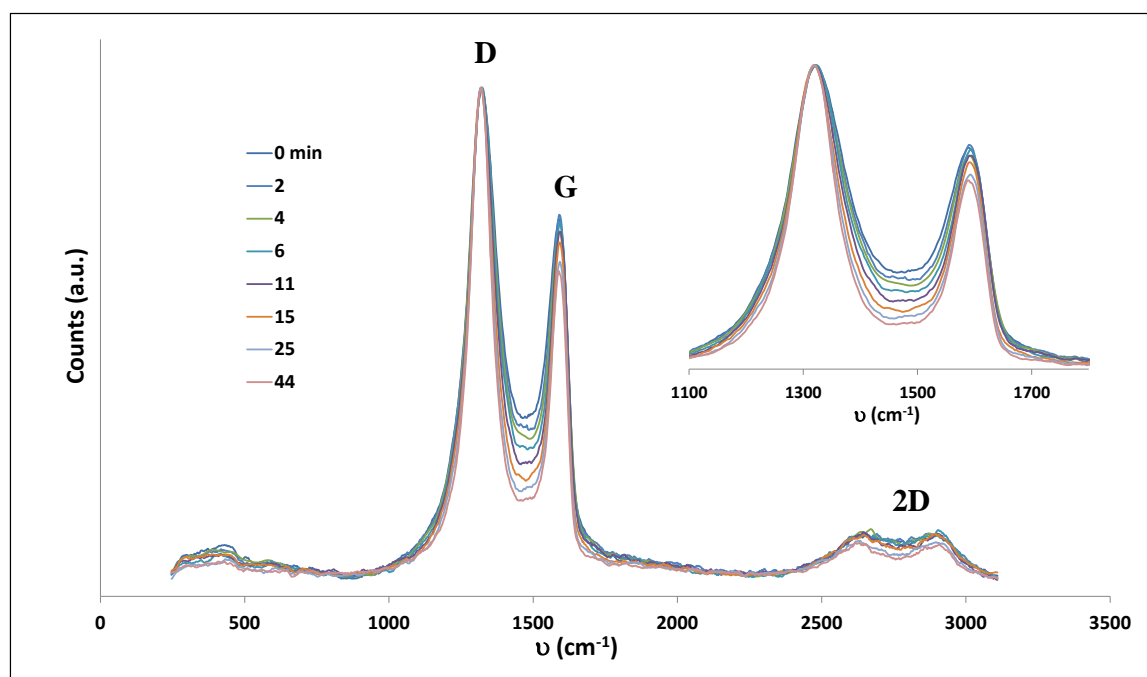


Figure V-22. Evolution with time of the Raman spectra of a graphene oxide sample upon polarization at -1.1 V vs. Ag/AgCl. Spectra were normalized vs. D peak intensity

The 2D mode is a second order two-phonon process and corresponds to an overtone of the D band. Upon reduction one can notice that D and G peaks become sharper and more separated, indicating that ERGO is more crystalline than GO (Figure V-22). Amorphous carbon indeed display broad and poorly defined D and G peaks, while graphitic carbon shows intense and well separated D and G peaks.

V-2.1.2. EQCM Study of the ERGO Thin Film Electrodes

The capacitive charge storage behavior of the ERGO electrodes were studied by cyclic voltammetry (CV), and the mass variations of the electrodes were simultaneously monitored by quartz crystal microbalance (QCM) measurements (Figure V-23). Figures V-23A, C and E show the cyclic voltammetry responses of ERGO thin films obtained in aqueous electrolytes of 0.5 M LiCl, NaCl and KCl. For all studied media, a growing capacitive current was observed when the scan rate increased. Purely capacitive materials exhibit perfect rectangular-shaped cyclic voltammetry responses.²³⁷ In the present study, the ERGO thin films show quasi-rectangular shaped responses indicating that the charge storage is mainly due to the reversible electroadsorption/insertion of electrolyte ions. The slight distortion from a perfect rectangular shape is due to the presence of a slight faradaic contribution to the charge storage. This small faradaic contribution can be due to several reactions such as the reduction of the proton present in the electrolyte, the reduction of remaining surface functional groups on ERGO *etc.*... Nevertheless, in the three different electrolytes the average values of the current are fairly similar.

The mass variations of the ERGO modified quartz resonators are determined simultaneously during the cyclic voltammetry. It can be noticed that similar current values are obtained in LiCl and KCl electrolytes (Figures V-23A and E), which indicates that the same amount of charge is electroadsorbed at the electrode/electrolyte interface. The mass variations are also fairly similar between LiCl and KCl (Figures V-23B and F).

In a theoretical view, if only the cation is transferred during the electroadsorption process, the mass variation should be about 5 times higher when cycled in aqueous KCl electrolyte because of the higher molar mass of K^+ ions compared to Li^+ ($M_{K^+}=39 \text{ g mol}^{-1}$, $M_{Li^+}=7 \text{ g mol}^{-1}$). This might indicate that the Li^+ species are adsorbed together with free solvent molecules, and this phenomenon is more pronounced compared to that in KCl electrolyte.

Another explanation, is that both species are electroadsorbed in their hydrated form, but Li^+ and K^+ ions have different degrees of hydration. In fact, Li^+ can be more easily hydrated because of its small size, whereas the interaction between the bigger K^+ atoms and water is weaker (electrostatic interaction inversely related to the distance separating the two species).

In other words, Li^+ ion species are more tightly bonded to their water molecules in their hydration shell, thus it is possible to have higher hydration level of the electroadsorbed lithium species compared to potassium species.

For NaCl medium, the ERGO modified quartz resonators exhibit slightly higher current values and mass response compared to the two other media. This indicates a more complex mechanism of ion electroadsorption than usually described in the literature, where a single negative charge on a capacitive material often is described as being compensated by the adsorption of a single electrolyte cation. It also indicates that the kinetic limitation is due to the ionic transfer rather than the electronic transfer as the same film was used to test the three different ions.

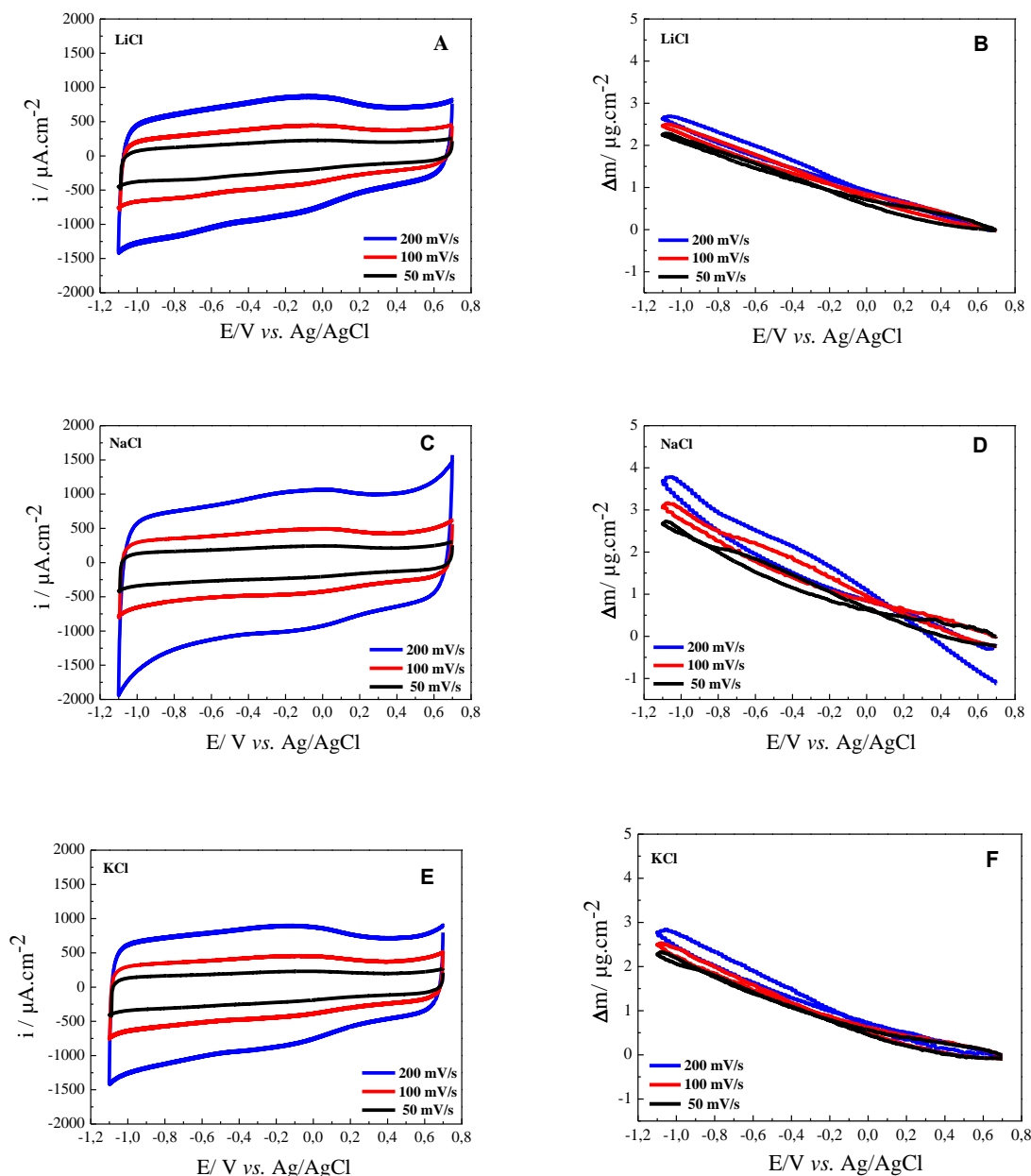


Figure V-23. EQCM results of ERGO thin films current vs. potential and mass variation vs. potential profiles measured in different aqueous electrolytes: 0.5 M LiCl (A and B), 0.5 M NaCl (C and D) and 0.5 M KCl (E and F).

Figures V-24 A, B and C show the capacitance curves as a function of the applied potential. The capacitance was calculated by using the relation expressed in Chapter III. According to Figure V-24, the capacitance values measured are almost the same in the three different electrolytes with a value around $100 \text{ F}\cdot\text{g}^{-1}$.

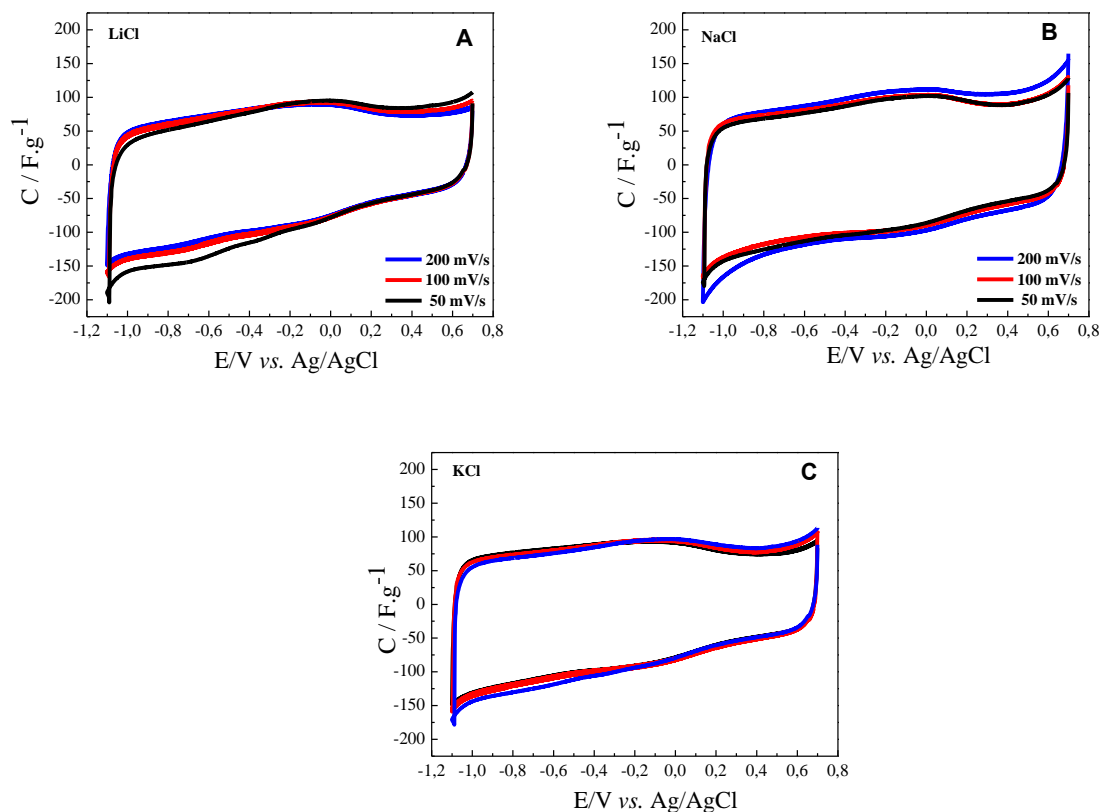


Figure V-24. Specific capacitance values (calculated from Figure 16) as a function of selected scan rate calculated for LiCl (A), NaCl (B) and KCl (C) aqueous electrolytes.

This value is slightly lower, but in the same order of magnitude as the reported values in the literature, such as the work of Gunasekaran *et. al* (175 F.g⁻¹ under similar conditions).²²⁵ This confirms that ERGO can be an interesting candidate to be used as a material for supercapacitors. Now, it seems interesting to understand the capacitive charge storage in these type of electrodes.

Figures V-25 A, B and C show the F_{dm}/dq values, which is equivalent to the global molecular mass of the species electroadsorbed. The values are calculated as a function of the potential in the three different electrolytes. The values vary in the range of 20-30 g.mol⁻¹, 30-50 g.mol⁻¹ and 30-40 g.mol⁻¹ in LiCl, in NaCl and in KCl, respectively. If there is strictly one non-hydrated species involved in the reversible electroadsorption process, this function should be equivalent to the molecular mass of the cation in the electrolyte. The observed higher values further indicate that the cations are hydrated and/or accompanied by free solvent molecules during their transfer. These results are somewhat in line with the previous reports on carbon based electrodes^{2,142} but clearly show the limitations of the classical EQCM technique. The EQCM does not provide unambiguous information on which of the possible scenarios that actually takes place.

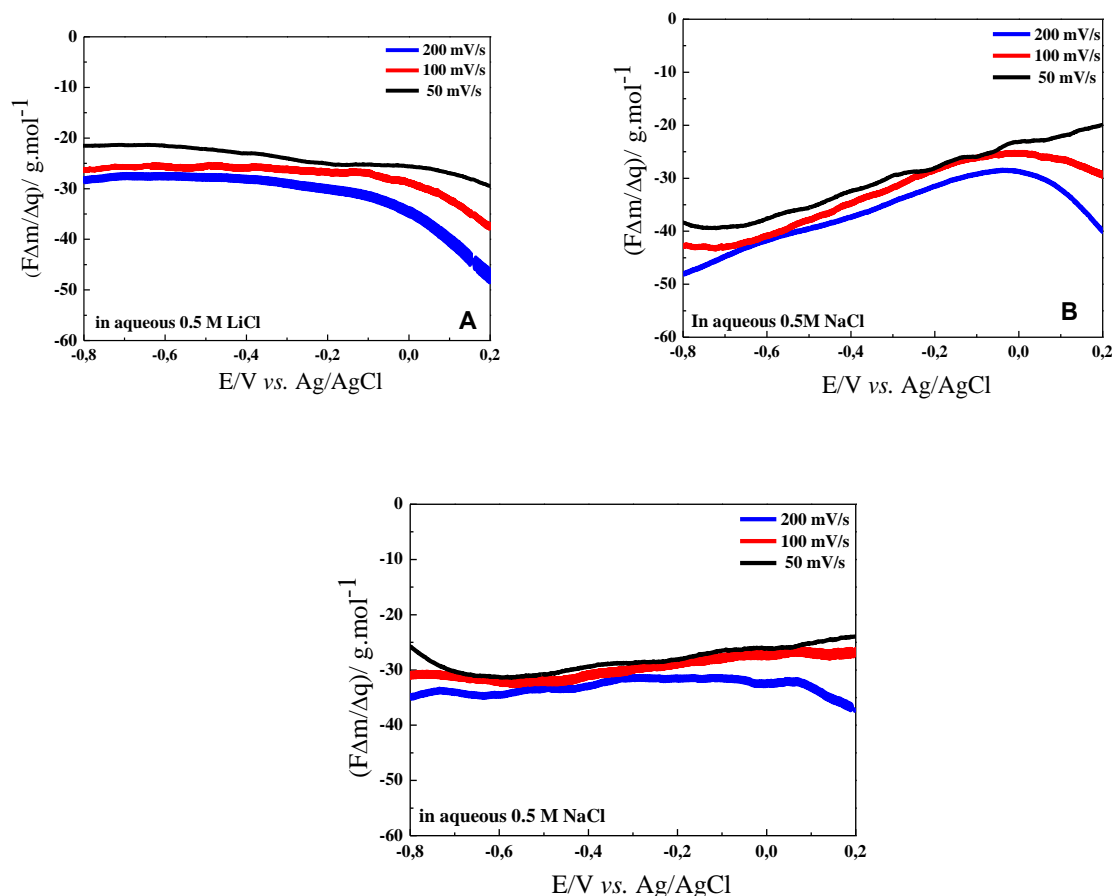


Figure V-25. The $F\Delta m/\Delta q$ values as a function of the potential applied, obtained from the reduction branch of the EQCM results measured in LiCl (A), NaCl (B) and KCl (C) aqueous electrolytes.

Therefore, an *ac*-electrogravimetry study is necessary to determine the electroadsorption/desorption mechanisms of the capacitive charge storage in ERGO thin films.

V-2.1.3. *Ac*-electrogravimetry Study of ERGO Thin Film Electrodes

Figure V-26 depicts an example of the experimental and theoretical transfer functions (TFs) obtained from *ac*-electrogravimetry of ERGO thin film in 0.5 M LiCl electrolyte at -0.6V vs Ag/AgCl. In fact, the measurements are performed in three different media, LiCl, NaCl and KCl, at each 100 mV in the potential range from 0 to -1V vs Ag/AgCl. The experimental data are fitted according to the model presented in chapter II. As shown in Figure V-26, there is a good agreement between the experimental data and the theoretical curves. First, the electrochemical impedance (Figure V-26A) presents a slightly distorted straight line indicating that there is multi-ions transfer contribution. The behaviour is mainly capacitive as indicated by the cyclic voltammetry characterization shown previously (Figure V-23). The charge/potential transfer function ($\Delta q/\Delta E$) (Figure V-26B) shows one flattened loop, which can be attributed at least to two species. The

differentiation between the two species is not possible, because the two time constants are not sufficiently different from each other.

The fitting of the experimental data by Mathcad software, using the equations given in Chapter II Section 3.5, showed the presence of two charged species: $\text{Li}^+\cdot\text{H}_2\text{O}$ at higher frequencies and Li^+ at lower frequencies. A beginning of a loop representing free solvent at very low frequencies, in the electrogravimetric function is observed (Figure V-26C). The identification of these species was achieved by the determination of their molar mass using Equation II-50 Chapter II and their respective kinetics of transfer were determined by the K_i values. Thus, the transfer is faster for hydrated species since they appear at higher frequencies, in spite of their larger size. This finding suggests that size is not the only criterion for the determination of the kinetics of transfer. The match between the size of the species and the electroadsorption sites also plays an important role.²³⁸ In the present ERGO thin films, electroadsorption may occur in two different sites; directly on the surface (sites more accessible) or between the graphene sheet stacks (less accessible sites), as shown schematically in Figure V-27. Bigger solvated ions, can be electroadsorbed on the more accessible sites, indicating a fast transfer rate as small dehydrated ions, can enter the film and therefore, exhibit lower transfer rate values.

The presence of three different species estimated by simulating the experimental data was further confirmed by carefully analysing the $F \frac{\Delta m}{\Delta q}(\omega)$ function as well as the partial electrogravimetric TFs (Figures V-26D, 26E and 26F). All these last TFs exhibited good agreement between the experimental and theoretical curves indicating that the hypothesis including three different species well describes the capacitive charge storage in ERGO electrodes, under these experimental conditions.

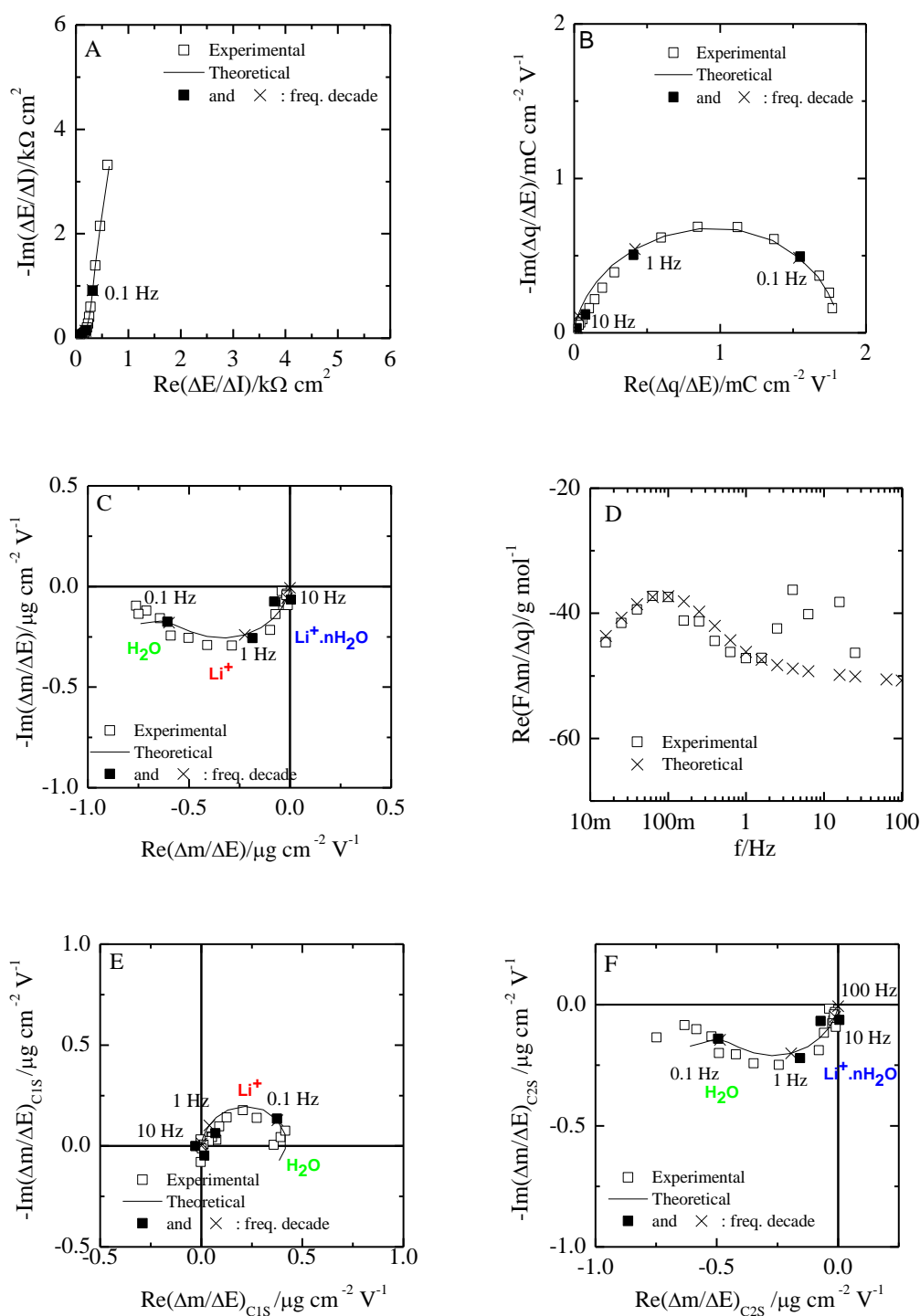


Figure V-26. Experimental and theoretical ac-electrogravimetry data of ERGO thin film in 0.5 M aqueous LiCl measured at -0.6V vs Ag/AgCl. (A). $\frac{\Delta E}{\Delta I}(\omega)$, (B). $\frac{\Delta q}{\Delta E}(\omega)$, (C). $\frac{\Delta m}{\Delta E}(\omega)$, and two partial transfer functions, (E). $\left. \frac{\Delta m}{\Delta E} \right|_{\text{c1s}}(\omega)$ and (F). $\left. \frac{\Delta m}{\Delta E} \right|_{\text{c2s}}(\omega)$ involving three species, specifically Li^+ , $\text{Li}^+ \cdot n\text{H}_2\text{O}$ and H_2O .

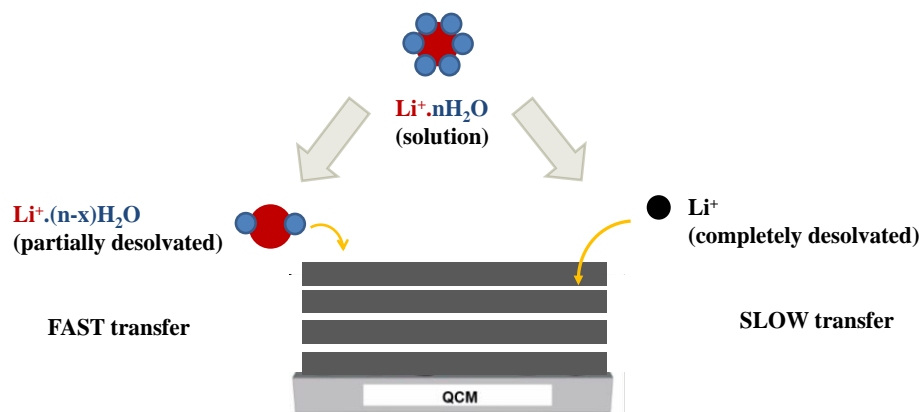


Figure V-27. Schematic representation of the electroadsorption sites for $\text{Li}^+ \cdot n\text{H}_2\text{O}$ and Li^+ in ERGO thin films.

Figure V-28 shows the K_i and R_{t_i} values for charged and non-charged species measured in the three different aqueous electrolytes, LiCl, NaCl and KCl. According to Figure V-28, the transfer is slower and more difficult for non-hydrated cations. The larger cations are transferred faster (Figures V-28A and B).

The cations are hydrated in the aqueous electrolytes and should partially or totally leave their hydration shells before getting electroadsorbed between the ERGO sheets or directly on the surface of the material.

Basically, the non-hydrated cations can be considered as the cations that leave all of their hydration shell and hydrated cations are those that leave a part of their hydration shell before electroadsorption between the ERGO sheets and on sites closer to the surface, respectively. The free solvent molecules follow the same flux direction as the cationic species but they are much slower and more difficult to be transferred (Figures V-28E and F) in the three different electrolytes studied.

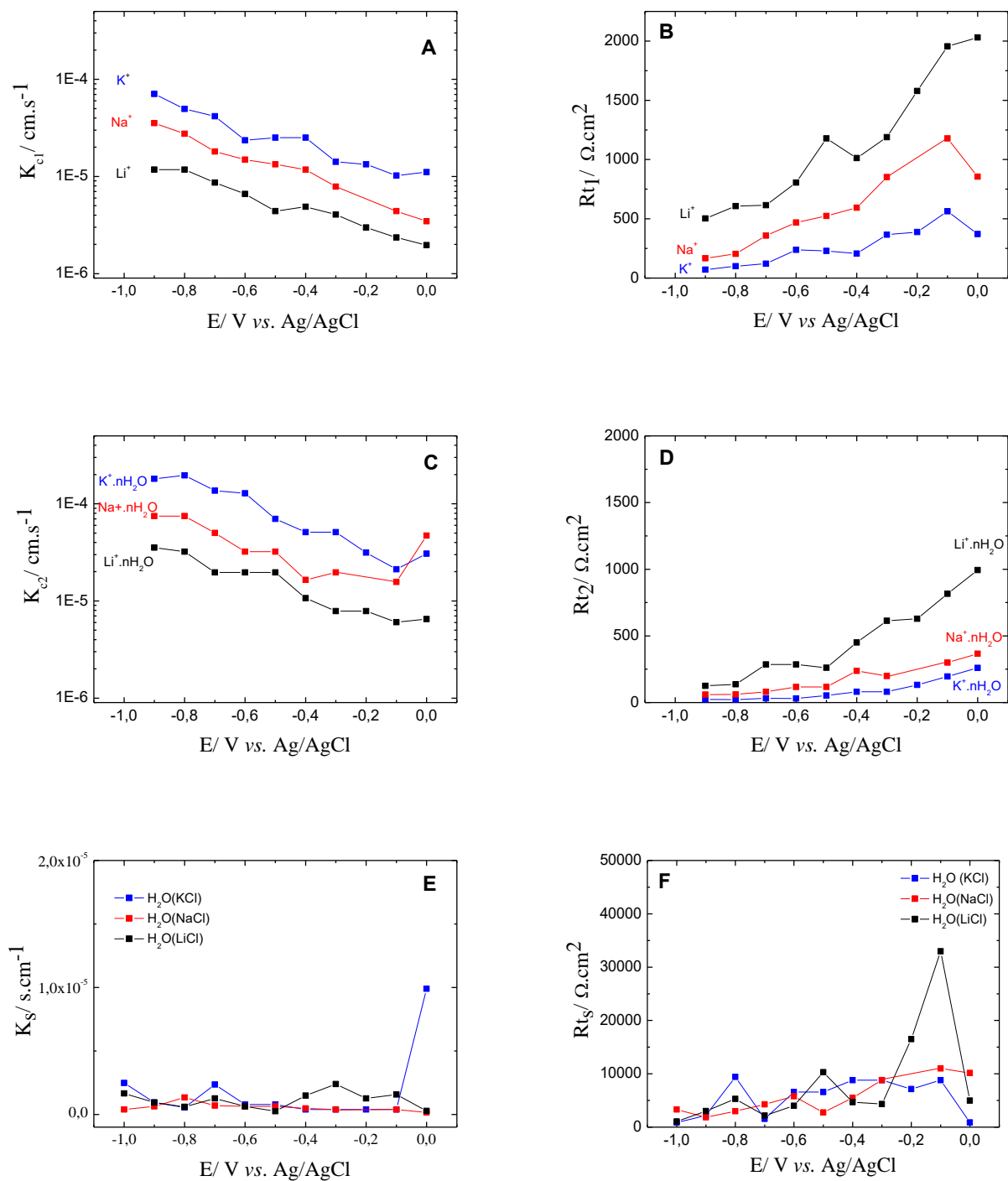


Figure V-28. The transfer kinetic constant, K_i , and transfer resistance, R_{t_i} for all species estimated from the fitting of the ac-electrogravimetry data measured in the three different aqueous electrolytes in $LiCl$, $NaCl$ and KCl .

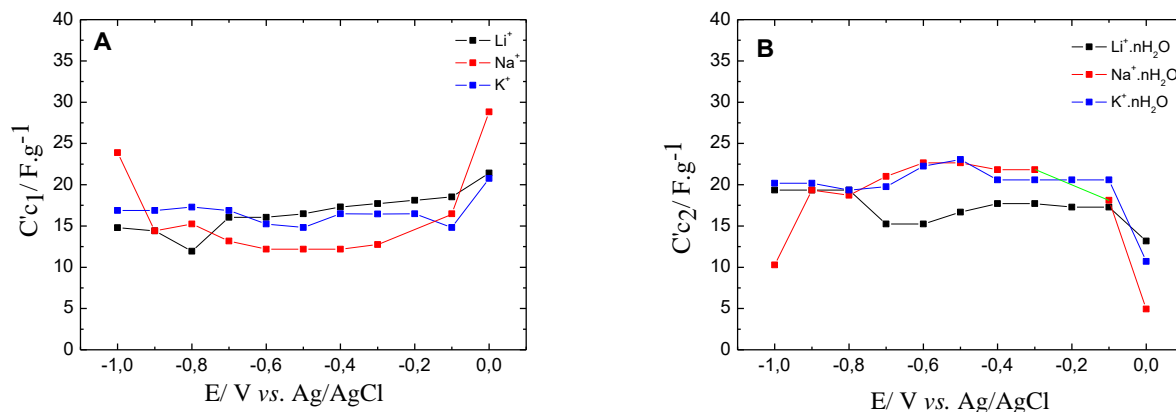


Figure V-29. The instantaneous capacitance, C'_i , values calculated from ac-electrogravimetry data for non-hydrated and hydrated species.

Figure V-29 shows the capacitance values relative to each cation (C'_{c1} and C'_{c2}) calculated as a function of the potential. The C'_{c1} and C'_{c2} correspond to the capacitance attributed to cation 1 (Li^+ , Na^+ or K^+) and cation 2 ($\text{Li}^+.n\text{H}_2\text{O}$, $\text{Na}^+.n\text{H}_2\text{O}$ or $\text{K}^+.n\text{H}_2\text{O}$), respectively. The capacitance values calculated from the ac-electrogravimetry data slightly differ from that obtained from the cyclic voltammetry, but they are in the same order of magnitude. The capacitance values from cyclic voltammetry correspond to relatively faster processes (high scan rate). However, here the capacitance contribution of two different species with different kinetic constants is calculated separately.

Another interesting variable can be described as the relative concentration change related to the individual species, $C_i - C_0$, following a potential step and calculated from the concentration potential transfer function at low frequencies ($\left. \frac{\Delta C_i}{\Delta E} \right|_{\omega \rightarrow 0}$). This quantity can be estimated through the

following relation $\left. \frac{\Delta C_i}{\Delta E} \right|_{\omega \rightarrow 0} = -\frac{G_i}{K_i}$ and then, after integration $C_i - C_0$ values can be estimated.

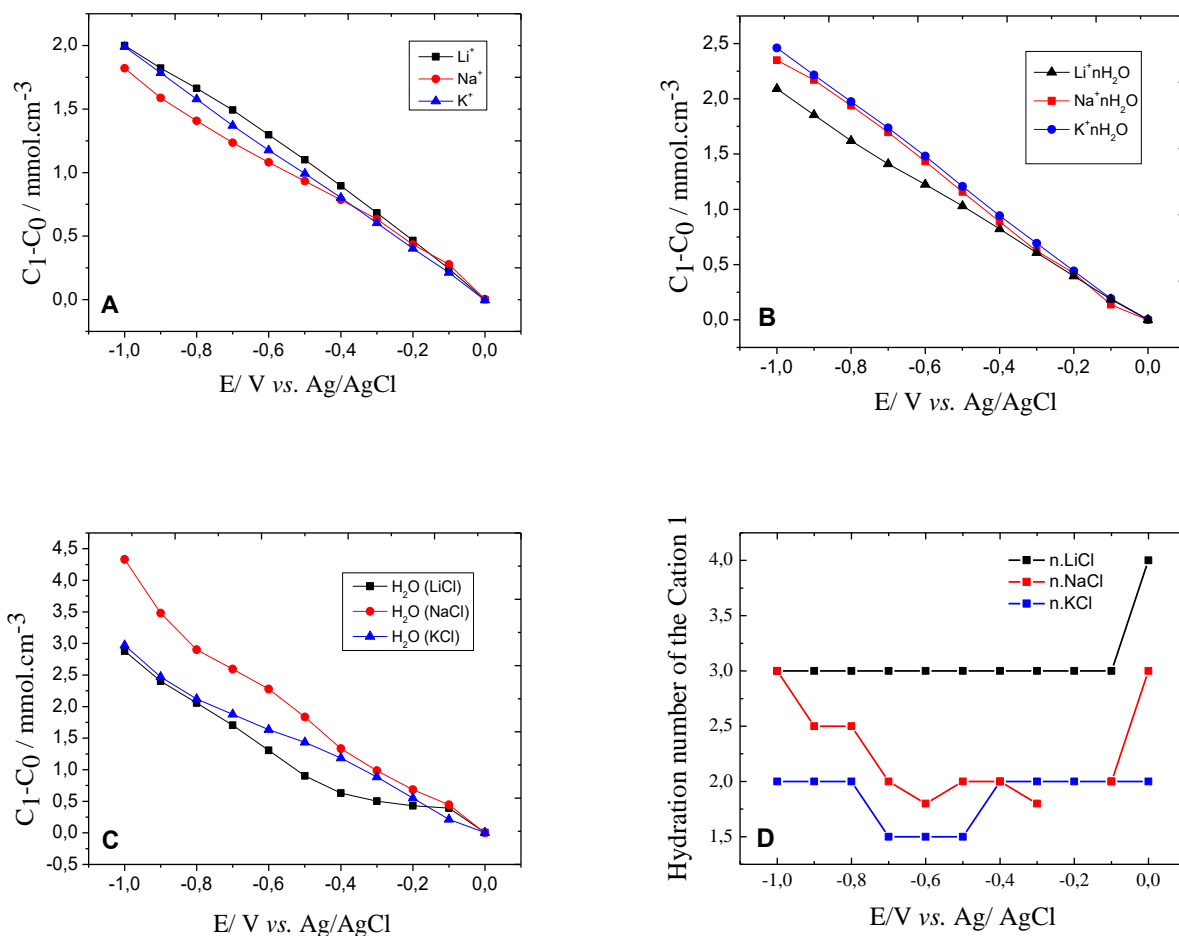


Figure V-30. Relative concentration variations of three different species non-hydrated cations (A), hydrated cations (B) and free solvent molecules (C) in aqueous LiCl, NaCl and KCl electrolytes together with the hydration values (*n*) estimated for the hydrated cation given by *ac*-electrogravimetric data.

In the potential window studied the concentration of all the species increases when the potential decreases as shown in Figure V-30 (A-C). The final concentration of hydrated and non-hydrated species does not differ significantly, which indicates that in spite of different kinetics, eventually the same amount of ionic species is electroadsorbed. This is probably not surprising since the concentration of the electroadsorbed cations should only be determined by the surface charge of the ERGO thin films. This is probably in line with the same current density obtained previously in cyclic electrogravimetry (Figure V-23). Interestingly, although they are the slowest species detected in the *ac*-electrogravimetry study, the final concentration of free solvent molecules is comparable to the cationic species. Indeed, H₂O is a polar molecule so its transfer may be achieved with electrostatic interactions. Another possible explanation can be the affinity of the residual surface functional groups on the ERGO thin films for water molecules. The free solvent

concentration seems to be higher in aqueous NaCl electrolyte (Figure V-30C). This is in accordance with cyclic electrogravimetry data where the mass variation was higher (Figure V-23D). Also, *ac*-electrogravimetry allowed the determination of the number of water molecules hydrating the cation species, which is shown in Figure V-30D. Although the hydration number does not change significantly as a function of potential, hydrated sodium species show a slight dependence as a function of potential. The estimated hydration numbers are the smallest for the potassium ions in our study, *i.e.* potassium ions are transferred at the interfaces with less of their hydration shell compared to sodium and lithium ions. Our findings are related to the phenomena that smaller ions are more tightly bound to their water molecules such that there exists an inverse relationship between the dehydration energy and the ion size (See Figure V-31). Potassium species (completely or partially dehydrated) require less energy to get rid of their water molecules (compared to sodium, and sodium ions compared to lithium ions), which probably confers a rapid (faster transfer kinetics, K_i) and an easy transfer (low transfer resistance R_{ti}) characteristics on potassium species (Figures V-28 and V-31). The literature results agree that ions with higher charge density have higher number of tightly bound water molecules. This has also been proposed as the mechanism behind the cellular ion channels being closed to strongly hydrated Na^+ ions while allowing formally larger, but more easily dehydrated, K^+ ions to pass through.^{219,222} Here, this phenomenon has been shown for the first time to play a role in the capacitive charge storage behavior of ERGO electrodes.

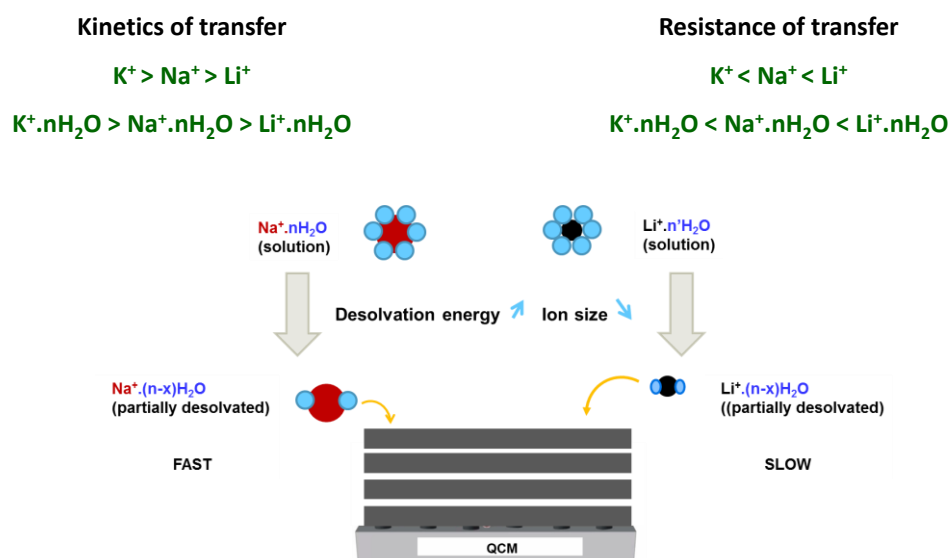


Figure V-31. Schematic representation of the interfacial phenomena of ionic species at the ERGO/electrolyte interfaces – cation size dependence.

V-3. Conclusions

SWCNT/PB

The electrochemical characterization was first done by cyclic electrogravimetry (EQCM), which was performed in 0.5M aqueous KCl electrolyte, from 0.45V *vs* Ag/AgCl to -0.45V *vs* Ag/AgCl. The capacitance of the film, the mass change and the F_{dm}/dq function were calculated as a function of the potential. The SWCNT/PB film shows a capacitive behavior in the CNT zone and a redox behavior in the PB zone. Additionally, to be able to characterize the EQCM response in depth, an *ac*-electrogravimetry study was performed in the same media under a sinusoidal potential perturbation. Experimental data were fitted using a theoretical model to find the kinetic parameters. It was found that the transfer of K^+ was faster than the transfer of Cl^- in the studied potential window. Probably, this is related to the fact that both the adsorption/desorption and the insertion/expulsion phenomena occur for K^+ , while only adsorption/desorption occurs for Cl^- . Indeed, for pure PB films, the anion contribution was never seen and for that, is related to only electroadsorption.

SWCNT/PPy

The electrochemical characterization was first done by cyclic electrogravimetry (EQCM), which was performed in 0.5M aqueous NaCl electrolyte, from 0.45V *vs* Ag/AgCl to -1.2V *vs* Ag/AgCl. The capacitance of the film, the mass change and the F_{dm}/dq function were calculated as a function of the potential. The SWCNT/PPy film shows a pseudo-capacitive behavior. Additionally, to be able to characterize the EQCM response in depth, an *ac*-electrogravimetric study was performed in the same media under a sinusoidal potential perturbation. Experimental data were fitted using a theoretical model to find the kinetic parameters. It was found that the transfer of $Na^+.nH_2O$ was faster than the transfer of H^+ and Cl^- in the studied potential window.

On the other hand, in SWCNT/PPy the transfer kinetic rates of $Na^+.nH_2O$ are equivalent to the transfer kinetic rates of the $Na^+.nH_2O$ from SWCNT and more significant than the transfer kinetic rates of the Na^+ mentioned in the literature²²⁴. The transfer kinetic rates of the H^+ in the SWCNT/PPy are more significant than the transfer kinetic rates of H^+ in the SWCNT. The transfer kinetic rates of the Cl^- in the SWCNT/PPy are more or less equivalent to the transfer kinetic rates of the Cl^- in the SWCNT and more significant than the transfer kinetic rates of the Cl^- mentioned in the literature.²²⁴

ERGO

The electrochemical characterization was first done by cyclic electrogravimetry, which was performed in 0.5M aqueous LiCl, NaCl and KCl electrolytes, from 0.7 V vs Ag/AgCl to -1.1V vs Ag/AgCl. The capacitance of the film, the mass variation and the F_{dm}/dq function were calculated as a function of the potential. The ERGO films presented relatively high double layer capacitance values with regard to classic systems such as carbon nanotube based electrodes. The capacitance and the mass variation estimated from EQCM response were almost the same in the different electrolytes studied. Due to the different atomic weights used in this experiment, this proposes that free solvent molecules and/or hydrated species were also involved in the electrochemical process.

There are studies on this aspect of the supercapacitive behavior that use EQCM. Additionally, to be able to deeply characterize the EQCM response, *ac*-electro gravimetric study was performed in the same media under a sinusoidal potential perturbation. Experimental data were fitted using a theoretical model to find kinetic parameters to compare the behavior of various species in different electrolytes. The transfer of K^+ was faster because it was easier for it to remove its hydration shell because of its big size. On the contrary, Li^+ was very strongly attached with its water molecules, making its transfer slower. This kind of discussion based on the ion size and kinetics exist in the supercapacitive material field. However, to the best of our knowledge, it is the first study showing this behavior experimentally thanks to the coupled electrochemical characterization methods.

Conclusions

General Conclusions

Carbon nanotubes (CNTs) of “single-wall” type (SWCNT), “double-walled” (DWCNT), “multi-walled” (MWCNT) and Electrochemically Reduced Graphene Oxide films were prepared on gold electrodes of microbalance and tested in different electrolytes such as LiCl, NaCl and KCl. The influence of pore morphology/structure over the classical electrochemical responses demonstrates that ERGO film is the best candidate for energy storage applications. To understand in details the electrochemical mechanism correlated to this high level of performances, different sophisticated techniques were performed to characterize the film morphology/structure and the transfer reactions involved in the storage reactions.

In CNTs the chemical nature and the role of each species, anion, cation, solvated cation, free solvent, directly or indirectly involved in the charge storage mechanism, have been clearly identified during the cathodic and anodic polarization through *ac*-electrogravimetry measurements for the very first time. For that, different experiments were done and the theoretical transfer functions have been calculated taking into account three different species ($\text{Li}^+ \cdot \text{H}_2\text{O}$, H^+ and H_2O), ($\text{Na}^+ \cdot \text{H}_2\text{O}$, H^+ and H_2O), (K^+ , H^+ and H_2O) for LiCl, NaCl and KCl, respectively. Very good agreements between experimental and theoretical data for all the transfer functions were obtained. From these modelling and data treatment, different subtleties were obtained concerning the transfer of the species between the electrolyte/film as the separation of the different contributions and also some key parameters as their identification, their rate of transfer or their ease of transfer. Of course, these characteristic parameters, correlated to the performances of the energy storage devices, cannot be obtained with classical methods of investigations such as classical EQCM. In the case of CNTs films, the transfer of hydrated lithium, hydrated sodium and potassium occurs at high frequencies (fast motion), the free solvent transfer occurs at medium frequencies and the proton transfer occurs at lower frequencies (slow motion). The transfer of hydrated lithium, hydrated sodium, potassium and free solvent is easier than that of the transfer of H^+ . These results suggest that the adsorption of these species takes place at different sites within the electrodes of the CNTs.

The deconvolution of the global response of EQCM into distinct contributions (identification of ions, solvation numbers and free solvent contributions) and the kinetics

information on the species electroadsorption are the strong assets of the *ac*-electrogravimetry and cannot be attained *via* EQCM alone.

The influence of electrolyte pH on the capacitive behavior of CNT films has also been analyzed by *ac*-electrogravimetry. The *ac*-electrogravimetric results confirm that the cations are predominantly electroadsorbed when the surface is negatively charged while the anions are electroadsorbed when the surface is positively charged. Furthermore, the displacement of the PZC is pH-dependent.

Finally, nanocomposite films, namely SWCNT/PB (Prussian Blue) and SWCNT/PPy (Polypyrrole) were electrochemically examined. The main idea was to emphasize the capacitive and faradic behavior of these different films by combining two materials. The chemical nature and the role of each species involved in the pseudo-capacitive and capacitive processes were highlighted by the *ac*-electrogravimetry.

For ERGO electrodes, the *ac*-electrogravimetry detected in aqueous electrolytes (LiCl, NaCl and KCl) two types of cationic species: hydrated and dehydrated cations. The hydrated ions are the fastest and the easiest species to be transferred, indicated by their higher K_i (kinetics of transfer) and lower Rt_i (transfer resistance) values. The free water molecules contribute at the lowest frequencies, making them the slowest species to contribute indirectly to the charge storage mechanism. These experimental results strengthen the idea that the complete dehydration of the ions require higher amount of energy, which renders the completed dehydrated ions slower than partially dehydrated counterparts.

When the aqueous electrolyte cation is replaced (from Li^+ or Na^+ or K^+ , both for the completely dehydrated and partially dehydrated cation populations) the following trend was observed: K^+ species are faster to be electroadsorbed compared to Na^+ species, and the Li^+ species are persistently the slowest species in this comparison. This, a priori anomalous behavior is an experimental proof of the relationship between the dehydration energy and the ion size. Our findings are related to the phenomena that smaller ions are more tightly bound to their water molecules such that an inverse relationship between the dehydration energy and the ion size exists. Potassium species (completely or partially dehydrated) require less energy to get rid of their water molecules (compared to sodium, and sodium ions compared to lithium ions), which probably confers a rapid (faster transfer kinetics, K_i) and an easy transfer (low transfer resistance, Rt_i) characteristics on potassium species. The literature results agree that ions with higher charge density

have higher number of tightly bound water molecules. This phenomenon has been shown for the first time to play a role in the capacitive charge storage behavior of carbon based electrodes.

The methodology adapted to characterize carbon based electrodes in this Ph.D. thesis can be suggested as a baseline diagnostic tool to study the pore/ion size relationship, the concentration and the solvent effects, the dynamics of the ions interactions at the interfaces (electroadsorption and/or faradaic process) of the electrode materials which may pave the way towards more performant electrode/electrolyte systems in energy storage devices.

Future work

Carbon nanotube films were tested in Aqueous and Organic electrolytes and characterized by EQCM and *ac*-electrogravimetric techniques. In future work, these carbon nanotubes could be tested in Ionic Liquids (ILs) or mixtures between ILs/organic solvent due to their commendable properties in terms of energy density and wider voltage window as well as the fact that they consist of only ions. A limited number of work have been found in the literature, employing EQCM to study carbon films in Ionic Liquids.¹⁴² However, as mentioned previously, EQCM alone provides a global response of the film. *Ac*-electrogravimetry could be employed for a better understanding of the mechanism of ion adsorption at the electrode/electrolyte interface.

The studies of mechanical properties of Carbon Nanotube films, particularly the motional resistance of films, could be monitored by techniques already used at the LISE-Laboratory like network analyzer methods. Gravimetric and mechanic results could be obtained and analyzed during the same experiment. However, the mechanical aspect could have an influence and the gravimetric results. For example, mechanic changes could occur in the film after a large amount of cycles (cyclic voltammetry). Therefore, the measures of electromechanic transfer functions similar to electrogravimetric transfer function techniques could be employed in future studies.

Materials more complex than CNT/PB or CNT/PPy composites will be studied in order to increase the performances of the pure CNT films either by functionalizing the CNT materials in ternary composites or by using CNT Hybrid Composite. Thereafter, the EQCM and *ac*-electrogravimetry could be employed in order to examine deeply the electrochemical behavior of such layers.

References

- 1 Levi, M. D. *et al.* Electrochemical Quartz Crystal Microbalance (EQCM) Studies of Ions and Solvents Insertion into Highly Porous Activated Carbons. *Journal of the American Chemical Society* **132**, 13220-13222, doi:10.1021/ja104391g (2010).
- 2 Levi, M. D., Salitra, G., Levy, N., Aurbach, D. & Maier, J. Application of a quartz-crystal microbalance to measure ionic fluxes in microporous carbons for energy storage. *Nat Mater* **8**, 872-875, doi:10.1038/nmat2559 (2009).
- 3 Gabrielli, C., García-Jareño, J. J., Keddam, M., Perrot, H. & Vicente, F. Ac-Electrogravimetry Study of Electroactive Thin Films. I. Application to Prussian Blue. *The Journal of Physical Chemistry B* **106**, 3182-3191, doi:10.1021/jp013924x (2002).
- 4 Gabrielli, C., Garcia-Jareño, J. J. & Perrot, H. Charge compensation process in polypyrrole studied by ac electrogravimetry. *Electrochimica Acta* **46**, 4095-4103, doi:[http://dx.doi.org/10.1016/S0013-4686\(01\)00685-5](http://dx.doi.org/10.1016/S0013-4686(01)00685-5) (2001).
- 5 Gabrielli, C., Keddam, M., Nadi, N. & Perrot, H. a.c. Electrogravimetry on conducting polymers. Application to polyaniline. *Electrochimica Acta* **44**, 2095-2103, doi:[http://dx.doi.org/10.1016/S0013-4686\(98\)00317-X](http://dx.doi.org/10.1016/S0013-4686(98)00317-X) (1999).
- 6 Gabrielli, C., Keddam, M., Nadi, N. & Perrot, H. Ions and solvent transport across conducting polymers investigated by ac electrogravimetry. Application to polyaniline. *Journal of Electroanalytical Chemistry* **485**, 101-113, doi:[http://dx.doi.org/10.1016/S0022-0728\(00\)00093-0](http://dx.doi.org/10.1016/S0022-0728(00)00093-0) (2000).
- 7 Ralph, J. B. in *Carbons for Electrochemical Energy Storage and Conversion Systems Advanced Materials and Technologies* 411-428 (CRC Press, 2009).
- 8 Etienne, A. *Etude de matériaux hydruables par émission acoustique-Application aux batteries Ni-MH* Ph.D thesis, Institut National des Sciences Appliquées de Lyon (2013).
- 9 Palacin, M. R. Recent advances in rechargeable battery materials: a chemist's perspective. *Chemical Society reviews* **38**, 2565-2575, doi:10.1039/b820555h (2009).
- 10 Shiferaw, T. *Investigation of the interfaces of solid electrolyte based supercapacitors and batteries* Ph.D thesis, Universität zu Kiel, (2008).
- 11 Bagotsky, V. Fuel cells, batteries, and the development of electrochemistry. *J Solid State Electrochem* **15**, 1559-1562, doi:10.1007/s10008-010-1281-8 (2011).
- 12 Volta, A. On the Electricity Excited by the Mere Contact of Conducting Substances of Different Kinds. In a Letter from Mr. Alexander Volta, F. R. S. Professor of Natural Philosophy in the University of Pavia, to the Rt. Hon. Sir Joseph Banks, Bart. K. B. P. R. S. *Philosophical Transactions of the Royal Society of London* **90**, 403-431 (1800).
- 13 Floyd, T. *Electronic devices* 3rd edn, (1992).
- 14 Leclanché. *Pile au peroxide de manganèse à seul liquide*, 1868).
- 15 Oakes, J. A Brief History of Batteries and Stored Energy, <www.netaworld.org> (2006).
- 16 Zito, R. in *Energy Storage* 265-282 (John Wiley & Sons, Inc., 2010).
- 17 Yai, S. *The history of the battery*, <<http://www.baj.or.jp/e/knowledge/history01.html>> (2015).
- 18 Medical Evaluation of Renal Effects of Cadmium Exposures, <<http://webapps.doh.gov/elaws/osha/cadmium/1.aspx>> (2013).
- 19 Armand, M. & Tarascon, J. M. Building better batteries. *Nature* **451**, 652-657, doi:10.1038/451652a (2008).
- 20 Huggins, R. in *Energy Storage* Ch. 2, 13-19 (Springer US, 2010).
- 21 Arning, M. D. & Minteer, S. D. in *Handbook of Electrochemistry* (ed Cynthia G. Zoski) 813-XXIII (Elsevier, 2007).
- 22 Kumar, R. V. & Sarakonsri, T. in *High Energy Density Lithium Batteries* 1-25 (Wiley-VCH Verlag GmbH & Co. KGaA, 2010).
- 23 Arora, P. & Zhang, Z. M. Battery separators. *Chemical Reviews* **104**, 4419-4462, doi:10.1021/cr020738u (2004).
- 24 (ed Allen J; Inzelt Bard, György; Scholz, Fritz) (Springer-Verlag Berlin Heidelberg, 2012).

- 25 Ji, L., Lin, Z., Alcoutlabi, M. & Zhang, X. Recent developments in nanostructured anode materials for rechargeable lithium-ion batteries. *Energy & Environmental Science* **4**, 2682, doi:10.1039/c0ee00699h (2011).
- 26 Cao, Z. & Wei, B. A perspective: carbon nanotube macro-films for energy storage. *Energy & Environmental Science* **6**, 3183-3201, doi:10.1039/C3EE42261E (2013).
- 27 de las Casas, C. & Li, W. A review of application of carbon nanotubes for lithium ion battery anode material. *Journal of Power Sources* **208**, 74-85, doi:10.1016/j.jpowsour.2012.02.013 (2012).
- 28 Faggioli, E. Supercapacitors for the energy management of electric vehicles. *J. Power Sources* **84**, 261-269 (1999).
- 29 Simon, P. & Gogotsi, Y. Materials for electrochemical capacitors. *Nat Mater* **7**, 845-854 (2008).
- 30 Kang, B. & Ceder, G. Battery materials for ultrafast charging and discharging. *Nature* **458**, 190-193, doi:http://www.nature.com/nature/journal/v458/n7235/supinfo/nature07853_S1.html (2009).
- 31 Chan, C. K. *et al.* High-performance lithium battery anodes using silicon nanowires. *Nature Nanotechnology* **3**, 31-35, doi:10.1038/nnano.2007.411 (2008).
- 32 in *Battery Management Systems* Vol. 9 *Philips Research Book Series* Ch. 2, 11-45 (Springer Netherlands, 2008).
- 33 Conte, M. Supercapacitors Technical Requirements for New Applications. *Fuel Cells* **10**, 806-818, doi:10.1002/fuce.201000087 (2010).
- 34 Béguin, F., Raymundo-Piñero, E. & Frackowiak, E. in *Carbons for Electrochemical Energy Storage and Conversion Systems Advanced Materials and Technologies* 329-375 (CRC Press, 2009).
- 35 Simon, P. & Gogotsi, Y. Charge storage mechanism in nanoporous carbons and its consequence for electrical double layer capacitors. *Philosophical Transactions: Mathematical, Physical and Engineering Sciences* **368**, 3457-3467, doi:10.2307/25699175 (2010).
- 36 BENHADDAD, L. *Elaboration et caractérisation de poudres nanostructurées de MnO₂ et de polypyrrole : Application comme matériaux d'électrodes dans des dispositifs de stockage de l'énergie* Ph.D thesis, UNIVERSITÉ PIERRE ET MARIE CURIE, (2014).
- 37 COME, J. *Caractérisation électrochimique de matériaux à insertion de Li pour supercondensateurs hybrides à haute densité d'énergie* Ph.D thesis, Université de Toulouse, (2012).
- 38 Kim, B. K., Sy, S., Yu, A. & Zhang, J. in *Handbook of Clean Energy Systems* (John Wiley & Sons, Ltd, 2015).
- 39 Lin, R. *FORMULATION OF ELECTROLYTES BASED ON IONIC LIQUIDS FOR SUPERCAPACITOR APPLICATIONS* Ph.D thesis, Université de Toulouse, (2012).
- 40 SEGALINI, J. *Etude de l'adsorption des ions dans des carbones microporeux ; application aux supercondensateurs* Ph.D thesis, Université de Toulouse (2012).
- 41 Gao, Q. *Optimizing carbon/carbon supercapacitors in aqueous and organic electrolytes* Ph.D thesis, Université d'Orleans, (2013).
- 42 zhang, L. L. *CARBON-BASED MATERIALS AS SUPERCAPACITOR ELECTRODES* Ph.D thesis, NATIONAL UNIVERSITY OF SINGAPORE, (2010).
- 43 Zhang, J. & Zhao, X. S. On the Configuration of Supercapacitors for Maximizing Electrochemical Performance. *ChemSusChem* **5**, 818-841, doi:10.1002/cssc.201100571 (2012).
- 44 Simon, P. & Gogotsi, Y. Charge storage mechanism in nanoporous carbons and its consequence for electrical double layer capacitors. *Philosophical transactions. Series A, Mathematical, physical, and engineering sciences* **368**, 3457-3467, doi:10.1098/rsta.2010.0109 (2010).
- 45 Béguin, F. & Raymundo-Piñero, E. in *Encyclopedia of Sustainability Science and Technology* (ed Robert A Meyers) Ch. 502, 6769-6790 (Springer New York, 2012).
- 46 Lu, W. & Dai, L. *Carbon Nanotube Supercapacitors*. (2010).
- 47 Roland, G. & Hamid, G. in *Carbons for Electrochemical Energy Storage and Conversion Systems Advanced Materials and Technologies* 429-467 (CRC Press, 2009).
- 48 Béguin, F., Presser, V., Balducci, A. & Frackowiak, E. Carbons and Electrolytes for Advanced Supercapacitors. *Advanced Materials* **26**, 2219-2251, doi:10.1002/adma.201304137 (2014).
- 49 Candelaria, S. L. *et al.* Nanostructured carbon for energy storage and conversion. *Nano Energy* **1**, 195-220, doi:10.1016/j.nanoen.2011.11.006 (2012).
- 50 Davies, A. & Yu, A. Material advancements in supercapacitors: From activated carbon to carbon nanotube and graphene. *The Canadian Journal of Chemical Engineering* **89**, 1342-1357, doi:10.1002/cjce.20586 (2011).

- 51 Halper, M. S. E., James C. Supercapacitors: A Brief Overview. Report No. Case # 06-0667, (The MITRE Corporation, McLean, Virginia, USA., 2006).
- 52 Simon, P. & Gogotsi, Y. Capacitive Energy Storage in Nanostructured Carbon–Electrolyte Systems. *Accounts of Chemical Research* **46**, 1094-1103, doi:10.1021/ar200306b (2013).
- 53 Zhang, L. L. & Zhao, X. S. Carbon-based materials as supercapacitor electrodes. *Chemical Society Reviews* **38**, 2520-2531, doi:10.1039/B813846J (2009).
- 54 Yan, J., Wang, Q., Wei, T. & Fan, Z. Recent Advances in Design and Fabrication of Electrochemical Supercapacitors with High Energy Densities. *Advanced Energy Materials* **4**, n/a-n/a, doi:10.1002/aenm.201300816 (2014).
- 55 Hu, L., Hecht, D. S. & Gruener, G. Carbon Nanotube Thin Films: Fabrication, Properties, and Applications. *Chemical Reviews* **110**, 5790-5844, doi:10.1021/cr9002962 (2010).
- 56 Szabó, A. *et al.* Synthesis Methods of Carbon Nanotubes and Related Materials. *Materials* **3**, 3092-3140, doi:10.3390/ma3053092 (2010).
- 57 Baddour, C. E., Briens, C. L., Bordere, S., Anglerot, D. & Gaillard, P. An investigation of carbon nanotube jet grinding. *Chemical Engineering and Processing: Process Intensification* **47**, 2195-2202, doi:10.1016/j.cep.2007.11.012 (2008).
- 58 Iijima, S. Helical microtubules of graphitic carbon. *Nature* **354**, 56-58 (1991).
- 59 Guo, T., Nikolaev, P., Thess, A., Colbert, D. T. & Smalley, R. E. Catalytic growth of single-walled nanotubes by laser vaporization. *Chemical Physics Letters* **243**, 49-54, doi:[http://dx.doi.org/10.1016/0009-2614\(95\)00825-O](http://dx.doi.org/10.1016/0009-2614(95)00825-O) (1995).
- 60 José-Yacamán, M., Miki-Yoshida, M., Rendón, L. & Santiesteban, J. G. Catalytic growth of carbon microtubules with fullerene structure. *Applied Physics Letters* **62**, 202-204, doi:<http://dx.doi.org/10.1063/1.109315> (1993).
- 61 Prasek, J. *et al.* Methods for carbon nanotubes synthesis—review. *Journal of Materials Chemistry* **21**, 15872, doi:10.1039/c1jm12254a (2011).
- 62 Cadek, M., Vostrowsky, O. & Hirsch, A. Carbon, 7. Fullerenes and Carbon Nanomaterials. doi:10.1002/14356007.n05_n06 (2010).
- 63 Raccichini, R., Varzi, A., Passerini, S. & Scrosati, B. The role of graphene for electrochemical energy storage. *Nat Mater* **14**, 271-279, doi:10.1038/nmat4170 (2015).
- 64 Hummers, W. S. & Offeman, R. E. Preparation of Graphitic Oxide. *Journal of the American Chemical Society* **80**, 1339-1339, doi:10.1021/ja01539a017 (1958).
- 65 Dreyer, D. R., Park, S., Bielawski, C. W. & Ruoff, R. S. The chemistry of graphene oxide. *Chemical Society Reviews* **39**, 228-240, doi:10.1039/B917103G (2010).
- 66 Vivekchand, S. R. C., Rout, C. S., Subrahmanyam, K. S., Govindaraj, A. & Rao, C. N. R. Graphene-based electrochemical supercapacitors. *Journal of Chemical Sciences* **120**, 9-13, doi:10.1007/s12039-008-0002-7 (2008).
- 67 Stoller, M. D., Park, S., Zhu, Y., An, J. & Ruoff, R. S. Graphene-Based Ultracapacitors. *Nano Letters* **8**, 3498-3502, doi:10.1021/nl802558y (2008).
- 68 Lv, W. *et al.* Low-Temperature Exfoliated Graphenes: Vacuum-Promoted Exfoliation and Electrochemical Energy Storage. *ACS Nano* **3**, 3730-3736, doi:10.1021/nn900933u (2009).
- 69 Wang, Y. *et al.* Supercapacitor Devices Based on Graphene Materials. *The Journal of Physical Chemistry C* **113**, 13103-13107, doi:10.1021/jp902214f (2009).
- 70 Du, X., Guo, P., Song, H. & Chen, X. Graphene nanosheets as electrode material for electric double-layer capacitors. *Electrochimica Acta* **55**, 4812-4819, doi:<http://dx.doi.org/10.1016/j.electacta.2010.03.047> (2010).
- 71 Zhang, L. & Shi, G. Preparation of Highly Conductive Graphene Hydrogels for Fabricating Supercapacitors with High Rate Capability. *The Journal of Physical Chemistry C* **115**, 17206-17212, doi:10.1021/jp204036a (2011).
- 72 Weng, Z. *et al.* Graphene-Cellulose Paper Flexible Supercapacitors. *Advanced Energy Materials* **1**, 917-922, doi:10.1002/aenm.201100312 (2011).
- 73 Yang, X., Zhu, J., Qiu, L. & Li, D. Bioinspired Effective Prevention of Restacking in Multilayered Graphene Films: Towards the Next Generation of High-Performance Supercapacitors. *Advanced Materials* **23**, 2833-+, doi:10.1002/adma.201100261 (2011).

- 74 Chen, Y., Zhang, X., Zhang, D., Yu, P. & Ma, Y. High performance supercapacitors based on reduced graphene oxide in aqueous and ionic liquid electrolytes. *Carbon* **49**, 573-580, doi:10.1016/j.carbon.2010.09.060 (2011).
- 75 Liu, Y.-Z. *et al.* Crumpled reduced graphene oxide by flame-induced reduction of graphite oxide for supercapacitive energy storage. *Journal of Materials Chemistry A* **2**, 5730-5737, doi:10.1039/c3ta15082h (2014).
- 76 Inagaki, M., Konno, H. & Tanaike, O. Carbon materials for electrochemical capacitors. *Journal of Power Sources* **195**, 7880-7903, doi:<http://dx.doi.org/10.1016/j.jpowsour.2010.06.036> (2010).
- 77 Lazzari, M. *Electrode Materials for Ionic Liquid Based-Supercapacitors* Ph.D thesis, Università di Bologna, (2010).
- 78 Matsuoka, K. *et al.* Extremely high microporosity and sharp pore size distribution of a large surface area carbon prepared in the nanochannels of zeolite Y. *Carbon* **43**, 876-879, doi:10.1016/j.carbon.2004.10.050 (2005).
- 79 Montes-Moran, M. A., Suarez, D., Menendez, J. A. & Fuente, E. On the nature of basic sites on carbon surfaces: An overview. *Carbon* **42**, 1219-1225, doi:10.1016/j.carbon.2004.01.023 (2004).
- 80 Yoon, S. H. *et al.* KOH activation of carbon nanofibers. *Carbon* **42**, 1723-1729, doi:10.1016/j.carbon.2004.03.006 (2004).
- 81 Vix-Guterl, C. *et al.* Electrochemical energy storage in ordered porous carbon materials. *Carbon* **43**, 1293-1302, doi:<http://dx.doi.org/10.1016/j.carbon.2004.12.028> (2005).
- 82 Ania, C. O., Pernak, J., Stefaniak, F., Raymundo-Piñero, E. & Béguin, F. Polarization-induced distortion of ions in the pores of carbon electrodes for electrochemical capacitors. *Carbon* **47**, 3158-3166, doi:<http://dx.doi.org/10.1016/j.carbon.2009.06.054> (2009).
- 83 Carter, C. B. & Norton, M. G. in *Ceramic Materials* Ch. 37, 699-712 (Springer New York, 2013).
- 84 Alresheedi, B. *SUPERCAPACITORS BASED ON CARBON NANOTUBE FUZZY FABRIC STRUCTURAL COMPOSITES* Ph.D thesis, UNIVERSITY OF DAYTON, (2012).
- 85 Pan, H., Li, J. & Feng, Y. Carbon Nanotubes for Supercapacitor. *Nanoscale Research Letters* **5**, 654 - 668 (2010).
- 86 Zhou, C., Kumar, S., Doyle, C. D. & Tour, J. M. Functionalized Single Wall Carbon Nanotubes Treated with Pyrrole for Electrochemical Supercapacitor Membranes. *Chemistry of Materials* **17**, 1997-2002, doi:10.1021/cm047882b (2005).
- 87 Zhou, Y. K., He, B. L., Zhou, W. J. & Li, H. L. Preparation and Electrochemistry of SWNT/PANI composite films for electrochemical capacitors. *Journal of the Electrochemical Society* **151**, A1052-A1057, doi:10.1149/1.1758812 (2004).
- 88 Visser, A. E. *et al.* Task-Specific Ionic Liquids Incorporating Novel Cations for the Coordination and Extraction of Hg₂⁺ and Cd₂⁺: Synthesis, Characterization, and Extraction Studies. *Environmental Science & Technology* **36**, 2523-2529, doi:10.1021/es0158004 (2002).
- 89 Armand, M., Endres, F., MacFarlane, D. R., Ohno, H. & Scrosati, B. Ionic-liquid materials for the electrochemical challenges of the future. *Nat Mater* **8**, 621-629 (2009).
- 90 Lin, R. *et al.* Capacitive Energy Storage from -50 to 100 °C Using an Ionic Liquid Electrolyte. *The Journal of Physical Chemistry Letters* **2**, 2396-2401, doi:10.1021/jz201065t (2011).
- 91 Yao, F., Pham, D. T. & Lee, Y. H. Carbon-Based Materials for Lithium-Ion Batteries, Electrochemical Capacitors, and Their Hybrid Devices. *ChemSusChem*, n/a-n/a, doi:10.1002/cssc.201403490 (2015).
- 92 Conway, B. E. (Nature Publishing Group, 1999).
- 93 Lee, H. Y. & Goodenough, J. B. Supercapacitor behavior with KCl electrolyte. *J. Solid State Chem.* **144**, 220-223 (1999).
- 94 Laforgue, A., Simon, P. & Fauvarque, J. F. Chemical synthesis and characterization of fluorinated polyphenylthiophenes: application to energy storage. *Synth. Met.* **123**, 311-319 (2001).
- 95 Naoi, K., Suematsu, S. & Manago, A. Electrochemistry of poly(1,5-diaminoanthraquinone) and its application in electrochemical capacitor materials. *J. Electrochem. Soc.* **147**, 420-426 (2000).
- 96 Rudge, A., Raistrick, I., Gottesfeld, S. & Ferraris, J. P. Conducting polymers as active materials in electrochemical capacitors. *J. Power Sources* **47**, 89-107 (1994).
- 97 Merlet, C. *Modélisation de l'adsorption des ions dans les carbones nanoporeux* Ph.D thesis, Université Pierre et Marie Curie, (2013).
- 98 Odru, P. *Le stockage de l'énergie.* (2013).

- 99 Chen, J.-j. *et al.* A hierarchical architecture S/MWCNT nanomicrosphere with large pores for lithium sulfur batteries. *Physical Chemistry Chemical Physics* **14**, 5376-5382, doi:10.1039/c2cp40141j (2012).
- 100 Gogotsi, Y. Nanoporous carbide-derived carbon with tunable pore size. *Nature Mater.* **2**, 591-594 (2003).
- 101 Li, Y. *et al.* An oxygen reduction electrocatalyst based on carbon nanotube-graphene complexes. *Nature Nanotechnology* **7**, 394-400, doi:10.1038/nnano.2012.72 (2012).
- 102 Pech, D. *et al.* Ultrahigh-power micrometre-sized supercapacitors based on onion-like carbon. *Nature Nanotechnology* **5**, 651-654, doi:10.1038/nnano.2010.162 (2010).
- 103 Yoon, J. *et al.* Ultrathin silicon solar microcells for semitransparent, mechanically flexible and microconcentrator module designs. *Nature Materials* **7**, 907-915, doi:10.1038/nmat2287 (2008).
- 104 Kim, D.-H. *et al.* Stretchable and foldable silicon integrated circuits. *Science* **320**, 507-511, doi:10.1126/science.1154367 (2008).
- 105 Kim, D.-H. *et al.* Materials and noncoplanar mesh designs for integrated circuits with linear elastic responses to extreme mechanical deformations. *Proceedings of the National Academy of Sciences of the United States of America* **105**, 18675-18680, doi:10.1073/pnas.0807476105 (2008).
- 106 Sekitani, T. *et al.* Organic Nonvolatile Memory Transistors for Flexible Sensor Arrays. *Science* **326**, 1516-1519, doi:10.1126/science.1179963 (2009).
- 107 Kötzt, R. & Carlen, M. Principles and applications of electrochemical capacitors. *Electrochimica Acta* **45**, 2483-2498, doi:[http://dx.doi.org/10.1016/S0013-4686\(00\)00354-6](http://dx.doi.org/10.1016/S0013-4686(00)00354-6) (2000).
- 108 Fakhry, A. *Synthèse par voie électrochimique de nanostructures de polymères conducteurs sans emploi d'une matrice support. Applications aux (bio)capteurs.* Ph.D thesis, Université Pierre et Marie Curie, (2014).
- 109 To Thi Kim, L. *Etude de films électroactifs par couplage de techniques électrochimique et gravimétrique. Application à la caractérisation de membranes à conduction protonique.* Ph.D thesis, Université Pierre et Marie Curie, (2009).
- 110 Thissandier, F. *Elaboration de micro-supercondensateurs à base d'électrodes en silicium nanostructuré : Des nanomatériaux aux dispositifs* Ph.D thesis, Université de Grenoble, (2006).
- 111 Frackowiak, E. & Béguin, F. Carbon materials for the electrochemical storage of energy in capacitors. *Carbon* **39**, 937-950, doi:[http://dx.doi.org/10.1016/S0008-6223\(00\)00183-4](http://dx.doi.org/10.1016/S0008-6223(00)00183-4) (2001).
- 112 Jean-François, F. & Patrice, S. in *Carbons for Electrochemical Energy Storage and Conversion Systems Advanced Materials and Technologies* 1-36 (CRC Press, 2009).
- 113 Portet, C., Taberna, P. L., Simon, P., Flahaut, E. & Laberty-Robert, C. High power density electrodes for Carbon supercapacitor applications. *Electrochimica Acta* **50**, 4174-4181, doi:<http://dx.doi.org/10.1016/j.electacta.2005.01.038> (2005).
- 114 Pacios Pujadó, M. in *Carbon Nanotubes as Platforms for Biosensors with Electrochemical and Electronic Transduction Springer Theses* Ch. 1, 1-78 (Springer Berlin Heidelberg, 2012).
- 115 Portet, C., Taberna, P. L., Simon, P. & Flahaut, E. Influence of carbon nanotubes addition on carbon-carbon supercapacitor performances in organic electrolyte. *Journal of Power Sources* **139**, 371-378, doi:10.1016/j.jpowsour.2004.07.015 (2005).
- 116 Segalini, J., Daffos, B., Taberna, P. L., Gogotsi, Y. & Simon, P. Qualitative Electrochemical Impedance Spectroscopy study of ion transport into sub-nanometer carbon pores in Electrochemical Double Layer Capacitor electrodes. *Electrochimica Acta* **55**, 7489-7494, doi:<http://dx.doi.org/10.1016/j.electacta.2010.01.003> (2010).
- 117 Allaf, R. M., Rivero, I. V., Spearman, S. S. & Hope-Weeks, L. J. On the preparation of as-produced and purified single-walled carbon nanotube samples for standardized X-ray diffraction characterization. *Materials Characterization* **62**, 857-864, doi:10.1016/j.matchar.2011.06.005 (2011).
- 118 Badey, Q. *Etude des mécanismes et modélisation du vieillissement des batteries lithium-ion dans le cadre d'un usage automobile.* Ph.D thesis, Université Paris Sud - Paris XI, (2012).
- 119 Inzelt, G. in *Conducting Polymers Monographs in Electrochemistry* Ch. 3, 83-147 (Springer Berlin Heidelberg, 2012).
- 120 Howard, J. A. K. & Batsanov, A. S. in *Encyclopedia of Inorganic and Bioinorganic Chemistry* (John Wiley & Sons, Ltd, 2011).

- 121 Dall'Agnese, Y., Taberna, P. L., Gogotsi, Y. & Simon, P. Two-Dimensional Vanadium Carbide (MXene) as Positive Electrode for Sodium-Ion Capacitors. *J Phys Chem Lett* **6**, 2305-2309, doi:10.1021/acs.jpcclett.5b00868 (2015).
- 122 Zhou, W., Apkarian, R., Wang, Z. & Joy, D. in *Scanning Microscopy for Nanotechnology* (eds Weillie Zhou & ZhongLin Wang) Ch. 1, 1-40 (Springer New York, 2007).
- 123 Su, D. S. & Schlögl, R. Nanostructured Carbon and Carbon Nanocomposites for Electrochemical Energy Storage Applications. *ChemSusChem* **3**, 136-168, doi:10.1002/cssc.200900182 (2010).
- 124 Audichon, T. *Synthèse et caractérisation de matériaux électrocatalytiques : activation anodique de l'eau dans un électrolyseur PEM* Ph.D thesis, Université de Poitiers, (2014).
- 125 Rousseau, S. *Développement de catalyseurs plurimétalliques multifonctionnels pour l'oxydation électrocatalytique de l'éthanol dans une pile à oxydation directe (DEFC)* Ph.D thesis, Université de Poitiers, (2004).
- 126 Nossol, E. *et al.* Mechanistic Insights Gained by Monitoring Carbon Nanotube/Prussian Blue Nanocomposite Formation With in Situ Electrochemically Based Techniques. *The Journal of Physical Chemistry C* **118**, 13157-13167, doi:10.1021/jp501442h (2014).
- 127 Raymundo-Piñero, E., Kierzek, K., Machnikowski, J. & Béguin, F. Relationship between the nanoporous texture of activated carbons and their capacitance properties in different electrolytes. *Carbon* **44**, 2498-2507, doi:<http://dx.doi.org/10.1016/j.carbon.2006.05.022> (2006).
- 128 Frackowiak, E., Metenier, K., Bertagna, V. & Beguin, F. Supercapacitor electrodes from multiwalled carbon nanotubes. *Applied Physics Letters* **77**, 2421-2423, doi:10.1063/1.1290146 (2000).
- 129 Inzelt, G. in *Electroanalytical Methods* (eds Fritz Scholz *et al.*) Ch. 13, 257-270 (Springer Berlin Heidelberg, 2010).
- 130 Sigalov, S., Levi, M. D., Daikhin, L., Salitra, G. & Aurbach, D. Electrochemical quartz crystal admittance studies of ion adsorption on nanoporous composite carbon electrodes in aprotic solutions. *Journal of Solid State Electrochemistry* **18**, 1335-1344, doi:10.1007/s10008-013-2171-7 (2013).
- 131 Arias, C. R. *et al.* New Insights into Pseudocapacitive Charge-Storage Mechanisms in Li-Birnessite Type MnO₂ Monitored by Fast Quartz Crystal Microbalance Methods. *The Journal of Physical Chemistry C* **118**, 26551-26559, doi:10.1021/jp508543h (2014).
- 132 Sel, O. *et al.* Proton Insertion Properties in a Hybrid Membrane/Conducting Polymer Bilayer Investigated by AC Electrogravimetry. *Journal of The Electrochemical Society* **157**, F69, doi:10.1149/1.3421969 (2010).
- 133 Agrisuelas, J. *SÍNTESIS Y CARACTERIZACIÓN DE POLÍMEROS ELECTROACTIVOS EN SISTEMAS MULTICAPA* Ph.D thesis, Universitat de Valencia, (2008).
- 134 Bruckenstein, S. & Swathirajan, S. Potential dependence of lead and silver underpotential coverages in acetonitrile using a piezoelectric crystal oscillator method. *Electrochimica Acta* **30**, 851-855, doi:[http://dx.doi.org/10.1016/0013-4686\(85\)80140-7](http://dx.doi.org/10.1016/0013-4686(85)80140-7) (1985).
- 135 Hepel, M. & Bruckenstein, S. Tracking anion expulsion during underpotential deposition of lead at silver using the quartz microbalance. *Electrochimica Acta* **34**, 1499-1504, doi:[http://dx.doi.org/10.1016/0013-4686\(89\)87032-X](http://dx.doi.org/10.1016/0013-4686(89)87032-X) (1989).
- 136 Hepel, M., Kanige, K. & Bruckenstein, S. In situ underpotential deposition study of lead on silver using the electrochemical quartz crystal microbalance: Direct evidence for lead(II) adsorption before spontaneous charge transfer. *Journal of Electroanalytical Chemistry and Interfacial Electrochemistry* **266**, 409-421, doi:[http://dx.doi.org/10.1016/0022-0728\(89\)85085-5](http://dx.doi.org/10.1016/0022-0728(89)85085-5) (1989).
- 137 Schumacher, R., Borges, G. & Kanazawa, K. K. The quartz microbalance: A sensitive tool to probe surface reconstructions on gold electrodes in liquid. *Surface Science* **163**, L621-L626, doi:[http://dx.doi.org/10.1016/0039-6028\(85\)90835-0](http://dx.doi.org/10.1016/0039-6028(85)90835-0) (1985).
- 138 Ostrom, G. S. & Buttry, D. A. Quartz crystal microbalance studies of deposition and dissolution mechanisms of electrochromic films of diheptylviologen bromide. *Journal of Electroanalytical Chemistry and Interfacial Electrochemistry* **256**, 411-431, doi:[http://dx.doi.org/10.1016/0022-0728\(88\)87015-3](http://dx.doi.org/10.1016/0022-0728(88)87015-3) (1988).
- 139 Levi, M. D., Sigalov, S., Aurbach, D. & Daikhin, L. In Situ Electrochemical Quartz Crystal Admittance Methodology for Tracking Compositional and Mechanical Changes in Porous Carbon Electrodes. *The Journal of Physical Chemistry C* **117**, 14876-14889, doi:10.1021/jp403065y (2013).
- 140 Sigalov, S. *et al.* Selective adsorption of multivalent ions into TiC-derived nanoporous carbon. *Carbon* **50**, 3957-3960, doi:10.1016/j.carbon.2012.04.002 (2012).

- 141 Sigalov, S., Levi, M. D., Salitra, G., Aurbach, D. & Maier, J. EQCM as a unique tool for
determination of ionic fluxes in microporous carbons as a function of surface charge distribution.
Electrochemistry Communications **12**, 1718-1721, doi:10.1016/j.elecom.2010.10.005 (2010).
- 142 Tsai, W.-Y., Taberna, P.-L. & Simon, P. Electrochemical Quartz Crystal Microbalance (EQCM)
Study of Ion Dynamics in Nanoporous Carbons. *Journal of the American Chemical Society* **136**,
8722-8728, doi:10.1021/ja503449w (2014).
- 143 Barisci, J. N., Wallace, G. G. & Baughman, R. H. Electrochemical quartz crystal microbalance studies
of single-wall carbon nanotubes in aqueous and non-aqueous solutions. *Electrochimica Acta* **46**, 509-
517 (2000).
- 144 Levi, M. D., Sigalov, S., Salitra, G., Aurbach, D. & Maier, J. The effect of specific adsorption of
cations and their size on the charge-compensation mechanism in carbon micropores: the role of anion
desorption. *Chemphyschem : a European journal of chemical physics and physical chemistry* **12**, 854-
862, doi:10.1002/cphc.201000653 (2011).
- 145 An, K. H. *et al.* High-Capacitance Supercapacitor Using a Nanocomposite Electrode of Single-Walled
Carbon Nanotube and Polypyrrole. *Journal of The Electrochemical Society* **149**, A1058,
doi:10.1149/1.1491235 (2002).
- 146 Yang, D. Application of Nanocomposites for Supercapacitors: Characteristics and Properties.
doi:10.5772/50409 (2012).
- 147 Nossol, E. & Gorgatti Zarbin, A. J. Transparent films from carbon nanotubes/Prussian blue
nanocomposites: preparation, characterization, and application as electrochemical sensors. *J. Mater.*
Chem. **22**, 1824-1833, doi:10.1039/c1jm14225a (2012).
- 148 Nossol, E. & Zarbin, A. J. G. A Simple and Innovative Route to Prepare a Novel Carbon
Nanotube/Prussian Blue Electrode and its Utilization as a Highly Sensitive H₂O₂Amperometric
Sensor. *Advanced Functional Materials* **19**, 3980-3986, doi:10.1002/adfm.200901478 (2009).
- 149 Sel, O. *Hierarchical meso- and micropore architectures by liquid crystalline and polymer colloid*
templating Ph.D thesis, Universität Potsdam (2006).
- 150 Massey, M. *Electrical Properties of Single-Wlled Carbon Nanotube Networks Produced by*
Langmuir-Blodgett Deposition Ph.D thesis, Durham University, (2013).
- 151 Williams, D. B. & Carter, C. B. in *A Textbook for Materials Science* (Springer US, 2009).
- 152 Walkosz, W. in *Atomic Scale Characterization and First-Principles Studies of Si₃N₄ Interfaces*
Springer Theses Ch. 3, 23-43 (Springer New York, 2011).
- 153 in *Fundamentals of Powder Diffraction and Structural Characterization of Materials* Ch. 7, 133-
149 (Springer US, 2009).
- 154 Cullity, B. D. & Stock, S. R. *ELEMENTS OF X-RAY DIFFRACTION THIRD EDITION.* (2001).
- 155 Béguin, F., Flahaut, E., Linares-Solano, A. & Pinson, J. in *Understanding Carbon Nanotubes* Vol.
677 *Lecture Notes in Physics* (eds Annick Loiseau *et al.*) Ch. 8, 495-549 (Springer Berlin Heidelberg,
2006).
- 156 Lowell, S., Shields, J. E., Thomas, M. A. & Thommes, M. *Characterization of Porous Solids and*
Powders: Surface Area, Pore Size and Density. (Springer Netherlands, 2012).
- 157 Sel, O., Kuang, D., Thommes, M. & Smarsly, B. Principles of Hierarchical Meso- and Macropore
Architectures by Liquid Crystalline and Polymer Colloid Templating. *Langmuir* **22**, 2311-2322,
doi:10.1021/la0520841 (2006).
- 158 Barrett, E. P., Joyner, L. G. & Halenda, P. P. The Determination of Pore Volume and Area
Distributions in Porous Substances. I. Computations from Nitrogen Isotherms. *Journal of the*
American Chemical Society **73**, 373-380, doi:10.1021/ja01145a126 (1951).
- 159 Vazquez, A. *Novel Piezoelectric Transducers for high voltage measurements* PhD thesis, Universitat
Politècnica de Catalunya, (2000).
- 160 Arnau, A. & Soares, D. in *Piezoelectric Transducers and Applications* (ed Antonio Arnau Vives) Ch.
1, 1-38 (Springer Berlin Heidelberg, 2008).
- 161 Tse, G. *Study of Piezoelectricity on III/V semiconductors from atomistic simulations to computer*
modelling Ph.D thesis, University of Manchester, (2012).
- 162 Ballato, A. in *Piezoelectricity* Vol. 114 *Springer Series in Materials Science* Ch. 2, 9-35 (Springer
Berlin Heidelberg, 2008).

- 163 Buttry, D. A. & Ward, M. D. Measurement of interfacial processes at electrode surfaces with the electrochemical quartz crystal microbalance. *Chemical Reviews* **92**, 1355-1379, doi:10.1021/cr00014a006 (1992).
- 164 Garcia, S., Kunitz, E. & Kim, S. Piezoelectric effect and its applications. (1998).
- 165 Prasad, S. E., Waechter, D. F. & Blacow, R. G. in *II ECCOMAS THEMATIC CONFERENCE ON SMART STRUCTURES AND MATERIALS* (ed C.A. Mota Soares et al.) (Lisbon, Portugal, 2005).
- 166 Smith, A. L. in *Handbook of Thermal Analysis and Calorimetry* Vol. Volume 5 (eds E. Brown Michael & K. Gallagher Patrick) 133-169 (Elsevier Science B.V., 2008).
- 167 Tran, T. A. *AlN piezoelectric films for sensing and actuation* Ph.D thesis, Technische Universiteit Delft, (2014).
- 168 Hempstead, C. Piecing Together the History of Piezoelectricity. *Metasci* **18**, 293-296, doi:10.1007/s11016-009-9278-6 (2009).
- 169 Durou, H. *Vers l'autonomie énergétique des réseaux de capteurs embarqués: conception et intégration d'un générateur piézoélectrique et d'un micro dispositif de stockage capacitif en technologie silicium* Ph.D thesis, Université Paul Sébastien-Toulouse III, (2010).
- 170 Cherif, A. *Optimisation du transformateur piézoélectrique. Application: contrôle semi-passive des vibrations* Ph.D thesis, UNIVERSITE FERHAT ABBAS - SETIF, (2012).
- 171 Bullo, M. *Modélisation et commande du moteur piézoélectrique à onde progressive* Ph.D thesis, Ecole Polytechnique Fédérale de Laussane, (2005).
- 172 Tichý*, J., Erhart, J., Kittinger*, E. & Přivratská, J. in *Fundamentals of Piezoelectric Sensorics* Ch. 1, 1-14 (Springer Berlin Heidelberg, 2010).
- 173 Gautschi, G. in *Piezoelectric Sensorics* Ch. 2, 5-11 (Springer Berlin Heidelberg, 2002).
- 174 Guilbault, G. G. in *Methods and Phenomena* Vol. Volume 7 (eds L. U. C & Czanderna A.W) 251-280 (Elsevier, 1984).
- 175 Goyal, A. *Ultrasensitive quartz crystal microbalance integrated with carbon nanotubes* Ph.D thesis, The Pennsylvania State University, (2006).
- 176 Tortissier, G. *Etude et développement d'une plateforme de détection chimique à ondes acoustiques de surface pour environnement sévère haute température* Ph.D thesis, Université de Bordeaux, (2009).
- 177 Jiménez, D. *MODELIZACION DE LA ELECTRODISOLUCION DEL CINCO EN MEDIO ACIDO* Ph.D thesis, Universitat de Valencia, (2004).
- 178 Perrot, H. in *Chemical Sensors and Biosensors* 71-91 (John Wiley & Sons, Inc., 2012).
- 179 Bănică, F.-G. in *Chemical Sensors and Biosensors* 1-20 (John Wiley & Sons, Ltd, 2012).
- 180 Calvo, E. & Otero, M. in *Piezoelectric Transducers and Applications* (ed Antonio Arnau Vives) Ch. 9, 241-257 (Springer Berlin Heidelberg, 2008).
- 181 Stipek, S. & Calvo, E. in *Piezoelectric Transducers and Applications* (ed Antonio Arnau Vives) Ch. 10, 259-270 (Springer Berlin Heidelberg, 2008).
- 182 Bruckenstein, S. & Shay, M. Experimental aspects of use of the quartz crystal microbalance in solution. *Electrochimica Acta* **30**, 1295-1300, doi:[http://dx.doi.org/10.1016/0013-4686\(85\)85005-2](http://dx.doi.org/10.1016/0013-4686(85)85005-2) (1985).
- 183 Dultsev, F. N., Kolosovsky, E. A. & Mik, I. A. New Procedure to Record the Rupture of Bonds between Macromolecules and the Surface of the Quartz Crystal Microbalance (QCM). *Langmuir : the ACS journal of surfaces and colloids* **28**, 13793-13797, doi:10.1021/la302907r (2012).
- 184 Arnau, A., Ferrari, V., Soares, D. & Perrot, H. in *Piezoelectric Transducers and Applications* (ed Antonio Arnau Vives) Ch. 5, 117-186 (Springer Berlin Heidelberg, 2008).
- 185 Rodriguez-Pardo, L. et al. in *Sensors, 2003. Proceedings of IEEE.* 1189-1193 Vol.1182.
- 186 Rodriguez-Pardo, L., Rodriguez, J. F., Gabrielli, C., Perrot, H. & Brendel, R. Sensitivity, noise, and resolution in QCM sensors in liquid media. *Sensors Journal, IEEE* **5**, 1251-1257, doi:10.1109/JSEN.2005.859257 (2005).
- 187 Rodriguez-Pardo, L., Fariña, J., Gabrielli, C., Perrot, H. & Brendel, R. Resolution in quartz crystal oscillator circuits for high sensitivity microbalance sensors in damping media. *Sensors and Actuators B: Chemical* **103**, 318-324, doi:<http://dx.doi.org/10.1016/j.snb.2004.04.060> (2004).
- 188 Sauerbrey, G. Verwendung von Schwingquarzen zur Wägung dünner Schichten und zur Mikrowägung. *Z. Physik* **155**, 206-222, doi:10.1007/BF01337937 (1959).
- 189 Bizet, K., Gabrielli, C. & Perrot, H. Immunodetection by quartz crystal microbalance. *Appl Biochem Biotechnol* **89**, 139-149, doi:10.1385/ABAB:89:2-3:139 (2000).

- 190 Marx, K. A. Quartz Crystal Microbalance: A Useful Tool for Studying Thin Polymer Films and
Complex Biomolecular Systems at the Solution–Surface Interface. *Biomacromolecules* **4**, 1099-1120,
doi:10.1021/bm020116i (2003).
- 191 Brett, C. in *Piezoelectric Transducers and Applications* (ed Antonio Arnau Vives) Ch. 15, 399-411
(Springer Berlin Heidelberg, 2008).
- 192 Atsushi, I. & Motoko, I. A frequency of the quartz crystal microbalance (QCM) that is not affected by
the viscosity of a liquid. *Measurement Science and Technology* **19**, 075205 (2008).
- 193 Calvo, E., Kanazawa, K., Perrot, H. & Jimenez, Y. in *Piezoelectric Transducers and Applications*
(ed Antonio Arnau Vives) Ch. 13, 307-330 (Springer Berlin Heidelberg, 2008).
- 194 Torres, R. *Instrumental techniques for improving the measurements based on quartz crystal
microbalances* Ph.D thesis, Universitat Politècnica de València (2013).
- 195 Torres, R., Arnau, A. & Perrot, H. ELECTRONIC SYSTEM FOR EXPERIMENTATION IN AC
ELECTROGRAVIMETRY I: TECHNIQUE FUNDAMENTALS. *Revista EIA* **5**, 9-21 (2006).
- 196 Gabrielli, C. & Keddam, M. Contribution of electrochemical impedance spectroscopy to the
investigation of the electrochemical kinetics. *Electrochimica Acta* **41**, 957-965,
doi:[http://dx.doi.org/10.1016/0013-4686\(95\)00426-2](http://dx.doi.org/10.1016/0013-4686(95)00426-2) (1996).
- 197 Bondu, F. *Etude de la conformation d'adsorption de l'acide isonicotinique sur Au par spectroscopie
d'impedance-Raman et modulation de capacité* Ph.D thesis, Université Pierre et Marie Curie, (2013).
- 198 Orazem, M. E. & Tribollet, B. *Electrochemical Impedance Spectroscopy*. (John Wiley & Sons, Inc.,
2008).
- 199 Dos Santos, L. *Mécanisme de conduction protonique au sein de membranes hybrides pour piles à
combustible* Ph.D thesis, Université Pierre et Marie Curie, (2014).
- 200 Thu, H. *Etude de matériaux conducteurs par couplages de mesures d'impedance électrochimique, de
gravimétrie et d'angle de contact* Ph.D thesis, Université Pierre et Marie Curie, (2012).
- 201 Bourkane, S., Gabrielli, C. & Keddam, M. Kinetic study of electrode processes by ac quartz
electrogravimetry. *Journal of Electroanalytical Chemistry and Interfacial Electrochemistry* **256**, 471-
475, doi:[http://dx.doi.org/10.1016/0022-0728\(88\)87021-9](http://dx.doi.org/10.1016/0022-0728(88)87021-9) (1988).
- 202 Gabrielli, C. *et al.* New frequency/voltage converters for ac-electrogravimetric measurements based
on fast quartz crystal microbalance. *The Review of scientific instruments* **78**, 074103,
doi:10.1063/1.2751093 (2007).
- 203 Gabrielli, C. & Perrot, H. in *Modern Aspects of Electrochemistry No. 44* Vol. 44 *Modern Aspects of
Electrochemistry* (ed Mordechai Schlesinger) Ch. 5, 151-238 (Springer New York, 2009).
- 204 Torres, R., Arnau, A., Perrot, H., Garcia, J. & Gabrielli, C. Analogue-digital phase-locked loop for
alternating current quartz electrogravimetry. *Electronics Letters* **42**, 1272-1273,
doi:10.1049/el:20062269 (2006).
- 205 Yang, H. & Kwak, J. Mass Transport Investigated with the Electrochemical and Electrogravimetric
Impedance Techniques. 1. Water Transport in PPy/CuPTS Films. *The Journal of Physical Chemistry
B* **101**, 774-781, doi:10.1021/jp962903d (1997).
- 206 Guillaume, M. *PURIFICATION ET FONCTIONNALISATION D'ECHANTILLONS DE NANOTUBES
DE CARBONE MONO-FEUILLETS: EFFICACITE ET SELECTIVITE DES TRAITEMENTS
CHIMIQUES* Ph.D thesis, Université de Lorraine (2012).
- 207 Sing, K. S. W. *et al.* REPORTING PHYSISORPTION DATA FOR GAS SOLID SYSTEMS WITH
SPECIAL REFERENCE TO THE DETERMINATION OF SURFACE-AREA AND POROSITY
(RECOMMENDATIONS 1984). *Pure and Applied Chemistry* **57**, 603-619,
doi:10.1351/pac198557040603 (1985).
- 208 Frackowiak, E., Vol. 9 (2007).
- 209 Frackowiak, E. & Beguin, F., Vol. 39 (2001).
- 210 Frackowiak, E. *et al.*, Vol. 261 (2002).
- 211 Frackowiak, E., Jurewicz, K., Delpeux, S. & Beguin, F., Vol. 822 (2001).
- 212 Frackowiak, E., Metenier, K., Bertagna, V. & Beguin, F., Vol. 77 (2000).
- 213 Hulicova, D., Yamashita, J., Soneda, Y., Hatori, H. & Kodama, M., Vol. 17 (2005).
- 214 Bruckenstein, S., Brzezinska, K. & Hillman, A. R. EQCM studies of polypyrrole films. 1. Exposure to
aqueous sodium tosylate solutions under thermodynamically permselective conditions.
Electrochimica Acta **45**, 3801-3811, doi:[http://dx.doi.org/10.1016/S0013-4686\(00\)00467-9](http://dx.doi.org/10.1016/S0013-4686(00)00467-9) (2000).

- 215 Bruckenstein, S., Brzezinska, K. & Robert Hillman, A. EQCM studies of polypyrrole films. Part 2. Exposure to aqueous sodium tosylate solutions under thermodynamically non-permselective conditions[dagger]. *Physical Chemistry Chemical Physics* **2**, 1221-1229, doi:10.1039/A908719B (2000).
- 216 Skompska, M. & Hillman, A. R. Electrochemical quartz crystal microbalance studies of the electrodeposition and subsequent cross-linking of poly(N-vinylcarbazole) films. *Journal of Electroanalytical Chemistry* **433**, 127-134, doi:[http://dx.doi.org/10.1016/S0022-0728\(97\)00274-X](http://dx.doi.org/10.1016/S0022-0728(97)00274-X) (1997).
- 217 Hillman, A. R., Mohamoud, M. A. & Bruckenstein, S. Modelling Mobile Species Dynamics within Electroactive Films under Mixed Thermodynamic and Kinetic Control. *Electroanalysis* **17**, 1421-1432, doi:10.1002/elan.200503296 (2005).
- 218 Escobar-Teran, F. *et al.* Gravimetric and dynamic deconvolution of global EQCM response of carbon nanotube based electrodes by Ac-electrogravimetry. *Electrochemistry Communications* **70**, 73-77, doi:10.1016/j.elecom.2016.07.005 (2016).
- 219 MacKinnon, R. Potassium channels and the atomic basis of selective ion conduction (Nobel Lecture). *Angewandte Chemie* **43**, 4265-4277, doi:10.1002/anie.200400662 (2004).
- 220 Waluyo, I. *et al.* The structure of water in the hydration shell of cations from x-ray Raman and small angle x-ray scattering measurements. *The Journal of chemical physics* **134**, 064513, doi:10.1063/1.3533958 (2011).
- 221 Li, X., Rong, J. & Wei, B. Electrochemical Behavior of Single-Walled Carbon Nanotube Supercapacitors under Compressive Stress. *Acs Nano* **4**, 6039-6049, doi:10.1021/nn101595y (2010).
- 222 Zhou, Y., Morais-Cabral, J. H., Kaufman, A. & MacKinnon, R. Chemistry of ion coordination and hydration revealed by a K⁺ channel-Fab complex at 2.0[thinsp][angst] resolution. *Nature* **414**, 43-48 (2001).
- 223 Agrisuelas, J. *et al.* Usefulness of F(dm/dQ) Function for Elucidating the Ions Role in PB Films. *Journal of The Electrochemical Society* **154**, F134, doi:10.1149/1.2728038 (2007).
- 224 Benmouhoub, C. *et al.* Influence of the Incorporation of CeO₂ Nanoparticles on the Ion Exchange Behavior of Dodecylsulfate Doped Polypyrrole Films: Ac-Electrogravimetry Investigations. *Electrochimica Acta* **145**, 270-280, doi:10.1016/j.electacta.2014.07.151 (2014).
- 225 Yang, J. & Gunasekaran, S. Electrochemically reduced graphene oxide sheets for use in high performance supercapacitors. *Carbon* **51**, 36-44, doi:10.1016/j.carbon.2012.08.003 (2013).
- 226 Mao, S., Pu, H. & Chen, J. Graphene oxide and its reduction: modeling and experimental progress. *RSC Advances* **2**, 2643-2662, doi:10.1039/C2RA00663D (2012).
- 227 An Wong, C. H., Ambrosi, A. & Pumera, M. Thermally reduced graphenes exhibiting a close relationship to amorphous carbon. *Nanoscale* **4**, 4972-4977, doi:10.1039/C2NR30989K (2012).
- 228 Amarnath, C. A. *et al.* Efficient synthesis of graphene sheets using pyrrole as a reducing agent. *Carbon* **49**, 3497-3502, doi:<http://dx.doi.org/10.1016/j.carbon.2011.04.048> (2011).
- 229 Thakur, S. & Karak, N. Green reduction of graphene oxide by aqueous phytoextracts. *Carbon* **50**, 5331-5339, doi:<http://dx.doi.org/10.1016/j.carbon.2012.07.023> (2012).
- 230 El Achaby, M., Arrakhiz, F. Z., Vaudreuil, S., Essassi, E. M. & Qaiss, A. Piezoelectric β -polymorph formation and properties enhancement in graphene oxide – PVDF nanocomposite films. *Applied Surface Science* **258**, 7668-7677, doi:<http://dx.doi.org/10.1016/j.apsusc.2012.04.118> (2012).
- 231 Wojtoniszak, M. *et al.* Synthesis, dispersion, and cytocompatibility of graphene oxide and reduced graphene oxide. *Colloids and Surfaces B: Biointerfaces* **89**, 79-85, doi:<http://dx.doi.org/10.1016/j.colsurfb.2011.08.026> (2012).
- 232 Thema, F. T. *et al.* Synthesis and Characterization of Graphene Thin Films by Chemical Reduction of Exfoliated and Intercalated Graphite Oxide. *Journal of Chemistry* **2013**, 6, doi:10.1155/2013/150536 (2013).
- 233 Warner, J. H., Schäffel, F., Bachmatiuk, A. & Rummeli, M. H. in *Graphene* 229-332 (Elsevier, 2013).
- 234 Peng, X.-Y., Liu, X.-X., Diamond, D. & Lau, K. T. Synthesis of electrochemically-reduced graphene oxide film with controllable size and thickness and its use in supercapacitor. *Carbon* **49**, 3488-3496, doi:<http://dx.doi.org/10.1016/j.carbon.2011.04.047> (2011).

- 235 Shao, Y., Wang, J., Engelhard, M., Wang, C. & Lin, Y. Facile and controllable electrochemical
reduction of graphene oxide and its applications. *Journal of Materials Chemistry* **20**, 743-748,
doi:10.1039/B917975E (2010).
- 236 Cançado, L. G. *et al.* Quantifying Defects in Graphene via Raman Spectroscopy at Different
Excitation Energies. *Nano Letters* **11**, 3190-3196, doi:10.1021/nl201432g (2011).
- 237 Conway, B. E. *Electrochemical Supercapacitors: Scientific Fundamentals And Technological
Applications.* (1999).
- 238 Chmiola, J. *et al.* Anomalous increase in carbon capacitance at pore sizes less than 1 nanometer.
Science **313**, 1760-1763 (2006).

*Résumé de la Thèse en
Français*

Résumé de la Thèse en Français

Introduction

Les phénomènes de transfert aux interfaces et de transport ionique influencent grandement les performances des matériaux d'électrode pour des applications dans le domaine du stockage de l'énergie.

Certaines études suggèrent l'utilisation de microbalances classiques comme moyen pour caractériser les flux d'ions entre des électrodes à base de carbone et un électrolyte. Il a été démontré que la réponse de la microbalance permet de caractériser ce flux ionique, celui-ci dépendant fortement du point de charge nulle (PZC) du matériau, de la taille des pores et de la taille des ions impliqués dans le processus électrochimique. Malheureusement, les subtilités ou des explications justes ne peuvent pas être atteintes par cette technique classique. De plus, il y a des questions auxquelles on ne peut répondre : pourquoi on obtient des masses molaires élevées qui ne correspondent à aucune espèce présente, qu'elles sont les espèces qui sont transférées rapidement et facilement, quel est le rôle du solvant libre, comment estimer la solvation des cations etc.

Dans cette thèse, des méthodes électrochimiques et gravimétriques, résolues au niveau temporel, comme la spectroscopie d'impédance électrochimique (EIS) couplée à une microbalance à quartz rapide (*ac*-électrogravimétrie), ont été utilisées pour étudier le comportement capacitif des électrodes à base de carbone.

L'utilisation de l'*ac*-électrogravimétrie fournit des informations très pertinentes : la cinétique et l'identification des espèces transférées à l'interface électrode/électrolyte, la séparation de la contribution des différentes espèces et le changement de la concentration relative des espèces au sein du film. Plus précisément, toutes les espèces impliquées dans les processus de compensation de charge peuvent être identifiées par leur masse atomique selon une adsorption réversible d'ions. Par conséquent, l'*ac*-électrogravimétrie apparaît comme un outil intéressant pour ces études.

Dans ce travail, des nanotubes de carbone (CNTs), de l'oxyde de graphène réduit et des nanocomposites CNTs/polypyrrole ou Bleu de Prusse ont été sélectionnés comme matériaux de base pour réaliser des dispositifs pseudo capacitifs. Pour réaliser cette étude, de nouveaux modèles électrogravimétriques qui tiennent compte des processus redox et capacitifs ont été utilisés pour la première fois.

Chapitre I.

Le premier chapitre de cette thèse présente une étude bibliographique sur les dispositifs de stockage de l'énergie (batteries et super-capacités) selon trois parties. Dans un premier temps, un petit historique, les principes d'opération et les domaines d'applications sont présentés. La deuxième partie est consacrée aux composants de ces systèmes en termes de matériaux et d'électrolytes. La troisième partie de ce chapitre est reliée aux différentes techniques utilisées pour la caractérisation et l'évaluation des performances des électrodes à base de carbone.

Les systèmes de stockage électrochimiques de l'énergie sont traditionnellement divisés entre les systèmes de forte densité (batteries) et les systèmes de forte puissance (capacités ou supercapacités). Ici, nous nous intéresserons à ces derniers dispositifs. Aujourd'hui, il en existe plusieurs types utilisant différents mécanismes de stockage.¹ Les deux principaux sont les systèmes à double couche électriques (EDCLs) et les pseudocapacités (Voir Figure 1).

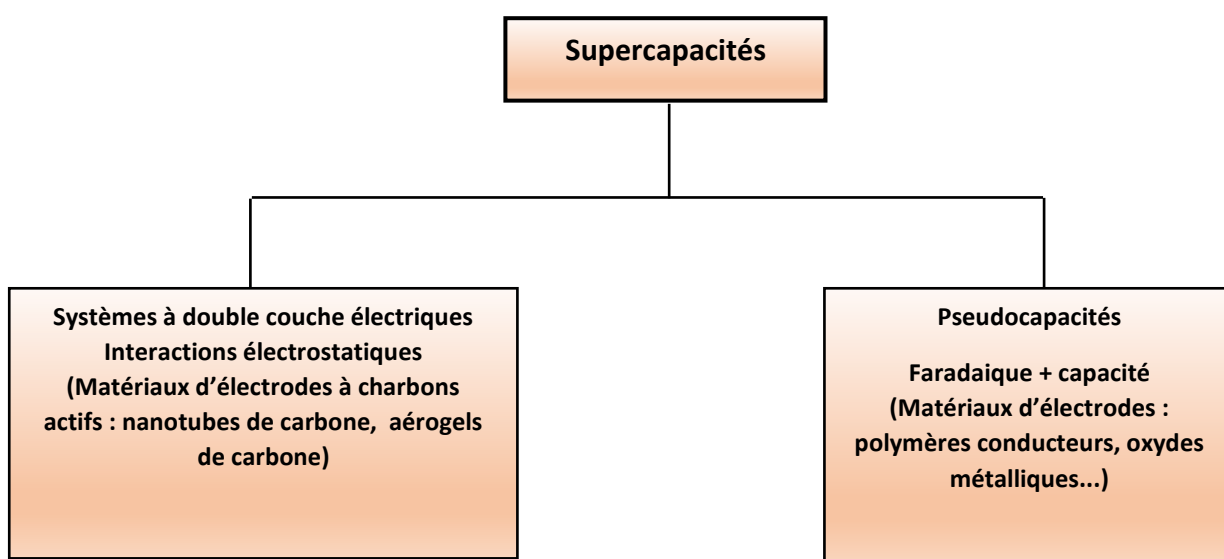

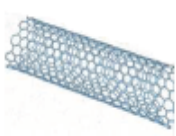


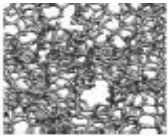



Figure 1. Différentes catégories des dispositifs de type super-capacité.

Ensuite, les principaux composants qui concernent les matériaux et les électrolytes employés sont détaillés. Actuellement, les trois principales catégories de matériaux d'électrodes actives sont basées sur les matériaux carbonés, les oxydes de métaux de transition^{2,3} et les polymères conducteurs.² De ces trois classes de matériaux, le carbone est le plus fréquemment utilisé dans les EDLCs. Ces carbones peuvent avoir des structures très diverses: (1) carbone de type sphère (OLCs),

(2) nanotubes de carbone (CNTs), (3) graphène, (4) carbone de type carbure (CDCs), (5) carbones actifs (ACs), et (6) carbones structurés (Voir Table 1).^{1,4,5}

Table 1. Différentes structures de carbone et ses principales caractéristiques.⁴

Material	Carbon onions	Carbon nanotubes	Graphene	Activated carbon	Carbide derived carbon	Templated Carbon
Dimensionality	0-D	1-D	2-D	3-D	3-D	3-D
Conductivity	High	High	High	Low	Moderate	Low
Volumetric Capacitance	Low	Low	Moderate	High	High	Low
Cost	High	High	Moderate	Low	Moderate	High
Structure						

Les critères pour un électrolyte idéal repose sur une large fenêtre électrochimique (>4 V), une conductivité spécifique supérieure à 75 mS.cm^{-1} , une bonne stabilité thermique jusqu'au 300°C et une faible toxicité.⁶ Cependant de nombreux efforts dans la recherche d'électrolytes performants ont été orientés vers des milieux très conducteurs, stables et avec une fenêtre de potentiel la plus large possible (voir Table 2).

Table 2. Tension admissibles et conductivité ionique pour différents types d'électrolytes.

Electrolyte	Fenêtre électrochimique (V)	Conductivité ionique (mS.cm^{-1})
Aqueuse	$\leq 1,2$ ^{7,8}	>400 ^{7,9}
Organique ($\text{NEt}_4\text{BF}_4/\text{PC}$)	$3,0$ ⁷	13 ⁷
Organique ($\text{NEt}_4\text{BF}_4/\text{ACN}$)	$2,7$ ⁷	56 ⁷
Liquides ioniques	$3-5$ ^{8,9}	<15 ^{7,9}

Finalement, différentes techniques telles que des méthodes d'imagerie/caractérisation (SEM-FEG, MET, BET, DRX), électrochimiques (voltamétrie cyclique, spectroscopie d'impédance électrochimique), de gravimétrie (microbalance à quartz) classique ont été employées pour caractériser la morphologie, la structure et la réponse électrochimique de ces différents films.

Chapitre II

Le chapitre 2 porte sur la partie expérimentale de ce travail. Les procédures de préparation des films, ainsi que les méthodes utilisées pour la caractérisation structurale/morphologique des films, en particulier, le principe de fonctionnement, le type d'instrument utilisé et les conditions dans lesquelles les expériences ont été effectuées, sont présentées. Les techniques de caractérisation électrochimiques en particulier l'*ac*-électrogravimétrie sont aussi détaillées dans ce chapitre.

Pour réaliser nos électrodes nanostructurées trois types de nanotubes de carbone, SWCNT, DWCNT et MWCNT ainsi qu'un oxyde de graphène ont été choisis en raison de leurs dimensions de pores et de leurs surfaces spécifiques. Les films de carbone ont été préparés selon la méthode de « *drop-casting* » décrite dans la littérature¹⁰⁻¹³ sur une électrode d'or ($S = 0,20 \text{ cm}^2$) de microbalance à quartz (9MHz - AWS, Valencia, Espagne), à partir d'une solution contenant les nanotubes ou l'oxyde de graphène. Les proportions suivantes ont été utilisées : 90% de Carbone et 10% de PVDF-HFP (Poly(vinylidene fluoride-hexafluoropropylène)) dans du NMP (N-méthylpyrrolidone). Puis, une fois déposés les films de carbone ont été soumis à un traitement thermique à 120°C pendant 30 minutes, avec une vitesse de montée en température de 5°C min^{-1} afin d'évaporer le solvant résiduel et améliorer les propriétés d'adhérence du film sur l'or (Voir Figure 2).

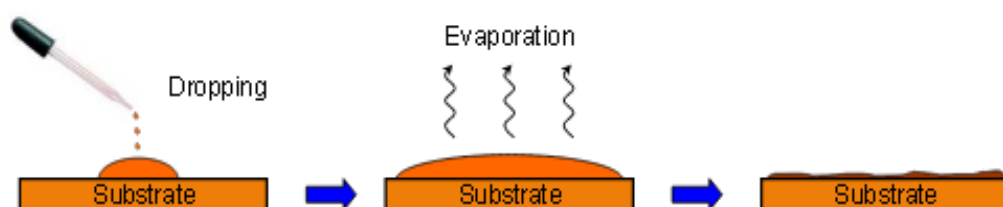


Figure 2. Représentation schématique de la préparation de films de CNTs ou d'oxyde de graphène.

La morphologie/structure de ces films a été caractérisée par des techniques telles que le MEB, le MET, la DRX et la BET (sur les récatifs initiaux). L'épaisseur des films a été estimée suffisamment mince ($\sim 500 \text{ nm}$) pour que l'équation de Sauerbrey s'applique ce qui permet de garder le régime gravimétrique.¹⁴

Des techniques gravimétriques telles que l'EQCM et particulièrement l'*ac*-électrogravimétrie ont été mises en œuvre pour expliquer en détail les phénomènes d'adsorption/désorption ou insertion/expulsion des espèces à l'interface électrode/électrolyte.

Résumé de Thèse

Le film de carbone est déposé sur l'électrode d'or d'une microbalance à quartz à 9 MHz et est soumis à une faible perturbation sinusoïdale en tension ($\Delta E=80\text{mV}$). Cette dernière entraîne une variation de masse, Δm , au sein du film électroactif suite au transfert des différentes espèces du film. La réponse en masse, Δm , est mesurée en même temps que le courant, ΔI , qui passe au travers de l'électrode de travail. Les signaux résultants sont envoyés à un analyseur de réponse en fréquence à quatre canaux (Solartron 1254), ce qui permet d'enregistrer simultanément la fonction de transfert électrogravimétrique, $\frac{\Delta m}{\Delta E}(\omega)$ et l'impédance électrochimique, $\frac{\Delta E}{\Delta I}(\omega)$ à chaque potentiel appliqué (Voir Figure 3).

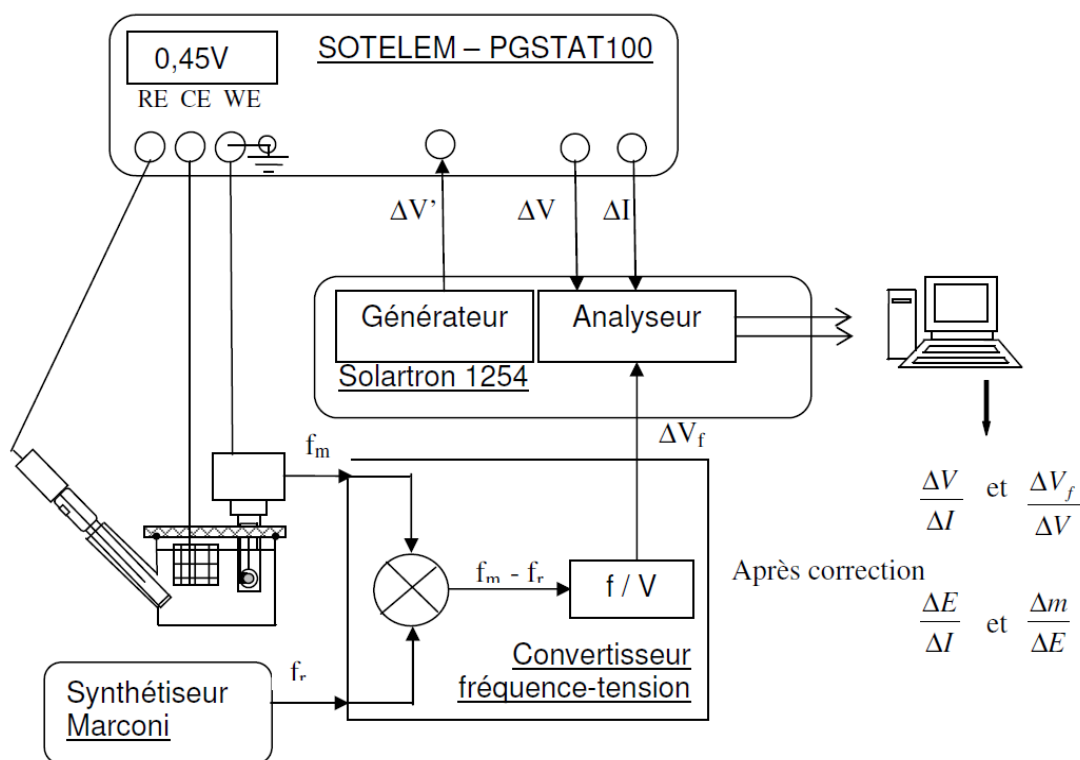


Figure 3. Dispositif expérimental de mesure d'ac-électrogravimétrie.¹⁵

Une modélisation des réponses d'ac-électrogravimétrie permet de remonter à la masse atomique des différentes espèces impliquées dans les processus électrochimiques. Les cinétiques de transfert et les résistances de transfert de ces mêmes espèces sont aussi estimées de la même manière.

Chapitre III

Le troisième chapitre est dédié à la clarification des mécanismes de transfert des ions à l'interface électrode à base de CNT/électrolyte. Il s'agit aussi de valider l'impact positif de l'utilisation d'électrodes nanostructurées dans des dispositifs de stockage d'énergie. Ici, un exemple détaillé est présenté afin de montrer la puissance de notre approche pour les films de type SWCNT testés en

milieu NaCl. À la fin, une déconvolution des réponses gravimétriques via une EQCM classique est montrée grâce à l'apport de la technique d'*ac*-électrogravimétrie. De plus, une étude des mécanismes en solvant organique est aussi présentée dans ce chapitre.

Mesures de microbalances classiques

La figure 4 (A et B) présente des courbes d'électrogravimétrie cyclique pour un film SWCNTs plongé dans NaCl 0,5M à pH neutre. La figure 4B donne la variation de masse du film accompagnée de la variation du courant dans une gamme de potentiel entre 0,45V et -0,45V vs Ag/AgCl. La voltammétrie cyclique a été effectuée à différentes vitesses de balayage et présente un comportement capacitif typique caractérisé par une forme rectangulaire dans le domaine de potentiel -0,1 V à 0,4 V vs Ag /AgCl. Ce résultat suggère que ce comportement est principalement dû à l'adsorption des ions sur la surface des nanotubes de carbone, c'est à dire sans aucune réaction faradique. L'écart par rapport à un comportement purement capacitif à des valeurs plus cathodiques (Fig. 4A) est probablement dû à la présence d'oxygène ou de groupes fonctionnels de surface ou du catalyseur restant après purification des nanotubes de carbone.¹⁶⁻¹⁹ En ce qui concerne les réponses en masse, une réponse similaire est observée pour toutes les vitesses de balayage (Fig. 4B). La variation de masse de l'électrode de SWCNT (Fig. 4B) présente un changement de pente, $\frac{\Delta m}{\Delta E} < 0$ pour le transfert de cations et $\frac{\Delta m}{\Delta E} > 0$ pour les anions, autour de 0,1 V vs Ag/AgCl. Cela correspond au point de charge nulle (pzc) qui est autour de cette valeur. Les valeurs de capacité spécifique ont été estimées en utilisant les courbes I-E de la Fig. 4A.

Les valeurs de capacités spécifiques atteignent 25 F g⁻¹ pour une vitesse de balayage de 100 mV s⁻¹ (fig. 4C). Cette valeur est du même ordre de grandeur que celles qui sont données dans la littérature.²⁰

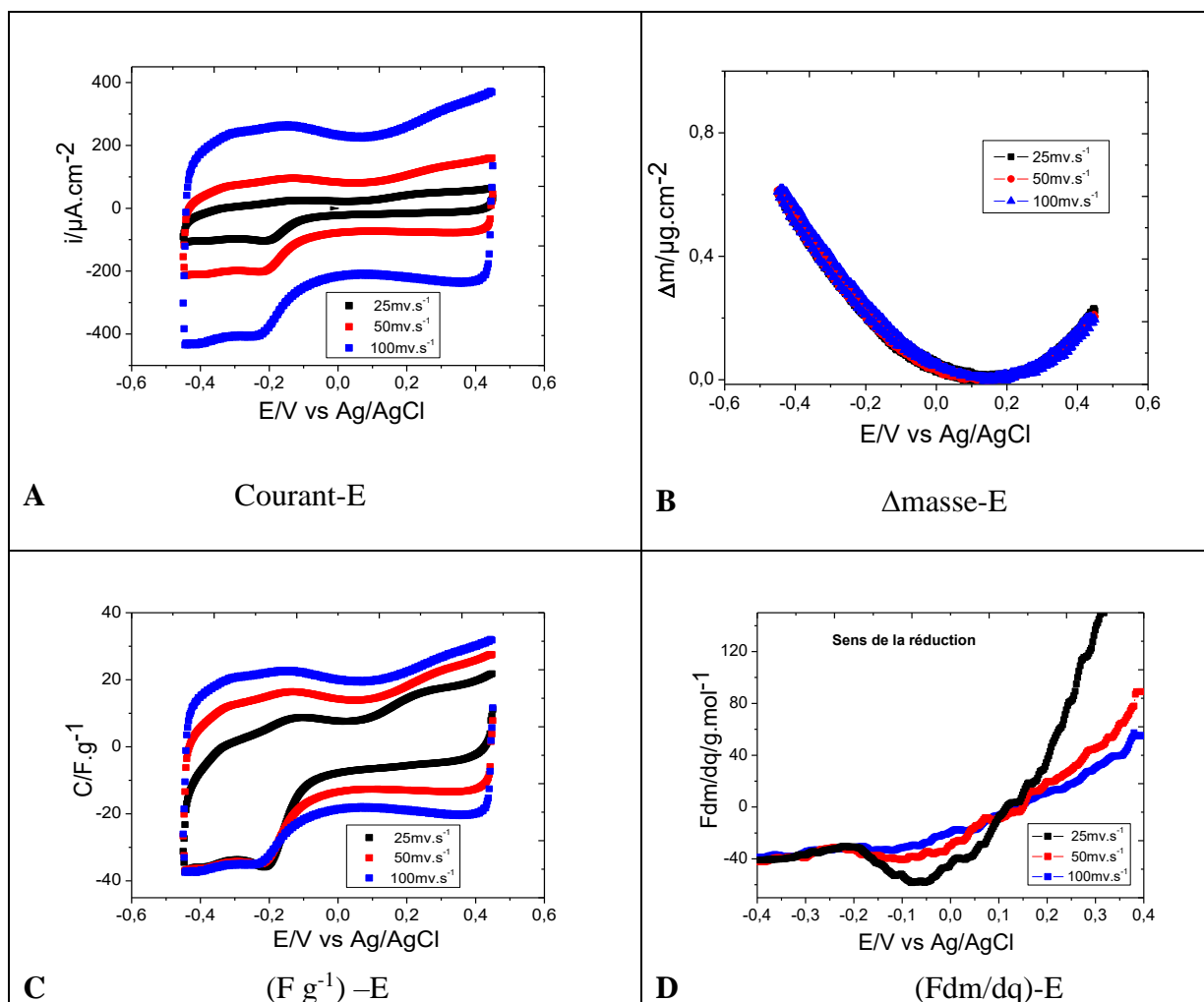


Figure 4. Courbes d'électrogravimétrie cyclique (A) et (B), de capacité spécifique (C) et de fonction Fdm/dq (D) pour un film de SWCNTs en milieu NaCl 0,5M - pH 7. Balayage de potentiel entre 0,45V et -0,45V vs Ag/AgCl pour 25, 50 et 100 mV s^{-1} .

Pour avoir plus d'indications sur la nature des espèces adsorbées ou désorbées, la fonction Fdm/dq a été calculée; elle correspond à la masse molaire de l'espèce échangée pour une vitesse de balayage donnée. La figure 4D présente la variation de la fonction Fdm/dq en fonction du potentiel entre -0,4 V et 0,4V vs Ag/AgCl. La fonction Fdm/dq , en particulier à haute vitesse de balayage, montre une valeur de Fdm/dq qui varie entre -40 et -23 g mole^{-1} pour des potentiels entre -0,4V et 0,05V vs Ag/AgCl. Cela correspond à la contribution de cations dont la masse molaire supérieure à 23 g mole^{-1} trouvée peut être expliquée par la participation soit du solvant libre transféré dans le même sens que les Na^+ , soit du solvant associé aux ions Na^+ . Pour répondre de manière plus précise, des mesures d'*ac*-électrogravimétrie ont été menées pour identifier les différentes espèces et déterminer le rôle de chaque espèce, anion, cation, cation solvaté, solvant libre, directement ou indirectement impliqués dans le processus électrochimique.

Mesures d'*ac*-électrogravimétrie

Les mesures d'*ac*-électrogravimétrie ont été effectuées dans une solution de NaCl 0,5 M à différents potentiels entre -0,4 V et 0,4 V vs. Ag/AgCl. À chaque potentiel imposé, la réponse de la masse Δm et du courant ΔI à une perturbation sinusoïdale de faible amplitude ΔE (80mV), a été mesurée à différentes fréquences de modulation comprises entre 63 kHz et 10 mHz. Les résultats seront limités à des mesures en solution aqueuse NaCl 0,5M.

Par exemple à -0,4 V vs Ag/AgCl, les fonctions de transfert théoriques ont été ajustées aux fonctions de transfert expérimentales en ne tenant compte que de trois espèces ($\text{Na}^+\cdot\text{H}_2\text{O}$, H^+ et H_2O). Dans ce cas, nous avons obtenu un très bon accord pour les différentes fonctions de transferts y compris partielles. Le transfert du Na^+ hydraté intervient aux hautes fréquences (plus rapide) et celui du proton intervient à plus basse fréquence (plus lent). La cinétique de l'eau libre est très proche de celle du Na^+ hydraté. Les valeurs de résistances de transfert ionique montrent que le transfert du sodium hydraté est beaucoup plus facile que celui du proton. La résistance de transfert du solvant libre est proche de celle de transfert de sodium hydraté. Malgré une cinétique lente et des valeurs de résistance de transfert élevées, la contribution des protons dans le processus de stockage de charge n'est pas négligeable. Ces résultats suggèrent que l'adsorption de ces différentes espèces a certainement lieu sur différents sites au sein des films de SWCNT. L'intérieur des tubes de SWCNT (diamètre ~ 1 nm) est probablement accessible pour les protons et pas pour les Na^+ plus gros. Les ions Na^+ hydratés peuvent être adsorbés à l'extérieur des nanotubes et/ou entre les faisceaux des SWCNT. En regardant les valeurs similaires des constantes cinétiques de transfert et des résistances de transfert pour le sodium hydraté et le solvant libre, ce dernier semble accompagner les ions Na^+ hydratés. Ces molécules d'eau libre peuvent également être des molécules d'eau qui quittent la coquille de solvation du Na^+ pour lui permettre d'accéder à des sites au sein des films. Le desolvation partielle des ions avant d'être adsorbés dans les pores plus petits a été décrite dans la littérature^{21,22} (Voir Figure 5).

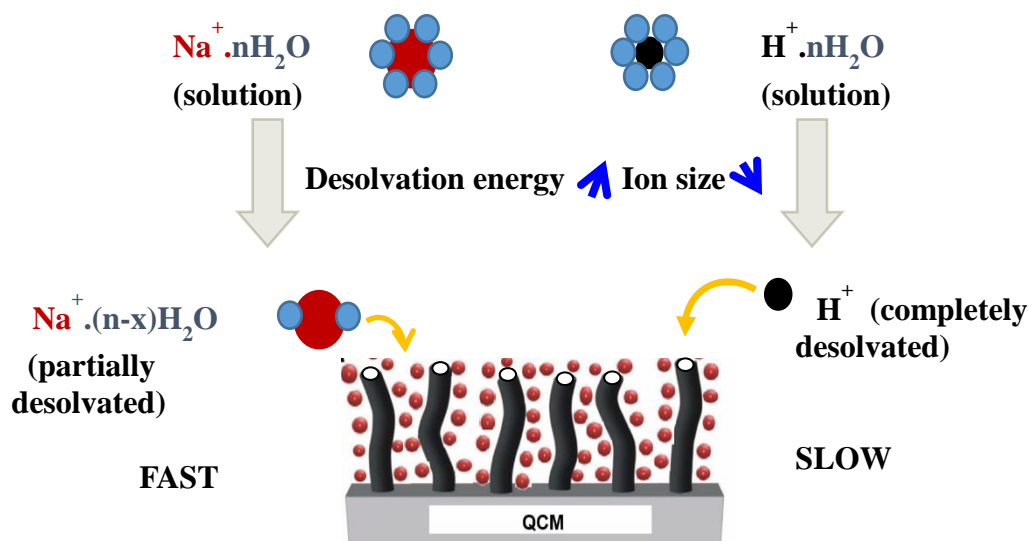


Figure 5. Représentation schématique de l'interaction des ions avec des électrodes à base de nanotubes de carbone déposés sur une électrode d'or de microbalance à quartz.

Déconvolution de la réponse gravimétrique de l'EQCM

En utilisant les résultats d'*ac*-électrogravimétrie, il est possible de recalculer les changements de masse du film par rapport aux potentiels appliqués. En effet, en utilisant la masse atomique de chacune des espèces impliquées dans le processus électrochimique, et les variations de concentration relative en relation avec ces espèces, la variation de masse globale a été estimée et comparée à la variation de masse déterminé par EQCM (électrogravimétrie cyclique)

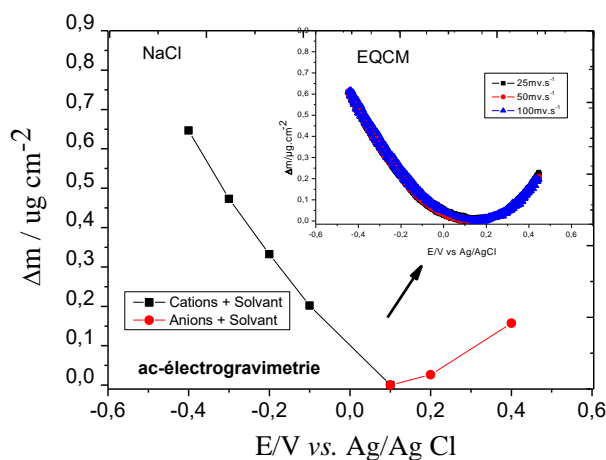


Figure 6. Reconstruction de la variation de masse totale obtenue par *ac*-électrogravimétrie et comparaison avec la réponse classique de l'EQCM.

Comme le montre la Figure 6, un bon accord est obtenu pour les deux réponses gravimétriques. C'est la première fois où cette déconvolution est montrée. Cela montre la puissance de cette méthode dynamique d'*ac*-électrogravimétrie.

Mesures d'*ac*-electrogravimétrie dans un solvant organique

Des mesures d'*ac*-électrogravimétrie ont été réalisées dans LiClO_4 0,5M en milieu PC (carbonate de propylène). Les fonctions de transfert théoriques ont été calculées et ajustées aux réponses expérimentales en tenant compte de trois espèces : Li^+ , H_3O^+ et solvant. Le transfert du Li^+ intervient aux hautes fréquences (plus rapide) et celui du proton hydraté intervient à plus basse fréquence (plus lent). La cinétique du solvant libre est très proche de celle du Li^+ . Les valeurs qui caractérisent la résistance de transfert ionique signifient que le transfert du lithium est beaucoup plus facile que celui de H_3O^+ . Ces résultats suggèrent que l'adsorption de ces différentes espèces a lieu sur différents sites. L'identification d'une espèce hydratée (H_3O^+) est certainement due à la présence de traces d'eau au sein du carbonate de propylène.

Chapitre IV

Ce chapitre étudie l'influence des différents types de CNTs et des propriétés de l'électrolyte (nature du cation et valeur du pH) sur la dynamique de transfert des ions. Pour cela des techniques de caractérisation électrogravimétriques classiques (EQCM) et dynamiques (*ac*-electrogravimétrie) mentionnées précédemment ont été employées.

Des Électrodes à base de SWCNT, DWCNT et MWCNT ont été préparées en milieu NaCl et des électrodes à base de SWCNT testées dans différents électrolytes tels que LiCl, NaCl et KCl. Les meilleurs candidats pour les applications de stockage de l'énergie en termes de courant et masse sont à base de SWCNT et DWCNT. En outre, la nature chimique et le rôle de chaque espèce, anion, cation, cation solvaté, solvant libre, directement ou indirectement impliqué dans le stockage de charge, ont été identifiés par des mesures d'*ac*-électrogravimétrie. Les fonctions de transfert théoriques ont été ajustées à celles expérimentales en ne prenant en compte que les trois espèces suivantes : ($\text{Li}^+\cdot\text{H}_2\text{O}$, H^+ et H_2O), ($\text{Na}^+\cdot\text{H}_2\text{O}$, H^+ et H_2O), (K^+ , H^+ et H_2O) pour LiCl, NaCl, KCl respectivement et cela à un potentiel de -0,4V vs Ag/AgCl. Pour chaque milieu, un bon accord entre les données expérimentales et théoriques, cela pour toutes les fonctions de transferts mesurés, a été obtenu. Le transfert du lithium hydraté, du sodium hydraté et du potassium hydraté se produit à des fréquences élevées (le plus rapide), le solvant à des fréquences intermédiaires et le proton à des

fréquences basses (le plus lent). Le transfert du lithium hydraté, du sodium hydraté, du potassium et du solvant est plus facile que celui du proton désolvaté. Ces résultats suggèrent que l'adsorption de ces espèces a lieu sur différents sites au sein des électrodes de CNTs.

Les résultats d'électrogravimétrie qui concernent l'influence du pH (valeurs de pH 2, 7, 10 en milieu NaCl 0.5M) indiquent que la variation de masse est plus importante aux potentiels les plus anodiques lorsque la surface est chargée positivement et cela pour des valeurs de pH faibles. Lorsque la surface est chargée négativement aux fortes valeurs de pH, la variation de masse est plus importante aux potentiels les plus cathodiques. La présence des anions à un pH acide est plus importante alors qu'à un pH plus basique la présence des cations devient plus importante. Pour confirmer cette hypothèse des mesures d'*ac*-électrogravimétrie ont été mises en œuvre. Les espèces prises en compte sont dans ce cas sont : $\text{Na}^+ \cdot \text{H}_2\text{O}$, H^+ , H_2O et Cl^- . Il a été constaté que la cinétique de transfert de $\text{Na}^+ \cdot \text{H}_2\text{O}$ est plus rapide à pH 7 et 10 qu'à pH 2 pour des potentiels cathodiques. La cinétique de transfert de H^+ est légèrement plus rapide à pH 2 qu'à pH 7 ou pH 10 aux potentiels les plus cathodiques. A des potentiels plus anodiques la cinétique de transfert de Cl^- est plus rapide à pH 2 qu'à pH 7 et pH 10. La résistance de transfert des cations est plus faible à pH 7 et pH 10 qu'à pH 2 et au contraire, la résistance de transfert des anions est plus faible à pH 2 par rapport à pH 7 et pH 10. Finalement les valeurs des paramètres cinétiques, de résistance de transfert et de variation de concentration montrent que le solvant est toujours dans le même sens de transfert que celui des anions ou des cations ce qui peut s'expliquer par un effet d'entraînement. Ces résultats confirment que les cations sont majoritairement adsorbés lorsque la surface est chargée négativement et que les anions sont majoritairement adsorbés lorsque la surface est chargée positivement.

Chapitre V

Le chapitre est focalisé sur l'étude de films composites, SWCNT/PB (Bleu de Prusse) et SWCNT/PPy (polypyrrole), et de films d'oxydes de graphène réduit (ERGO). Cette approche avec des films composites a été examinée afin d'augmenter les performances des films à base de CNT purs.

Mesures sur des films SWCNT/PB

La Figure 7 montre les changements de courant et de masse d'un film de SWCNT/PB quand il est oxydé et réduit entre -0.45V et 0.45V vs Ag/AgCl à une vitesse de balayage de 50 mV s^{-1} dans une solution 0.5M de KCl à pH 3.

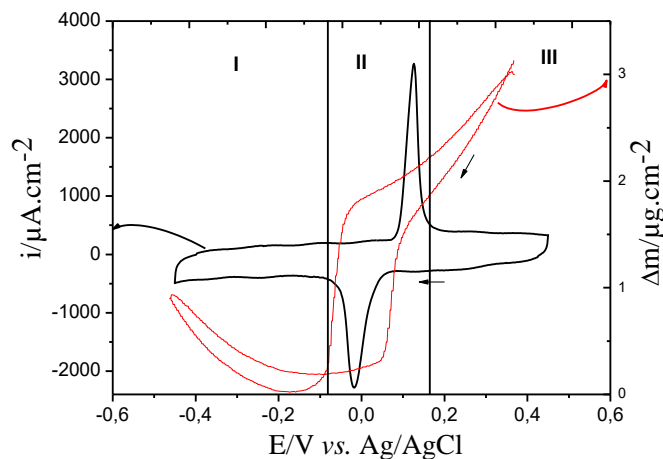


Figure 7. Réponses électrogravimétriques d'un film SWCNT/PB : courant vs potentiel et variation de masse vs potentiel mesurées dans une solution aqueuse 0.5M KCl à 50mV s⁻¹.

La voltammetrie cyclique présentée Figure 7 présente un comportement capacitif entre -0,1V et -0,45V et entre 0,2V et 0,45V. Ceci est caractéristique de la réponse électrochimique des films de CNTs purs. Dans la gamme entre 0,05V et 0,15V, des pics d'oxydation/réduction sont observés, ce qui est caractéristique de la réponse du PB. Les valeurs de courant sont plus importantes ici comparativement à celles indiquées dans la littérature.^{15,23,24} Ceci est certainement lié à la plus grande surface spécifique. Compte tenu de la variation de masse de l'électrode, un comportement particulier est observé : la contribution des cations est présente entre -0.45V et -0.15V alors que la contribution des anions est visible entre 0,2V et 0,45V. De plus, les valeurs de variation de masse sont plus importantes que celles trouvées dans la littérature^{15,24} et aussi plus importantes que les valeurs de variation de masse pour les films de SWCNT seuls.

Les données expérimentales obtenues par *ac*-électrogravimétrie ont été ajustées en utilisant les modèles présentés auparavant. Ainsi, il a été observé que le transfert de K⁺ était plus rapide que le transfert de Cl⁻ dans la fenêtre de potentiel étudiée. Ceci est probablement lié au fait qu'à la fois des phénomènes d'électro adsorption/désorption et redox sont impliqués pour K⁺, tandis que Cl⁻ n'est lié qu'aux phénomènes d'adsorption/désorption. En effet, pour les films de PB purs, la contribution d'anions n'a jamais été vue et pour cela, elle ne peut être liée qu'à un mécanisme d'électroadsorption. La cinétique de transfert de K⁺ est équivalente celle observée dans le cas de SWCNT tout seul et celle de H⁺ est plus rapide que la cinétique de transfert de H⁺ dans SWCNT seul. , probablement en raison de la différence de pH. La cinétique de transfert de Cl⁻ pour SWCNT/PB est plus lente que celle de Cl⁻ dans le SWCNT pur. Les valeurs de résistance de transfert de K⁺ sont équivalentes pour les deux types de film, SWCNT/PB et SWCNT tout seul. Le

H^+ pour SWCNT/PB est plus facile à transférer que le H^+ pour SWCNT tout seul. Finalement, le Cl^- de SWCNT/PB est plus facile à transférer que le Cl^- de SWCNT tout seul.

Résultats SWCNT/PPy

Les Figures 8A et B montrent les variations de courant et de masse d'un film SWCNT/ PPy quand il est oxydé et réduit entre -1,2V et 0,45V vs Ag/AgCl dans une solution de NaCl 0,5M à pH 7.

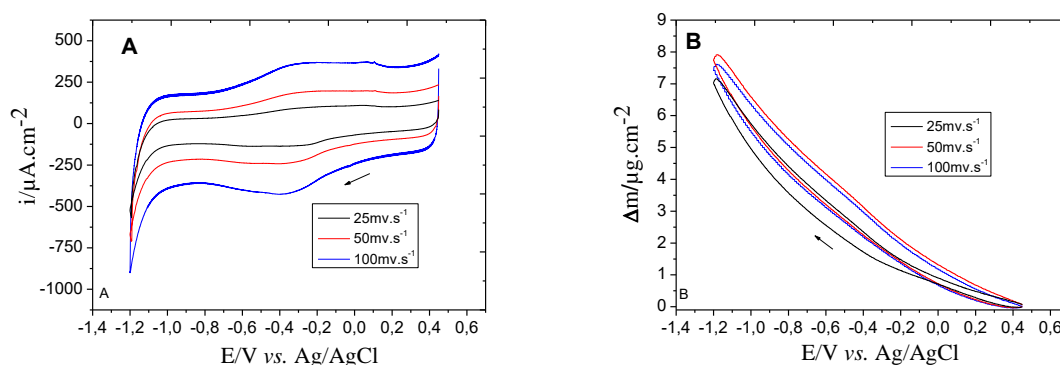


Figure 8. Réponses électrogravimétriques d'un film de SWCNT/PPy : (A) courant vs potentiel et (B) variation de masse vs potentiel mesurée dans une solution aqueuse de NaCl 0.5M.

Lorsque le film composite est réduit, une augmentation de masse est observée et quand il est oxydé, une perte de masse est observée. Toutefois, il paraît difficile d'interpréter ces variations en n'utilisant que cette approche basique. Les données expérimentales obtenues par *ac*-électrogravimétrie permettent de mieux expliquer ces variations de masse. Après ajustement des données expérimentales avec les modèles développés, il a été constaté que le transfert de $Na^+ \cdot nH_2O$ est plus rapide que le transfert de H^+ et de Cl^- dans la fenêtre de potentiel étudiée.

D'autre part, avec les films composites SWCNT/PPy les cinétiques de transfert de $Na^+ \cdot nH_2O$ sont équivalentes à celles mesurées pour SWCNT seul et plus importantes que les cinétiques de Na^+ mentionné dans la littérature.²⁵ Les cinétiques de transfert de H^+ pour SWCNT/PPy sont plus importantes que les cinétiques de transfert de H^+ pour SWCNT seul alors que les cinétiques de transfert du Cl^- dans le SWCNT/PPy sont équivalentes aux cinétiques de transfert du Cl^- dans le SWCNT et plus important que la cinétiques de transfert du Cl^- mentionnées dans la littérature.²⁵

Mesures sur des films d'oxyde de graphène réduit (ERGO)

Les Figures 9A, C et D représentent les réponses de voltamétrie cyclique d'un film d'ERGO obtenue dans trois électrolytes aqueux : LiCl, NaCl et KCl 0,5 M. Pour tous ces électrolytes, un

courant capacitif a été observé avec une plus grande valeur lorsque la vitesse de balayage élevée. La capacité spécifique a été aussi trouvée autour de 100 F.g⁻¹.

Dans cette étude, les films minces ERGO montrent des réponses en courant avec une forme quasi-rectangulaire ce qui indique que le stockage de charge est principalement dû à un processus réversible d'électro-adsorption d'ions.

La légère distorsion qui apparaît est corrélée à la présence d'une légère contribution faradique. Ceci peut être lié à de nombreuses réactions telles que la réduction du proton présent dans l'électrolyte, la réduction de groupes fonctionnels à la surface des films d'ERGO... Toutefois, pour les trois électrolytes les valeurs de courant sont assez semblables (Figure 9 A, C et D).

Les variations de masse au sein des films d'ERGO sont déterminées simultanément au cours de la voltamétrie cyclique. Celles-ci sont également assez similaires entre deux milieux, LiCl et KCl (Figure 9B et F). D'un point de vue théorique, si seulement le cation nu est transféré pendant le processus d'électroadsorption, la variation de masse devrait être 5 fois plus élevée lors du cyclage dans une solution aqueuse de KCl en raison de la masse molaire plus élevée des ions K⁺ par rapport à Li⁺ ($M_{K^+} = 39 \text{ g mol}^{-1}$, $M_{Li^+} = 7 \text{ g mol}^{-1}$) pour des variations de charges identiques. Cela pourrait indiquer que l'espèce Li⁺ est transférée conjointement avec des molécules de solvant.

Une autre explication est que les deux espèces sont électroadsorbées sous une forme hydratée, mais selon différents degrés d'hydratation. En effet, l'espèce Li⁺ est plus étroitement liée à des molécules d'eau en raison de sa petite taille où les interactions électrostatiques sont par conséquent plus fortes. Il est donc possible d'avoir un plus haut niveau d'hydratation de l'espèce lithium électroadsorbée par rapport à l'espèce potassium.

En milieu NaCl, l'ERGO présente des valeurs de courant légèrement plus élevées ainsi que des réponses en masse plus élevées par rapport aux deux autres électrolytes (LiCl et KCl). Ceci indique des mécanismes plus complexes d'électroadsorption que ceux décrits habituellement dans la littérature où une charge négative est souvent compensée par l'adsorption d'un seul et unique cation de l'électrolyte. Cela indique également que la limitation cinétique est due au transfert ionique plutôt qu'au transfert électronique.

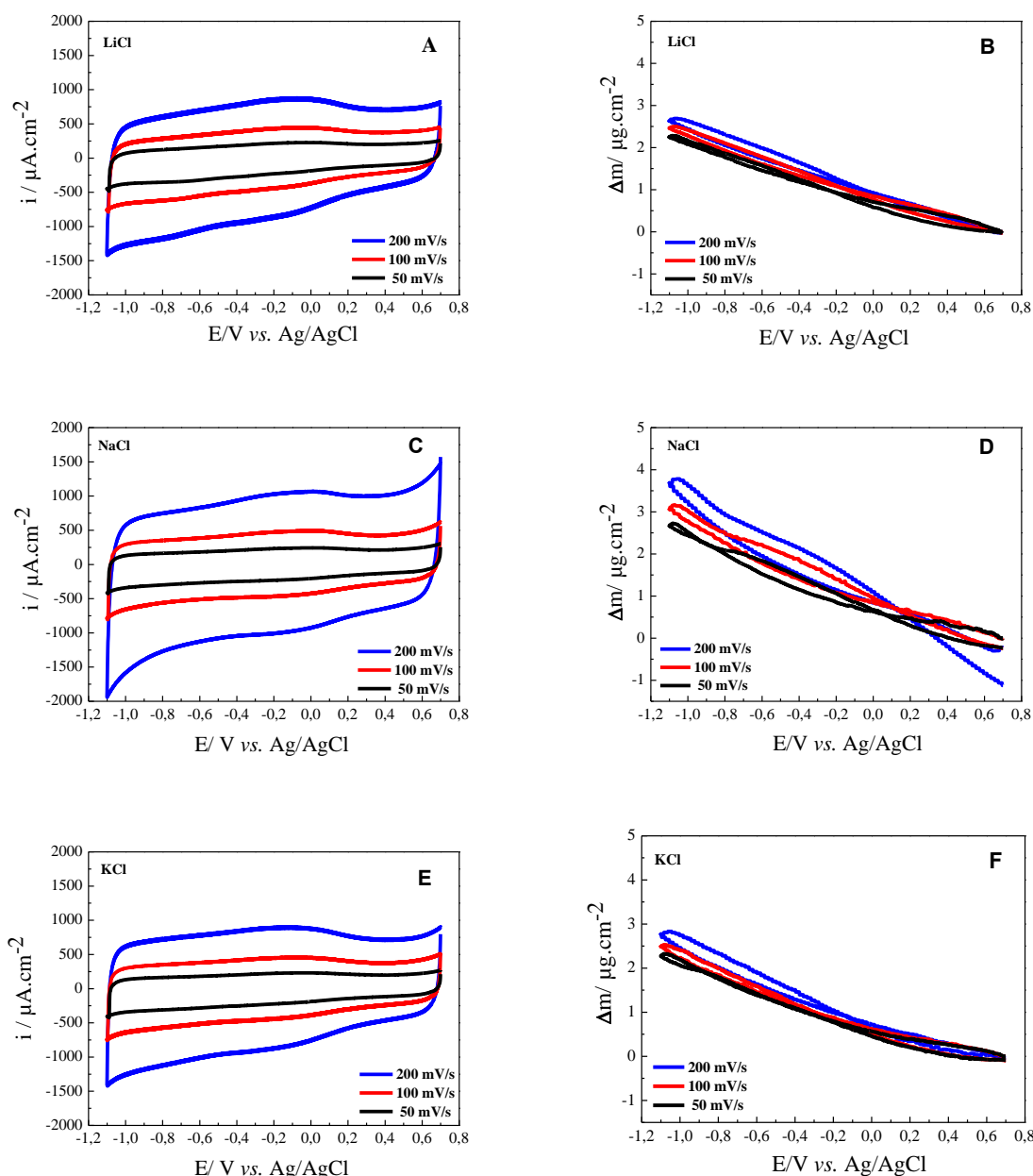


Figure 9. Réponses électrogravimétriques d'un film d'ERGO obtenues dans différents électrolytes aqueux : 0.5 M LiCl (A et B), 0.5 M NaCl (C et D) et 0.5 M KCl (E et F). Le même film a été testé dans les trois électrolytes.

En outre, pour être en mesure de mieux comprendre ces mécanismes d'électroadsorption des mesures d'*ac*-électrogravimétrie ont été réalisées dans les trois mêmes milieux. Les données expérimentales obtenues d'*ac*-électrogravimétrie ont été ajustées grâce à un modèle théorique afin de trouver les paramètres cinétiques, d'identifier les espèces transférées et surtout de comparer le comportement de ces différentes espèces selon les différents électrolytes. Le transfert du K^+ est le plus rapide car il est plus facile à désolvater en raison de sa grande taille. Au contraire, les ions Li^+

sont fortement liés aux molécules d'eau ce qui rend le transfert plus lent. Dans un même électrolyte, deux cations sont détectés, l'un rapide et partiellement hydraté et l'autre plus lent, du même cation mais totalement désolvaté. Ainsi, l'électroadsorption de ces deux cations au sein des films d'ERGO pourrait se produire sur deux sites différents ; directement sur la surface (sites les plus accessibles) ou entre les piles des feuillets de graphène (sites moins les moins accessibles) (voir Figure 10).

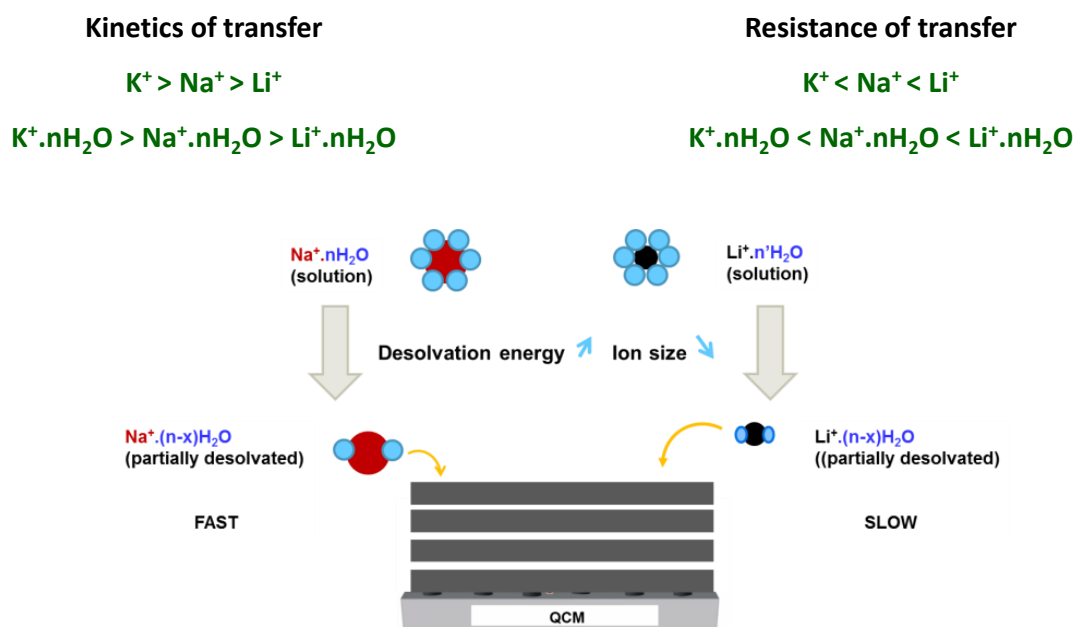


Figure 10. Représentation schématique des sites d'adsorption pour Li⁺.nH₂O et Li⁺ dans les films minces d'ERGO.

Conclusion générale

Des films à base de nanotubes de carbone et d'oxyde de graphène réduit (ERGO) ont été préparées sur des électrodes d'or de microbalances et testés dans différents électrolytes tels que LiCl, NaCl et KCl. Les résultats obtenus par des mesures d'électrochimie classique, particulièrement en termes de capacité spécifique, ont montré que le film d'ERGO est le meilleur candidat pour les applications dans le domaine du stockage de l'énergie.

Pour des électrodes à base de nanotubes de carbone la nature chimique et le rôle de chaque espèce, qui intervient potentiellement dans le processus d'électroadsorption, ont été déterminés par des mesures d'*ac*-électrogravimétrie. Les fonctions de transfert théoriques ont été calculées en prenant en compte trois espèces différentes (Li⁺.H₂O, H⁺ et H₂O), (Na⁺.H₂O, H⁺ et H₂O), (K⁺, H⁺ et H₂O) pour LiCl, NaCl, KCl respectivement pour un potentiel de -0,4V vs Ag/AgCl. Un bon accord entre les données expérimentales et théoriques pour toutes les fonctions de transfert calculées a été obtenu. Le transfert du lithium hydraté, du sodium hydraté et du potassium se produit à des

fréquences élevées (le plus rapide), le solvant est transféré à des fréquences intermédiaires et le proton désolvaté à des fréquences plus basses (le plus lent). Le transfert du lithium hydraté, du sodium hydraté, du potassium et du solvant est plus facile que celui des ions H^+ . Ces résultats suggèrent que l'adsorption de ces espèces chargées a lieu sur différents sites dans les électrodes de CNTs avec des accessibilités différentes. De plus ces résultats permettent de déconvoluer la réponse gravimétrique globale obtenue avec une microbalance classique et cela pour la première fois.

L'étude de l'effet du pH sur la réponse des films de CNTs confirment que les cations sont majoritairement électroadsorbés lorsque la surface est chargée négativement et que les anions sont majoritairement adsorbés lorsque la surface est chargée positivement.

Finalement pour des films nanocomposites SWCNT/PB et SWCNT/PPy, la nature chimique et le rôle de chaque espèce dans les processus capacitifs et pseudo-capacitifs a été mis en évidence par *ac*-électrogravimétrie. Une réponse mixte, capacitive liée aux CNTs et redox, liée à PB ou PPY, est discriminée dans ce cas.

Dans le cas des films d'ERGO le scénario semble un peu différent. Le transfert du K^+ est le plus rapide car il est le plus facile à désolvater en raison de sa grande taille. Au contraire, Li^+ est fortement lié aux molécules d'eau ce qui rend son transfert plus lent. L'électroadsorption des espèces dans les films d'ERGO peut se produire elle-aussi sur deux sites différents ; directement sur la surface (sites les plus accessibles) ou entre les piles de feuillets de graphène réduit (sites les moins accessibles). Ce genre de discussion basée sur la taille de l'ion et la cinétique existent dans le domaine des matériaux supercapacitif. Toutefois, dans ce travail une parfaite identification des espèces associées à des cinétiques différentes a été rendue possible grâce à l'approche de l'*ac*-électrogravimétrie.

Références

- 1 Lin, R. *FORMULATION OF ELECTROLYTES BASED ON IONIC LIQUIDS FOR SUPERCAPACITOR APPLICATIONS* Ph.D thesis, Université de Toulouse, (2012).
- 2 BENHADDAD, L. *Elaboration et caractérisation de poudres nanostructurées de MnO₂ et de polypyrrole : Application comme matériaux d'électrodes dans des dispositifs de stockage de l'énergie* Ph.D thesis, UNIVERSITÉ PIERRE ET MARIE CURIE, (2014).
- 3 Lu, W. & Dai, L. *Carbon Nanotube Supercapacitors*. (2010).
- 4 Gao, Q. *Optimizing carbon/carbon supercapacitors in aqueous and organic electrolytes* Ph.D thesis, Université d'Orleans, (2013).
- 5 Halper, M. S. E., James C. Supercapacitors: A Brief Overview. Report No. Case # 06-0667, (The MITRE Corporation, McLean, Virginia, USA., 2006).
- 6 Simon, P. & Gogotsi, Y. Materials for electrochemical capacitors. *Nat Mater* **7**, 845-854 (2008).
- 7 COME, J. *Caractérisation électrochimique de matériaux à insertion de Li pour supercondensateurs hybrides à haute densité d'énergie* Ph.D thesis, Université de Toulouse, (2012).
- 8 Kim, B. K., Sy, S., Yu, A. & Zhang, J. in *Handbook of Clean Energy Systems* (John Wiley & Sons, Ltd, 2015).
- 9 SEGALINI, J. *Etude de l'adsorption des ions dans des carbones microporeux ; application aux supercondensateurs* Ph.D thesis, Université de Toulouse (2012).
- 10 Levi, M. D., Salitra, G., Levy, N., Aurbach, D. & Maier, J. Application of a quartz-crystal microbalance to measure ionic fluxes in microporous carbons for energy storage. *Nat Mater* **8**, 872-875, doi:10.1038/nmat2559 (2009).
- 11 Sigalov, S., Levi, M. D., Daikhin, L., Salitra, G. & Aurbach, D. Electrochemical quartz crystal admittance studies of ion adsorption on nanoporous composite carbon electrodes in aprotic solutions. *Journal of Solid State Electrochemistry* **18**, 1335-1344, doi:10.1007/s10008-013-2171-7 (2013).
- 12 Sigalov, S. *et al.* Selective adsorption of multivalent ions into TiC-derived nanoporous carbon. *Carbon* **50**, 3957-3960, doi:10.1016/j.carbon.2012.04.002 (2012).
- 13 Sigalov, S., Levi, M. D., Salitra, G., Aurbach, D. & Maier, J. EQCM as a unique tool for determination of ionic fluxes in microporous carbons as a function of surface charge distribution. *Electrochemistry Communications* **12**, 1718-1721, doi:10.1016/j.elecom.2010.10.005 (2010).
- 14 Sauerbrey, G. Verwendung von Schwingquarzen zur Wägung dünner Schichten und zur Mikrowägung. *Z. Physik* **155**, 206-222, doi:10.1007/BF01337937 (1959).
- 15 To Thi Kim, L. *Etude de films électroactifs par couplage de techniques électrochimique et gravimétrique. Application à la caractérisation de membranes à conduction protonique*. Ph.D thesis, Université Pierre et Marie Curie, (2009).
- 16 Frackowiak, E., Vol. 9 (2007).
- 17 Frackowiak, E. & Béguin, F. Carbon materials for the electrochemical storage of energy in capacitors. *Carbon* **39**, 937-950, doi:[http://dx.doi.org/10.1016/S0008-6223\(00\)00183-4](http://dx.doi.org/10.1016/S0008-6223(00)00183-4) (2001).
- 18 Frackowiak, E., Metenier, K., Bertagna, V. & Beguin, F. Supercapacitor electrodes from multiwalled carbon nanotubes. *Applied Physics Letters* **77**, 2421-2423, doi:10.1063/1.1290146 (2000).
- 19 Hulicova, D., Yamashita, J., Soneda, Y., Hatori, H. & Kodama, M., Vol. 17 (2005).
- 20 Pan, H., Li, J. & Feng, Y. Carbon Nanotubes for Supercapacitor. *Nanoscale Research Letters* **5**, 654 - 668 (2010).
- 21 Chmiola, J. *et al.* Anomalous Increase in Carbon Capacitance at Pore Sizes Less than 1 Nanometer. *Science* **313**, 1760-1763, doi:10.2307/20031355 (2006).
- 22 Merlet, C., Salanne, M., Rotenberg, B. & Madden, P. A. Influence of solvation on the structural and capacitive properties of electrical double layer capacitors. *Electrochimica Acta* **101**, 262-271, doi:<http://dx.doi.org/10.1016/j.electacta.2012.12.107> (2013).
- 23 Agrisuelas, J. *et al.* Usefulness of F(dm/dQ) Function for Elucidating the Ions Role in PB Films. *Journal of The Electrochemical Society* **154**, F134, doi:10.1149/1.2728038 (2007).

- 24 Gabrielli, C., García-Jareño, J. J., Keddam, M., Perrot, H. & Vicente, F. Ac-Electrogravimetry Study of Electroactive Thin Films. I. Application to Prussian Blue. *The Journal of Physical Chemistry B* **106**, 3182-3191, doi:10.1021/jp013924x (2002).
- 25 Benmouhoub, C. *et al.* Influence of the Incorporation of CeO₂ Nanoparticles on the Ion Exchange Behavior of Dodecylsulfate Doped Polypyrrole Films: Ac-Electrogravimetry Investigations. *Electrochimica Acta* **145**, 270-280, doi:10.1016/j.electacta.2014.07.151 (2014).